

Christian Volmer

**Compact antenna arrays in
mobile communications**

A quantitative analysis of radiator coupling

Compact antenna arrays in mobile communications

A quantitative analysis of radiator coupling

Christian Volmer



Universitätsverlag Ilmenau
2010

Impressum

Bibliografische Information der Deutschen Nationalbibliothek

Die Deutsche Nationalbibliothek verzeichnet diese Publikation in der Deutschen Nationalbibliografie; detaillierte bibliografische Angaben sind im Internet über <http://dnb.d-nb.de> abrufbar.

Diese Arbeit hat der Fakultät für Elektrotechnik und Informationstechnik der Technischen Universität Ilmenau als Dissertation vorgelegen.

Tag der Einreichung: 20. März 2009

1. Gutachter: Univ.-Prof. Dr. rer. nat. habil. Matthias A. Hein
(Technische Universität Ilmenau)

2. Gutachter: Univ.-Prof. Dr.-Ing. habil. Reiner S. Thomä
(Technische Universität Ilmenau)

3. Gutachter: Univ.-Prof. Dr.-Ing. Klaus Solbach
(Universität Duisburg-Essen)

Tag der Verteidigung: 26. November 2009

Technische Universität Ilmenau/Universitätsbibliothek

Universitätsverlag Ilmenau

Postfach 10 05 65

98684 Ilmenau

www.tu-ilmenau.de/universitaetsverlag

Herstellung und Auslieferung

Verlagshaus Monsenstein und Vannerdat OHG

Am Hawerkamp 31

48155 Münster

www.mv-verlag.de

ISSN (Druckausgabe)

ISBN 978-3-939473-71-8 (Druckausgabe)

urn:nbn:de:gbv:ilm1-2009000416

Titelfoto: photocase.com | AlexFlint

Abstract

To meet the ongoing demand for higher data rates and greater user mobility, modern mobile communications systems increasingly employ adaptive antenna arrays. By moving antenna elements closer together, to fit them inside a cellular phone for instance, mutual coupling effects impair their radiation capabilities. To describe these impairments more descriptively in contrast to current approaches, the present thesis extends the familiar notion of radiation efficiency from a single radiator to arbitrary antenna arrays by introducing an orthogonal set of radiating degrees of freedom. Detailed examples illustrate the effects of mutual coupling. Decoupling and matching networks are introduced to counteract mutual coupling. Thus, a design method applicable to a broad class of antenna arrays is described and verified by numerous examples, thereby ohmic losses and narrow bandwidths are identified as major weaknesses of decoupling and matching networks in general. For an investigation of the influence of mutual coupling on a mobile diversity receiver system, closed-form expressions for its diversity gain are derived and discussed. The analysis is complemented by a comprehensive receiver noise model. Practical diversity and noise measurements confirm the validity of the theoretical concepts developed. The present work aims to convey a more descriptive understanding of radiator coupling and to raise awareness of the fact that aspects of the entire system must be accounted for for an objective assessment of the potentials of mutually coupled antenna arrays.

Kurzdarstellung

Um der anhaltenden Nachfrage nach höheren Übertragungsraten und größerer Mobilität zu begegnen, setzen moderne Mobilfunksysteme zunehmend adaptive Gruppenantennen ein. Rückt man Strahlerelemente zur Unterbringung in kleinen tragbaren Endgeräten (z.B. Handys) jedoch eng zusammen, so beeinträchtigen Verkopplungseffekte deren Abstrahleigenschaften. Um diese Beeinträchtigungen im Vergleich zu den üblichen Betrachtungsweisen anschaulicher zu beschreiben, erweitert die vorliegende Arbeit den bekannten Effizienzbegriff einer Einzelantenne auf beliebige Antennengruppen durch die Einführung orthogonaler Strahlungsfreiheitsgrade. Die Auswirkungen von Strahlerverkopplung werden anhand von Beispielen aufgezeigt. Anpass- und Entkoppelnetzwerke können der Strahlerverkopplung entgegenwirken. Für eine breite Klasse von Antennengruppen wird eine systematische

Entwurfsvorschrift vorgestellt und durch zahlreiche Beispiele bestätigt, dabei stellen sich Ohm'sche Netzwerkverluste und schmale Bandbreiten als allgemeine Hauptschwächen derartiger Netzwerke heraus. Zur Untersuchung des Einflusses der Strahlerverkopplung auf die Übertragungsqualität eines Diversitätsempfängersystems werden geschlossene Ausdrücke für seinen Diversitätsgewinn hergeleitet und diskutiert. Diese Analyse wird anschließend durch ein umfassendes Rauschmodell erweitert. Diversitäts- und Rauschmessungen bestätigen die theoretischen Betrachtungen. Die vorliegende Arbeit möchte ein anschaulicheres Verständnis von Strahlerverkopplung vermitteln und Bewusstsein dafür schaffen, dass eine Betrachtung des Gesamtsystems essentiell für eine objektive Beurteilung der Leistungsfähigkeit kompakter Gruppenantennen ist.

Theses of the dissertation

Modern mobile communications systems enhance their capabilities by exploiting the **spatial degrees of freedom** inherent in antenna arrays. Compact antenna arrays, for application in mobile phones for instance, exhibit undesirable **mutual coupling** of their radiators.

The radiation process of an n -port antenna array can always be described as the superposition of n **orthogonal modes of radiation**. Mutual coupling can be interpreted as impedance mismatch of these degrees of freedom.

Each degree of freedom can uniquely be assigned a radiation efficiency. This extends the **classical notion of efficiency** to arbitrary multi-port antennas. Mutual coupling inevitably causes a reduction of these efficiencies.

For lossless arrays these efficiencies can readily be established from the array **scattering matrix**. An analysis that accounts for ohmic array losses necessitates the **far-field patterns**.

Decoupling and matching networks are able to improve the matching efficiencies. Such networks generally exhibit a **narrow bandwidth** and considerable **ohmic losses**. Their design thus calls for suitable **quality metrics**.

By exploiting certain array symmetries, decoupling networks can often be designed **independent of the scattering parameters** of the compact antenna array. This property is attractive for **mass production**.

The diversity gain of mutually coupled antenna arrays can be estimated by virtue of **closed-form expressions**. In good approximation, mutual coupling introduces an equivalent **insertion loss** into the system. These figures of merit are inevitable for the development of **broadband** or **multi-band** designs.

The approximation formulae fit seamlessly into **widely applied models** for diversity analysis, and thus enhance the **practical applicability** of established approaches.

The diversity capabilities of a realistic receiver system can only be assessed if the **noise properties** of all receiver components are included in the analysis.

An **objective assessment** of the quality of decoupling and matching networks necessitates an extensive analysis of **network losses** and **network noise**. The actual enhancements due to these networks may be considerably **less than anticipated** in certain receiver applications.

The receiver model developed allows for **realistic predictions** in respect of the actual diversity capabilities of mutually coupled antenna arrays and receivers.

Although mutual coupling **always** impairs the system diversity gain in a Rayleigh-fading environment regardless of other factors that affect diversity performance, maximising beam-pattern orthogonality is a **theoretical** goal of array miniaturisation, but **not a practical** one.

Thesen zur Dissertation

In modernen mobilen Kommunikationssystemen kann die Übertragungsqualität durch Ausnutzung der **räumlichen Freiheitsgrade** von Gruppenantennen verbessert werden. Bei kompakten Gruppenantennen, wie sie z. B. für Mobiltelefone erforderlich sind, kommt es zur unerwünschten **Verkopplung der Strahlerelemente**.

Der Strahlungsvorgang einer n -Tor Antenne lässt sich immer als Superposition von n **orthogonalen Strahlungsmoden** beschreiben. Strahlerverkopplung kann als Impedanzfehlانpassung dieser Strahlungsfreiheitsgrade aufgefasst werden.

Jedem Freiheitsgrad kann eindeutig eine Abstrahleffizienz zugeordnet werden. Dies verallgemeinert den **klassischen Effizienzbegriff** auf beliebige Gruppenantennen. Strahlerverkopplung führt zwangsläufig zu einer Verminderung dieser Effizienzen.

Bei verlustlosen Gruppenantennen lassen sich die Effizienzen einfach aus den **Streuparametern** ermitteln. Die Berücksichtigung Ohm'sche Verluste erfordert die Einbeziehung der **Fernfelddaten**.

Die Anpasseffizienzen können mithilfe von **Anpass- und Enkoppelnetzwerken** verbessert werden. Derartige Netzwerke sind **schmalbandig** und stark **verlustbehaftet**. Ihr Entwurf erfordert daher entsprechende **Qualitätskenngrößen**.

Durch Ausnutzung bestimmter Symmetrieeigenschaften lassen sich Entkoppelnetzwerke oft **unabhängig von den Streuparametern** der kompakten Gruppenantenne entwerfen. Diese Eigenschaft ist für die **Massenproduktion** interessant.

Der Diversitätsgewinn verkoppelter Gruppenantennen lässt sich durch **geschlossene Näherungsformeln** berechnen. Verkopplung kann in guter Näherung als **Systemeinfügedämpfung** betrachtet werden. Derartige Kenngrößen sind für **Breitband-** und **Mehrbandanwendungen** unentbehrlich.

Die Näherungsformeln fügen sich nahtlos in **bekannte Ansätze und Modelle** zur Diversitätsanalyse ein, und vereinfachen somit deren **praktische Anwendung**.

Die Diversitätseigenschaften eines realen Empfängers lassen sich nur unter Einbeziehung der **Rauscheigenschaften** aller Empfängerkomponenten ermitteln.

Die **objektive Beurteilung** der Qualität von Anpass- und Entkoppelnetzwerken erfordert ebenfalls eine umfangreiche **Verlust- und Rauschanalyse**. Der Einsatz solcher Netzwerke an einem Empfänger ist, je nach Anwendung, möglicherweise **fragwürdig**.

Das entwickelte Empfängermodell ermöglicht **realistische Vorhersagen** bezüglich der tatsächlichen Diversitätseigenschaften verkoppelter Gruppenantennen und dazugehöriger Empfänger.

Obwohl Strahlerverkopplung die Diversitätseigenschaften in einem Rayleigh-Kanal unabhängig von anderen Faktoren **stets** negativ beeinflusst, stellt die Maximierung der Orthogonalität der Torrichtcharakteristiken ein **theoretisches**, jedoch **kein praktisches Optimierungsziel** für die Miniaturisierung von Gruppenantennen dar.

Preface

The present work is a compilation of the results and insights collected during my time as a research assistant at the RF and Microwave Research Laboratory of the Ilmenau University of Technology. My research was part of the project “Miniaturised Diversity Antennas for Satellite Communications” (MIDIAS). The project and thus my position at the laboratory were funded by the German Aerospace Centre (grant no. 50YB0509) on behalf of the German Federal Ministry of Economics and Research, for which I am very grateful.

I thank the head of the laboratory, Prof. Matthias Hein, for the opportunity to work under his supervision and for the freedom to develop my own ideas and approaches to the subject.

Furthermore, I am grateful to Prof. Reiner Thomä and Prof. Klaus Solbach for reviewing my thesis.

Several people supported me in the pursuit of this work. In particular I would like to mention: my fellow-researcher Dr. Jörn Weber for fruitful discussions regarding the project; my other office-mate Dipl.-Ing. Mario Schühler for technical and non-technical discussions; Dr. Kurt Blau and Dr. Ralf Stephan for their assistance with both academic and administrative matters; Mr. Michael Huhn and Mr. Matthias Zocher for their untiring support on technical issues; my student assistants Dipl.-Ing. Ulf Wetzker and Mr. Christian Großmann for introducing me to the art of FPGA and USB programming; Dipl.-Ing. Hendrik Bayer for doing the LNA designs; all the rest of my colleagues for the pleasant work climate.

The following companies have provided me with free samples of their products: Analog Devices Corp., BFi OPTiLAS GmbH, Cypress Semiconductor Corp., Hittite Microwave Corp., Maxim Integrated Products, Microchip Technology, MSC Vertriebs GmbH, and Richardson Electronics.

I thank my brother Matthias, my girlfriend Maren Thole, M. Schühler, K. Blau, and J. Weber for proof-reading my thesis.

Finally, I thank my parents, my brother, and my girlfriend for their understanding and encouragement throughout the past years.

Christian Volmer
Ilmenau, 17th December 2009

Contents

1	Introduction	1
2	Power considerations at multi-port antennas	5
2.1	Earlier work	6
2.2	Eigenmode description of lossless arrays	8
2.2.1	Single-port antenna matching efficiency	8
2.2.2	Generalisation to multi-port antennas	10
2.2.3	The fundamental modes of radiation	14
2.2.4	Reflections of eigenmodes	16
2.3	Eigenmode far-field patterns	18
2.3.1	Far-field patterns and the radiation matrix	18
2.3.2	Beam-pattern orthogonalisation	22
2.4	Non-distinct eigenefficiencies	25
2.5	Ohmic array losses	26
2.6	An equivalent circuit for lossless arrays	27
2.7	Examples of the consequences of radiator coupling	30
2.7.1	Analysis of a manufactured $\lambda_0/10$ three-port array	30
2.7.2	Influence of number of radiators and separation	41
2.8	Summary	43
3	Decoupling and matching networks	45
3.1	General conditions for decoupling and matching	46
3.2	Decoupling by eigenmode excitation	48
3.3	Directional couplers as decoupling networks	51
3.3.1	Example: symmetric two-port antenna array	51

3.3.2	Example: symmetric three-port antenna array	52
3.4	A systematic design procedure for decoupling networks . . .	54
3.4.1	Two-element decoupling	55
3.4.2	Decoupling across a symmetry plane	57
3.4.3	Radiator merging	59
3.4.4	Eigenmode matching	63
3.5	Efficiency considerations	64
3.6	Example implementations	67
3.6.1	Linear $\lambda_0/4$ three-port array	67
3.6.2	LTCC implementation of a three-port DMN	74
3.6.3	Broadband matched two-port array	78
3.6.4	Circular $\lambda_0/10$ four-port array	85
3.7	Summary	88
4	Diversity reception with compact antenna arrays	91
4.1	Overview and past work	92
4.2	Figures of merit for correlated fading	94
4.2.1	A simplified diversity model	95
4.2.2	Array gain of a mutually coupled array	101
4.2.3	Diversity gain over a single receive antenna	102
4.2.4	Diversity loss over an ideal antenna array	105
4.3	Extensions to the diversity model	110
4.3.1	Influence of the communications environment	111
4.3.2	Effects of a decoupling and matching network	114
4.3.3	Spatially coloured receiver noise	116
4.4	A complete receiver model	118
4.4.1	Antenna array noise	122
4.4.2	Network noise	122
4.4.3	Front-end amplifier noise	124
4.4.4	Discussion of the front-end model	125
4.5	Summary	131
5	Compact antenna arrays in practice: a diversity receiver	135
5.1	Overview of the diversity system	136
5.1.1	The transmitter	137
5.1.2	The receiver front-end	143
5.1.3	Baseband processing	147

5.1.4	The graphical user interface	150
5.2	Benefits of decoupling and matching networks	152
5.3	Verification of the diversity figures of merit	157
5.4	Measurements of the signal envelope covariance matrix . . .	163
5.5	Front-end noise characterisation	168
5.5.1	Noise characterisation of a single receiver-branch . .	170
5.5.2	Noise characterisation of the multi-port receiver . . .	174
5.5.3	Influence of noise on the SNR diversity gain	179
5.6	Summary	188
6	Summary and outlook	191
7	Zusammenfassung und Ausblick	197
A	Proofs and derivations	205
A.1	Diagonalisation of eigen-reflections	205
A.2	Ohmic eigenefficiencies and DMNs	206
A.3	Matrix-form of a single-port matching network	207
A.4	Matrix-form of a decoupling and matching network	209
A.5	Eigenmodes fade independently	213
A.6	Series expansion of the diversity gain	215
B	Waves, scattering parameters, and noise	219
B.1	Scattering parameters	221
B.1.1	Definition	221
B.1.2	Interconnection of multi-port junctions	222
B.1.3	Renormalisation	225
B.2	Noise wave description	227
	Bibliography	231
	Notation and abbreviations	247

Chapter 1

Introduction

In mobile communications there is a continuing demand for greater user mobility at even higher data rates. Since the frequency spectrum is a limited and thus expensive resource, modern systems attempt to increase their capacity by exploiting the spatial dimension of the communications environment. This is made possible with the implementation of multiple antennas at one or both ends of the mobile link. As the 1400 page compilation by Van Trees [20] suggests, communications engineers are very inventive in the development of corresponding multi-antenna signal processing techniques. Without going into much detail here, these algorithms have in common that they exploit the *degrees of freedom* available in an antenna array, that is, the ability of an array to transmit and to receive *different and independent* signals at the *same* time and frequency.

In a multi-path environment, where the line-of-sight between transmitter and receiver is obstructed, the transmitted signal reaches the receiver from several directions simultaneously as the result of reflections and scattering effects. A receiver equipped with a single antenna can only detect the superposition of these wave fronts, which can be either constructive or destructive in nature depending on the paths travelled by the signal. If the receiver or any other part of the communications environment moves, these paths change. In consequence, the received signal strength typically exhibits strong and rapid variations with time. This effect is known as *short-term fading* and considerably degrades the quality of the link, especially when operated near the border

of the system coverage area. If two or more receive antennas are employed, each antenna receives the same information but impaired by a different fading characteristic. Substantial improvements of the link quality are now achievable simply by choosing the antenna receiving the strongest signal. A familiar example of such a *diversity system* is a professional WLAN (wireless local area network) access point, which often employs two, sometimes even three antennas for enhanced performance.

So-called multiple-input-multiple-output (MIMO) systems take the idea one step further and use several transmit antennas to broadcast parallel data streams in a way that allows clean reconstruction at a multi-antenna receiver system. This approach promises considerable improvements of the channel capacity over existing non-MIMO systems. As modern digital signal processors become smaller, more powerful, and yet less expensive, MIMO techniques presently begin to find their way into consumer equipment. Already available are preliminary implementations of the upcoming IEEE 802.11n WLAN standard. Another example is the UMTS-LTE (long-term evolution) mobile telecommunications standard presently under development.

There seems no question that multi-antenna systems present the key to meeting our future mobile communications needs. To exploit the benefits at hand-held mobile terminals, such as cellular phones or personal data assistants (PDAs), the radiating elements that constitute an antenna array must be placed close together. In this context, “close” is generally considered closer than half a free-space wavelength. With decreasing separation, however, electromagnetic coupling causes distinct radiators to increasingly coalesce and act as a single antenna. The ability of the antenna array to resolve multiple paths of signal propagation becomes impaired and thus the effective number of degrees of freedom available is reduced.

The detrimental effects of mutual coupling are widely known in the literature. Yet the commonly applied method for judging the quality of an antenna array is largely limited to qualitative statements of the form “good” or “not good”. A comparison between different antenna array designs, especially when more than two radiators are involved, is rather difficult, except for few very special cases. In order to push the limits of miniaturisation further, we need a *quantitative* measure not only of mutual coupling itself, but, most importantly, of the *influence* that mutual coupling exerts on a particular mobile communications *application*.

Of course, there is always the possibility to have simulation software for

mobile communications channels and systems compute all conceivable kinds of system quality parameters. The accuracy of these results could be arbitrarily high depending on the amount of effort spent on the development of the software and the system models employed. On the downside, such simulators are comparatively laborious and time-consuming to apply. For this reason, the present work aims at the development and the verification of *simple metrics* that are *applied quickly in practice*, capture the *essential parameters* related to array performance, and nonetheless provide the design engineer with an *accurate overview* of the capabilities of mutually coupled antenna arrays. Such figures of merit are particularly helpful for the broadband characterisation and optimisation of very compact arrays, which can often be impedance-matched over a narrow bandwidth only.

Due to the vast number of different multi-antenna processing techniques, the present thesis cannot provide a universal solution to the general problem of mutual coupling. It can, however, encourage to look beyond the phenomenon “mutual coupling” as such, propose *alternative means* of its interpretation to complement established approaches, and demonstrate that the effects of mutual coupling cannot genuinely be comprehended unless aspects of the *entire system* are taken into account.

This thesis is organised as follows:

Chapter 2, Power considerations. The efficiency is not only a crucial parameter describing system performance in general, but also a simple and intuitive one. Based on the concept of degrees of freedom, this chapter demonstrates how the notion of efficiency can be generalised to arbitrary n -port arrays.

Chapter 3, Decoupling and matching networks. Recently, passive decoupling and matching networks have come under discussion as a promising way to counteract the effects of mutual coupling. This chapter presents a general design approach applicable to a wide class of antenna arrays, and comes up with an accurate performance analysis that accounts for ohmic network losses.

Chapter 4, Diversity considerations. In this chapter we study the effects of mutual coupling on diversity reception. Closed-form expressions for

the diversity gain achievable with mutually coupled arrays are devised. These figures of merit enable an evaluation of array performance over frequency and thus foster the design and optimisation of broadband and multi-band systems. The chapter includes a complete receiver noise framework to accurately model the effects of noise coupling and mismatch.

Chapter 5, Practical verification. The claims of Chapter 4 are confirmed in a practical setting by means of measurements conducted with a specifically designed diversity receiver. The chapter concludes with a detailed analysis of several mutually coupled antenna arrays and decoupling and matching networks. The results clearly prove that a careful analysis of all system aspects is essential to predict its actual performance.

Chapter 6, Summary and outlook. This concluding chapter discusses how the insights developed in the course of this thesis can be put into practice in order to maximise the performance of future communications devices. In the context of mutual coupling and decoupling and matching networks it is crucial to avoid misleading conclusions that often have little to do with reality.

Chapter 2

Power considerations at multi-port antennas

In this chapter, we are going to investigate the radiation efficiency of multi-port antennas. “Power” is a valuable resource in a number of regards. It is therefore desirable that most of the power fed into the input terminal of an antenna is actually turned into radiation. Far more important perhaps is the fact that, by the principle of reciprocity, the same efficiency takes effect in the receive direction as well. Whereas it is basically possible to arbitrarily increase the power level at the transmitter to overcome a lowly efficient transmit antenna, this is not feasible at the receiver.

The analysis that will be presented here is particularly suited for compact antenna arrays because it automatically takes coupling between radiators into account. We will find that any n -port antenna array can be interpreted in terms of n fundamental modes of radiation. These modes, which we call the *eigenmodes* of the array, possess orthogonal beam patterns. Consequently, they do not exchange power and thus represent an uncoupled description of the radiation process. Associated with the eigenmodes is a set of n radiation efficiencies that characterises the radiation capabilities of the degrees of freedom available. As radiators move closer together, these efficiencies begin to diminish rapidly. The principal goal of this model is to convey an intuitive perception of mutual radiator coupling in respect of mobile communications applications.

If a lossless antenna array is assumed, the efficiencies can be determined conveniently from scattering parameter measurements. This equips the designer with a simple yet powerful means to quantify and subsequently optimise the radiation properties. In the case of very strong radiator coupling, more realistic results are obtainable from far-field measurements, which complement the analysis with information about ohmic losses inside the antenna array.

First, an overview of past work in the field of compact antenna arrays will be given. We then begin our efficiency analysis by looking at lossless antenna arrays. In a subsequent step, this theory is extended with a description of ohmic losses. At the end, a detailed practical example will demonstrate the usefulness of the concepts developed in this chapter.

2.1 Earlier work

Many antenna array textbooks (e.g., Balanis [2], Hansen [5], Kraus and Marhefka [10]) omit the possible role of radiator coupling throughout major parts of their analysis and then include a chapter on mutual coupling and the associated *mutual impedance* between elements. The mutual impedance is a quantity that can undeniably be measured, modelled, and treated theoretically; its expressiveness in respect of power efficiency investigations, however, is rather limited.

A natural consequence seems to switch from the impedance domain to the power-wave related scattering parameter description, which has the added advantage of simple measurability. Obviously, power that is reflected at the excited port or coupled to other ports is unavailable for radiation. Non-zero scattering parameters therefore indicate reduced array radiation efficiency, and it is a desirable goal to minimise the input reflection coefficients as well as the coupling coefficients between ports [34, 57, 105].

In practice, port reflections and coupling cannot be eliminated entirely. Therefore, the immediate question arises how much coupling is tolerable for a given purpose. To this end, the *active reflection coefficient* [48, 71, 87] and the *total active reflection coefficient* (TARC) [27, 28, 58] are encountered in the literature as the ratio of the power reflected at to the power incident on the array input ports. Since power that becomes reflected cannot radiate, the TARC is directly linked to the radiation efficiency. As we soon shall see, however, the TARC, and thus the array efficiency, depends on the amplitude

and phase distribution exciting the antenna array terminals.

Gilbert and Morgan [42] recognised that highly compact antenna arrays become sensitive to manufacturing tolerances for certain excitations and expressed this insight as the classic *sensitivity factor*. Further analysis revealed that the sensitivity factor is an immediate indicator for the radiation efficiency of an antenna array. In the same way as the TARC, however, it is excitation-dependent and thus not a suitable measure for the radiation capabilities of the antenna array itself.

More related to antenna diversity than efficiency is the *correlation coefficient* ρ of the signals received at the antenna ports [66, 79]. Increased correlation impairs the diversity capabilities of an antenna array and this, in some regard, may be interpreted as loss of efficiency. The correlation coefficient is a well-established parameter in the literature [35, 37, 43, 44, 52, 55, 70, 92, 106]. Its popularity stems from the fact that it may be estimated from the real *envelope correlation coefficient* ρ_e , which was easier to measure in the early days of mobile communications [66]. We are going to deal with antenna diversity later in Chapter 4. Although ρ is a quantity independent of array excitation, it only captures the influence of radiator coupling but not the effects of impedance mismatch at individual array terminals. Both aspects are, however, relevant to both the diversity performance as well as the radiation efficiency. Another drawback is that a clear statement about what range of values of ρ is acceptable for good performance is only available for symmetric two-port antenna arrays.

There have also been publications more closely related to the concepts of the present thesis. Most notably, Stein [75] in 1962 was the first author who rigorously described the relationship between array scattering parameters, far-field radiation patterns, and ohmic losses within the array. He also observed the existence of “canonical beam-patterns”, i.e., the eigenmodes in our terminology, and their orthogonality properties. As Stein himself writes at the end of [75, Section XI], he is unsure whether these “patterns may be of direct physical interest” and concludes that “no obvious engineering advantage ensues”. In the context of mutual radiator coupling, his work has since attracted no particular attention.

Recently, Chaloupka et al. [88, 89, 95, 119, 120] followed an approach similar to Stein’s with the introduction of impedance-domain based *eigenmodes*, *modal admittances*, and *modal matching factors*, all of which are properties inherent to the antenna array. This novel conception of array radiation

allows an array description independent of its excitation. Still, the particular way by which eigenmodes were defined restricts the analysis to certain symmetric cases.

2.2 Eigenmode description of lossless arrays

The following work builds upon the conceptual foundations laid by Stein and Chaloupka to come up with a more consistent eigenmode formulation of the radiation process of arbitrary multi-port antennas. The only requirement is reciprocity of the array. Contrary to Stein's concluding remark, the advantages for the array engineer should soon become evident [142].

There are two basic mechanisms in an antenna by which the power available from an exciting source (the *generator*) is “lost” by means other than radiation: *power dissipation* and *power reflection*. Both effects negatively affect radiation efficiency. Power dissipation takes place in conductors due to *ohmic losses*, but also in dielectric substrate materials used for instance for printed antenna structures. Although ohmic losses play a notable role in the development of compact antenna arrays, their practical characterisation is rather taxing. We therefore defer further discussions until Section 2.5 and assume that ohmic losses are negligible for the following analysis of reflection losses.

2.2.1 Single-port antenna matching efficiency

Consider a lossless single-port antenna with generally complex port impedance Z connected to some generator with complex internal impedance Z_{in} . It is a well-known fact that maximum power transfer occurs if and only if $Z = Z_{\text{in}}^*$. This condition is commonly referred to as *conjugate impedance matching* or *power matching*. The amount of power radiated by the antenna is then equal to the *available power* P_{av} of the source, where P_{av} is a generator-specific constant. Note that it is irrelevant whether the generator is a voltage source or a current source as both are equivalent. When the impedances are not matched, the power radiated is always less than P_{av} and the degree of *mismatch* is expressed by the complex *reflection coefficient* Γ defined as [11, Eqn. (1.56)]

$$\Gamma = \frac{Z - Z_{\text{in}}^*}{Z + Z_{\text{in}}}. \quad (2.1)$$

For our purposes, the square of the absolute value of the reflection coefficient is of particular interest because it represents the fraction of power not accepted by the antenna. More specifically, the power P_{rad} radiated by the lossless antenna may now be written in terms of Γ and P_{av} as [11, p. 37]

$$P_{\text{rad}} = (1 - |\Gamma|^2)P_{\text{av}}. \quad (2.2)$$

Consequently, the quantity $1 - |\Gamma|^2$ may be considered the *matching efficiency* between generator and antenna. For passive antennas, where $\text{Re}\{Z\} > 0$, the matching efficiency is always between 0 and 1.

The notion of power reflection is borrowed from transmission line theory where an impedance mismatch at one end of the line causes power to be reflected physically. This picture often serves as a descriptive explanation of the interplay between a generator and a load. Naturally, there are fundamental differences between transmission lines and power sources that are important to apprehend.

First and most obviously, the above definition of Γ contains the complex conjugate of Z_{in} in its numerator, which is different from the definition known from transmission line theory. It is, however, consistent with the concept of power waves and scattering parameters (Appendix B) and permits the application of scattering parameter theory even if the *normalising impedance*, here Z_{in} , is complex.

Second, the term “reflection coefficient” suggests that the fraction of power not radiated by the antenna due to mismatch is dissipated in the generator’s internal impedance. Thus, one may argue that power matching is an essential precondition for an energy-efficient system. In fact, the energy-efficiency of a power-matched system is always 50 %: the same amount of power that is radiated by the load antenna is also dissipated in the internal resistance of the source. In systems where large power levels are involved, e.g., at television broadcast aerials, this seems a dissatisfying fact. Therefore, a certain degree of mismatch is often deliberately introduced into the system to *increase* the overall system efficiency. This aspect of *source efficiency* is not considered any further in this work and the interested reader is referred to Hoffmann [6, pp. 66-68].

Before we move on to multi-port systems and realise that the matching efficiency is nonetheless a crucial parameter for mutually coupled antenna arrays, two numerical examples are given. A resonant half-wave dipole antenna has a terminal impedance of about $Z = 73 \, \Omega$ [2, p. 446]. If driven from

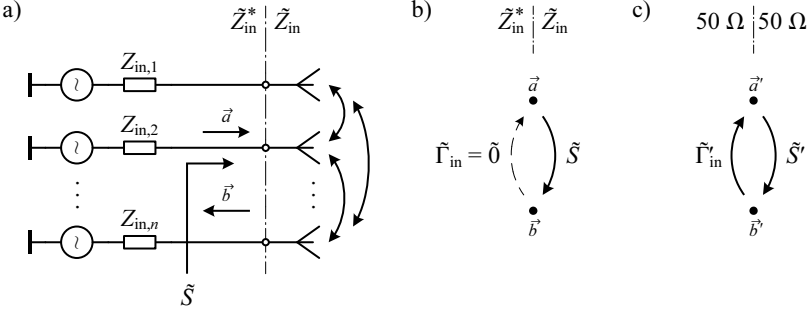


Fig. 2.1: A set of n generators with internal impedances $Z_{in,i}$ connected to a coupled n -port array of antennas with scattering matrix \tilde{S} . (a) Schematic diagram, (b) signal flow graph when the wave quantities are normalised with respect to the generator impedances, and (c) signal flow graph with the familiar $50\ \Omega$ normalisation.

a generator with $Z_{in} = 50\ \Omega$, then $\Gamma = 0.187$ and the matching efficiency of this setup is 96.5 %. A fraction of 3.5 % is reflected to the generator, which corresponds to a *return loss* of 14.6 dB. A folded dipole with $Z \approx 300\ \Omega$ [2, Eqn. (9-25)] driven from the same source has an efficiency of 49 % and a return loss of 2.9 dB.

As a rule of thumb, antennas with a return loss better than 10 dB, whose matching efficiency is therefore greater than 90 %, qualify as “good” radiators (e.g., [22, p. 354]). Depending on the particular application, other criteria may apply of course.

2.2.2 Generalisation to multi-port antennas

Scattering matrices are the logical extension of the reflection coefficient (2.1) to multiple ports. We use them here for the description of multi-port antenna arrays because, unlike impedance or admittance matrices, they are ultimately related to the *power flow* within an electronic device and thus lend themselves to power efficiency investigations. The reader is expected to be familiar with basic scattering parameter concepts, e.g., [6, 11, 13].

Figure 2.1a shows a set of n generators driving an arbitrary coupled linear n -port antenna array with scattering matrix \tilde{S} . The term “linear” refers to the linearity of the materials employed in the array and not to the arrange-

ment of the radiating elements. In fact, the latter is irrelevant to the following theory. Mutually coupled antenna arrays will have a scattering matrix with off-diagonal elements considerably different from zero. The waves a_i incident on each port i will be denoted by the complex incident wave column vector $\vec{a} = (a_1 \ a_2 \ \cdots \ a_n)^T$. Similarly, the waves reflected from the antenna will be denoted by the column vector \vec{b} , with the familiar relationship

$$\vec{b} = \tilde{S} \vec{a}. \quad (2.3)$$

All field quantities encountered in this thesis, and these include \vec{a} and \vec{b} , represent complex frequency-dependent harmonic root-mean-square amplitudes. The total power incident on and the total power reflected from the antenna array are thus expressed by

$$P_{\text{in}} = \sum_{i=1}^n |a_i|^2 = |\vec{a}|^2 = \vec{a}^H \vec{a} \quad \text{and} \quad P_{\text{re}} = \sum_{i=1}^n |b_i|^2 = |\vec{b}|^2 = \vec{b}^H \vec{b}, \quad (2.4)$$

respectively. From this point on, we deviate from the standard convention of using a normalising impedance of $50 \ \Omega$ for scattering matrices. As with (2.2), where the reflection coefficient of the single-port load is expressed with respect to the impedance of the driving source, we normalise the antenna array scattering matrix to the internal impedances $Z_{\text{in},i}$ of the generators. In consequence, the diagonal matrix $\tilde{\Gamma}_{\text{in}}$ of the generator reflection coefficients vanishes, i.e., $\tilde{\Gamma}_{\text{in}} = 0$. In other words, the normalisation ensures that, mathematically, power in form of \vec{b} -waves reflected by the antenna array is fully absorbed within the generators and is not reflected again only to oscillate back and forth between generators and array. Viewed from the antenna array's perspective, these generators are non-reflective terminations of its ports.

Figures 2.1b and 2.1c portray the signal flow graphs of our system with normalisation to the $Z_{\text{in},i}$ and with the standard $50 \ \Omega$ normalisation, respectively. The $50 \ \Omega$ normalisation introduces a loop into the flow graph, which demands special treatment in the form of matrix inverses [72]. Figure 2.1b on the other hand is trivial; the following theory is free of explicit occurrences of $Z_{\text{in},i}$ or $\tilde{\Gamma}_{\text{in}}$ and can thus concentrate on the properties of the antenna array. The information about the generators is not lost, of course; rather it is now implicated by the normalisation of \tilde{S} .

It is important to understand that the above normalisation requirement does *not* in any way restrict the applicability of the following theory. Appendix B presents an overview of advanced scattering parameter topics not

covered by standard microwave textbooks. There are conversion formulae between different normalising impedances as well as to and from impedance and admittance matrices *without loss of information*. Different ports may even be assigned distinct normalising impedances.

As the result of the normalisation, there is now a simple relationship between the total power P_{av} available from the generators and what we call the *antenna excitation vector* \vec{d} :

$$P_{\text{av}} = P_{\text{in}} = \vec{d}^{\text{H}} \vec{d}. \quad (2.5)$$

Since we assume lossless antenna arrays at this point, we may conclude that the power P_{rad} radiated by the antenna array is the difference between P_{in} and P_{re} . Further substitution yields

$$\begin{aligned} P_{\text{rad}} &= P_{\text{in}} - P_{\text{re}} = \vec{d}^{\text{H}} \vec{d} - \vec{b}^{\text{H}} \vec{b} \\ &= \vec{d}^{\text{H}} \vec{d} - \vec{d}^{\text{H}} \tilde{S}^{\text{H}} \tilde{S} \vec{d} \\ &= \vec{d}^{\text{H}} (\tilde{I} - \tilde{S}^{\text{H}} \tilde{S}) \vec{d} \\ &= \vec{d}^{\text{H}} \tilde{H} \vec{d}. \end{aligned} \quad (2.6)$$

The matrix

$$\tilde{H} = \tilde{I} - \tilde{S}^{\text{H}} \tilde{S}, \quad (2.7)$$

which we call the *radiation matrix* of the array, can be considered the multi-port equivalent of the term $1 - |\Gamma|^2$ encountered above in (2.2). Since \tilde{H} is Hermitian ($\tilde{H}^{\text{H}} = \tilde{H}$), P_{rad} is a real quantity for arbitrary excitation \vec{d} , as required [8, Theorem 4.1.3].

By relating P_{rad} to the power $P_{\text{av}} = P_{\text{in}}$ available from the generators, we obtain a matching efficiency function $\lambda(\vec{d})$:

$$\lambda(\vec{d}) = \frac{P_{\text{rad}}}{P_{\text{av}}} = \frac{\vec{d}^{\text{H}} \tilde{H} \vec{d}}{\vec{d}^{\text{H}} \vec{d}}. \quad (2.8)$$

We realise that, in contrast to single antennas, the matching efficiency of an antenna array is *not* a constant. There are cases where it exhibits strong dependence on the array excitation vector \vec{d} , as the following numerical example reveals.

Consider a symmetric two-port antenna array with scattering matrix

$$\tilde{S} = \begin{pmatrix} 0.4 & -0.5 \\ -0.5 & 0.4 \end{pmatrix}. \quad (2.9)$$

The return loss and the isolation correspond to about 8 dB and 6 dB, respectively. Judging by these numbers, we would not expect this antenna to be exceptionally efficient. But can we give a more precise statement?

Before we answer this question, let us evaluate (2.8) for a few example excitations. We start with exciting one radiator and terminating the other. This makes $\vec{d} = (1 \ 0)^T$ and $\lambda(\vec{d}) = 59 \%$. As expected, the efficiency is moderate. We now excite both radiators with equal power and equal phase, so $\vec{d} = (1 \ 1)^T$ and $\lambda(\vec{d}) = 99 \%$. Suddenly the antenna array possesses super-radiation properties. When we excite both radiators with equal power but with a phase difference of 180° , however, $\vec{d} = (1 \ -1)^T$ and the efficiency becomes a mere 19 %. We observe that in this example the matching efficiency of the array varies as much as 7 dB depending on the port excitation.

There are limits on the maximum and the minimum efficiency of an antenna array. Expression (2.8) has the form of a Rayleigh-quotient, whose range is bounded by the smallest and the largest eigenvalue of \tilde{H} [8, p. 176]:

$$\lambda_{\min} \leq \lambda(\vec{d}) \leq \lambda_{\max}, \quad \text{for all } \vec{d} \in \mathbb{C}^n. \quad (2.10)$$

In our example the eigenvalues are $\lambda_{\min} = 0.19$ and $\lambda_{\max} = 0.99$, two numbers, which we recognise from the previous paragraph as the efficiencies of the out-of-phase and the in-phase excitation of the array. Knowing the eigenvalues we can now be certain that no array excitation yields an efficiency lower than 19 %. In this regard, the smallest eigenvalue of \tilde{H} is an important figure of merit for the radiation quality of a multi-port antenna array and is easily determined by scattering parameter measurements.

An alternative way of expressing the worst-case matching efficiency is by the spectral matrix norm [8, p. 295] of the scattering matrix:

$$\lambda_{\min} = 1 - \|\tilde{S}\|_2^2. \quad (2.11)$$

By analogy to (2.2) the quantity $\|\tilde{S}\|_2$ may thus be thought of as the worst-case reflection coefficient of the array.

Besides a reduction of the overall antenna efficiency, a strongly varying matching efficiency brings about an additional challenge in a transmitting system. Amplifiers driving the array confront greatly changing termination impedances. Depending on the momentary impedance, an antenna driver may be required to deliver considerably higher voltage or current amplitudes than if it were driving its nominal load; it may even be required to sink the power

coupling from neighbouring amplifiers and still maintain the correct amplitude and phase of its a -wave. These facts elevate the linearity requirements imposed on the transmit amplifiers.

2.2.3 The fundamental modes of radiation

Since the radiation matrix \tilde{H} is Hermitian, it diagonalises under a unitary similarity transformation [8, p. 104]. Hence, we may write

$$\tilde{H} = \tilde{Q}\tilde{\Lambda}\tilde{Q}^H, \quad \text{with } \tilde{\Lambda} = \text{diag}\{\lambda_1, \lambda_2, \dots, \lambda_n\}, \quad (2.12)$$

and \tilde{Q} unitary (i.e., $\tilde{Q}\tilde{Q}^H = \tilde{I}$). Because

$$\tilde{\Lambda} = \tilde{Q}^H \tilde{H} \tilde{Q} = \tilde{I} - \tilde{Q}^H \tilde{S}^H \tilde{S} \tilde{Q}, \quad (2.13)$$

with the product $\tilde{S}^H \tilde{S}$ being non-negative definite, all eigenvalues λ_i are real and less than or equal to one. Furthermore, all eigenvalues can be shown to be non-negative for passive arrays. To keep the subsequent discussion simple, we postulate that all eigenvalues are distinct; issues with non-distinct eigenvalues are addressed later in Section 2.4.

Substituting (2.12) into (2.6) and remembering that $\tilde{\Lambda}$ is diagonal, we obtain for the radiated power

$$\begin{aligned} P_{\text{rad}} &= \vec{d}^H \tilde{H} \vec{d} = \vec{d}^H \tilde{Q} \tilde{\Lambda} \tilde{Q}^H \vec{d} \\ &= \vec{d}_m^H \tilde{\Lambda} \vec{d}_m \\ &= \sum_{i=1}^n \lambda_i |a_{m,i}|^2, \end{aligned} \quad (2.14)$$

with

$$\vec{d}_m = \tilde{Q}^H \vec{d}, \quad \text{or} \quad a_{m,i} = \vec{q}_i^H \vec{d}. \quad (2.15)$$

We call the i th column of \tilde{Q} the i th *eigenmode* \vec{q}_i of the antenna array [142]. By their defining equation (2.12), eigenmodes are normalised to unit power with $|\vec{q}_i|^2 = 1$ for all i . Transformation (2.15) decomposes an arbitrary incident wave vector \vec{d} into a weighted sum of eigenmodes \vec{q}_i , whose modal weights are given by the individual elements $a_{m,i}$ of \vec{d}_m . For this reason, the vector \vec{d}_m will be called the *modal excitation vector*.

Whereas $|a_i|^2$ expresses the power fed into the i th *port* of the array, $|a_{m,i}|^2$ can be interpreted as the power *excited* in the i th *eigenmode*. The unitary property of \tilde{Q} ensures that $|\vec{a}|^2 = |\vec{a}_m|^2$, implying that the total power incident on the array equals the sum of the powers excited in its eigenmodes. Each eigenmode i has an associated modal radiation efficiency, or *eigenefficiency* λ_i , which equals the proportion of excited eigenmode power that actually radiates into the far field.

This eigenmode decomposition allows Eqn. (2.14) to express the total radiated power as a single sum over the respective powers radiated in the individual eigenmodes. This suggests an interpretation of the radiation process in terms of n orthogonal and thus independent “mechanisms” or *degrees of freedom*. Furthermore, we may consider the set of eigenefficiencies $\lambda_1, \lambda_2, \dots, \lambda_n$ a *unique description* of the radiation qualities of those degrees of freedom. There are always as many degrees of freedom as there are array terminals. The eigenefficiencies consequently serve as a *logical generalisation* of the familiar efficiency of single radiators to multi-port antennas. In the course of this chapter, we will collect additional pieces of evidence for the fundamental signification of this eigenmode conception.

If we wished to specify some kind of “average” array efficiency, it would be natural to consider the arithmetic mean of the eigenefficiencies a fitting parameter. It may be determined without explicit computation of the eigenefficiencies:

$$\lambda_{\text{avg}} = \frac{1}{n} \sum_{i=1}^n \lambda_i = \frac{1}{n} \text{tr}\{\tilde{\Lambda}\} = \frac{1}{n} \text{tr}\{\tilde{H}\}. \quad (2.16)$$

The average radiation efficiency thus equals the mean of the diagonal elements of \tilde{H} , a result which has also been obtained by Kahn [47, Eqn. (11)].

While there is nothing wrong with the above expression, let us contrast a three-port array with $\lambda_1 = \lambda_2 = \lambda_3 = 0.65$ with an array with $\lambda_1 = \lambda_2 = 0.97$ and $\lambda_3 = 0.01$. Both have the same average efficiency $\lambda_{\text{avg}} = 0.65$. If we had the choice, however, we would presumably prefer the first array; it provides three degrees of freedom with equal efficiency, whereas the second provides only two degrees of freedom with the third one almost nonexistent. Also, in view of the aforementioned excitation-dependent impedance variations, the first array is clearly the more favourable choice.

Depending on the requirements of the particular application, the worst-case efficiency λ_{\min} introduced previously seems a more appropriate measure

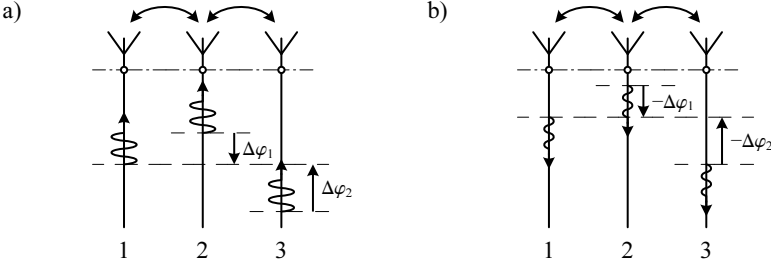


Fig. 2.2: An incident eigenmode excitation travelling towards an antenna array (a), and its reflection (b). Relative phases are denoted by $\Delta\varphi_1$ and $\Delta\varphi_2$.

for comparing antenna array designs. Later, in Chapter 4 about receive diversity, we will derive yet another figure of merit that takes the entire set of eigenefficiencies into account. This will confirm that example number two is in fact considerably worse than the first example from the perspective of antenna diversity.

2.2.4 Reflections of eigenmodes

So far, the results presented are valid for any type of linear and lossless antenna array. From now on we will impose the additional requirement of reciprocity where $\tilde{S}^T = \tilde{S}$ can be assumed.

We have learned that only part of the power supplied to an antenna array is actually radiated; the other part is reflected at the array ports. We will now examine the special properties of these reflections. Still under the assumption of distinct eigenefficiencies, Appendix A.1 proves that if \tilde{Q} diagonalises \tilde{H} by virtue of (2.12), then it also diagonalises \tilde{S} via the following transformation:

$$\tilde{\Gamma}_m = \tilde{Q}^T \tilde{S} \tilde{Q}, \quad \text{with} \quad \tilde{\Gamma}_m = \text{diag} \{ \gamma_{m,1}, \gamma_{m,2}, \dots, \gamma_{m,n} \}. \quad (2.17)$$

The coefficients $\gamma_{m,i}$ are complex and represent the *modal reflection coefficients* of the antenna array. This will become clearer if the wave relation (2.3) is rewritten in terms of $\tilde{\Gamma}_m$:

$$\vec{b} = \tilde{S} \vec{a} = \underbrace{\tilde{Q}^*}_{3.} \underbrace{\tilde{\Gamma}_m}_{2.} \underbrace{\tilde{Q}^H}_{1.} \vec{a} = \sum_{i=1}^n \underbrace{\vec{q}_i^*}_{3.} \underbrace{\gamma_{m,i}}_{2.} \underbrace{\vec{q}_i^H}_{1.} \vec{a}. \quad (2.18)$$

An interpretation of the individual terms is as follows:

1. Decomposition of the antenna excitation vector \vec{d} into modal excitations according to (2.15).
2. Computation of the reflected eigenmode amplitudes via the modal reflection coefficients $\gamma_{m,i}$.
3. Transformation of the reflected eigenmode amplitudes into reflected wave vectors.

Figure 2.2a illustrates the significance of the complex conjugation in step 3. There, we see a set of power waves travelling towards the antenna array ports. Together these waves form an eigenmode \vec{q}_i . The wave at port 2 is ahead of the wave at port 1 by a phase difference of $\Delta\varphi_1$. Similarly, the wave at port 3 lags behind port 1 by $\Delta\varphi_2$. Upon reflection (Fig. 2.2b) some power has been radiated, and the waves thus travel in the opposite direction with smaller amplitudes. Notice that this time, however, the wave at port 2 is *behind* the wave at port one by the same amount $\Delta\varphi_1$; similarly at port 3, where the wave is now *ahead* by $\Delta\varphi_2$. Reflection apparently reverses the phase relationship within an eigenmode; complex conjugation is the mathematical description of this phase reversal.

If we took a time-snapshot of the waves on the transmission lines, or, in other words, if there were no arrows in Fig. 2.2 indicating the directions of propagation, there would be no way to judge whether the eigenmode is travelling towards or away from the array, even though we know \vec{q}_i . Thus, a prominent feature of eigenmodes is that the “shape” of an eigenmode reflection cannot be distinguished from its original. We will use this property to our advantage for the discussion of decoupling networks in the next chapter.

The phases of the $\gamma_{m,i}$ depend upon the particular choice of the set of eigenmodes \vec{Q} . They are therefore not unique and, unlike the eigenefficiencies λ_i , play a subordinate role for array characterisation. They do appear, however, in the later development of an array equivalent circuit and in the mathematics behind decoupling and matching networks. The absolute values of the $\gamma_{m,i}$ are related to the eigenefficiencies by conservation of energy in the eigenmode domain; the following is straightforward to prove:

$$\tilde{\Lambda} = \tilde{I} - \tilde{\Gamma}_m^H \tilde{\Gamma}_m, \quad \text{or} \quad \lambda_i = 1 - |\gamma_{m,i}|^2. \quad (2.19)$$

2.3 Eigenmode far-field patterns

In the preceding section, a lot could be deduced about the radiation properties of antenna arrays by examining the power flow taking place at their terminals. We now proceed to apply the eigenmode theory to the radiation process itself.

2.3.1 Far-field patterns and the radiation matrix

The electric field radiated by a single-port antenna is a function of distance r , azimuth $\phi \in [-\pi; \pi)$, and elevation $\theta \in [-\pi/2; \pi/2]$. In our notation, zero elevation describes the horizontal plane and $\theta = \pi/2$ refers to the zenith. If we consider radiation in the far-field region of the antenna, then the electric field vector $\vec{E}(r, \phi, \theta)$ consists of two orthogonal polarisations. The choice of these polarisations is arbitrary, linear or circular polarisation pairs work equally well. We follow the common nomenclature and call the components of \vec{E} the co-polar component and the cross-polar component, in that order. The total power radiated P_{rad} is then found by integrating the flow of the Poynting-vector through some closed surface. If the surface of integration is a sphere with radius r large enough for the far-field approximation to apply, P_{rad} is given by [75, Eqn. (6)]

$$P_{\text{rad}} = \frac{r^2}{\eta_0} \int_{-\pi/2}^{\pi/2} \int_{-\pi}^{\pi} |\vec{E}(r, \phi, \theta)|^2 \cos \theta \, d\phi \, d\theta, \quad (2.20)$$

where $\eta_0 \approx 377 \, \Omega$ is the impedance of free space. In order to remove the dependence on r and η_0 , we introduce the *normalised far-field pattern* (cf. [75, Eqn. (4)]):

$$\vec{F}(\phi, \theta) = \sqrt{\frac{4\pi r^2}{\eta_0}} \vec{E}(r, \phi, \theta) e^{i2\pi r/\lambda_0}. \quad (2.21)$$

In descriptive terms, $\vec{F}(\phi, \theta)$ is the complex realised amplitude gain with respect to an ideal isotropic radiator. It accounts for matching losses as well as ohmic losses. For example, a lossless isotropic radiator sensitive to the co-polar component only would have $\vec{F}(\phi, \theta) = (1 \ 0)^T$. With the aid of the infinitesimal solid angle element $d\Omega = \cos \theta \, d\phi \, d\theta$, we write the total power in compact form as

$$P_{\text{rad}} = \frac{1}{4\pi} \oint |\vec{F}(\phi, \theta)|^2 d\Omega. \quad (2.22)$$

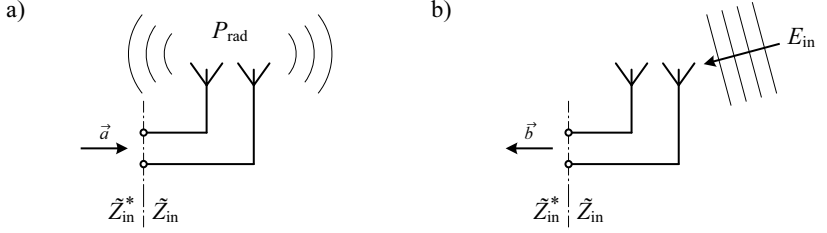


Fig. 2.3: Naming convention used in the text for a transmitting (a) and a receiving antenna array (b).

Besides its independence of r and η_0 , another advantage of the normalised far field is that it can be calculated intuitively from far-field measurements if a calibrated standard antenna is available.

Now consider a reciprocal and passive n -port antenna array. The complex far field radiated upon excitation of the i th port with unit power and with all other ports terminated with their normalising impedance is called the i th *port pattern* $\vec{F}_i(\phi, \theta)$. This is sometimes referred to as the *embedded pattern* or the *active pattern* of the i th element. By the principle of superposition the total far field produced by a given excitation \vec{a} is

$$\vec{F}_{\text{total}}(\phi, \theta) = \sum_{k=1}^n a_k \vec{F}_k(\phi, \theta). \quad (2.23)$$

With (2.22) we obtain the total radiated power (Fig. 2.3a) as a function of \vec{a} :

$$P_{\text{rad}}(\vec{a}) = \frac{1}{4\pi} \oint \left| \sum_{k=1}^n a_k \vec{F}_k(\phi, \theta) \right|^2 d\Omega. \quad (2.24)$$

After rewriting the integrand and expanding the resulting product we arrive at

$$\begin{aligned} P_{\text{rad}}(\vec{a}) &= \frac{1}{4\pi} \oint \left(\sum_{k=1}^n a_k \vec{F}_k(\phi, \theta) \right)^H \cdot \left(\sum_{l=1}^n a_l \vec{F}_l(\phi, \theta) \right) d\Omega \\ &= \frac{1}{4\pi} \oint \left(\sum_{k=1}^n \sum_{l=1}^n a_k^* a_l \vec{F}_k^H(\phi, \theta) \cdot \vec{F}_l(\phi, \theta) \right) d\Omega \end{aligned}$$

$$\begin{aligned}
&= \frac{1}{4\pi} \sum_{k=1}^n \sum_{l=1}^n \left(a_k^* a_l \oint \vec{F}_k^H(\phi, \theta) \cdot \vec{F}_l(\phi, \theta) d\Omega \right) \\
&= \vec{a}^H \tilde{H}_{\text{rad}} \vec{a},
\end{aligned} \tag{2.25}$$

where the individual elements of the matrix \tilde{H}_{rad} are given by

$$\tilde{H}_{\text{rad},ij} = \frac{1}{4\pi} \oint \vec{F}_i^H(\phi, \theta) \cdot \vec{F}_j(\phi, \theta) d\Omega. \tag{2.26}$$

Comparison of the last two equations to (2.6) reveals that there are two ways to calculate the radiation matrix \tilde{H} . Unlike (2.6), however, the above equations do not assume a lossless array. They account for ohmic losses inside the array in addition to reflection losses.

Because far fields are usually measured with respect to the standard 50Ω impedance, Appendix B lists formulae that let us re-express the far-field data and the corresponding radiation matrix for arbitrary normalising impedances.

We will meet the radiation matrix at many places throughout this thesis and most expressions are meaningful with the radiation matrix based on scattering parameter measurements or on far-field measurements. Scattering parameters are much easier and quicker to obtain both by simulations as well as by experimental setups and present a perfectly valid approach if ohmic losses of the array are negligible. Care must be taken though, because seemingly small losses can have significant impact on the array eigenefficiencies in the presence of strong mutual coupling, as the example at the end of this chapter demonstrates. Especially, if the array employs a feed network of some kind, far fields should generally be preferred over scattering parameters unless the properties of the network are otherwise accounted for, for instance by (3.16). In any case, scattering parameters are useful to get an initial, optimistic impression of an antenna array.

The notation \tilde{H}_{acc} will be used explicitly to signify a radiation matrix based on scattering parameters. The subscript refers to the power *accepted*, i.e., not reflected, by the antenna array. At places where we specifically refer to the far-field based radiation matrix, we will use the notation \tilde{H}_{rad} to indicate the power *radiated* by the antenna array. Whenever the choice is up to the engineer, the subscript will be omitted. Where appropriate, subscripts will also be used on \tilde{Q} and \tilde{A} as well as \tilde{q}_i and λ_i . Of course, we have [76, Eqns. (8)

and (9)]

$$\tilde{H}_{\text{rad}} = \tilde{H}_{\text{acc}} = \tilde{I} - \tilde{S}^H \tilde{S} \quad \text{for lossless arrays.} \quad (2.27)$$

The diagonal elements of \tilde{H}_{rad} correspond to (2.22) and stand for the power radiated by the beams associated with individual array terminals. The off-diagonal elements are a measure for the overlap between two beams i and j . If these elements evaluate to zero, the far-field patterns are said to be *orthogonal* or *uncorrelated*.

In this thesis we use the term “ideal multi-port array” to refer to a lossless, reciprocal, and perfectly matched antenna array where \tilde{H} is the identity matrix. Such an array has 100 % radiation and matching efficiency at all ports and exhibits no beam overlap or port coupling. The specific shape of the beam patterns is irrelevant to this definition.

For lossless arrays, we can assert that decoupled input ports are a sufficient condition for orthogonal port patterns. This follows from the fact that it is impossible to find a diagonal matrix \tilde{S} such that \tilde{H} is non-diagonal. In other words, overlapping beams necessarily imply coupled input ports. The converse, however, is not always true. A specifically constructed example is a lossless two-port array with

$$\tilde{S} = \begin{pmatrix} 0.5 & j0.5 \\ j0.5 & 0.5 \end{pmatrix}. \quad (2.28)$$

Although its ports are significantly coupled, the radiation matrix turns out as

$$\tilde{H} = \begin{pmatrix} 0.5 & 0 \\ 0 & 0.5 \end{pmatrix}, \quad (2.29)$$

indicating orthogonal beams. If ohmic losses are allowed, then it will always be possible to find examples that do not conform to this principle.

In the literature, the pattern correlation coefficient ρ_{ij} is often encountered as a figure of merit for mutually coupled arrays. It normalises the beam overlap to the powers of the individual beams [76, Eqn. (12)], [24, 70]:

$$\rho_{ij} = \frac{\tilde{H}_{ij}}{\sqrt{\tilde{H}_{ii} \tilde{H}_{jj}}}. \quad (2.30)$$

This way, ρ_{ij} is a complex number with absolute value 1 for full beam overlap and value 0 for orthogonal beams. As the result of the normalisation,

however, information about the individual port efficiencies (power mismatch or ohmic loss) cannot be extracted from the correlation coefficients alone. In the example above, the pattern correlation ρ_{12} is zero, but the array nonetheless possesses an efficiency of only 50 % for all excitations. Although the example is a specifically constructed one, it does suggest that the significance of pattern orthogonality often proclaimed in the literature may be somewhat overrated (cf. the discussions in Section 2.1 and Chapter 4).

2.3.2 Beam-pattern orthogonalisation

Let us proceed with the investigation of array radiation patterns, and assume that the radiation matrix \tilde{H}_{rad} has been determined from a given set of n port patterns $\vec{F}_i(\phi, \theta)$. The eigendecomposition is $\tilde{H}_{\text{rad}} = \tilde{Q}_{\text{rad}} \tilde{\Lambda}_{\text{rad}} \tilde{Q}_{\text{rad}}^H$ in accordance with (2.12). We now establish a new set of beam-patterns called $\vec{F}_{m,i}(\phi, \theta)$ by exciting the array in turn with each of its eigenmodes $\vec{q}_{\text{rad},i}$ and normalising the resulting pattern to the square-root of the associated eigen-efficiency. This is accomplished by the following linear transformation on the set $\vec{F}_i(\phi, \theta)$:

$$\vec{F}_{m,i}(\phi, \theta) = \frac{1}{\sqrt{\lambda_{\text{rad},i}}} \sum_{k=1}^n \tilde{Q}_{\text{rad},ki} \vec{F}_k(\phi, \theta). \quad (2.31)$$

The beam overlap between these *eigenpatterns* is found by virtue of (2.26):

$$\begin{aligned} & \frac{1}{4\pi} \oint \vec{F}_{m,i}^H(\phi, \theta) \cdot \vec{F}_{m,j}(\phi, \theta) d\Omega \\ &= \frac{1}{4\pi} \oint \left(\frac{1}{\sqrt{\lambda_{\text{rad},i}}} \sum_{k=1}^n \tilde{Q}_{\text{rad},ki} \vec{F}_k(\phi, \theta) \right)^H \cdot \left(\frac{1}{\sqrt{\lambda_{\text{rad},j}}} \sum_{l=1}^n \tilde{Q}_{\text{rad},lj} \vec{F}_l(\phi, \theta) \right) d\Omega \\ &= \frac{1}{4\pi \sqrt{\lambda_{\text{rad},i} \lambda_{\text{rad},j}}} \sum_{k=1}^n \sum_{l=1}^n \left(\tilde{Q}_{\text{rad},ki}^* \tilde{Q}_{\text{rad},lj} \oint \vec{F}_k^H(\phi, \theta) \cdot \vec{F}_l(\phi, \theta) d\Omega \right) \\ &= \frac{1}{\sqrt{\lambda_{\text{rad},i} \lambda_{\text{rad},j}}} \sum_{k=1}^n \sum_{l=1}^n \tilde{Q}_{\text{rad},ki}^* \tilde{Q}_{\text{rad},lj} \tilde{H}_{\text{rad},kl} \\ &= \frac{1}{\sqrt{\lambda_{\text{rad},i} \lambda_{\text{rad},j}}} \tilde{\Lambda}_{\text{rad},ij} = \begin{cases} 1 & i = j, \\ 0 & \text{otherwise.} \end{cases} \end{aligned} \quad (2.32)$$

It turns out that the beam patterns associated with eigenmodes are mutually orthogonal (cf. Stein [75, Section XI]). Since these patterns in (2.31) are normalised, the $\vec{F}_{m,i}(\phi, \theta)$ constitute an *orthonormal* basis for the linear *pattern space* that can possibly be formed by a given antenna array. In conjunction with the eigenefficiencies $\lambda_{\text{rad},i}$, these patterns completely describe the degrees of freedom available in the array: eigenpatterns define the shape, and the eigenefficiencies the corresponding radiation efficiencies due to power mismatch and ohmic losses. This insight once again emphasises the fundamental character of the eigenmode representation initially observed in Section 2.2.3.

Because \tilde{Q}_{rad} is unitary, i.e., $\tilde{Q}_{\text{rad}}^{-1} = \tilde{Q}_{\text{rad}}^{\text{H}}$, we may write the inverse of transformation (2.31) as

$$\vec{F}_i(\phi, \theta) = \sum_{k=1}^n \tilde{Q}_{\text{rad},ik}^* \sqrt{\lambda_{\text{rad},k}} \vec{F}_{m,k}(\phi, \theta). \quad (2.33)$$

Substitution into (2.23) yields the following form of the excitation dependent far field $\vec{F}_{\text{total}}(\phi, \theta)$:

$$\begin{aligned} \vec{F}_{\text{total}}(\phi, \theta) &= \sum_{l=1}^n a_l \left(\sum_{k=1}^n \tilde{Q}_{\text{rad},lk}^* \sqrt{\lambda_{\text{rad},k}} \vec{F}_{m,k}(\phi, \theta) \right) \\ &= \sum_{k=1}^n \left(\vec{F}_{m,k}(\phi, \theta) \sqrt{\lambda_{\text{rad},k}} \sum_{l=1}^n \tilde{Q}_{\text{rad},lk}^* a_l \right) \\ &= \sum_{k=1}^n \underbrace{\vec{F}_{m,k}(\phi, \theta)}_{3.} \underbrace{\sqrt{\lambda_{\text{rad},k}}}_{2.} \underbrace{\tilde{q}_{\text{rad},k}^{\text{H}} \vec{a}}_{1.}. \end{aligned} \quad (2.34)$$

Analogous to the discussion of eigenmode reflections in Section 2.2.4, the radiation process may be described in terms of eigenmodes and eigenpatterns as follows:

1. Decomposition of the antenna excitation vector \vec{a} into modal excitations, cf. (2.15).
2. Computation of the radiated modal power via eigenefficiency $\lambda_{\text{rad},k}$.
3. Radiation in form of eigenpattern $\vec{F}_{m,i}(\phi, \theta)$ associated with mode i .

Suppose the antenna array is used as part of a digital beam-forming transmitter, where the power supplied to the array ports may be changed arbitrarily. In principle, we can compensate for the losses within the array by pre-distorting the excitation vector \vec{d} to increase the power selectively in lowly efficient eigenmodes. This may for example be accomplished by the transformation

$$\vec{d} = \tilde{Q}_{\text{rad}} \tilde{\Lambda}_{\text{rad}}^{-1/2} \tilde{Q}_{\text{rad}}^H \vec{x}, \quad (2.35)$$

which cancels the $\sqrt{\lambda_{\text{rad},i}}$ term in (2.34) and yields

$$\vec{F}_{\text{total}}(\phi, \theta) = \sum_{i=1}^n \vec{F}_{\text{m},i}(\phi, \theta) \tilde{q}_{\text{rad},i}^H \vec{x}, \quad (2.36)$$

where the total power radiated is always equal to the total power in the desired excitation vector \vec{x} .

In practice, however, the approach described raises the linearity requirements of the amplifiers driving the array beyond what was mentioned above at the end of Section 2.2.2: the amplifiers must deliver still higher voltage and current amplitudes in order to overcome the efficiency impairments due to coupling. Therefore, the feasibility of this approach is dependent on the output power and on the specific eigenefficiencies of the target system.

Now suppose the receiving case. A plane wave with amplitude \vec{E}_{in} impinges on the antenna array from direction (ϕ_0, θ_0) as in Fig. 2.3b. The waves b_1, b_2, \dots, b_n that consequently arise at the antenna ports are given by [76, Eqn. (10)]

$$b_i = \frac{\lambda_0}{\sqrt{4\pi\eta_0}} \vec{F}_i^T(\phi_0, \theta_0) \cdot \vec{E}_{\text{in}}, \quad (2.37)$$

where λ_0 is the wavelength of electromagnetic radiation in free space. After substitution of (2.33) we may express the received waves \vec{b} in vector form as

$$\vec{b} = \underbrace{\sum_{i=1}^n}_{3.} \underbrace{\tilde{q}_{\text{rad},i}^*}_{2.} \underbrace{\sqrt{\lambda_{\text{rad},i}} \frac{\lambda_0}{\sqrt{4\pi\eta_0}} \vec{F}_{\text{m},i}^T(\phi_0, \theta_0) \cdot \vec{E}_{\text{in}}}_{1.}. \quad (2.38)$$

Thus, the modal interpretation of reception is as follows:

1. Reception in mode i via eigenpattern $\vec{F}_{\text{m},i}(\phi, \theta)$, cf. (2.37).

2. Computation of the received modal power via eigenefficiency $\lambda_{\text{rad},i}$.
3. Transformation from eigenmode representation to the received waves domain \vec{b} .

As expected by the principle of reciprocity, the eigenefficiencies are effective in the receive direction as well. In contrast to the transmitting case, however, the eigenefficiencies *cannot* be compensated for by means of digital beam-forming algorithms. The reason is that receiver sensitivity depends on the signal-to-noise ratio (SNR). Additional noise is generated within receiver components such as amplifiers, mixers, or analogue-to-digital converters. Thus, if the signal received by the antenna array is weakened due to coupling, then the SNR will be degraded permanently, since there is no way to improve the SNR of a non-deterministic signal. The influence of noise on the receiving properties of compact antenna arrays will be addressed in detail in Chapter 4.

2.4 Non-distinct eigenefficiencies

We know already that any eigenmode \vec{q}_i multiplied by a unit phasor is again an eigenmode. This follows from the definition of eigenvectors of a matrix. In consequence, the phases of the modal reflection coefficients $\gamma_{m,i}$ (2.17) as well as the phases of the eigenpatterns (2.31) are dependent on the particular choice of the matrix of eigenmodes \tilde{Q} .

When there are eigenefficiencies with multiplicity greater than one, additional degrees of freedom arise in the determination of \tilde{Q} . In this case any linear combination of eigenmodes with the same eigenefficiency also constitutes an eigenmode.

This fact has a noteworthy impact on eigenmode reflections. Let us revisit the lossless example antenna array discussed towards the end of Section 2.3.1 with

$$\tilde{S} = \begin{pmatrix} 0.5 & j0.5 \\ j0.5 & 0.5 \end{pmatrix} \quad \text{and thus} \quad \tilde{H} = \begin{pmatrix} 0.5 & 0 \\ 0 & 0.5 \end{pmatrix}. \quad (2.39)$$

The eigenvalues of \tilde{H} obviously share the same value, namely $\lambda_1 = \lambda_2 = 0.5$. We have already observed that its port patterns are orthogonal although its input ports are coupled. Moreover, the two excitations $\vec{q}_1 = (1 \ 0)^T$ and $\vec{q}_2 = (0 \ 1)^T$ are valid eigenmodes according to definition (2.12). Yet they

are an example for the fact that in the presence of multiple eigenefficiencies eigenmode shapes are not necessarily maintained upon reflection as in (2.17). Similar examples may be constructed for larger arrays. The fact that (2.17) is guaranteed to hold for non-distinct eigenefficiencies only, is a general manifestation of the previous insight that beam-orthogonality is not a sufficient requirement for uncoupled ports.

The multiplicity of eigenefficiencies is irrelevant to the description of the radiation properties of antenna arrays, since the eigenefficiencies λ_i , as well as the pattern space spanned by the set of eigenpatterns, characterise the degrees of freedom available; these parameters remain unambiguous under *all* circumstances. For the mathematical analysis of decoupling and matching networks in the following chapter, however, it is crucial that both (2.12) as well as (2.17) are fulfilled. This is accomplished by a matrix decomposition known as Takagi's factorisation [8, pp. 204], [128, 136] which, given a symmetric complex matrix \tilde{S} , always finds a non-negative real diagonal matrix $\tilde{\Gamma}_m$ and a unitary matrix \tilde{Q} according to (2.17). It is straightforward to show that (2.17) implies (2.12). The existence of some \tilde{Q} that fulfills (2.12) and (2.17) is thus guaranteed in all cases.

2.5 Ohmic array losses

So far, we have looked at the power accepted by an antenna array via the matrix \tilde{H}_{acc} and the power radiated by the array using the matrix \tilde{H}_{rad} . In the presence of ohmic losses, it is expedient to round out the concept of eigenefficiencies by including a quantification of these losses.

Consider the excitation-dependent quotient $\chi(\vec{d})$ of the radiated power to the accepted power:

$$\chi(\vec{d}) = \frac{P_{\text{rad}}}{P_{\text{acc}}} = \frac{\vec{d}^H \tilde{H}_{\text{rad}} \vec{d}}{\vec{d}^H \tilde{H}_{\text{acc}} \vec{d}}. \quad (2.40)$$

This function gives information on what fraction of the *accepted power* is actually radiated for a given port excitation \vec{d} . It disregards power mismatch at the input terminals and is therefore characteristic of ohmic losses within the array itself. In the absence of ohmic losses, $\chi(\vec{d})$ evidently equals unity for all excitations.

The information about a worst-case *ohmic efficiency* χ_{\min} is of particular practical interest. It is given by the smallest eigenvalue of the product $\tilde{H}_{\text{acc}}^{-1} \tilde{H}_{\text{rad}}$ (cf. the derivations in Section 4.3.3). The important consequence

for an antenna designer is that, no matter what measures are undertaken to improve power matching to the antenna array (without modification to the array itself), there will be some excitation where the efficiency of this system does not exceed χ_{\min} .

Networks that aim to restore power matching at the array terminals are called *decoupling and matching networks* (DMN) and are discussed in the next chapter. In the context of DMNs, the statement behind ohmic efficiencies is in fact very specific: Appendix A.2 demonstrates that the set of eigenvalues χ_i of the product $\tilde{H}_{\text{acc}}^{-1} \tilde{H}_{\text{rad}}$ defines an upper limit to the eigenefficiencies that can possibly be achieved with a passive DMN. Any practical DMN realisation will naturally perform worse due to additional network losses. To the above definition of ohmic efficiencies, the origin of the losses is irrelevant. They can be part of the radiating parts of the array, caused by the insertion losses of connecting cables, or even be part of some type of feed-network—not necessarily a DMN—in front of the array.

Mind that, in the presence of strong mutual coupling, one or more eigenvalues of \tilde{H}_{acc} will be very small; the matrix \tilde{H}_{acc} will therefore be close to singular. In this case, the computation of the matrix inverse and thus the computation of the ohmic efficiencies χ_i is an ill-conditioned problem [8, Section 5.8] and as such sensitive to measurement errors. We will see an example of this implication later on.

2.6 An equivalent circuit for lossless arrays

The results of the eigenmode analysis may be put together conveniently as a descriptive equivalent circuit model for lossless coupled antenna arrays [144]. Since in this case $\tilde{H}_{\text{rad}} = \tilde{H}_{\text{acc}}$, the corresponding subscripts are omitted for clarity. The lossless circuit model extends the discussion by Stein [75, Section XI].

Consider the equivalent circuit in Fig. 2.4. Shown is a set of n impedances with reflection coefficients $\gamma_{m,i}$ connected to some lossless and reciprocal $2n$ -port network \tilde{S}_{Q} with

$$\tilde{S}_{\text{Q}} = \begin{pmatrix} \tilde{0} & \tilde{Q}^* \\ \tilde{Q}^{\text{H}} & \tilde{0} \end{pmatrix}. \quad (2.41)$$

The first n ports of this network correspond to the left-hand side ports in the figure from top to bottom. Likewise, the last n ports correspond to the right-hand side.

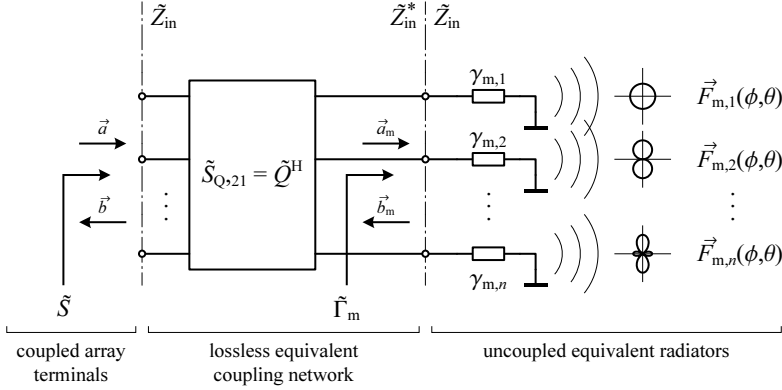


Fig. 2.4: Equivalent circuit model for lossless coupled n -port antenna arrays comprising a set of uncoupled equivalent radiators with diagonal scattering matrix $\tilde{\Gamma}_m$, and a coupling network \tilde{S}_Q . The pictograms on the right-hand side represent the eigenpatterns $\vec{F}_{m,i}(\phi, \theta)$ associated with the equivalent radiators.

The scattering matrix \tilde{S} resulting from the interconnection of the above networks is readily obtained using (B.14):

$$\tilde{S} = \tilde{S}_{Q,12} \tilde{\Gamma}_m \tilde{S}_{Q,21} = \tilde{Q}^* \tilde{\Gamma}_m \tilde{Q}^H, \quad (2.42)$$

where $\tilde{\Gamma}_m$ is the diagonal matrix of the reflection coefficients $\gamma_{m,i}$. We observe that if \tilde{Q} and $\tilde{\Gamma}_m$ are determined by the eigenmode analysis, then Fig. 2.4 models the input port behaviour of an antenna array with scattering matrix \tilde{S} .

Suppose the antenna array is used for transmission. The matrix signal flow graph [72] in Fig. 2.5a is a graphical representation of the power flow taking place in the equivalent circuit. Power is supplied from n external sources via the wave vector \vec{a} . These waves are transformed through \tilde{Q}^H to yield waves \vec{a}_m with

$$\vec{a}_m = \tilde{Q}^H \vec{a}. \quad (2.43)$$

This transformation has been identified earlier in (2.15) as the decomposition of the incident wave vector into modal excitations. These excitations $a_{m,i}$ are now incident on the load impedances with reflection coefficients $\gamma_{m,i}$. The power P_i dissipated in impedance i is therefore

$$P_i = (1 - |\gamma_{m,i}|^2) |a_{m,i}|^2 = \lambda_i |a_{m,i}|^2, \quad (2.44)$$

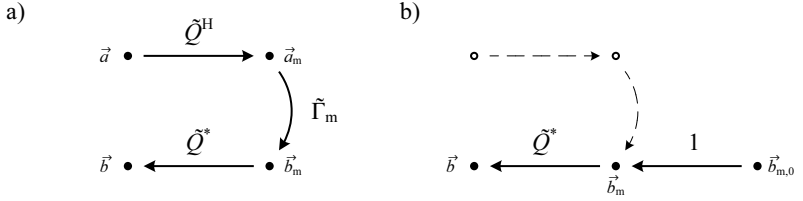


Fig. 2.5: Matrix signal flow graphs illustrating the power flow in a transmitting (a) and a receiving antenna array (b).

which, being the power *available* in eigenmode i times the corresponding eigenefficiency, expresses the power radiated in the i th eigenmode. We may therefore regard the impedances $\gamma_{m,i}$ as *equivalent power sinks* for the power radiated in the individual eigenmodes. Moreover, the contribution of the i th eigenmode to the overall far-field radiation pattern is given by

$$\vec{F}_{m,i}(\phi, \theta) \sqrt{\lambda_i} a_{m,i}, \quad (2.45)$$

the superposition of which leads us to our previous interpretation according to (2.34). Power not radiated by the array is reflected to the sources in the form of modal reflections $\vec{b}_m = \tilde{\Gamma}_m \vec{a}_m$, which are subsequently transformed into port reflections via $\vec{b} = \tilde{Q}^* \vec{b}_m$.

Reciprocity allows us to apply the same model in the receive direction. The only difference is that the impedances $\gamma_{m,i}$ are now regarded as *equivalent power sources* with internal reflection coefficient $\gamma_{m,i}$. According to Hoffmann [6, Eqn. (5.46)], a power source with available power $P_{m,av,i}$ and internal reflection coefficient $\gamma_{m,i}$ can be modelled by some wave $b_{m,0,i}$ as in Fig. 2.5b, with

$$|b_{m,0,i}|^2 = (1 - |\gamma_{m,i}|^2) P_{m,av,i} = \lambda_i P_{m,av,i}. \quad (2.46)$$

Although this equation leaves the phase of $b_{0,i}$ undetermined, we assert the following relationships involving an *available modal power wave* $b_{m,av,i}$:

$$b_{m,0,i} = \sqrt{\lambda_i} b_{m,av,i}, \quad (2.47)$$

with

$$b_{m,av,i} = \frac{\lambda_0}{\sqrt{4\pi\eta_0}} \vec{F}_{m,i}^\Gamma(\phi_0, \theta_0) \cdot \vec{E}_{in}. \quad (2.48)$$

In other words, $b_{m,av,i}$ represents the modal power wave available in eigenmode i in response to a plane wave \vec{E}_{in} incident on the antenna array. Continuing with the transformation along the signal flow graph we obtain

$$\vec{b} = \tilde{Q}^* \vec{b}_{m,0} = \tilde{Q}^* \sqrt{\tilde{\Lambda}} \vec{b}_{m,av} \quad (2.49)$$

for the waves received at the array ports; the waves available in the eigenmodes are weighted with their eigenefficiencies and are finally transformed into received port waves. If we now substitute (2.48), we arrive at our previous interpretation of array reception (2.38).

In summary, the proposed equivalent circuit is an accurate embodiment of the eigenmode concept developed in this chapter—at least for lossless arrays. All important pieces are brought together: eigenefficiencies λ_i , modal reflection coefficients $\gamma_{m,i}$, eigenmodes \tilde{Q} , eigenpatterns $\vec{F}_{m,i}(\phi, \theta)$, modal excitations \vec{d}_m , modal reflections \vec{b}_m , and available modal power waves $\vec{b}_{m,av}$. The circuit model decomposes a coupled antenna array into a set of uncoupled equivalent radiators and a lossless and reciprocal coupling network. Viewed this way, the only sources of radiation, the *degrees of freedom* of the antenna array, are the equivalent radiators; their matching efficiencies and consequently the radiation capabilities of the antenna array as a whole are characterised uniquely by the set of eigenefficiencies λ_i .

2.7 Examples of the consequences of radiator coupling

It is about time to apply the ideas developed in this chapter to a practical context. The intention of the examples provided here is to convince the reader of the usefulness of the eigenmode approach in engineering problems. Questions about what range of values can be expected for the eigenefficiencies, what eigenpatterns look like, and what other factors influence the performance of a compact antenna array are addressed in the following.

2.7.1 Analysis of a manufactured $\lambda_0/10$ linear three-port monopole antenna array

We start with a rather thorough analysis of a manufactured three-port monopole array for a frequency of 2.45 GHz. The ground plane is a 14 cm by 14 cm copper plate with a thickness of 1 mm. Silver-plated copper wires with a



Fig. 2.6: Photographs of the fabricated $\lambda_0/10$ three-port monopole array for 2.45 GHz.

diameter of 1 mm and a length of 29 mm ($\approx 0.24 \lambda_0$, where λ_0 is the wavelength of free space) were used as radiators with a spacing of one tenth of the wavelength. The radiators were soldered to SMA flange jacks, which were subsequently inserted through holes in the ground plane and bolted on to it. Photographs are shown in Fig. 2.6.

The scattering parameters of the antenna array are plotted in Fig. 2.7. Due to manufacturing deviations, the scattering parameters are not perfectly symmetrical. At the centre frequency of 2.45 GHz the decibel absolute values of the scattering coefficients are:

$$\tilde{S} \Big|_{\text{dB}} = \begin{pmatrix} -8.9 & -7.2 & -9.9 \\ -7.2 & -6.3 & -6.8 \\ -9.9 & -6.8 & -9.0 \end{pmatrix} \text{ dB}. \quad (2.50)$$

Coupling between elements is characterised by the off-diagonal elements. Values lie between -9.9 dB and -6.8 dB, which corresponds to 10 % and 21 % power coupling to neighbouring elements. At first glance this may not seem a lot. However, if we take a closer look at the second radiator, for instance, we find that 23 % of power are lost due to impedance mismatch, and that another 40 % are lost through coupling to the first and the third port. Only 37 % are left for radiation.

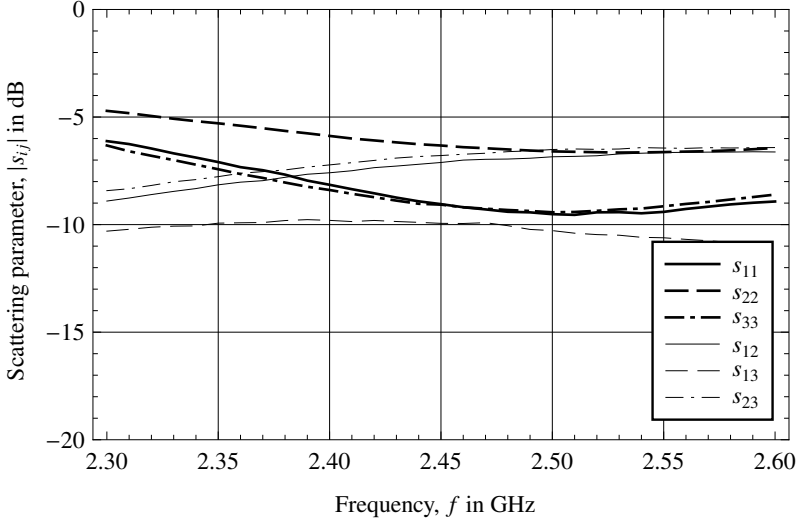


Fig. 2.7: Measured scattering parameters of a $\lambda_0/10$ linear array of three monopoles.

These port efficiencies constitute the diagonal elements of the radiation matrix \tilde{H}_{acc} :

$$\tilde{H}_{\text{acc}} = \begin{pmatrix} 0.578 & 0.293 - j0.069 & -0.0312 - j0.0081 \\ 0.293 + j0.069 & 0.366 & 0.304 + j0.046 \\ -0.0312 + j0.0081 & 0.304 - j0.046 & 0.565 \end{pmatrix}. \quad (2.51)$$

They express the radiation efficiency if one port is excited while the others are terminated with matched loads. The off-diagonal elements in the radiation matrix quantify the amount of overlap between beam patterns. Normalised to the port efficiencies they yield the popular correlation coefficient defined earlier (2.30):

$$|\rho_{12}| = 0.653, \quad |\rho_{13}| = 0.0564, \quad \text{and} \quad |\rho_{23}| = 0.677. \quad (2.52)$$

These numbers indicate significant beam overlap between the first and the second as well as the second and the third radiator. The similarity between the outermost elements seems considerably less. When we look at azimuth

cuts through the port beam patterns in Fig. 2.8a, we notice that it is virtually impossible to use them as a basis for judging the magnitudes of the correlation coefficients. The reason why the seemingly similar and greatly overlapping patterns of ports one and three can nevertheless exhibit very low correlation is that the entire three-dimensional patterns are relevant to the calculation of ρ , and also the relative phases of the power radiated towards different angles.

Another thing we notice about the shapes of the beam patterns is that they are greatly distorted from the circular pattern of an isolated monopole radiator. One cause of this effect is the close proximity between radiators. Power fed into one antenna port not only excites the radiator directly connected to that port but also, due to field coupling effects, its neighbouring elements. Another contributing factor not specifically related to radiator coupling is the small size of the ground plane. Currents flowing in the antenna elements induce currents on the ground plane surface that contribute to the radiated field. Clearly visible is the effect of the ground plane corners in the beam pattern of the centre port.

In this chapter, eigenmodes were introduced as a means for the unique characterisation of the radiation capabilities of a mutually coupled antenna array. The set of eigenefficiencies was considered the logical extension to the radiation efficiency of a single radiator. In our example the eigenefficiencies as determined from its scattering matrix are

$$\lambda_{\text{acc},1} = 89.2 \%, \quad \lambda_{\text{acc},2} = 60.2 \%, \quad \text{and} \quad \lambda_{\text{acc},3} = 1.44 \%. \quad (2.53)$$

Therefore, depending on its excitation, the radiation efficiency of the array (based on the accepted power) varies between 89.2 % and as little as 1.44 %. The eigenmodes, which were shown to represent the excitations that give rise to these efficiencies, are given by the columns of the matrix

$$\tilde{Q}_{\text{acc}} = \begin{pmatrix} 0.553 \angle 0^\circ & 0.710 \angle 0^\circ & 0.437 \angle 0^\circ \\ 0.632 \angle 15.3^\circ & 0.0306 \angle -105.0^\circ & 0.774 \angle -168.0^\circ \\ 0.544 \angle 8.90^\circ & 0.704 \angle -174.0^\circ & 0.457 \angle 2.62^\circ \end{pmatrix}, \quad (2.54)$$

written in polar form. The first eigenmode excites all elements with roughly equal amplitude and equal phase. Mutual coupling can be expected to be ineffective in this case, which is supported by the excellent radiation efficiency. Due to the close proximity of the radiators, the corresponding beam pattern shown in Fig. 2.8b resembles that of a single radiator. In view of the even

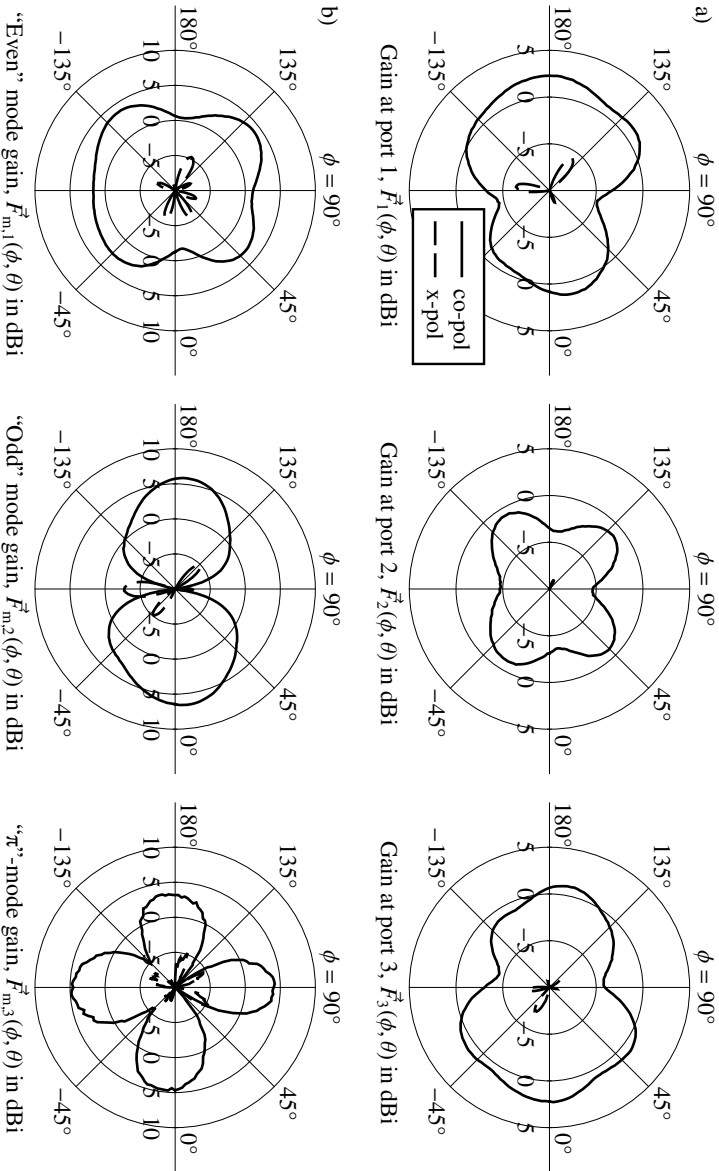


Fig. 2.8: (a) Measured azimuth cuts of the port beam patterns of the $\lambda_0/10$ linear three-port array. (b) The eigenpatterns computed from the far-field data. All diagrams are plotted at an elevation of $\theta = 20^\circ$.

symmetry of the far-field pattern and of the excitation vector, we call this mode the “even” mode.

Eigenmode number two only excites the outermost radiators and spends negligible power on the centre radiator. The phase difference is close to 180° . This time the correlation between the associated patterns takes effect and adversely affects the radiation efficiency. Since the correlation is small though, the effect is only moderately pronounced and the efficiency is still 60.2 %. The resulting beam pattern in Fig. 2.8b is the difference pattern with a distinct radiation-zero perpendicular to the line of radiators. There is a 180° phase difference between the left-hand and the right-hand lobe. Owing to its odd symmetry, this mode is called the “odd” mode.

The last eigenmode involves all three radiators with a phase difference of around 180° (equivalent to π radians) between adjacent elements. On this account, we call it the “ π ”-mode. In consequence of the small element separation, the superposition of the beam patterns produced by the individual radiators is primarily characterised by destructive interference. Thus, only little power finds its way into the far field and the larger proportion is reflected to the sources. The extent, to which cancellation of energy takes place, is evident from the minute radiation efficiency of this mode. The phase difference between adjacent lobes in Fig. 2.8b is 180° .

Since mainly the phase differences within an eigenmode vector determine the extent of destructive or constructive interference, we will occasionally employ the following notation in the course of this thesis:

$$\text{“even”}: \begin{bmatrix} + & + & + \end{bmatrix}, \quad \text{“odd”}: \begin{bmatrix} + & 0 & - \end{bmatrix}, \quad \text{and “}\pi\text{”}: \begin{bmatrix} + & - & + \end{bmatrix}.$$

Roughly speaking, the more adjacent phase changes there are in an eigenmode the more annihilation takes places in the far field and the lower is the corresponding eigenefficiency.

Let us now investigate how arbitrary excitations can be expressed in terms of eigenmodes. For simplicity we take the excitation of the centre port as an example, so the excitation vector is $\vec{a} = (0 \ 1 \ 0)^T$. With (2.15) \vec{a} is decomposed into its modal constituents \vec{a}_m . The magnitude squares of the elements of \vec{a}_m represent the amount of power available for the individual eigenmodes. In our example 40 % contribute to the “even” mode and 60 % to the “ π ”-mode. For symmetry reasons, negligible power is assigned to the “odd” mode.

The total radiation efficiency of the centre port comes about as follows: of the 40 % available for the first mode, 89.2 % are radiated. In the third mode, only 1.44 % of the available 60 % are radiated. This amounts to an efficiency of $0.4 \times 0.892 + 0.6 \times 0.0144 = 0.365$, a number which we recognise from (2.51) above. (The missing 0.1 % go into the second mode because the manufactured array is not perfectly symmetric.) The discussion explains why the resulting beam pattern closely resembles that of the “even” mode, although the larger proportion of input power is assigned to the “ π ”-mode. It should also be clear by now that, in general, the third mode will be mostly underrepresented during array operation, unless measures are undertaken to pre-distort the array excitation \vec{d} to compensate for the mode-dependent efficiency loss.

So far the discussion was based on information that had been deduced from the scattering matrix of the antenna array. Previously in this chapter we derived the close relationship between scattering parameters and far-field patterns. The important difference is that far-field patterns, unlike scattering parameters, convey information about ohmic losses in the array. Since the array was built from the best conductors available, namely copper and silver, we can surely neglect the influence of losses. Can we really?

To answer this question, the radiation matrix \tilde{H}_{rad} was determined by numeric integration over the measured far-field patterns. The result is

$$\tilde{H}_{\text{rad}} = \begin{pmatrix} 0.579 & 0.288 - j0.072 & -0.0397 - j0.0098 \\ 0.288 + j0.072 & 0.347 & 0.292 + j0.046 \\ -0.0397 + j0.0098 & 0.292 - j0.046 & 0.562 \end{pmatrix},$$

in comparison with the matrix of accepted power

$$\tilde{H}_{\text{acc}} = \begin{pmatrix} 0.578 & 0.293 - j0.069 & -0.0312 - j0.0081 \\ 0.293 + j0.069 & 0.366 & 0.304 + j0.046 \\ -0.0312 + j0.0081 & 0.304 - j0.046 & 0.565 \end{pmatrix}, \quad (2.55)$$

obtained previously. Their remarkable agreement not only confirms the validity of the theory but also demonstrates that practical far-field measurements are accurate enough to produce meaningful results. However, we do spot some notable differences between the eigenefficiencies $\vec{\lambda}_{\text{rad}}$ and $\vec{\lambda}_{\text{acc}}$ associated with these matrices (see Table 2.1). For the “odd” mode excitation,

Excitation \vec{d}	$\lambda_{\text{acc}}(\vec{d})$	$\lambda_{\text{rad}}(\vec{d})$	$\chi(\vec{d})$	Directivity	Realised gain
Port 1	58 %	58 %	100 %	5.6 dBi	3.2 dBi
Port 2	37 %	35 %	95 %	5.3 dBi	0.73 dBi
Port 3	57 %	56 %	99 %	5.1 dBi	2.6 dBi
“Even” mode	89 %	87 %	97 %	5.3 dBi	4.7 dBi
“Odd” mode	60 %	61 %	101 %	6.9 dBi	4.7 dBi
“ π ”-mode	1.4 %	1.0 %	69 %	5.5 dBi	−14.5 dBi

Table 2.1: Selected parameters of the example array. The values for the directivity and the gain are included for information only.

the array displays unphysical behaviour in that the amount of power radiated (61 %) is seemingly greater than the power accepted by the array (60 %). The discrepancy, in both absolute and relative terms, is small enough, though, to be ascribed to measurement tolerances.

The numbers of the “ π ”-mode on the other hand suggest the presence of significant ohmic losses for that particular excitation. It appears only about 70 % of the power accepted by the array are actually radiated. Since this observation is caused by only a small absolute difference between $\lambda_{\text{rad}}^{(\pi)}$ and $\lambda_{\text{acc}}^{(\pi)}$ of 0.4 %, it is crucial that we confirm the plausibility of the measurement data.

To this end, the variations of the modal ohmic efficiencies χ_i are plotted versus frequency in Fig. 2.9a. The ripple clearly apparent in these graphs is because their computation is ill conditioned as mentioned at the end of Section 2.5. Small numerical variations in the matrix \tilde{H}_{acc} due to measurement noise or calibration errors for instance cause large changes to the χ_i . In order to investigate whether or not the materials of the antenna array are responsible for the degraded “ π ”-mode efficiency, a second version of the array was fabricated, this time with a stainless steel ground plane. The conductivity of stainless steel ($1.4 \times 10^6 \text{ Sm}^{-1}$) is more than one order of magnitude smaller than the conductivity of copper ($5.8 \times 10^7 \text{ Sm}^{-1}$), so any influence of the material should clearly show up in the measurements.

Figure 2.9b portrays the results. The ripple in these curves is considerably larger, possibly because it was deemed unnecessary to recalibrate the

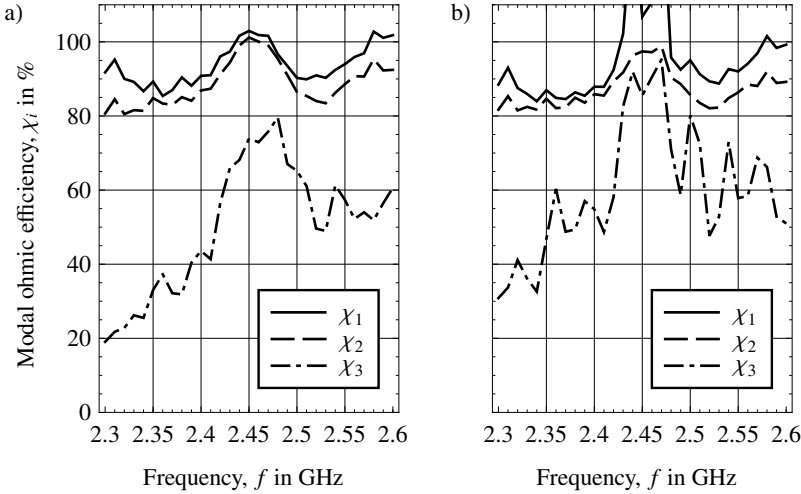


Fig. 2.9: Modal ohmic efficiencies as determined from scattering parameter and far-field measurements. These plots portray the results for a copper ground plane (a), and a stainless steel ground plane (b).

network analyser a second time for the stainless steel measurements. If we ignore the outliers in the plots, we nonetheless find that there is not much difference between the efficiencies of the stainless steel array and the copper array. The conductivity of the ground plane material evidently has no measurable bearing on array efficiency. This fact has subsequently been confirmed by computer simulations using CST Microwave Studio [126].

Still, there is one further array component that we have not yet paid any attention to: the SMA connectors used to feed the radiators. They use PTFE (Polytetrafluoroethylene, Teflon®) as the dielectric, which is a low-loss material with relative permittivity $\epsilon_r = 2.05$ and a dielectric loss tangent ($\tan \delta$) of around 2.5×10^{-4} at microwave frequencies [123].

In order to understand the effects of these connectors we consider the setup of Fig. 2.10a. Shown is a lossless single-port antenna with reflection coefficient Γ fed through an attenuating element. The attenuating element, which models the effect of the SMA port, is characterised by its insertion loss a (in decibels) or, alternatively, its s_{21} scattering parameter. Since eigen-

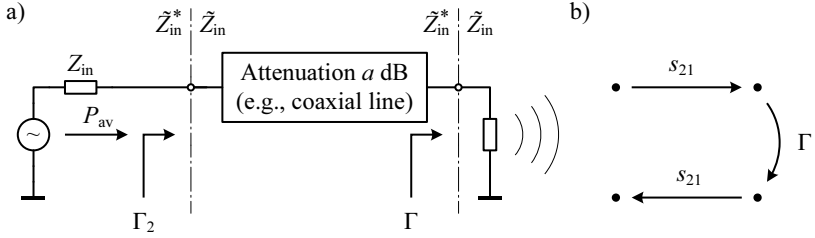


Fig. 2.10: (a) An antenna with reflection coefficient Γ is connected to a generator with available power P_{av} through a reflectionless attenuating element (e.g., a piece of transmission line) with decibel insertion loss a . (b) The equivalent signal flow graph.

modes were shown to provide essentially a description of a coupled array in terms of uncoupled equivalent radiators, Fig. 2.10a may conveniently be used to model the losses of, say, the “ π ”-mode.

Due to the attenuation, the reflection coefficient Γ_2 measured at the input port deviates from the actual reflection coefficient Γ of the antenna. Figure 2.10b shows the corresponding signal flow graph, by which we can deduce the following relationships between the variables:

$$|\Gamma_2| = |s_{21}|^2 |\Gamma|, \quad \text{with} \quad |s_{21}| = 10^{-a/20}, \quad (2.56)$$

where a is measured in dB. If we let P_{av} denote the power available from the driving source, P_{acc} the power accepted at the input port, and P_{rad} the power finally radiated by the (lossless) antenna, we can establish the “acceptance efficiency” $\lambda_{acc} = P_{acc}/P_{av}$ and the radiation efficiency $\lambda_{rad} = P_{rad}/P_{av}$ of the system as

$$\lambda_{acc} = 1 - |\Gamma_2|^2 = 1 - |s_{21}|^4 |\Gamma|^2, \quad \text{and} \quad \lambda_{rad} = |s_{21}|^2 (1 - |\Gamma|^2). \quad (2.57)$$

Solving for $|s_{21}|^2$ and $|\Gamma|^2$ in terms of λ_{acc} and λ_{rad} yields

$$|s_{21}|^2 = \frac{\lambda_{rad}}{2} + \sqrt{1 - \lambda_{acc} + \left(\frac{\lambda_{rad}}{2}\right)^2} \quad \text{and} \quad |\Gamma|^2 = 1 - \frac{\lambda_{rad}}{|s_{21}|^2}. \quad (2.58)$$

Substituting the data of the “ π ”-mode, i.e., $\lambda_{acc} = 1.4\%$ and $\lambda_{rad} = 1.0\%$, the above formulae result in

$$a = 0.0087 \text{ dB}, \quad \Gamma = 0.995, \quad \text{and} \quad \Gamma_2 = 0.993. \quad (2.59)$$

In other words, an attenuation as small as 0.009 dB reduces the efficiency of the “ π ”-mode by as much as 30 %. Subsequent electromagnetic simulations of the SMA-connector reported an insertion loss between 0.005 dB and 0.01 dB, depending on the configuration of the solver. This confirms that the values obtained by measurement for $\lambda_{acc,i}$, $\lambda_{rad,i}$, and χ_i , reflect the performance of the array in terms of both impedance mismatch and ohmic losses to within reasonable accuracy.

The insight that even tiny losses in a compact array can have substantial impact on its efficiency is a crucial one. Whereas in principle it is possible to compensate for mismatch or coupling losses via a matching network (Chapter 3), nothing can be done to overcome ohmic losses—other than to redesign the array. Suppose a matching network is inserted between the generator and the input of the attenuating element in Fig. 2.10. The operation of the matching network can be pictured in the way that it stores the energy reflected by the antenna and then appropriately releases it again on the next cycle until all energy is radiated. The higher the impedance mismatch, the more often the energy must travel between the load antenna and the matching network. If there are losses on the way, the energy becomes successively absorbed each time it passes by.

SMA connectors are not the only potential source of losses. Cables and antenna feed networks, such as decoupling and matching networks, possess considerably larger losses that will severely degrade array performance. For a graphical assessment of the influence of these losses, Fig. 2.11 plots the ohmic efficiency χ of the system in Fig. 2.10 versus the matching efficiency $1 - |\Gamma|^2$ of the (lossless) radiating element for varying attenuation a . According to the graphs, if our example array were connected to a decoupling and matching network through coaxial cables with an attenuation of 0.1 dB, then its “ π ”-mode efficiency would not exceed 20 % under any circumstances.

As a rule of thumb, if the decibel attenuation a has the same value as the decibel return loss Γ , then the efficiency is 33 %: one third is absorbed on the way to the antenna, one third is radiated, and one third is absorbed on the way back to the generator.

The examples demonstrate that mutual radiator coupling defines a physical limit to the feasible compactness of antenna arrays. This limit cannot be overcome, for the plain reason that completely lossless materials do not exist. With the concepts introduced in this chapter, however, we have the necessary tools at hand to accurately assess the quality of an antenna array and thus the

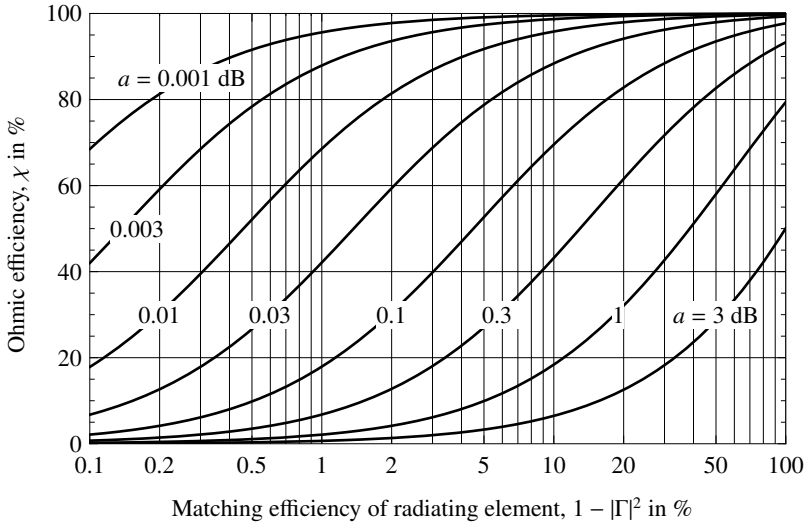


Fig. 2.11: Maximum achievable total efficiency of the system in Fig. 2.10 dependent on the matching efficiency $1 - |\Gamma|^2$ of the lossless antenna and the insertion loss a of the attenuating element.

ability to come to a decision whether or not an array design is suited for a particular engineering application.

2.7.2 Influence of the number of radiators and their separation

To get an idea of the amount of space reduction possible with uniform linear arrays, Fig. 2.12 plots the worst-case efficiency λ_{\min} (2.11) as a function of the number of radiators n and the spacing d between them. The graphs were obtained by simulating arrays of $\lambda_0/2$ -dipoles consisting of thin, lossless cylinders placed in free space using CST Microwave Studio [126]. Lumped 50Ω -ports were used to excite the dipoles. Detuning of the resonant frequency due to the mutual coupling has been taken into account by looking for the frequency of best power match and adjusting the positions of the sampling points in the graph accordingly.

The trends conveyed by the figure are obvious. As expected, lower ra-

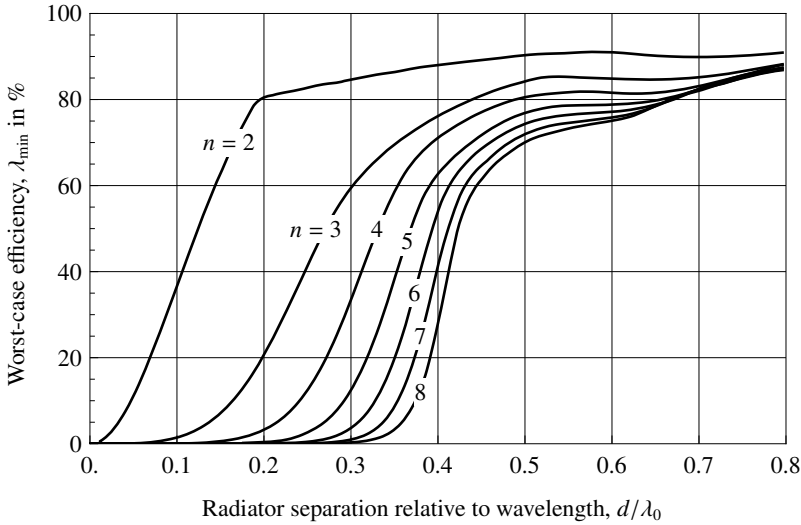


Fig. 2.12: Worst-case eigenefficiencies of uniform linear dipole arrays for varying radiator spacing d and different numbers of radiators n . The graphs have been obtained by electromagnetic simulation and subsequent interpolation between the results.

diator spacings give rise to a degraded efficiency of at least one eigenmode. Whereas a spacing of $\lambda_0/4$ appears feasible at $n = 4$ or perhaps $n = 5$, an array with eight elements is probably of little use in most applications because at least one degree of freedom is unavailable. According to the graphs, remarkably small separations are achievable with two radiators.

With increasing number of antenna elements, the transition region between high and low efficiency not only moves towards greater separations, but becomes sharper, i.e., the dependence on the radiator separation becomes more sensitive. On the one hand, the graphs indicate that a noteworthy reduction of the radiator spacing is only sensible with few radiators; for larger n , however, even a small reduction of the spacing has considerable effect on the overall dimensions of the array. It is remarkable that for “conventional” $\lambda_0/2$ arrays, some degradation due to residual coupling is still observable.

Note that the graphs are specific to linear dipole arrays and $50\ \Omega$ loads. Naturally, the eigenefficiencies depend on a number of additional factors,

such as the impedances of the loads, the radiator arrangement (e.g., linear or circular), but also the directivity, orientation, and efficiency of the isolated radiators.

2.8 Summary

In this chapter, we have investigated the transport of power from a set of generators to a mutually coupled antenna array. We have found that as the result of mutual coupling, the radiation efficiency λ is not constant but rather a function of the amplitude and phase excitation of the antenna array terminals. The range of efficiencies that can be observed is bounded by the smallest and by the largest eigenvalue of the radiation matrix. It was consequently suggested that this worst-case efficiency is used as a *figure of merit* for the quality of an antenna array. In the typical lossless case, the worst-case efficiency is easily extracted from the *scattering matrix* of the antenna array and thus lends itself to *simple comparisons* between different compact array designs.

The eigenvalues of the radiation matrix were examined further. It turned out that they can be interpreted as the efficiencies of the degrees of freedom, the *eigenmodes*, available in an antenna array. There are always as many *eigen efficiencies* as there are array terminals. In this sense, they generalise the notion of *radiation efficiency* from a single radiator to multi-port antennas. Mutual coupling generally causes one or more eigen efficiencies to degrade. In this context we have to keep in mind, however, that the eigenmodes are not a property inherent to the antenna array itself but rather characterise a particular *combination* of antenna array and the internal impedances of the signal sources (power amplifiers) or signal sinks (receiver front-end amplifiers) employed in the system.

Later sections proceeded to identify the interrelationship between the radiation matrix and the far-field patterns of the array. The fundamental significance of the eigenmode concept is supported by the fact that eigenmodes possess orthogonal beam-patterns that do not exchange power. It was concluded that these *eigenpatterns* and the corresponding eigen efficiencies uniquely characterise the radiation capabilities of the array, in terms of both the available *pattern space* and its efficiency. The eigenmode theory was subsequently extended to include possible ohmic losses of the array in addition to reflection and coupling losses. An equivalent circuit model for lossless arrays was developed that puts together the various mathematical pieces of

this chapter. Examples finally demonstrated the usefulness of the eigenmode theory for the characterisation of practical arrays. It became clear that seemingly negligible ohmic losses can cause additional efficiency impairments in the presence of strong mutual coupling.

Chapter 3

Decoupling and matching networks

With the information from the last chapter we have a number of tools available to assess the radiation capabilities of an antenna array, both in terms of power mismatch but also in terms of ohmic losses within the array.

There is not much one can do about ohmic antenna losses other than using better materials. On the other hand, if array performance is degraded by input port mismatch or coupling, then there is the possibility of inserting a decoupling and matching network (DMN) between the antenna array and the rest of the system. A DMN can be thought of as the multi-dimensional equivalent of the well-known single-port impedance matching circuit. Its purpose is to provide full power matching for all excitations. In mathematical terms, this means that the scattering matrix resulting from the interconnection of the coupled antenna array and the DMN becomes the zero matrix: zero off-diagonal elements imply that no coupling exists between ports; zero diagonal elements indicate perfect matching. Both conditions together ensure that the incident power waves \vec{a} remain inside the antenna system and do not reflect to the exciting sources. DMNs possess as many input terminals as the antenna array. Fewer ports seem pointless, as they would remove degrees of freedom from the array. A larger number of decoupled and matched ports necessitates ohmic losses inside the DMN. Otherwise, the network would add radiating degrees of freedom to the system, which obviously is unphysical.

We must understand that DMNs only affect the *power transfer* between the system and the antenna array. Hence, they only influence the eigenefficiencies λ_i . The beam pattern space, on the other hand, is solely defined by the radiating parts of the array and therefore remains unchanged. Furthermore, DMNs cannot generally counteract the fact that the excitation of one radiator induces currents in neighbouring elements thereby causing the resulting (embedded) radiation pattern to deviate considerably from the pattern of the isolated radiator [23]. It is thus impossible to equip a $\lambda_0/10$ linear dipole array, for instance, with a lossless DMN whose input terminals produce appropriately phase-shifted instances of the familiar “donut”-shaped pattern of the isolated dipole. This follows from the non-orthogonality of the resulting beam-pattern set.

Similar to single-port matching networks, DMNs can be implemented using distributed transmission line structures, lumped (i.e., discrete) elements, or a mixture of both. After the following section about the basic mathematics behind DMNs, the rest of this chapter mainly concerns one particular type of transmission line based DMNs. The primary reason is that these networks are closely linked to the eigenmode theory of the previous chapter. Furthermore, lumped and quasi-lumped designs are treated extensively by Wang [120], Chaloupka et al. [88–90], and Weber [121]. References to additional DMN approaches will be given where appropriate.

3.1 General conditions for decoupling and matching

Before a practical design method for DMNs is presented, the general conditions for its scattering matrix are derived. We will consider reciprocal and lossless matching networks only, although practical realisations will be lossy, of course. A study on how to account for network losses during the DMN design procedure is presented by Weber et al. [148].

We begin with the most trivial form of a DMN, the single-port matching network. Practical ways for their implementation are found in most textbooks on microwave engineering, e.g., [13, Chapter 5]. At this point, however, we are interested in a mathematical description of the scattering matrix of this kind of network.

We assume the setup in Fig. 3.1a where a network \tilde{S}_M is used to match the load (e.g., a single antenna) with impedance Z to the internal impedance Z_{in} of the generator. The reflection coefficient of the load is denoted by Γ and

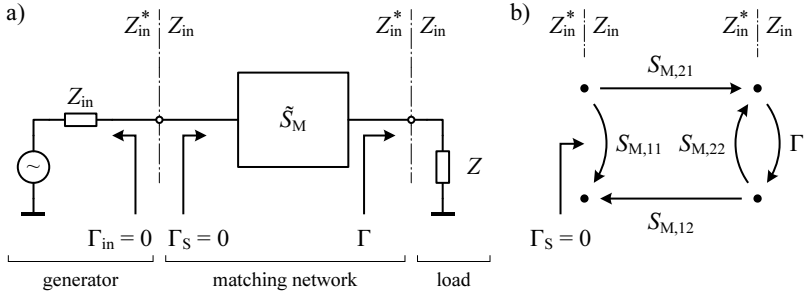


Fig. 3.1: (a) Illustration of a matching network inserted between a load impedance Z and a generator with internal impedance Z_{in} . (b) The corresponding signal flow graph.

the reflection coefficient of the *system* (matching network including the load) is denoted by Γ_S . The signal flow graph in Fig. 3.1b clarifies the naming of the scattering coefficients of \tilde{S}_M . For given Γ , the goal is to find a lossless and reciprocal network \tilde{S}_M so that $\Gamma_S = 0$. According to Appendix A.3 the solution is given by

$$\tilde{S}_M = \begin{pmatrix} -u^2\Gamma & u\sqrt{1-|\Gamma|^2} \\ u\sqrt{1-|\Gamma|^2} & \Gamma^* \end{pmatrix}. \quad (3.1)$$

The parameter u is an arbitrary unit phasor (i.e., $u = e^{j\varphi}$ with φ arbitrary real), implying that for a given load Γ there exists an infinite set of impedance matching circuits. From a mathematical point of view, it may be tempting to think of the parameter u merely as a piece of lossless transmission line with line impedance Z_{in} inserted at the input port. It is this degree of freedom, however, which gives rise to the great number of different practical network *implementations*. Examples are LC matching networks, quarter-wave transformers, or double-stub tuners. All these perform the same mathematical impedance transformation, yet each network has its distinct implementation-specific advantages and disadvantages.

For multi-port arrays, the setup is very similar to the single-port case. This time we have an n -port antenna array \tilde{S} instead of the single radiator Γ and the DMN is consequently described by a $2n \times 2n$ network matrix \tilde{S}_M . The goal is to determine \tilde{S}_M for given \tilde{S} so that the system scattering matrix \tilde{S}_S becomes the zero-matrix. Following the derivation in Appendix A.4 the solution can

be expressed in block matrix form as

$$\tilde{S}_M = \begin{pmatrix} -\tilde{U}^T \tilde{S} \tilde{U} & \tilde{U}^T [\tilde{I} - \tilde{S} \tilde{S}^H]^{1/2} \\ ([\tilde{I} - \tilde{S} \tilde{S}^H]^{1/2})^T \tilde{U} & \tilde{S}^* \end{pmatrix}, \quad (3.2)$$

where the superscript $^{1/2}$ denotes the matrix square-root as defined in the appendix on page 209. The first n ports are referred to as the input ports of the network and the last n ports are the output ports. As with the single-port case (3.1), the solution is not unique and the degrees of freedom are reflected in the unitary but otherwise arbitrary matrix \tilde{U} . All solutions have in common that the reflection coefficients as well as the coupling coefficients at the output ports $\tilde{S}_{M,22}$ of the DMN are conjugately matched to the load array.

As with single-port matching networks, the parameter \tilde{U} may be adjusted to yield different practical DMN implementations. Weber [121], [148] not only demonstrates how the degrees of freedom in \tilde{U} can be harnessed to minimise the number of network elements required, but also points out the possibility to assign arbitrary radiation patterns to each network port within the limits imposed by pattern orthogonality and the pattern space provided by the array.

In the following sections, we will introduce one specific type of DMN implementation that intuitively relates to the eigenmode theory presented in the previous chapter. One resulting advantage is that this kind of network is especially straightforward to design.

3.2 Decoupling by eigenmode excitation

Let us start by setting \tilde{U} equal to the matrix of eigenmodes \tilde{Q}_{acc} as determined from the scattering matrix of the antenna array. With (2.17) and (A.32) the solution (3.2) then becomes:

$$\tilde{S}_M = \begin{pmatrix} -\tilde{\Gamma}_m & \sqrt{\tilde{\Lambda}_{acc}} \tilde{Q}_{acc}^T \\ \tilde{Q}_{acc} \sqrt{\tilde{\Lambda}_{acc}} & \tilde{S}^* \end{pmatrix}, \quad (3.3)$$

where $\tilde{\Gamma}_m$ is the diagonal matrix of modal reflection coefficients and $\tilde{\Lambda}_{acc}$ is the diagonal matrix of eigenefficiencies. By inspection of the signal flow graphs in Fig. 3.2, it becomes clear that this network is mathematically equivalent to

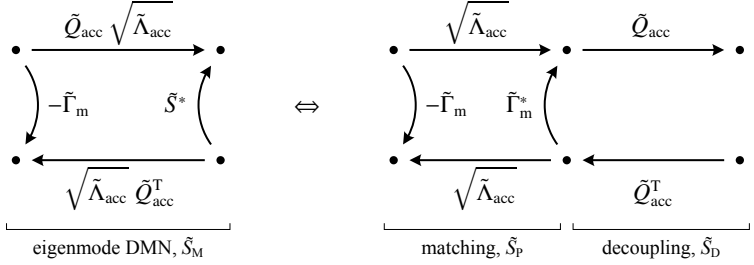


Fig. 3.2: Separation of an eigenmode decoupling and matching network into a decoupling network and a bank of single-port matching networks.

the interconnection of two networks \tilde{S}_P and \tilde{S}_D with

$$\tilde{S}_P = \begin{pmatrix} -\tilde{\Gamma}_m & \sqrt{\tilde{\Lambda}_{acc}} \\ \sqrt{\tilde{\Lambda}_{acc}} & \tilde{\Gamma}_m^* \end{pmatrix} \quad \text{and} \quad \tilde{S}_D = \begin{pmatrix} \tilde{0} & \tilde{Q}_{acc}^T \\ \tilde{Q}_{acc} & \tilde{0} \end{pmatrix}, \quad (3.4)$$

respectively.

Since \tilde{S}_P is composed of diagonal sub-matrices only, it actually represents n independent two-port networks. If we compare \tilde{S}_P to (3.1) and remember that $\lambda_{acc,i} = 1 - |\gamma_{m,i}|^2$, we discover that \tilde{S}_P describes a bank of single-port matching networks whose input ports are matched to the normalising impedance and whose output ports are matched to the modal reflection coefficients $\gamma_{m,i}$ of the antenna array.

About network \tilde{S}_D we notice that its input and output ports are matched and decoupled among themselves. Power is transferred from the input ports to the output ports according to the matrix of eigenmodes \tilde{Q}_{acc} . For instance, if input port 1 of \tilde{S}_D is excited, the waves emerging from the output ports form the first eigenmode $\tilde{q}_{acc,1}$. In other words, each input port of the decoupling network *excites* a different eigenmode of the antenna array. In Section 2.2.4 we learned that the “shapes” of an eigenmode and its reflection cannot be distinguished from one another. Consequently, if a reciprocal network produces an eigenmode $\tilde{q}_{acc,i}$ at its output ports as the response to an excitation of *one* of its input ports i , then, due to reciprocity, the reflection of that eigenmode will be combined by the network so to arrive at input terminal i *only*. No power will appear at the remaining terminals. We therefore refer to the network \tilde{S}_D as a *decoupling network*.

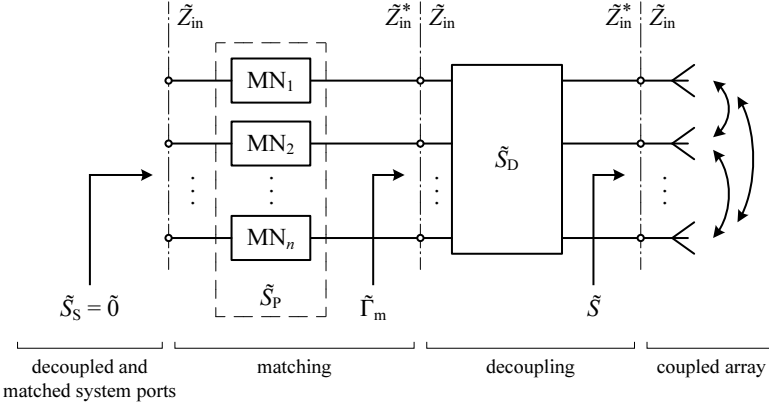


Fig. 3.3: Two-step approach to n -port array decoupling and matching: a decoupling network $\tilde{\mathbf{S}}_D$ is inserted in front of the antenna array whose inputs are individually matched in a subsequent step with network $\tilde{\mathbf{S}}_P$. MN = Matching network.

This decoupling property of $\tilde{\mathbf{S}}_D$ is readily verified mathematically with the help of (B.14), which calculates the system scattering matrix $\tilde{\mathbf{S}}_S$ resulting from the interconnection of the decoupling network to the antenna array $\tilde{\mathbf{S}}$. We have

$$\begin{aligned}\tilde{\mathbf{S}}_S &= \tilde{\mathbf{S}}_{D,11} + \tilde{\mathbf{S}}_{D,12} \tilde{\mathbf{S}} (\tilde{\mathbf{I}} - \tilde{\mathbf{S}}_{D,22} \tilde{\mathbf{S}})^{-1} \tilde{\mathbf{S}}_{D,21} \\ &= \tilde{\mathbf{Q}}_{acc}^T \tilde{\mathbf{S}} \tilde{\mathbf{Q}}_{acc} = \tilde{\mathbf{I}}_m,\end{aligned}\tag{3.5}$$

which is diagonal and therefore describes an uncoupled set of ports. Given that we previously (Section 2.6) identified the reflection coefficients $\gamma_{m,i}$ as the ultimate origins of port coupling and mismatch, it should not be surprising to see them emerge at the inputs of the decoupling network. Another way to picture the actions of a decoupling network is to think of it as the inverse to the coupling network $\tilde{\mathbf{S}}_Q$ in the equivalent circuit of Fig. 2.4. Since after decoupling, the input ports have become independent, all we need to do is match the individual ports to the desired impedances. This is precisely what is accomplished by the network $\tilde{\mathbf{S}}_P$.

The separation into two network parts (3.4) not only helps us understand the operation of the DMN in terms of eigenmodes, but it also serves us the information necessary to do an implementation. This dual step principle of

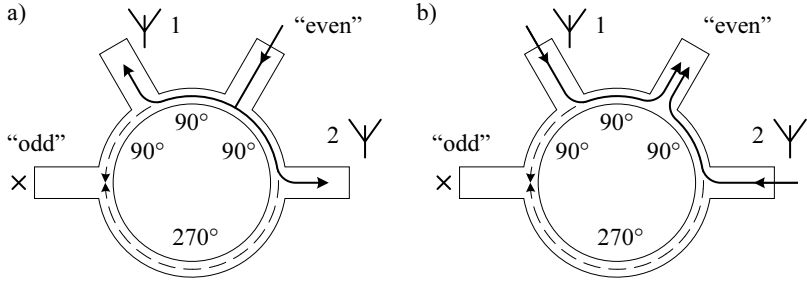


Fig. 3.4: A microstrip implementation of a 180° “rat-race” hybrid coupler decouples a symmetric two-port antenna array. The figure illustrates the power flow through the hybrid when the “even” mode of the antenna array is excited. (a) shows the waves travelling towards the antennas and (b) the associated reflections.

operation is sketched in Fig. 3.3. The matching networks \tilde{S}_P (“MN” in the figure) are easily designed using textbook techniques. Methods for designing the decoupling part \tilde{S}_D of the network are covered below.

3.3 Directional couplers as decoupling networks

Before we devise a systematic design procedure for eigenmode DMNs let us start with a descriptive discussion of two common practical examples, namely the symmetric two-port array and the symmetric three-port array.

3.3.1 Example: symmetric two-port antenna array

In an early example on page 12 we learned that the eigenmodes of a symmetric two-port array are the in-phase and the out-of-phase excitation of both radiators. We call these modes the “even” and the “odd” mode:

$$\text{“even”}: \begin{bmatrix} + & + \end{bmatrix}, \quad \text{and} \quad \text{“odd”}: \begin{bmatrix} + & - \end{bmatrix}.$$

What is needed for decoupling is a lossless and reciprocal four-port device that produces these modes at its outputs in response to feeding the individual input ports. Such a device is known as a 180° hybrid coupler.

Its implementation using microstrip transmission lines is called the “rat-race hybrid” [13, Section 7.8] and is depicted in Fig. 3.4. The ring consists of

four transmission line sections of equal line impedance. Three of these sections have a length of $\lambda_g/4$, and one section has a length of $3\lambda_g/4$, where λ_g denotes the guided wavelength on the transmission line. These sections therefore incur a phase-shift of 90° and 270° , respectively.

Figure 3.4 illustrates the behaviour of the hybrid when used as a decoupling network. When the port labelled “even” is excited in Fig. 3.4a, power splits evenly at the T-junction and reaches both radiators with equal amplitude and phase. This port obviously excites the even mode of the array. In order to reach the remaining port (“odd”), however, the waves have to travel 360° clockwise around the ring and 180° in the counter-clockwise direction. The waves therefore cancel.

Since eigenmodes are preserved upon reflection by the array, the reflected waves travel towards the hybrid coupler equal in both amplitude and phase. The waves sum at the “even” port and again superimpose destructively at the “odd” port (Fig. 3.4b). We observe that no power arrives at the “odd” port at any time, i.e., the “odd” port is *decoupled* from the “even” port. By similar reasoning it can be shown that the “even” port is decoupled if the “odd” port, which introduces a 180° phase difference between the antenna elements, is excited.

Note that the decoupling action of the hybrid is the consequence of exciting the array eigenmodes. It does *not* come about because the decoupled port is termed the “isolated” port in standard directional coupler nomenclature; it is easily verified that the above network will not decouple an asymmetric array where the eigenmodes differ from the even and odd excitation of the symmetric array.

3.3.2 Example: symmetric three-port antenna array

We saw in Section 2.7.1 on page 30 that the eigenmodes of a symmetric linear three-port array could be classified as the “even” mode, the “odd” mode, and the “ π ”-mode. The approximate relative phases within the eigenmode vectors were notated

$$\text{“even”}: \begin{bmatrix} + & + & + \end{bmatrix}, \quad \text{“odd”}: \begin{bmatrix} + & 0 & - \end{bmatrix}, \quad \text{and} \quad \text{“}\pi\text{”}: \begin{bmatrix} + & - & + \end{bmatrix}.$$

The decoupling network in Fig. 3.5 consists of two directional couplers.¹

¹The initial idea of employing two directional couplers for three-port decoupling is due to Dr. Jörn Weber, a former colleague of the author.

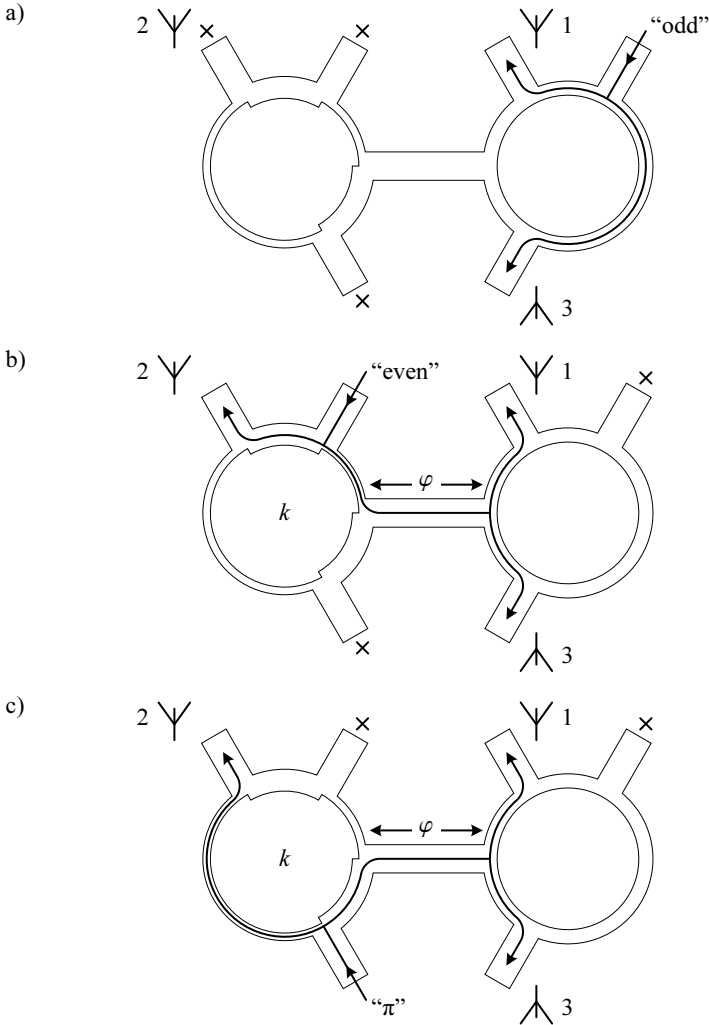


Fig. 3.5: Network for exciting the three eigenmodes of a mutually coupled symmetric linear three-port array. The directional coupler on the right-hand side is a hybrid coupler (symmetric power division). The left-hand side directional coupler possesses a non-symmetric coupling factor k . Both k and the length φ of the interconnecting transmission line must be matched to the antenna array. The centre radiator is labelled “2”.

When we excite the top right-hand side port in Fig. 3.5a, then radiators “1” and “3”, i.e., the outer radiators, are excited with equal amplitude but opposite phase. The rest of the network and the centre radiator “2” do not receive any power. This input port evidently excites the “odd” mode of the array.

Figures 3.5b and 3.5c illustrate the power flow for the “even” and for the “ π ”-mode, which involve all three radiators. The directional coupler on the left-hand side exhibits a non-symmetric power division ratio, i.e., the coupling factor is different from 3 dB. Both the coupling factor k and the electrical length φ of the interconnecting transmission line must be matched to the eigenmodes of the antenna array in order to account for the generally uneven power distribution and phase imbalance between the centre radiator and the outer radiators.

The following section will prove that this kind of network can always be designed to decouple arbitrary reciprocal three-port antenna arrays with port symmetry around their centre radiator.

3.4 A systematic design procedure for decoupling networks

The last, introductory section has shown that directional couplers can be used to decouple certain two and three-port antenna arrays. An early attempt to extend this idea to an arbitrary number of radiators is due to Riech [71]. Although it was found that a directional coupler can be used to decouple arbitrary pairs of ports, problems arose in subsequent stages to decouple any remaining ports: ports that had been decoupled in previous steps usually became coupled again. The proposed solution was to repeat the decoupling procedure until any residual coupling has become negligible.

A truly general and exact approach is presented by Geren et al. [41]. It is based on the insight that any matrix is diagonalised by a finite number of Givens-rotations, which in turn can be implemented as directional couplers. The major drawback of this method is that the required number of directional couplers is very large, even if array symmetries are exploited by the algorithm.

The design procedure presented here is only applicable to antenna arrays possessing certain port symmetries [142]. Despite this limitation, we will find that it includes a large number of practically relevant array constellations. For those cases to which it applies, the algorithm is mathematically exact.

We begin by proving that a four-port directional coupler can be designed

to excite the eigenmodes of *arbitrary* two-port arrays, not just symmetric ones. In order to avoid the problems encountered by Riech [71], a method is proposed to split an antenna array into two independent halves across a plane of symmetry. This process is repeated until effectively only two-port arrays remain, which can be decoupled individually without affecting one another. With the help of a mathematical trick, it becomes possible to devise decoupling networks for antenna arrays having an odd number of radiators. A further result is that the decoupling network for a circularly symmetric four-port array can be simplified compared with the networks found in the literature [31, 94, 110, 116].

We will denote the normalising impedance of the scattering matrices involved by the symbol Z_0 and require it to be positive real. The reason is that practical directional couplers and transmission line components in general can only be fabricated with positive real characteristic line impedances. This assumption has no influence on the possibility to manufacture DMNs for arbitrary complex Z_{in} . In this case we would design the decoupling part of the network based on $Z_0 = 50 \Omega$, for instance, and then individually match the resulting ports to Z_{in} .

3.4.1 Two-element decoupling

The two-port decoupling network constitutes the foundation for decoupling larger antenna arrays. A two-element array possesses two eigenmodes, so the matrix \tilde{Q}_{acc} has the general form

$$\tilde{Q}_{\text{acc}} = \begin{pmatrix} a & c \\ b & d \end{pmatrix}, \quad (3.6)$$

where $(a \ b)^T$ is the first and $(c \ d)^T$ is the second eigenmode. Since the absolute phase of an eigenmode is undetermined, we may normalise \tilde{Q}_{acc} such that $a, c \in \mathbb{R}^+$ without loss of generality. The unitary nature of \tilde{Q}_{acc} imposes the following constraints on the matrix elements:

$$|a|^2 + |b|^2 = |c|^2 + |d|^2 = 1, \quad \text{and} \quad ac^* = -bd^*, \quad (3.7)$$

which can be shown to be equivalent to

$$|c| = |b|, \quad |d| = |a|, \quad \text{and} \quad \arg d = \arg b + \pi. \quad (3.8)$$

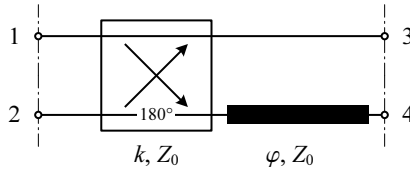


Fig. 3.6: A generalised directional coupler resulting from the connection of a 180° directional coupler with coupling factor k to a transmission line of electrical length φ . The line impedance matches the normalising impedance Z_0 of the system.

Now consider the general directional coupler in Fig. 3.6. It is matched at all ports and may thus be described by some block matrix \tilde{S}_D of the form [6, Eqn. (13.62)]

$$\tilde{S}_D = \begin{pmatrix} \tilde{0} & \tilde{S}_{D,21}^T \\ \tilde{S}_{D,21} & \tilde{0} \end{pmatrix}, \quad \text{with} \quad \tilde{S}_{D,21} = -j \begin{pmatrix} k & \sqrt{1-k^2} \\ e^{-j\varphi} \sqrt{1-k^2} & k e^{-j(\pi+\varphi)} \end{pmatrix}. \quad (3.9)$$

The coupling factor and the electrical length of the transmission line are denoted by k and φ , respectively. It is easily verified that $\tilde{S}_{D,21}$ satisfies the above constraints; therefore, the directional coupler can be designed to excite the eigenmodes of an *arbitrary* reciprocal two-port antenna array. Provided that k and φ are chosen to match the eigenmodes of the antenna array, the circuit of Fig. 3.6 presents a two-port decoupling network. Note that any type of directional coupler is appropriate for practical implementation. For realisation as a microstrip network, rat-race couplers [21, 68], [13, Section 7.8] and branch-line couplers [13, Section 7.5] are probably the most convenient forms.

We have reasoned already that a hybrid coupler with $k^2 = 1/2$ and $\varphi = 0$ decouples a symmetric antenna array with $s_{11} = s_{22}$. Then (3.9) becomes

$$\tilde{S}_{D,21} = \frac{-j}{\sqrt{2}} \begin{pmatrix} 1 & 1 \\ 1 & -1 \end{pmatrix} \quad (3.10)$$

and the decoupling action is also confirmed mathematically when $\tilde{S}_{D,21}$ is substituted into (3.5). A useful feature of the symmetric case is that the exact scattering parameters *do not* have to be known for the design of the decoupling network.

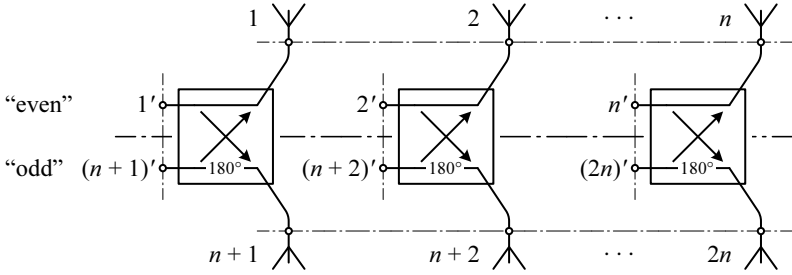


Fig. 3.7: A bank of symmetric 180° hybrid couplers is used to decouple an antenna array across a plane of symmetry.

As mentioned earlier, decoupling two ports of an array usually destroys decoupling that has been achieved in previous steps. The next section explains how larger antenna arrays can be partitioned into independent subparts.

3.4.2 Decoupling across a symmetry plane

Figure 3.7 portrays a $2n$ -port antenna array connected to bank of symmetric 180° hybrid couplers. The scattering parameters of the array must possess at least one plane of symmetry; i.e., whereas antenna elements 1 to n may be different, they must be indistinguishable from elements $n+1$ to $2n$ by measurement. Usually, but not necessarily, this port symmetry is the result of geometric symmetries. Although the figure suggests a rectangular arrangement of radiators, the above requirements are also fulfilled by certain linear or circular constellations, as we will see later. By inspection, it becomes evident that the scattering matrix of the antenna array can be written in block matrix notation as

$$\tilde{S} = \begin{pmatrix} \tilde{S}_{11} & \tilde{S}_{12} \\ \tilde{S}_{12} & \tilde{S}_{11} \end{pmatrix}, \quad (3.11)$$

with both $\tilde{S}_{11}, \tilde{S}_{12} \in \mathbb{C}^{n \times n}$ and symmetric.

Consider the bank of all n hybrid couplers as one $4n$ -port junction. The primed ports shall be its input ports and the unprimed ports shall be its output ports. Borrowing the notation from (3.9), this hybrid network is described by

$$\tilde{S}_{D,21} = \frac{-j}{\sqrt{2}} \begin{pmatrix} \tilde{I} & \tilde{I} \\ \tilde{I} & -\tilde{I} \end{pmatrix}, \quad (3.12)$$

where \tilde{I} is the $n \times n$ identity matrix. The scattering matrix \tilde{S}_S of the system resulting from the interconnection of the antenna array and the bank of hybrids is readily obtained by applying (3.5):

$$\tilde{S}_S = \begin{pmatrix} \tilde{S}_{12} + \tilde{S}_{11} & \tilde{0} \\ \tilde{0} & \tilde{S}_{12} - \tilde{S}_{11} \end{pmatrix}. \quad (3.13)$$

Here the important observation is that the network not only decouples array ports i and $n + i$, that is, the two ports each individual hybrid coupler is connected to. Rather the hybrids separate the fully coupled $2n$ -port antenna array into two mutually independent sets of n ports with scattering matrices $\tilde{S}_1 = \tilde{S}_{12} + \tilde{S}_{11}$ and $\tilde{S}_2 = \tilde{S}_{12} - \tilde{S}_{11}$, respectively. Following the terminology of Section 3.3.1 we call these the “even” and the “odd” set of ports. Subsequent decoupling may now be performed on each set separately without influencing the other. The procedure may be repeated if the newly derived system ports again fulfil the symmetry requirements.

Decoupling across symmetry planes can be accomplished without knowledge of the array scattering matrix. In combination with the two-port decoupling technique discussed in the last subsection, we are now able to design decoupling networks for certain antenna arrays whose number of radiators is a power of two.

Figure 3.8 illustrates some example array constellations that are decoupled with the techniques described so far. A square arrangement of four radiators is depicted in Fig. 3.8a. According to Fig. 3.7 this array is decoupled by connecting two hybrid couplers across the plane of symmetry “a”. One hybrid is applied to decouple elements 1 and 3 and another one decouples elements 2 and 4. This creates an “even” and an “odd” set of ports which are independent of each other. As a result of the additional symmetry plane “b”, both sets are port-symmetric themselves and can therefore be decoupled with a hybrid coupler as in Section 3.3.1. The final decoupling network consists of four hybrid couplers. Its design does not depend on any measurement data.

The array of Fig. 3.8b is decoupled in a similar fashion. Since this arrangement lacks a second symmetry plane, however, the second step of decoupling requires the asymmetric technique from the previous subsection. Although this time the scattering matrix of the antenna array must be known, the network complexity remains the same: four directional couplers, two of which are hybrids.

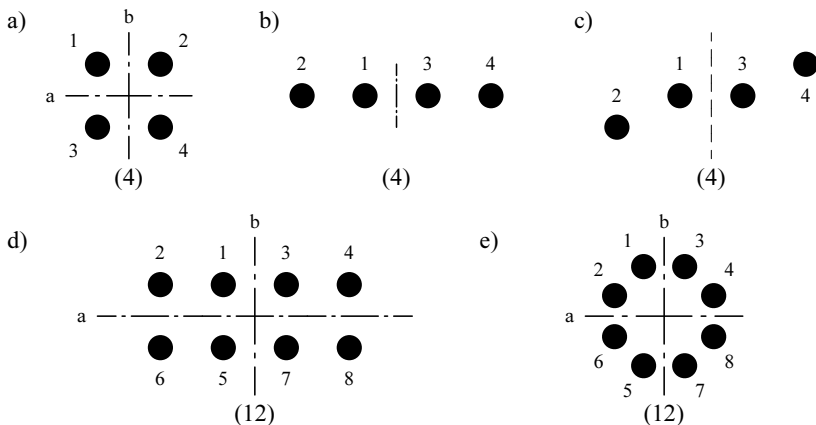


Fig. 3.8: Examples of antenna array constellations with one or two planes of symmetry. Parenthesized numbers indicate the number of directional couplers required.

Figure 3.8c exhibits the same port-symmetry as Fig. 3.8b and can therefore be decoupled with the same type of network. The example demonstrates that geometric reflection symmetry is not a prerequisite for port symmetry.

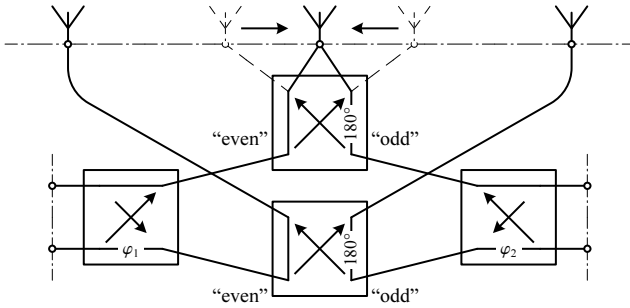
An array of eight radiators is depicted in Fig. 3.8d. Decoupling across symmetry plane “a” causes the array to decompose into two sets of ports that exhibit the same symmetry as Fig. 3.8b. The full decoupling network therefore requires twelve directional couplers, eight of them being hybrids. The same decoupling network also applies to the circular array of Fig. 3.8e.

3.4.3 Radiator merging

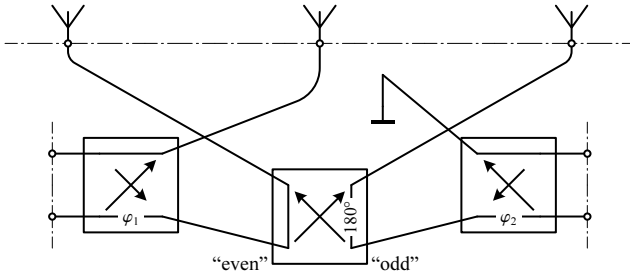
Additional constellations and decoupling scenarios arise, when two radiators are virtually merged into one across a plane of symmetry. The number of radiators is reduced by one and, in consequence, one or more directional couplers degenerate into short circuits or uncoupled “couplers”. There are two applications for this procedure. One is to derive decoupling networks for arrays with an odd number of radiators. The other application is to create simpler versions of decoupling networks for arrangements, for which networks already exist.

The example of Fig. 3.9 illustrates how, starting with a linear four-element

a)



b)



c)

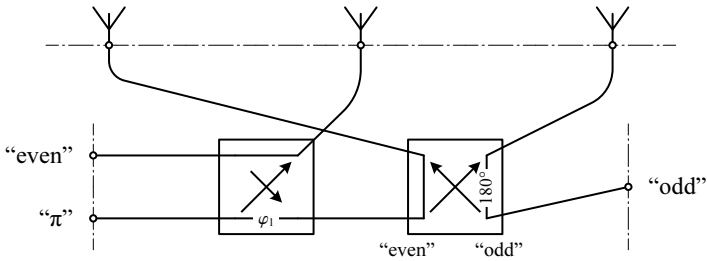


Fig. 3.9: A symmetric four-element linear array is transformed into a linear array of three radiators (a), whereby the number of directional couplers is reduced by two (b, c). The final network was introduced earlier in Section 3.3.2.

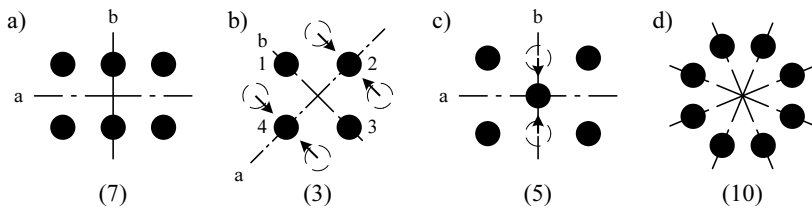


Fig. 3.10: Examples of antenna array constellations that benefit from radiator merging. Parenthesized numbers indicate the number of directional couplers required for decoupling.

array, the decoupling network for a linear three-element antenna array can be derived systematically. We have seen in the last subsection that, in the most general case, a four-port array with one plane of symmetry requires four directional couplers for decoupling, two of which are hybrids.

In a first step, the two centre radiators are merged into one (Fig. 3.9a). Because the “odd mode” of the single radiator is a short circuit, this causes the “odd” port of the coupler to be effectively grounded whereas the “even” port becomes directly connected to the radiator. The hybrid coupler may therefore be removed from the network (Fig. 3.9b). Clearly, the “odd” port of the remaining hybrid coupler and the newly created ground connection are not coupled. We can therefore eliminate the right-hand side coupler as well (Fig. 3.9c). The final decoupling network was introduced earlier in Section 3.3.2. We have thus provided proof that this network is in fact applicable to arbitrary linear three-port arrays with port symmetry around the centre radiator.

Four additional examples of antenna arrays that benefit from radiator merging are depicted in Fig. 3.10. The arrangement of six elements in Fig. 3.10a is first decoupled across symmetry plane “a” and then employs two instances of the three-port decoupling network on the remaining ports. Seven directional couplers are required, of which five are hybrids.

A four-port array is created in Fig. 3.10b by merging the outer radiators on each side of a six-port array. This removes four directional from the six-port decoupling network so that the final network consists of two hybrids and one directional coupler. Note that simply by placing the symmetry planes in a different way, the number of directional couplers required is reduced by one

in comparison with Fig. 3.8a and with the networks previously described in the literature [31, 94, 110, 116].

The reason why two different decoupling network topologies exist for the circularly symmetric (i.e., square) arrangement is that the array has one repeated eigenefficiency as the result of its symmetry. Consequently, any linear superposition of the corresponding eigenmodes is again an eigenmode. Consider the excitations produced by the network of Fig. 3.8a:

$$\text{“even”}: \begin{bmatrix} + & + \\ + & + \end{bmatrix}, \text{“odd 1”}: \begin{bmatrix} + & + \\ - & - \end{bmatrix}, \text{“odd 2”}: \begin{bmatrix} + & - \\ + & - \end{bmatrix}, \text{“}\pi\text{”}: \begin{bmatrix} + & - \\ - & + \end{bmatrix}.$$

Any orthogonal pair of linear combinations of the modes “odd 1” and “odd 2” is again a decoupled pair of eigenmodes. If we compose the sum and the difference of these two modes, we obtain the following set:

$$\text{“even”}: \begin{bmatrix} + & + \\ + & + \end{bmatrix}, \text{“odd 1”}: \begin{bmatrix} + & \circ \\ \circ & - \end{bmatrix}, \text{“odd 2”}: \begin{bmatrix} \circ & + \\ - & \circ \end{bmatrix}, \text{“}\pi\text{”}: \begin{bmatrix} + & - \\ - & + \end{bmatrix},$$

which is precisely the one excited by the network of Fig. 3.10b.

Figure 3.10c depicts a rather unusual constellation of five radiators. The decoupling network is derived from the six-port network. It requires four hybrids and one directional coupler, and excites the following modes:

$$\begin{bmatrix} + & & + \\ & + & \\ + & & + \end{bmatrix}, \begin{bmatrix} + & & + \\ & - & \\ + & & + \end{bmatrix}, \begin{bmatrix} + & & + \\ & \circ & \\ - & & - \end{bmatrix}, \begin{bmatrix} + & & - \\ & \circ & \\ + & & - \end{bmatrix}, \begin{bmatrix} + & & - \\ & \circ & \\ - & & + \end{bmatrix}.$$

Notice how these modes are essentially the modes of the four-port array with an additional decoupling step inserted between the centre radiator and the “even” mode of the outer radiators. If the planes of symmetry are chosen as in Fig. 3.10b, then, again, one hybrid can be saved.

As a final example, we consider the circular eight-port array in Fig. 3.10d. If pairwise diagonally opposed radiators are decoupled using symmetry decoupling with four hybrid couplers, then the resulting “even” port-set will exhibit the same mathematical symmetry as the array of Fig. 3.10b and can consequently be decoupled with three hybrids. The “odd” port set does not possess this kind of symmetry; however, it will have two pairs of ports that are decoupled already. Decoupling *one* of these pairs *a second time* using a hybrid yields two mutually isolated pairs of ports that require one hybrid each as

the final decoupling step. This is another example where judicious placement of the symmetry planes saves directional couplers: the final network consists of ten hybrids as opposed to twelve directional couplers for Fig. 3.8e.

3.4.4 Eigenmode matching

In the preceding sections, we have learned a systematic method to decouple the ports of various antenna array constellations. The proposed decoupling networks are eigenmode excitation networks. If the above steps are performed correctly, the resulting network will have a scattering matrix of the form (3.4). The fact that only the *relative* phases within eigenmode vectors matter facilitates the interconnection of directional couplers in a decoupling network using transmission lines. Since the input ports of the decoupled antenna array are independent, matching them to the impedances $Z_{in,i}$ of the driving generators is readily accomplished with textbook methods.

Matching a highly mismatched load, such as the higher order eigenmodes of a compact antenna array, generally results in a narrow matching bandwidth [39]. Furthermore, component and manufacturing tolerances can cause the manufactured network to fall outside the desired frequency range. In this context, the approach presented has the specific advantage that the decoupling bandwidth is usually very wide compared with the matching bandwidth. The frequency response of individual ports can therefore be adjusted even after fabrication. One matching network implementation with the specific goal of tunability is the double-stub network [13, p. 266]. Another benefit of this two-step approach is that established methods for broadband or multi-band matching can be employed to implement a desired frequency response. Yet another idea is a varactor-tuned matching network approach to adapt the antenna array to different frequency channels and operating conditions.

Although the directional coupler approach discussed so far is systematic and has been shown to apply to a wide range of antenna array topologies it does bear its disadvantages. One is its large size and the other one is the resulting insertion loss. On this account, it is pointed out that the directional coupler-based two-port decoupling network introduced in Section 3.4.1 can be replaced by any type of two-port decoupling network. In multi-port decoupling networks, all directional couplers *directly* attached to the input terminals can be so replaced. Wang [120], Nilsson et al. [102], and Chen et al. [29], for instance, suggest a systematic and generally valid method for

two-port decoupling (and matching) that is not based on directional couplers. The approach, which is illustrated in Fig. 3.11a, employs transmission lines in front of the radiators to make the real part of the Z_{12} element in the impedance matrix vanish. The remaining imaginary part is then compensated for by a transverse reactive element. Thereby the two ports become decoupled. In a final step, the inputs are matched to Z_{in} .

An even more compact network arises with the following approach: impedance transformation networks transform the antenna port impedances in such a way that the subsequent connection of a transverse reactive element not only neutralises the mutual coupling but also causes the ports to be matched. This principle is illustrated in Fig. 3.11b. An example implementation in microstrip is depicted in Fig. 3.11c. The major advantage is that the energy storing elements are moved as close to the array as possible, which not only reduces the footprint of the network but also, most importantly, mitigates ohmic losses.

Although no closed-form formulae for the component values of this type of network could be derived, the design is straightforward with the help of the non-linear optimisers found in modern RF design software, such as the Agilent Advanced Design System (ADS) [122]. In contrast to the hybrid coupler based network, the full scattering parameters of the antenna array must be known. Example implementations are covered in Sections 3.6.3 and 3.6.4 below.

3.5 Efficiency considerations

The networks considered have been assumed lossless, which is rarely the case in reality. The return losses measured at the input ports of a practical decoupling network implementation (without matching) will be notably better than the modal reflection coefficients $\gamma_{m,i}$ predicted by the eigenmode analysis of the array. This is due to ohmic losses in the network, which dissipate power and in this way improve the apparent power matching. Impedance matching networks implemented at the inputs of the decoupling network will not only improve power transfer to the antenna array, but also to these losses. In Section 2.7.1 we have previously investigated the extent to which even small losses in the feeding structure degrade the efficiency of the entire system, especially, if the insertion loss introduced by the decoupling network approaches the return loss of a particular eigenmode. Consequently, good

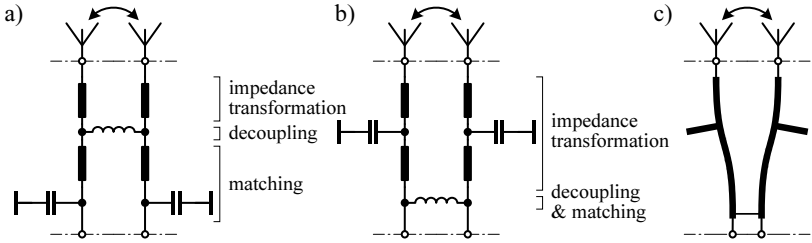


Fig. 3.11: An alternative two-port decoupling and matching method. (a) The approach found in the literature, (b) an improved version, which eliminates one impedance transformation step, and (c) possible microstrip implementation of (b).

decoupling and matching indicates that any power supplied is accepted by the system, but it provides by no means sufficient evidence for its efficient operation.

We have already learned that the matrix \tilde{H} or, more specifically, the associated set of eigenefficiencies, contains all information necessary to characterise an antenna array in terms of its efficiency. Two versions of the matrix were introduced: the matrix \tilde{H}_{acc} considers only port mismatch and coupling, whereas the matrix \tilde{H}_{rad} additionally includes ohmic losses of the antenna array. For the optimisation and comparison of decoupling and matching networks, it would be very helpful if a *system* matrix \tilde{H}_S could be constructed that takes into account the influence of the network based on its scattering matrix \tilde{S}_N . The eigenvalues of this matrix would then represent the eigenefficiencies of the newly established antenna array system.

Figure 3.12 illustrates the situation. The solution of the corresponding set of matrix equations lets us express the waves \vec{d} travelling in the reference plane of the array ports in terms of the waves \vec{d}_S supplied at the system terminals:

$$\vec{d} = \tilde{t}_a \vec{d}_S, \quad \text{with} \quad \tilde{t}_a = (\tilde{I} - \tilde{S}_{N,22} \tilde{S})^{-1} \tilde{S}_{N,21}. \quad (3.14)$$

Matrix \tilde{t}_a is the “ \vec{d} -wave transfer matrix”. The familiar block-matrix notation is used for the network matrix \tilde{S}_N with the ports indexed “2” connected to the antenna array, and the ports indexed “1” being the new system ports. If we recall the previous assumption that the scattering matrices used in the calculations are normalised to the impedances $Z_{\text{in},i}$ of the driving generators,

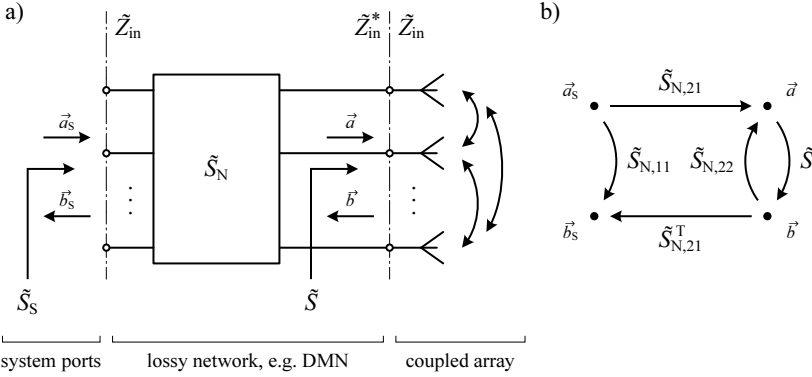


Fig. 3.12: Illustration of the power waves \vec{a}_s and \vec{b}_s at the inputs of an antenna system consisting of an arbitrary network \tilde{S}_N and an antenna array \tilde{S} . The waves travelling in the reference plane at the antenna ports are \vec{a} and \vec{b} .

then the power radiated by the antenna array is

$$P_{\text{rad}} = \vec{a}^H \tilde{H} \vec{a} = \vec{a}_s^H (\tilde{t}_a^H \tilde{H} \tilde{t}_a) \vec{a}_s, \quad (3.15)$$

where \tilde{H} is the radiation matrix of the sole antenna array, either \tilde{H}_{acc} or \tilde{H}_{rad} . Thus, the radiation matrix \tilde{H}_S of the complete system equals

$$\tilde{H}_S = \tilde{t}_a^H \tilde{H} \tilde{t}_a. \quad (3.16)$$

It should be emphasised at this point that the above formulation holds for *any* network connected to the antenna array and is not restricted to DMNs. Ohmic losses as well as residual coupling and impedance mismatch at the input ports are taken into account. This enables the broadband evaluation of networks where the decoupling and matching properties diminish for frequencies away from the centre frequency. By comparing the eigenvalues of \tilde{H} and \tilde{H}_S the engineer receives information about the true improvements brought about by the designed network. For this analysis, the full $2n$ -port scattering parameters of the network must be known, either by measurement or by simulation. It is not sufficient to measure the scattering parameters at the system ports only.

The scattering matrix \tilde{S}_S at the system terminals can be expressed in terms

of \tilde{t}_a . With (B.14) we have

$$\begin{aligned}\tilde{S}_S &= \tilde{S}_{N,11} + \tilde{S}_{N,21}^T \tilde{S} (\tilde{I} - \tilde{S}_{N,22} \tilde{S})^{-1} \tilde{S}_{N,21} \\ &= \tilde{S}_{N,11} + \tilde{S}_{N,21}^T \tilde{S} \tilde{t}_a.\end{aligned}\tag{3.17}$$

3.6 Example implementations

The following subsections demonstrate how the design concepts developed in this chapter can be put into practice, and reveal what levels of DMN performance are actually achieved if ohmic losses are considered in the analysis. The examples use monopole arrays over a ground plane as they are not only easy to manufacture, but produce repeatable results in scattering parameter and far-field measurements.

3.6.1 Linear $\lambda_0/4$ three-port array

Our first example is a linear three-port monopole array with a radiator separation of $\lambda_0/4$, which corresponds to 7.5 cm at the design frequency of 1 GHz. The monopoles were mounted to an aluminium ground plane with dimensions 50 cm \times 50 cm. This antenna array would evidently not pass as a compact antenna array for use in mobile phones; yet the example will clearly reveal the problems that arise with even moderate attempts of antenna array miniaturisation [140, 142].

We refrain from plotting the scattering parameters of the antenna array and only quote the absolute numbers at the centre frequency:

$$\left| \tilde{S} \right|_{\text{dB}} = \begin{pmatrix} -14.9 & -8.37 & -13.8 \\ -8.37 & -10.2 & -8.37 \\ -13.8 & -8.37 & -14.9 \end{pmatrix} \text{ dB}.\tag{3.18}$$

As we are aware of by now, the scattering matrix itself delivers no useful information about the radiation quality of the array. For this reason, we inspect its eigenefficiencies instead:

$$\lambda_{\text{acc},1}^{(\text{even})} = 91 \%, \quad \lambda_{\text{acc},2}^{(\text{odd})} = 99 \%, \quad \text{and} \quad \lambda_{\text{acc},3}^{(\pi)} = 27 \%.\tag{3.19}$$

As opposed to the $\lambda_0/10$ design of Section 2.7.1, the first two modes show little degradation. This is not surprising since for the “odd” mode, which

excites the outer two elements only, the radiators have a separation of $\lambda_0/2$ in which case mutual coupling is known to have little effect. In fact, the residual coupling evidently improves impedance match in the “odd” mode slightly compared with the “even” mode.

The degradation found in the “ π ”-mode is less severe than for the $\lambda_0/10$ separation. Still, an efficiency of 27 % corresponds to 5.7 dB insertion loss in that mode or, put another way, to a return loss of less than 1.4 dB, which is generally considered unacceptable for an antenna.

Since the decoupling network in Fig. 3.5 on page 53 consists of a 180° -hybrid and a directional coupler whose coupling factor and phase relations must be adapted to the antenna array, we need to know the matrix of eigenmode excitations \tilde{Q}_{acc} of the array. It is more convenient to consider the *power* distribution (rather than the amplitudes) within an eigenmode, separate from the corresponding phase relations. The magnitude squares of the individual matrix elements and the phases are

$$|\tilde{Q}_{\text{acc}}|^2 = \begin{pmatrix} 0.234 & 0.5 & 0.266 \\ 0.532 & 0 & 0.468 \\ 0.234 & 0.5 & 0.266 \end{pmatrix} \quad (3.20)$$

and

$$\angle \tilde{Q}_{\text{acc}} = \begin{pmatrix} 0^\circ & 0^\circ & 0^\circ \\ 22.5^\circ & \text{n/a} & -157.5^\circ \\ 0^\circ & 180^\circ & 0^\circ \end{pmatrix}, \quad (3.21)$$

respectively.

The decoupling and matching network was fabricated as a microstrip network on 0.5 mm Rogers RO3203 substrate with $\epsilon_r = 3.02$ and $\tan \delta = 0.0016$ [134]. Figure 3.13 portrays the layout. As the result of the relatively low frequency of 1 GHz the network is rather large, it measures about $20 \text{ cm} \times 20 \text{ cm}$. The directional couplers, labelled “a” and “c” in the figure, are miniaturised by periodic capacitive loading of the ring. This technique is known as an “artificial transmission line” and is explained in detail by Eccleston and Ong [38].

The hybrid coupler “a” is responsible for exciting the outer two radiators out of phase for the “odd” mode on the one hand, and, on the other hand, for the equal phase excitation in the “even” mode and in the “ π ”-mode. Thus,

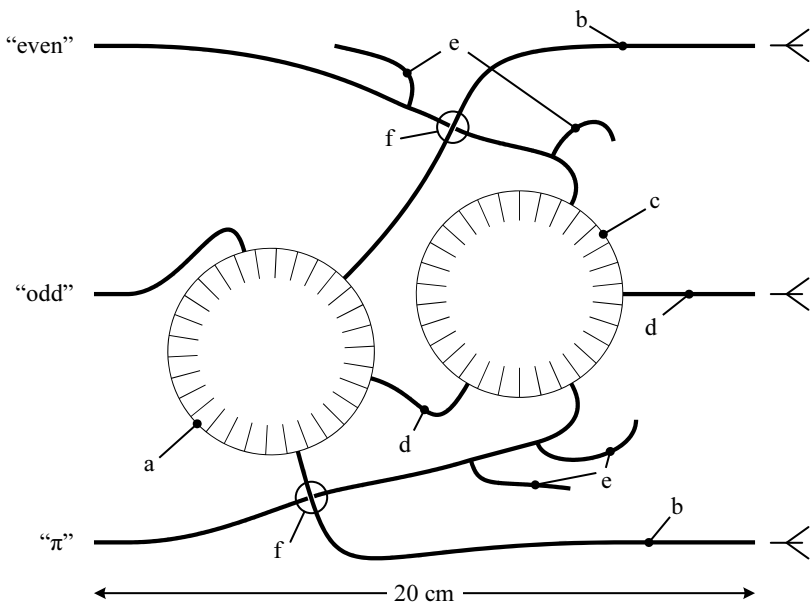


Fig. 3.13: Prototype realisation of the three-port decoupling and matching network. a) hybrid coupler, b) “odd” mode connecting lines, c) asymmetric directional coupler d) “ π ”-mode connecting lines, e) double-stub matching networks, f) air-bridges.

the electrical lengths of the two transmission lines labelled “b” leading to the outer radiators must be equal. At this point, it should be clear that exciting the “odd” terminal on the left-hand side in the figure excites the “odd” mode of the array with the rest of the network isolated.

The complete decoupling network requires a second directional coupler “c”. A look at the first column of the left-hand matrix in (3.20) reveals that the “even” mode directs 53.2 % of the power to the centre element, and equally shares the remaining 46.8 % between the outer radiators. Coupler “c” must therefore be designed with a coupling loss of 2.74 dB. Furthermore, the network must conform to the phase relations within the eigenmode vectors. To this end, the electrical lengths of the two transmission lines “d” were adjusted to account for the 22.5° phase difference in the “even” mode between the centre radiator and the outer radiators. Since this type of decoupling net-

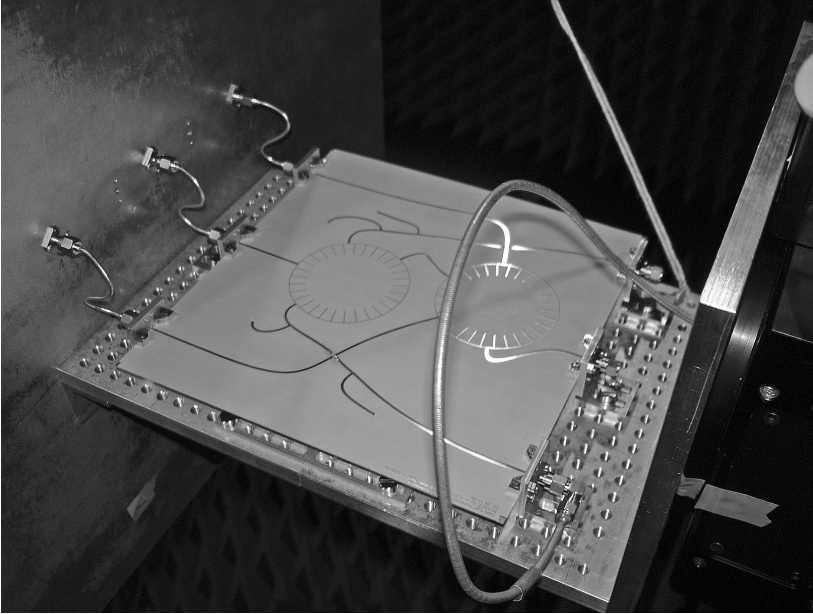


Fig. 3.14: Photograph of the manufactured three-port DMN connected to the back side (left-hand side) of the antenna array. Both network and array are mounted to a positioner (right-hand side) in an anechoic antenna measurement chamber. The radiator separation is $\lambda_0/4$ at 1 GHz.

work was shown to decouple any symmetric linear three-port array we can rest assured that the correct implementation of the “even” mode completes the “ π ”-mode as well.

Matching networks were implemented at the terminals of the “even” mode and of the “ π ”-mode as double-stub tuners “e”, which can be tuned to the desired impedance by changing only the lengths of the stubs [13, p. 266]. This way, the centre frequency of the matching network could be re-adjusted after fabrication. No matching network was implemented at the “odd” terminal since it exhibits excellent matching already. The final network requires two air-bridges “f”, which do not cause problems at 1 GHz. Figure 3.14 shows a photograph of the setup.

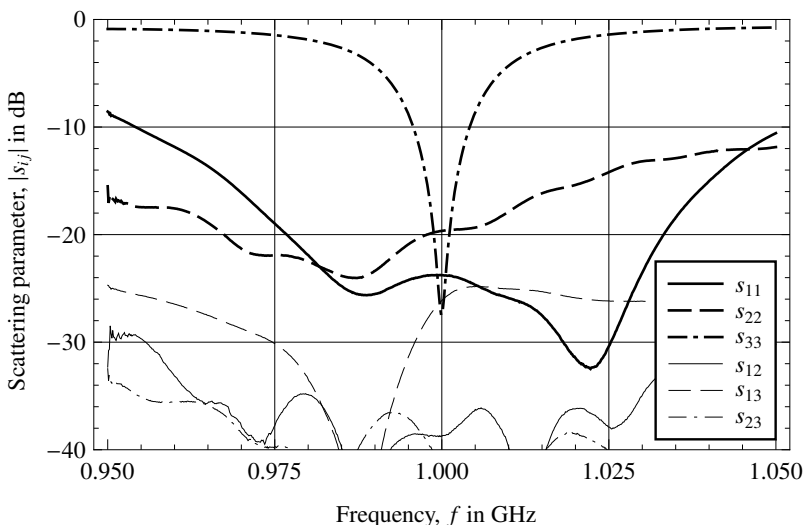


Fig. 3.15: Measured scattering parameters of the decoupled and matched $\lambda_0/4$ three-port antenna array.

Figure 3.15 plots the measured scattering parameters with the decoupling and matching network in place and after the “ π ”-mode centre frequency had been adjusted. We notice excellent decoupling (thin lines) better than 20 dB over a bandwidth of at least 100 MHz. For “ π ”-mode, we may argue that this is mainly caused by its poor return loss away from the centre frequency. After all, if most power is reflected at the input port in the first place, it can hardly couple. However, a more realistic line of thought is the other way round: if the decoupling performance of the network were insufficient, the “ π ”-mode return loss would be better since power could flow off at the remaining ports.

Matching better than 19 dB was achieved at the centre frequency at all ports (thick lines in Fig. 3.15). As the result of the poor eigenefficiency of the “ π ”-mode of the antenna array, the corresponding 10 dB return-loss bandwidth is a mere 8 MHz, i.e., less than 1 % with respect to the centre frequency.

Considering the large size of the network, we can expect network losses to have significant effect on the overall efficiency. For this reason, the six-port scattering matrix of the network was measured and the analysis pursuant to

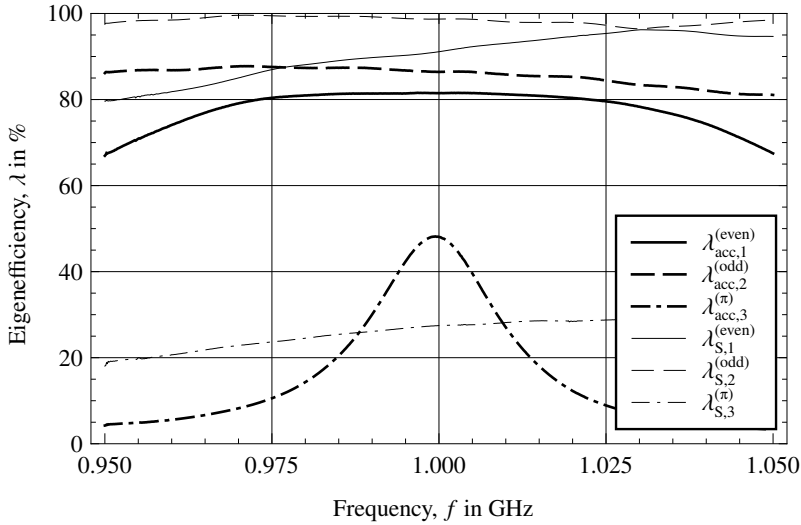


Fig. 3.16: Eigenefficiencies of the three-port antenna array before ($\lambda_{\text{acc},i}$, thin lines) and after decoupling and matching ($\lambda_{S,i}$, thick lines).

Section 3.5 was carried out. The results are graphed in Fig. 3.16, where the thin lines and the thick lines represent the situation before and after decoupling and matching, respectively. Although the network exhibits excellent decoupling and matching at the centre frequency, the efficiency of the “ π ”-mode could be improved from 27 % to merely 49 %. The efficiencies of the other two modes were reduced from 91 % to 81 % in the “even” mode and from 99 % to 86 % in the “odd” mode. The net improvement provided by this network implementation is little indeed. In a diversity system, (see Chapter 4 and (4.37)) the network delivers a signal gain of 0.5 dB.

The far-field patterns associated with the input ports of the network are plotted in Fig. 3.17. Their clear resemblance to the eigenmode patterns obtained by numerical orthogonalisation in Fig. 2.8 on page 34 confirms that the network indeed excites the eigenmodes of the array. Furthermore, the eigenefficiencies $\lambda_{S,1}^{(\text{even})} = 82\%$, $\lambda_{S,2}^{(\text{odd})} = 86\%$, and $\lambda_{S,3}^{(\pi)} = 48\%$ calculated by far-field integration excellently agree with the numbers from the previous paragraph that had been estimated by virtue of (3.16).

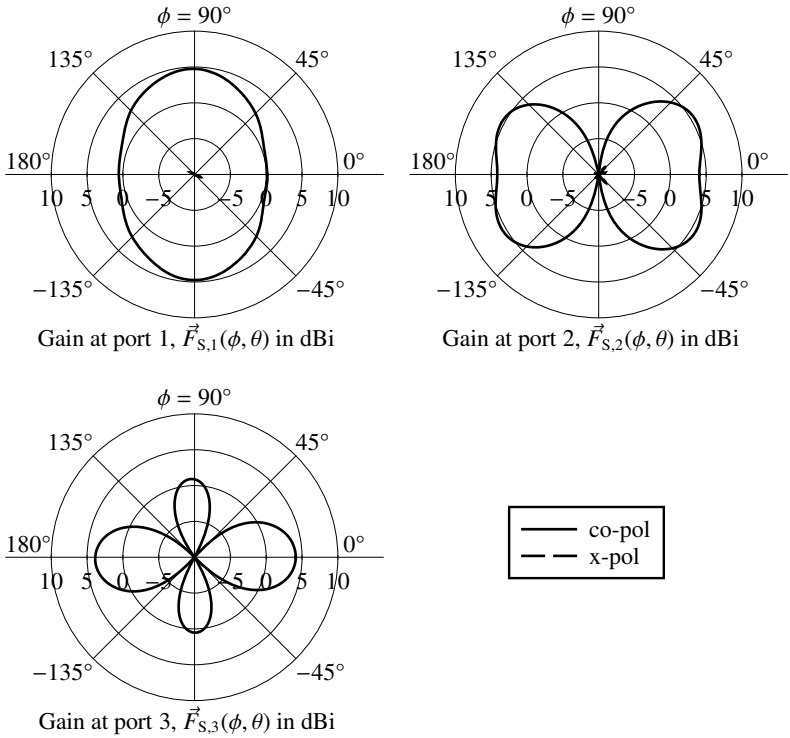


Fig. 3.17: Calibrated azimuth cuts of the beam patterns associated with the input ports of the decoupling and matching network. All diagrams are plotted at an elevation of $\theta = 30^\circ$.

3.6.2 LTCC implementation of a three-port DMN

The main purpose of the preceding example was to provide proof for the concepts developed in this chapter. Of course, its large size and its poor performance render it inappropriate for most practical applications.

In this example, the implementation of a decoupling “chip” in multi-layer LTCC technology (low temperature co-fired ceramics) is discussed [137]. The antenna array operates at 2.45 GHz and consists of three monopoles arranged in an equilateral triangle with a separation of $\lambda_0/10 = 1.2$ mm. Figure 3.18 shows photographs of the antenna array and the manufactured decoupling chip. Due to the circular symmetry of the array’s scattering parameters, the matrix of eigenmodes \tilde{Q}_{acc} is always

$$\tilde{Q}_{\text{acc}} = \begin{pmatrix} \sqrt{1/3} & \sqrt{1/2} & \sqrt{1/6} \\ \sqrt{1/3} & 0 & -\sqrt{2/3} \\ \sqrt{1/3} & -\sqrt{1/2} & \sqrt{1/6} \end{pmatrix} \quad (3.22)$$

irrespective of the actual values of the scattering parameters. Consequently, a decoupling network can be designed without any previous measurements of the array. Such a network is made up of one 180° hybrid coupler and one directional coupler with a coupling loss of 4.77 dB. Matching networks are not part of the chip and were implemented empirically after fabrication of the decoupled array.

In order to achieve a particularly small network footprint, the directional couplers were *not* implemented as transmission line structures but rather as their lumped equivalent circuits. Additional simplifications were possible because a special form of 90° couplers in place of the 180° couplers was used as the starting point for the development of the lumped circuit. The traditional textbook “branch-line coupler” consists of four $\lambda_g/4$ transmission line sections [6, p. 336]. However, one pair of opposing lines may be replaced by $3\lambda_g/4$ segments as shown in Fig. 3.19a. This results in the equivalent circuit shown in Fig. 3.19b and Fig. 3.19c. It is especially suited for implementation as a multi-layer LTCC circuit because it comprises mostly capacitors, which are straightforward to fabricate as parallel plates. The two series inductors were fabricated as spiral inductors over multiple layers [104].

The final network in Fig. 3.20 includes a 90° phase shifting network in addition to the directional couplers in order to excite the eigenmode phases correctly. It requires eleven layers of LTCC tape and occupies a footprint

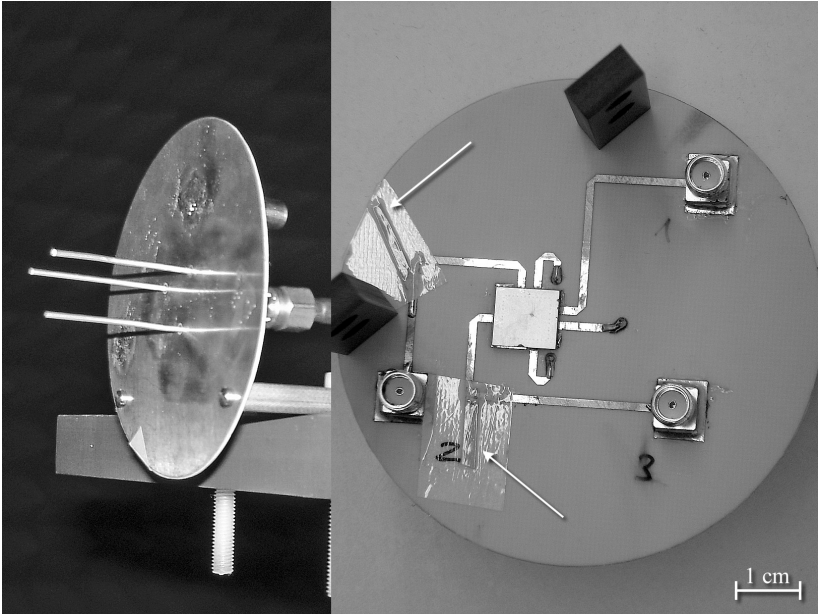


Fig. 3.18: Photograph of the three-port decoupling network manufactured as an LTCC-chip. The radiator separation of the circular array is $\lambda_0/10$. Strips of copper foil (arrows) were used to match the ports of the decoupling network manually.

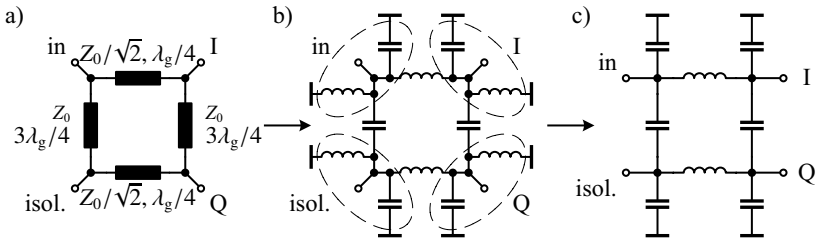


Fig. 3.19: The 90° branch-line hybrid. (a) Transmission line structure with a pair of $3\lambda_g/4$ segments. (b) Lumped equivalent circuit using Π -networks. (c) Simplification of the shunt elements. “in” = input, “iso” = isolated, “I” = in-phase, “Q” = quadrature.

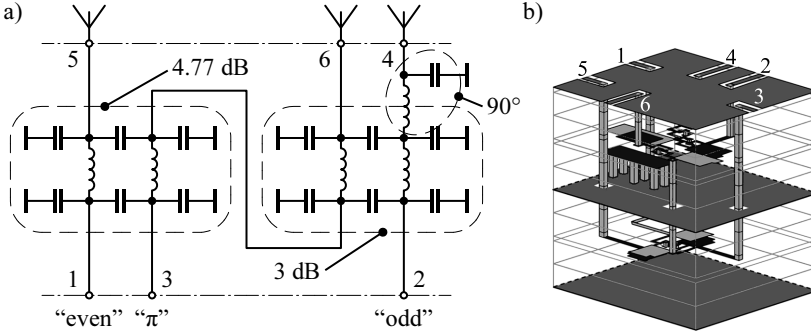


Fig. 3.20: (a) Schematic of the LTCC decoupling network consisting of a 90° hybrid, a 90° directional coupler with 4.77 dB coupling loss, and a 90° phase shifting network. (b) Its three-dimensional, multi-layered implementation.

size of $9.6 \text{ mm} \times 8.8 \text{ mm}$ at a thickness of 1.8 mm. With its pads pointing downward, the chip was soldered directly onto a microstrip transmission line structure on a circular printed circuit board. Three wire radiators were subsequently inserted through holes in the board and soldered to the microstrip structure. The backside of the board, which is solid copper, acts as a ground plane for both the printed transmission lines and the monopole radiators.

After the radiators had been decoupled by the chip, matching networks were implemented manually at the input ports with small strips of copper foil (indicated by arrows in Fig. 3.18). These were moved along the input microstrip lines until an acceptable return loss had been achieved. Figure 3.21 plots the scattering parameters. All parameters are better than -15 dB at the centre frequency. The bandwidth with all parameters below -10 dB is about 35 MHz corresponding to 1.4 % with respect to the design frequency.

Figure 3.21 provides information about the eigenefficiencies of the antenna array with and without the network. The graphs for the system eigenefficiencies λ_S are based on far-field measurements, the graphs for the sole antenna array λ were obtained by simulation. Note that the circularly symmetric antenna array has one repeated eigenefficiency; the corresponding graphs thus lie on top of each other. At the centre frequency, the network yields an efficiency improvement from $\vec{\lambda} = (0.93 \ 0.24 \ 0.24)^T$ to $\vec{\lambda}_S = (0.94 \ 0.31 \ 0.50)^T$.

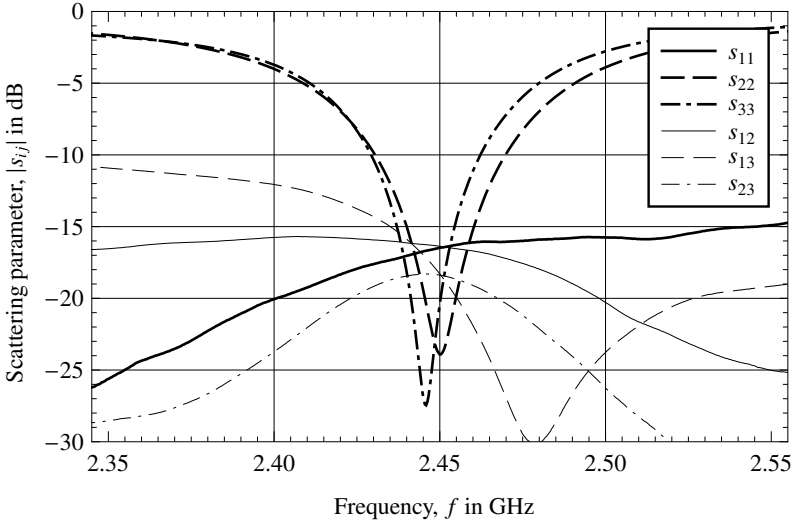


Fig. 3.21: Measured scattering parameters of the decoupled and matched $\lambda_0/10$ circular three-port antenna array with LTCC decoupling network.

The reduced efficiencies of the higher order modes are the result of the insertion loss of the decoupling chip of 0.6 dB in the “odd” mode and 0.9 dB in the “ π ”-mode.

The mean power gain (2.16) due to the network is just less than 1 dB, the signal gain in a diversity application is almost 1.5 dB. The bandwidth over which the network provides positive diversity gain is about 60 MHz, or 2.4 %. A diversity gain of 1.5 dB actually corresponds to energy savings of up to 29 % at a base station and consequently leads to a clear reduction in operation costs. Bear in mind, though, that these numbers are estimates, as they are partly based on simulations.

This example has demonstrated the practical feasibility of small-scale decoupling and matching networks. The fact that, under certain symmetry conditions, the decoupling chip can be fabricated without knowledge of the antenna array’s scattering parameters fosters mass production and cost-effective application in mobile end-user devices. Due to its robust surface mount package the chip seamlessly integrates into present manufacturing

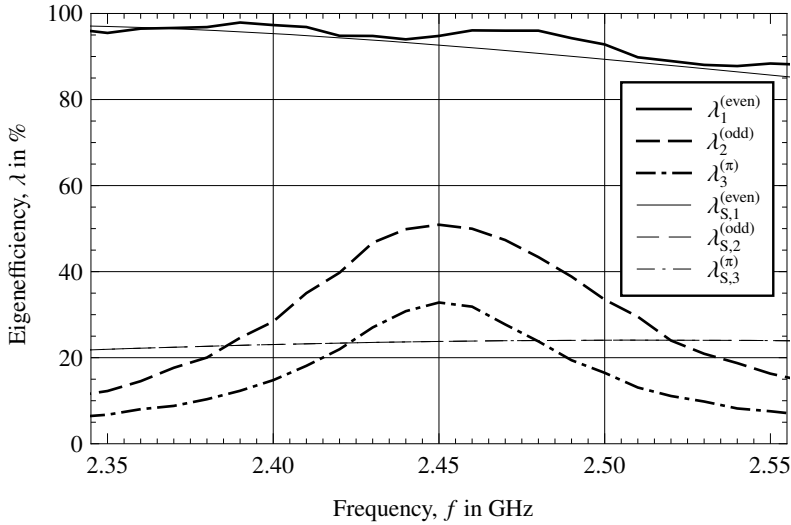


Fig. 3.22: Eigenefficiencies of the $\lambda_0/10$ circular three-port antenna array without (λ_i , thin lines, *simulation*), and with the LTCC-based DMN ($\lambda_{S,i}$, thick lines, *measurement*).

workflows in terms of automatic component placement and reflow soldering. Since this chip is a first prototype design, further improvements with regard to size and insertion loss are conceivable.

3.6.3 Broadband matched two-port array

In this example, we investigate the possibility of broadband matching [141] by exploiting the fact that the eigenmode decoupling approach allows for independent matching networks at each port. In addition to a standard matching network and two different multi-stage broadband networks, the alternative decoupling and matching method mentioned in Section 3.4.4, which does not use a hybrid coupler for decoupling, will be discussed.

A brass chassis was manufactured in which the various networks can be replaced (Fig. 3.23). For easy handling, the radiators were printed on the same circuit board as the network. As seen on the photograph, there is a

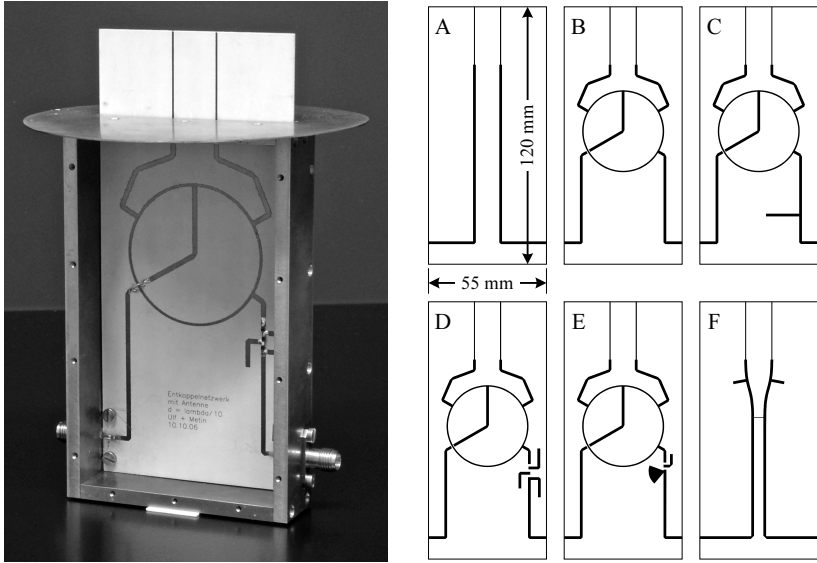


Fig. 3.23: Photograph of the $\lambda_0/10$ two-port antenna chassis, and layouts of the feed networks used for comparing the performances of different DMN techniques.

slit at the top of the housing to allow the radiators to stick out. The idea behind the additional circular ground plane is to suppress surface waves on the chassis and to support the repeatability of both scattering parameter and far-field measurements.

Six different network versions for the same $\lambda_0/10$ -spaced array that operates at 2.45 GHz have been manufactured. Also shown in Fig. 3.23 are the network layouts, which were printed on 55 mm × 120 mm Rogers RO3203 microwave substrate (thickness 0.5 mm, $\epsilon_r = 3.02$, $\tan \delta = 0.0016$, [134]). The different networks under test will be referred to with their corresponding letter.

- Network “A” merely connects the SMA-jacks near the base of the chassis to the radiators and performs no further action.
- Network “B” decouples the radiators with a hybrid coupler without matching.

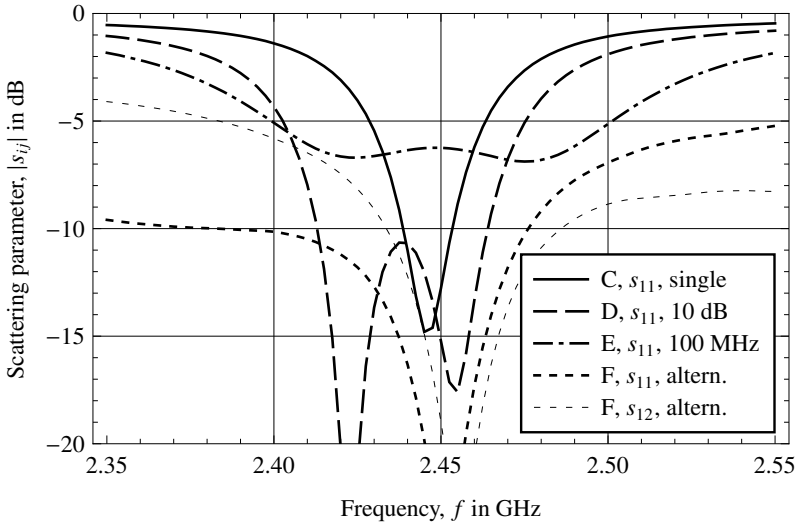


Fig. 3.24: Plots of select scattering coefficients of the networks shown in Fig. 3.23.

- Network “C” employs a standard single-stub network for “odd” mode matching.
- Network “D” includes a multi-stage matching network that aims at better than 10 dB return loss over a broadened bandwidth.
- Network “E” was designed to provide a constant improvement of matching over a bandwidth of 100 MHz.
- Network “F” follows the aforementioned alternative decoupling approach.

Before we carry out an eigenmode analysis of these networks, let us examine their scattering parameters. At the SMA-jacks the coupling coefficients s_{12} , s_{21} and the reflection coefficients s_{11} , s_{22} of network “A” were measured as -9.7 dB and -5.5 dB, respectively. Note that these numbers include the insertion loss of the feed lines of 0.2 dB each. From 2.4 GHz to 2.5 GHz network “B” achieved isolation better than 25 dB between the ports. The

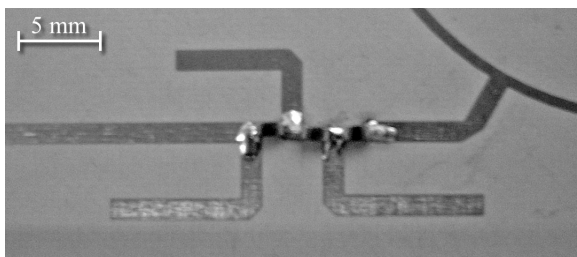


Fig. 3.25: Close-up of the multi-stage matching network of network “D”.

“even”-port return-loss was 8 dB, equivalent to 84 % matching efficiency. To keep things simple, the “even” port was not considered during matching network design. On the other hand, a return loss of 1.3 dB was measured at the “odd” port. On this account, the intention of networks “C”, “D”, and “E” was to improve matching over as wide a bandwidth as possible.

Matching network “C” is the classical narrow-band single-stub tuner [13, Section 5.2]. The measured input reflection coefficient is shown in Fig. 3.24 where the 10 dB (matching efficiency 90 %) bandwidth is 15 MHz.

Matching network “D” was designed by means of the “simplified real frequency technique” (SRFT) with the goal of a broad matching bandwidth with 10 dB return loss [85, 107]. The advantages of the technique can be summarised as follows: there is no need for an explicit expression or a circuit realisation of the load; measured impedance data can be used. In addition, there is no need to select any network topology as it is the natural consequence of the matching process. Using SRFT it is possible to design broadband matching networks converging to the upper flat transducer power gain limit based on measured antenna impedance data. The matching network was designed using lumped components, resulting in a sixth-order low-pass ladder structure. Inductors were replaced by available standard values from muRata’s LQW18A high-Q series [132]. Since the capacitor values obtained after post-optimisation are not available as standard values, they were replaced by shunt open stubs implemented in microstrip. A close-up of the final manufactured matching network is shown in Fig. 3.25. Measurements revealed that matching better 10 dB had been achieved over a bandwidth of 51 MHz—a more than three-fold improvement over the single-stub tuner (Fig. 3.24).

The goal of matching network “E” was to achieve an improvement in

matching over 100 MHz bandwidth from 2.4 GHz to 2.5 GHz. This time no systematic design procedure was followed. Rather, the non-linear optimisation features included with the ADS simulation software [122] were used in conjunction with the transmission line models provided to determine the required component values and dimensions. Such “blind” optimisation is often successful and yields quick results if only few components are involved. In order to obtain a better accuracy of the geometry of the transmission-line-based parts of the network, an electromagnetic optimisation was carried out. The final network comprises two series inductors (chip inductors) and two shunt capacitors implemented as printed shunt open stubs. Scattering parameter measurements revealed matching better than 5 dB (matching efficiency 68 %) over the stipulated frequency range (Fig. 3.24).

In order to assess the alternative decoupling and matching network “F”, the coupling coefficient s_{12} and one matching coefficient s_{11} is plotted in Fig. 3.24. In contrast to the eigenmode-based networks, its decoupling bandwidth is considerably narrower. At its centre frequency, the network achieves better than 17 dB return loss and better than 20 dB isolation. The bandwidth where both coefficients are below -10 dB is about 43 MHz.

The far-field based efficiencies are compared in Fig. 3.26. The top graphs represent the “even” mode efficiencies, which are very similar for all types of networks. This is because no matching networks were implemented at the “even” port of the hybrid coupler. Only network “F” shows some improvement because it is not based on the eigenmode concept and therefore always affects both modes at the same time. The bottom graphs in Fig. 3.26 represent the “odd”-mode efficiency. Thin lines show the efficiency of the direct feed network “A” (solid line) and the decoupling-only network “B” (dashed line), respectively. In contrast to the matching efficiency of 25 % mentioned in Section II, the actual radiation efficiency including all losses is less than 10 %—a dramatic difference caused by the insertion loss of the respective network.

Thick graphs in Fig. 3.26 compare the efficiencies of networks “C” to “F”. The single-stub matching network “C” is plotted as the solid curve and displays a more than 2.5-fold efficiency improvement at the centre frequency. The bandwidth, over which this simple network performs better than the antenna array without network, is almost 80 MHz.

The efficiency of the 10 dB broadband matching network “D”, which is plotted as the thick curve with the long dash pattern, turned out as a disap-

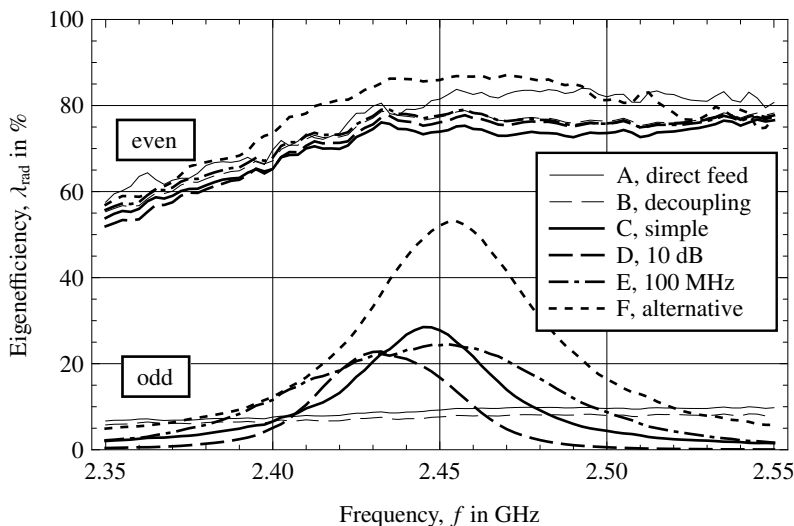


Fig. 3.26: Eigenefficiencies of the networks of Fig. 3.23 determined from measured far-field data.

pointment. Contrary to its broad matching performance, its peak efficiency is not only lower than that of the single-stub network, but it is also narrower in bandwidth. The reasons are the large number of (lossy) reactive elements involved and the attempt to achieve good matching at the input. Both facts increase the amount of energy stored within the system and thus contribute additional losses.

With matching network “E”, where the design focus was on the 100 MHz bandwidth rather than on the matching efficiency, it was possible to increase the bandwidth over the single-stub network. The dash-dot graph in Fig. 3.26 reveals a bandwidth of about 110 MHz where the matching network outperforms the sole array. The peak efficiency is 86 % of the single-stub implementation.

Finally, the alternative matching network “F” surpasses all previous networks in terms of both efficiency and bandwidth, as the curve with the short dash pattern in Fig. 3.26 reveals. This is only natural since the network is a lot smaller in size and minimises the electrical distance between the an-

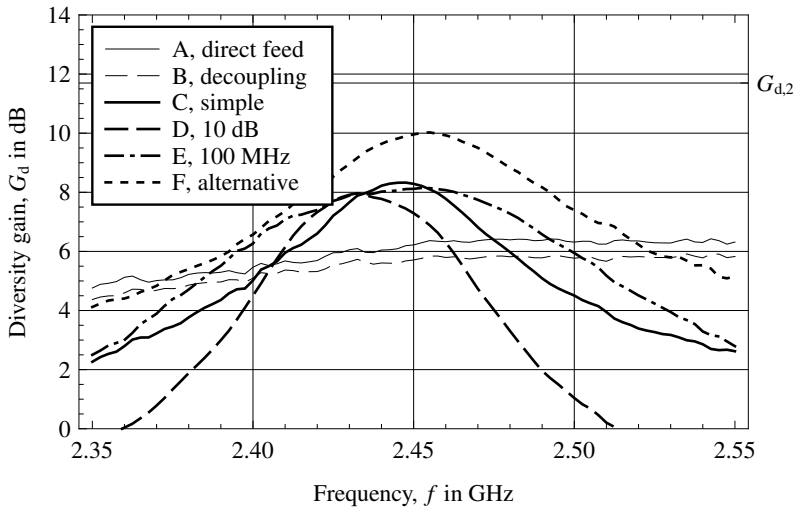


Fig. 3.27: Diversity gains of the networks of Fig. 3.23 at the 1 % probability level. The gain of an ideal two-port system is indicated by $G_{d,2}$.

tenna array and the reactive, energy-storing elements of the network. Its peak efficiency is around 53 %, which is twice the efficiency of the single-stub network. Its bandwidth is about 130 MHz.

Figure 3.27 plots the diversity gains (Chapter 4) of the various networks versus frequency. The peak improvement achieved with a hybrid coupler based network is about 2 dB, whereas the alternative network delivers a diversity gain of almost 4 dB.

The example has demonstrated three things. First, the possibility to employ broadband matching techniques with the eigenmode decoupling network. Second, that the input port scattering parameters convey *insufficient* and *misleading* information about DMN performance, and that instead the power efficiency of the system must be analysed. Third, that the alternative two-port DMN approach is greatly superior to the hybrid-based network in terms of both footprint size and efficiency. On this account, the next subsection illustrates how this alternative network is incorporated into a hybrid-coupler based four-port DMN.

3.6.4 Circular $\lambda_0/10$ four-port array

We will now provide proof-of-concept of a hybrid-based four-port DMN for a “circular” (square) arrangement of radiators. We will also demonstrate how the alternative decoupling and matching technique implemented in the previous example (network “F”) can be incorporated into multi-port matching networks.

Figure 3.28 portrays a photograph of the antenna system. The radiator separation is 12 mm corresponding to $\lambda_0/10$ at the operating frequency of 2.45 GHz. The ground plane measures 7 cm \times 7 cm. The layout of the DMN in the photograph is outlined in Fig. 3.29a. Meandering was employed to reduce the footprints of the hybrid couplers. The numbers adjacent to the ports at the top correspond to the numbering in Fig. 3.10b, i.e., the two hybrids closest to the array decouple diagonally opposing elements. Matching networks were omitted from the printed network and were implemented manually with strips of copper foil. Since there are ten scattering coefficients, we refrain from showing the full plot and only state that all matching coefficients are better than -12 dB and all coupling coefficients are below -17 dB at the centre frequency. The eigenefficiencies of the matrix of *accepted power* after decoupling and matching are $\vec{\lambda}_{S,acc} = (1.0 \ 0.99 \ 0.97 \ 0.89)^T$ implying a matching efficiency of at least 89 % for all excitations.

In the network of Fig. 3.29b, one hybrid has been replaced by the alternative matching network. According to measurements, all matching coefficients are better than -17 dB and all coupling coefficients are below -15 dB at the centre frequency. The eigenefficiencies of the *accepted power* are $\vec{\lambda}_{S,acc} = (1.0 \ 0.99 \ 0.95 \ 0.90)^T$ and thus confirm the correct operation of the network.

Plots of the eigenefficiencies derived from measured far-field data are given in Fig. 3.30. Alike plot styles refer to the same antenna system. Both networks are able to improve the efficiencies of the impaired eigenmodes notably. The two “odd” modes—the medium efficient pair of modes—are improved by a factor around 1.6 at the centre frequency. In the “ π ”-mode, the networks achieve an enhancement by the factor 3, from 3.3 % to 10 %. The fact that the alternative network is only marginally better is not too surprising since power dissipation primarily takes place within the remaining hybrid couplers and within the coaxial cables seen in Fig. 3.28 between the array and the DMN. It remains to be investigated what efficiency gains will be

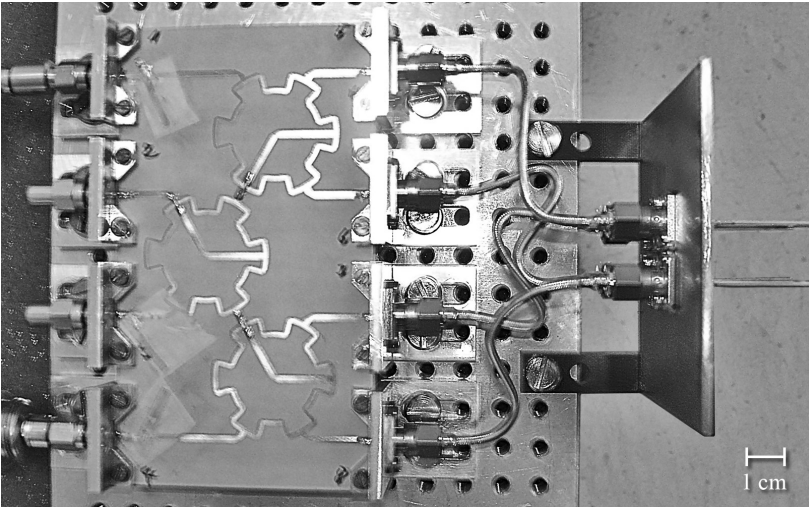


Fig. 3.28: Photograph of a four-port circular array with decoupling and matching network. The radiator separation is $\lambda_0/10$ at 2.45 GHz.

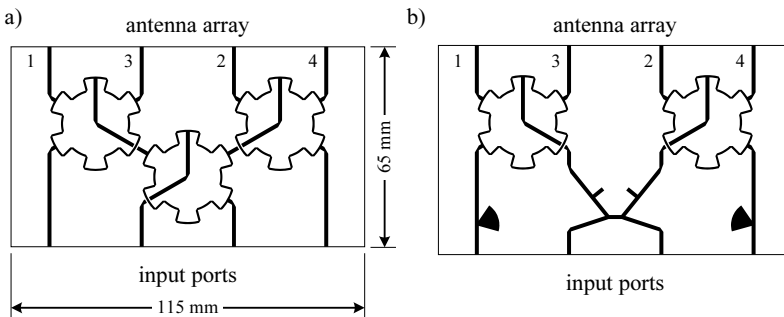


Fig. 3.29: Layouts of the two different four-port decoupling and matching networks.

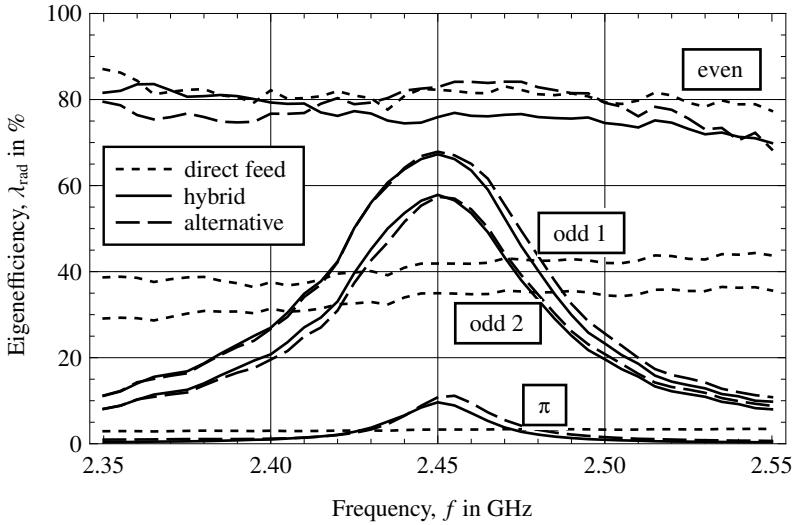


Fig. 3.30: Eigenefficiencies of the four-port antenna array without DMN, with a hybrid-only DMN, and with an alternative decoupling and matching method.

achievable if the connecting transmission lines are kept as short as possible.

From the point of view of diversity reception both networks deliver an additional gain of about 2 dB. The bandwidth over which an improvement comes about is just over 50 MHz, as Fig. 3.31 reveals. Whereas 2 dB represent a remarkable gain, particularly in view of the insertion loss of the coaxial cables, the overall diversity performance is still inferior to an ideal three-port system. Of course, the question of whether such an ideal three-port system can be realised within the same space constraints is another matter.

The beam patterns produced by the eigenmode (hybrid-only) DMN are reported in Fig. 3.32. The two “odd” modes, each of which feed one pair of diagonally opposing radiators, are readily identified as beam-patterns 1 and 4 by their pronounced radiation zeros. The beam-pattern of one “odd” mode is a rotated copy of the other “odd” mode, therefore these modes share the same eigenefficiency, at least in theory. In practice there are considerable differences in the eigenefficiencies plotted in Fig. 3.30 but also in the beam-patterns, which is mainly caused by mechanical inaccuracies of the array. The

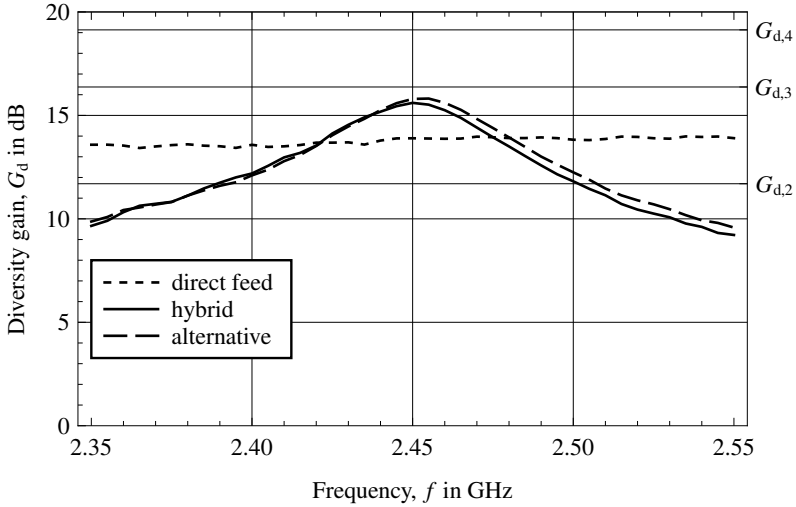


Fig. 3.31: Diversity gains of the four-port array without DMN, with hybrid-only DMN, and with alternative DMN. The right-hand axis indicates ideal n -port gains.

more obvious asymmetries in the “even” mode and the “ π ”-mode on the other hand stem from shortcomings of the DMN. The meandering of the hybrid ring in conjunction with the air-bridges distorts the symmetry both of the power and of the phase balance.

3.7 Summary

The central topic of this chapter was a particular family of decoupling and matching networks (DMN) that exploit the orthogonal nature of array eigen-modes. These networks have the prominent advantage that, if a network exists for a given constellation of radiators, it will be especially simple to design. They consist of a series of *directional couplers*, which decouple the radiator as a first step. The decoupled ports are subsequently matched using *familiar* single-port techniques. If the antenna array exhibits certain symmetries, considerable parts, if not the entire decoupling section, of the DMN can be designed *without knowledge* of the scattering parameters of the array. As

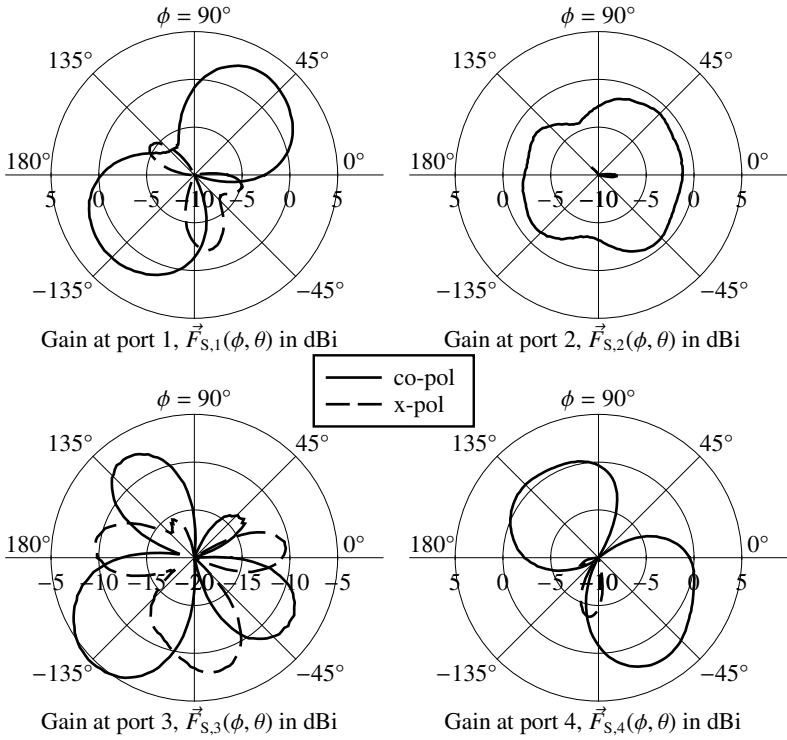


Fig. 3.32: Measured azimuth cuts of the beam patterns associated with the input ports of the four-port eigenmode DMN (Fig. 3.29a). All diagrams are plotted at an elevation of $\theta = 30^\circ$.

the LTCC example has shown, this last property is particularly attractive to mass-produced applications if one day compact and low-loss hybrid couplers should become available. Another advantage is the broad decoupling bandwidth, which enables post-production adjustments simply by tuning of the single-port matching networks. It also allows for broadband or varactor-tuned matching techniques.

An accurate means to predict the influence of an arbitrary lossy feed network (DMN or other network) on the antenna array radiation matrix and thus

on its eigenefficiencies was presented. This analysis revealed that the goal of achieving decoupled and matched input ports comes at the high cost of a high DMN insertion loss. Considerable ohmic losses are present in all types of DMNs, yet researchers seem to focus on the scattering matrix of the input terminals only. For the first time a formula for the *quantification of ohmic losses* in terms of the DMN scattering parameters was given and confirmed by far-field measurements.

Ohmic losses present a general problem with DMNs, yet their impact is certainly more pronounced with the present approach. This is because the insertion loss of the directional couplers, although only of the order of a few tenths of a decibel, becomes amplified by the impedance transformation of the matching networks. For this reason, an *alternative* two-port decoupling and matching technique was introduced that can also be incorporated into higher-order eigenmode DMNs.

Two parameters are important to the assessment of DMN performance. First, the relative gain (eigenefficiency gains or diversity gain) between the antenna array without and with DMN determines whether the implementation is actually worth its while. Second, we must also look at the absolute performance and critically examine whether an array with fewer radiators, and thus a less complex DMN, may in fact perform equally well.

Although noteworthy DMN gains of up to 3.8 dB were demonstrated in the present chapter and also elsewhere [121], a major inhibiting factor for the practical use of DMNs is their generally narrow bandwidth. Until the time writing, investigations had been focussed on “mathematically correct” approaches, i.e., with *decoupling and matching* as the design goal. However, with the knowledge and the efficiency formula of the present chapter, it seems worthwhile to concentrate future efforts on design strategies with the *overall* network efficiency and bandwidth in mind. It is anticipated that networks exist that do not create a perfectly decoupled and matched system, but that nonetheless, due to their simplicity and compactness, perform better than present approaches.

Chapter 4

Diversity reception with compact antenna arrays

Between a wireless transmitter and a receiver there is usually more than one path of signal propagation due to shadowing by and scattering off nearby objects such as the ground, mountains, buildings, or people. Therefore, the field strength actually available at the receiver is the result of the superposition of a multitude of signals. Depending on the paths and the distances travelled, the superposition may be constructive or destructive in nature.

If any part of the communications scenario moves, these path lengths change and so will the received signal strength. Depending on whether or not a direct path (“line-of-sight”) is present between the communicating parties, the instantaneous signal-to-noise ratio (SNR) may *fade* away by as much as 40 dB [9, Fig. 1.1-1]. At receivers operating indoors or on the border of a transmitter’s coverage area, fading may severely degrade the quality of the mobile link. Fading is random in nature and therefore described with statistical means.

The problems associated with fading may be alleviated with multiple antennas at the receiver—a technique known as *antenna diversity*. If these antennas are spaced apart far enough, they all receive the same information but

are subjected to independent fading characteristics. With increasing number of radiators n , the chance that at least one antenna receives sufficient signal power grows. Thus, one way to enhance the stability of the communications link is to continuously choose the antenna receiving the strongest signal. This represents a simple form of a so-called *diversity combiner*, and more advanced techniques are available. As the antenna array is made smaller and mutual radiator coupling starts to set in, however, fading becomes increasingly correlated and the effectiveness of antenna diversity diminishes [56, 79].

In the present chapter, we carry out an analysis of this effect and suggest new figures of merit to support the diversity performance evaluation of compact antenna arrays. The influence of a non-uniform communications environment will be outlined by means of a widely accepted channel model for mobile terminals. The chapter concludes with a detailed model of receiver noise and a discussion of the consequences that arise thereof.

4.1 Overview and past work

Eventually, any diversity receiver is bound to combine the signals received by its antennas into a new, single signal with improved fading characteristics. The inputs to this combiner are also referred to as the *branches* of the diversity system. There are various types of combiners with more complex implementations generally performing better. The improvements due to diversity are usually expressed as a decibel gain, called the *diversity gain* [26], which we define in the next section.

The focus of this chapter will be on *maximal ratio combining* (MRC), which, of all combiner types, yields the maximum SNR possible. Although MRC is the most complex combiner to implement in practice, its mathematical analysis is comparatively straightforward. The probability density function of MRC in the presence of correlated fading for Rayleigh-type environments is derived in an early paper by Pierce and Stein [66]. Additional details follow in [17, Chapter 10].

These works identified the branch correlation coefficient ρ (cf. (2.30)) as the principal factor determining diversity performance. Later, the relationship between mutual radiator coupling, the correlation coefficient ρ , and array diversity performance was published in a pioneering paper by Vaughan and Bach Andersen [79]. It was concluded that $\rho < 0.5$ is a sufficient criterion for “good” diversity performance, provided that the radiating elements them-

selves are sufficiently “good”.

Nowadays, the branch correlation coefficient has become the standard way of assessing array diversity. Its popularity stems from the fact that, in the early days, it required no sophisticated measurement equipment. In addition, the few formulae involving ρ are so simple, they can be evaluated on a slide rule; additional parameters are read off graphs [56, 79]. Since then, many papers have been published that affirm its role as *the* measure of choice [35, 37, 43, 44, 52, 55, 70, 92, 106].

This analysis, however, does have its shortcomings. For the theory to be applicable, all branches must receive the same mean power. In this case, methods for estimating the diversity gain exist for two array elements only; larger arrays require special attention. Even then a concluding statement is only qualitative and of the form “appropriate” or “not appropriate for diversity reception”. In many cases it is impossible to distinguish a better array from the worse, which hampers the optimisation of array designs subject to certain constraints (e.g., space) because a cost-function cannot be formulated.

Comprehensive studies of a two-element array and a four-element array are for example given by Kildal and Rosengren [50] and by Chiau et al. [30], respectively. The reader might agree that the introduction of the terms “mean effective gain”, “apparent diversity gain”, “actual diversity gain” and “effective diversity gain” [51] complicates matters unnecessarily. Additional sources of error arise since the “envelope correlation coefficient” and the “correlation coefficient” are related, yet substantially different quantities. Another disadvantage is that no diversity-based bandwidth can be established for an array; instead the radiator efficiency and the correlation coefficient must be considered separately [55]—a rather unwieldy undertaking, especially if three or more radiators are involved.

Times have changed since the first introduction of ρ and it is about time to move on and to adapt the way of diversity analysis to the tools available to the average antenna engineer in present days [144]. This chapter demonstrates how useful yet compact expressions for the diversity capabilities of mutually coupled arrays are only few steps away from the original theory by Pierce and Stein [66]. These formulae are closed-form expressions that allow a simple *quantitative* comparison between different designs and that are eligible as cost-functions for array optimisation.

The close relationship to the eigenmode analysis in Chapter 2 is pointed out. It is also shown that, in certain cases, the antenna array cannot be cha-

acterised unless the noise properties of the receiver front-end are taken into account [84]. As the existing ways of analysis, the new formulae are also limited to communications environments that lack a line-of-sight component and that therefore may be modelled by the Rayleigh probability distribution.

Past work includes papers by Nørklit et al. [64, 103] who propose the effective (fractional) number of ideal diversity branches that would perform similar to a given coupled system as a diversity figure of merit. No closed-form expression or approximation exist for this metric, however, and the effective diversity order must be read off graphs manually. Closed-form approximations for the two-port diversity gain are given by Mattheijssen et al. [61] and by Turkmani et al. [78]. The former is a six-term series and requires the branch efficiencies to be equal. The latter is given for an outage probability (defined below) of 10 % only.

MIMO (multiple-input multiple-output) systems, which employ antenna arrays at both the transmitting and the receiving end of the link [12, 40], promise a substantial increase of the mobile channel capacity and have thus attracted considerable attention recently. Although these systems are *not* addressed further in the present thesis, the question of the effects of mutual radiator coupling is still an important one. Several authors (e.g., [80, 82, 112, 114]) have carried out investigations on this topic by generating a large set of random channel realisations to obtain an estimate of the statistical distribution of the channel capacity numerically. Smith et al. [74] derive a corresponding approximation in closed-form. Although the latter presents a promising step towards the right direction, a compact expression directly related to the MIMO performance of mutually coupled arrays has yet to be found. These examples demonstrate that the quest for more general and easier to handle figures of merit is indeed justified.

4.2 Figures of merit for correlated fading

In a communications scenario lacking a dominant path of propagation, such as a line-of-sight, the signals that arrive at a moving receiver's antenna impinge from random directions with random amplitude and phase. By the central limit theorem, the complex signal envelope (envelope including phase information) of the superposition of these paths will be distributed according to a zero-mean circularly symmetric complex Gaussian distribution [15, p. 159]. (I.e., its real and imaginary parts are independent zero-mean Gaussian ran-

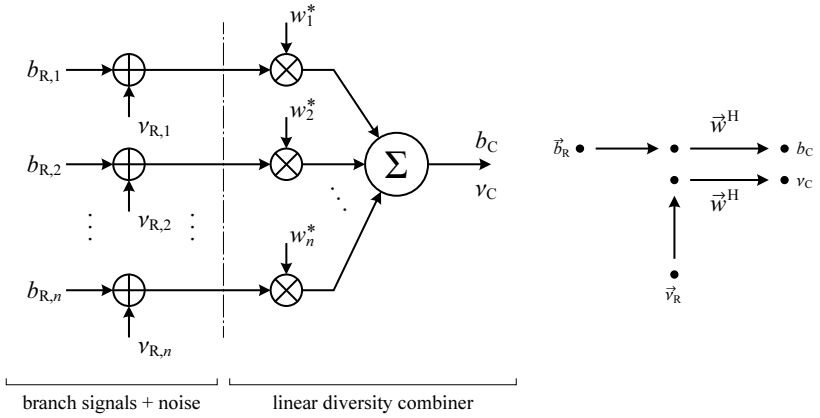


Fig. 4.1: General block diagram and signal flow graph of a linear diversity combiner. The complex received signal envelopes and the receiver noise are denoted by $b_{R,i}$ and $v_{R,i}$, respectively. Branches are multiplied by weights w_i^* before summing. The combined signal and noise are denoted by b_C and v_C , respectively.

dom variables with equal variance.) The received signal *power* consequently follows a chi-square distribution with two degrees of freedom [14, p. 41]; the resulting distribution of the signal *amplitude* is called the Rayleigh distribution [14, p. 44]. Since few random paths suffice to produce a reasonable approximation to the Gaussian distribution, the Rayleigh distribution often shows up in practice [17, Fig. 9-2-1]. It therefore represents an appropriate channel model for systems operating indoors or inside a street canyon, for instance.

4.2.1 A simplified diversity model

Figure 4.1 depicts the general form of a linear diversity combiner. The received complex signal envelopes are denoted by $b_{R,i}$ with i being the branch number. We keep in mind that, as the result of fading, these signal envelopes are time-varying random processes. Before the branches are added together to yield a single combined signal b_C , they are weighted by complex branch weighting coefficients w_i^* . (The complex conjugation is just a notatio-

nal convenience). Writing $b_{R,i}$ and w_i^* as vectors, we have

$$b_C = \vec{w}^H \vec{b}_R. \quad (4.1)$$

The instantaneous combined signal power is

$$P_{C,\text{signal}} = |\vec{w}^H \vec{b}_R|^2 = \vec{w}^H [\vec{b}_R \vec{b}_R^H] \vec{w}. \quad (4.2)$$

In any communications system, the presence of noise imposes a fundamental limit on the quality of the transmission and therefore on the amount of information that can be reliably transmitted in a given span of time. Several different physical mechanisms, which are beyond the scope of this thesis, are responsible for the creation of noise. The interested reader is referred to [67] for an introduction and references for further reading. We shall follow the generally accepted approach and model noise as a zero-mean Gaussian random process $v_{R,i}$ superimposed on each receiver branch, as indicated in the figure.

In this initial discussion, we assume that all receiver branches are equally noisy and that noise is uncorrelated between branches. The additive noise power in each receiver branch i may be expressed in terms of the equivalent temperature T_R [16, Section 2.1.5] of the received noise:

$$P_{R,\text{noise},i} = E \{ |v_{R,i}|^2 \} = k T_R B, \quad (4.3)$$

where $k = 1.3806504 \text{ J/K}$ is the Boltzmann constant and B the equivalent receiver noise bandwidth, which typically equals the equivalent noise bandwidth of the matched filter employed at the receiver. The spectral noise power density is assumed constant inside this bandwidth. The noise power after weighting and branch combination is then given by

$$P_{C,\text{noise}} = E \{ |\vec{w}^H \vec{v}_R|^2 \} = \vec{w}^H E \{ |\vec{v}_R|^2 \} \vec{w} = k T_R B \vec{w}^H \vec{w}. \quad (4.4)$$

For the subsequent analysis, the signal-to-noise ratio (SNR) ϱ_C at the combiner output is of further interest since it expresses the quality of the received signal. It is a function of the combiner weights \vec{w} :

$$\varrho_C(\vec{w}) = \frac{P_{C,\text{signal}}}{P_{C,\text{noise}}} = \frac{1}{k T_R B} \frac{\vec{w}^H [\vec{b}_R \vec{b}_R^H] \vec{w}}{\vec{w}^H \vec{w}}. \quad (4.5)$$

The goal of a diversity combiner is to choose \vec{w} so to maximise $\varrho_C(\vec{w})$. We recognise the second factor of the above product as a Rayleigh-quotient [8,

p. 176], which is maximised if \vec{w} equals the eigenvector associated with the largest eigenvalue of the $n \times n$ matrix $\vec{b}_R \vec{b}_R^H$ in the numerator. Since this matrix is Hermitian and rank-one, there is only one non-zero eigenvalue. It is easily verified [8, Equation (1.1.3)] that the corresponding eigenvector is \vec{b}_R itself and that the eigenvalue is $|\vec{b}_R|^2$. The optimum weight vector is therefore

$$\vec{w}_{\text{opt}} = \vec{b}_R, \quad (4.6)$$

and the maximum achievable combined SNR becomes

$$\varrho_{C,\text{max}} = \varrho_C(\vec{w}_{\text{opt}}) = \frac{|\vec{b}_R|^2}{kT_R B}. \quad (4.7)$$

A combiner that achieves this optimum result was introduced before as the maximal ratio combiner, or MRC [17, Section 10-5]. Its operation can be pictured as a co-phased sum with all branches weighted with their instantaneous SNR. Because an actual implementation is rather demanding in terms of the processing power required, practical systems often employ simpler combiner types with less-than-optimal results [26]. There is the additional fact that the received signal envelopes $b_{R,i}$ are not known in advance and vary with time. Therefore, the combiner weights have to be estimated continuously from the received signal. The quality of this estimate is naturally subject to the rate at which the channel changes (cf. Doppler-spread, [12, p. 14]) and to the amount of noise and interference present. We will nonetheless assume that the receiver has perfect knowledge of the received envelope vector \vec{b}_R and thus of the optimum weights \vec{w}_{opt} at all times.

The following model will investigate diversity as a function of frequency. We therefore require that the abovementioned noise bandwidth B of the receiver is sufficiently narrow so that not only the electrical parameters of the receiver components (antenna array, amplifiers, noise) can be assumed constant over that bandwidth, but also that all frequencies within B undergo exactly the same fading process. This is called a frequency-flat fading channel [12, p. 15].

Practical systems are unlikely to fulfil any of the above assumptions. They either accept the impairments or employ techniques to counteract the effects of fast fading and frequency-selective fading (e.g., interpolation between channel estimates, RAKE-reception [69], OFDM (orthogonal frequency division multiplex) [12, Section 9.2], turbo-equalisation [53]). Our presumptions

are nonetheless justified since the goal is to describe the consequences of mutual radiator coupling itself rather than the properties of a particular receiver implementation. The following should therefore be considered a best-case description with practical systems usually performing worse.

The same processes that produce Rayleigh-fading at a single-port antenna also take place at antenna arrays. So the complex envelopes $b_{R,i}$ at the receiver branches all follow a zero-mean circularly symmetric complex Gaussian random process. Together, the $b_{R,i}$ describe a complex multivariate Gaussian distribution. The multivariate Gaussian distribution is uniquely characterised by the vector of first moments, i.e., the means, and the matrix of second moments, i.e., the variances and covariances [15, p. 158]. Since the means are zero, the *covariance matrix* of the received signal envelopes suffices to describe the joint statistical distribution of the received amplitudes at multi-port antennas in a Rayleigh environment.

For the first part of our discussion, we require the directions of arrival of all wave fronts reaching the array to be uniformly distributed in azimuth, elevation, and polarisation. Such an environment is created, for instance, in a reverberation chamber [51] used to measure the diversity gain of manufactured antenna arrays. Irrespective of whether or not this is a realistic assumption to make, it seems sensible if nothing is known about the target environment. Later in Section 4.3.1, we will discuss more appropriate models to include known aspects of the communications environment. We also assume a lossless antenna array. Although the covariance matrix was derived previously by Wallace and Jensen [81] based on purely mathematical reasoning, a descriptive interpretation in terms of the eigenmode concept and the equivalent circuit developed in Section 2.6 on page 27 is given here.

It is shown in Appendix A.5 that, under the above conditions, the eigenmodes of an arbitrary antenna array *fade independently*. This insight supports our perception of eigenmodes as the principal degrees of freedom of an array. Moreover, since the array is assumed lossless and all directions of the incident wave fronts are uniformly distributed, the powers $P_{m,av,i}$ available in the eigenmodes are all equal as a consequence of power conservation and reciprocity. So, recalling the discussion around Eqn. (2.46), the covariance matrix of the received modal power wave vector $\vec{b}_{m,av}$ is simply a scaled version of the identity matrix:

$$\text{Var} \{ \vec{b}_{m,av} \} = \text{E} \{ \vec{b}_{m,av} \vec{b}_{m,av}^H \} = P_{\text{signal}} \tilde{I}, \quad (4.8)$$

where P_{signal} signifies the mean available signal power. With (2.49), we can write down the covariance matrix of the signal envelopes at the receiver straight away:

$$\begin{aligned}
 \text{Var} \{ \vec{b}_R \} &= \text{Var} \{ \vec{b} \} = \text{E} \left\{ \tilde{\mathcal{Q}}_{\text{acc}}^* \sqrt{\tilde{\Lambda}_{\text{acc}}} \vec{b}_{\text{m,av}} \vec{b}_{\text{m,av}}^H \sqrt{\tilde{\Lambda}_{\text{acc}}} \tilde{\mathcal{Q}}_{\text{acc}}^T \right\} \\
 &= \tilde{\mathcal{Q}}_{\text{acc}}^* \sqrt{\tilde{\Lambda}_{\text{acc}}} \text{E} \{ \vec{b}_{\text{m,av}} \vec{b}_{\text{m,av}}^H \} \sqrt{\tilde{\Lambda}_{\text{acc}}} \tilde{\mathcal{Q}}_{\text{acc}}^T \\
 &= P_{\text{signal}} \tilde{\mathcal{Q}}_{\text{acc}}^* \tilde{\Lambda}_{\text{acc}} \tilde{\mathcal{Q}}_{\text{acc}}^T \\
 &= P_{\text{signal}} \tilde{H}_{\text{acc}}^T = P_{\text{signal}} (\tilde{I} - \tilde{S}^T \tilde{S}^*) = P_{\text{signal}} (\tilde{I} - \tilde{S} \tilde{S}^H). \quad (4.9)
 \end{aligned}$$

Evidently, under the above conditions, the covariance matrix of the complex signal envelopes is easily found from the scattering matrix of the antenna array. This result agrees with the result of Wallace and Jensen [81], who also showed that in the presence of ohmic losses the signal covariance matrix is given by $P_{\text{signal}} \tilde{H}_{\text{rad}}^T$ according to (2.26).

The signal covariance matrix itself, however, does not provide any meaningful information about the resulting performance of the diversity receiver. This fact was already criticised in the introductory section as the major shortcoming of existing approaches to assessing the diversity capabilities in the presence of mutual coupling. We shall therefore proceed to analyse the distribution function of the SNR $\varrho_{\text{C,max}}$ at the MRC combiner output to see what kinds of practically useful parameters can be derived from it.

In order to keep the following formulae as clear as possible, we do not wish to carry P_{signal} and $kT_R B$ through the entire derivation. We therefore define a combined ϱ that is normalised to the mean SNR of a single, lossless, and perfectly matched radiator $\varrho_0 = P_{\text{signal}}/(kT_R B)$. Then

$$\varrho = \frac{\varrho_{\text{C,max}}}{\varrho_0} = \left| \vec{b}_R \right|^2 \quad \text{with} \quad \text{Var} \{ \vec{b}_R \} = \tilde{H}^T, \quad (4.10)$$

instead of (4.7) and (4.9). For the time being, we stick to the matrix \tilde{H} to emphasise the relationship between diversity performance and the efficiency considerations of Chapter 2. Later in Section 4.3.1, the matrix will be renamed to \tilde{H}_R for reasons of notational consistency. Note that our covariance matrix \tilde{H} has nothing to do with the channel matrix \tilde{H} commonly encountered in MIMO theory.

The probability density function (PDF) $p(\varrho)$ of ϱ was derived by Pierce and Stein [66]. A general expression can only be given in terms of its Laplace transform $P(s)$, though:

$$P(s) = \det\{\tilde{I} + s\tilde{H}\}^{-1} = \left[\prod_{i=1}^n (1 + s\lambda_i) \right]^{-1}, \quad (4.11)$$

where s is the Laplace variable. We observe that the PDF is uniquely determined by the eigenvalues λ_i of the matrix \tilde{H} . In other words, the eigenefficiencies introduced to characterise the available degrees of freedom of an antenna array in terms of their radiation efficiency also uniquely determine the array's quality in a diversity application.

With the help of the inverse Laplace transform of $P(s)$, the PDF $p(\varrho)$ can always be found in terms of exponential functions. The reason why no generally valid closed-form expression can be given is that its particular form depends on the multiplicities of the eigenefficiencies. For an ideal n -port antenna array, all eigenefficiencies are 1 and

$$p(\varrho) = \frac{\varrho^{n-1} e^{-\varrho}}{(n-1)!}, \quad \text{for } \varrho > 0. \quad (4.12)$$

This type of distribution is a chi-square distribution with $2n$ degrees of freedom and parameter $\sigma = 1/\sqrt{2}$ [9, Eqn. (5.2-14)], [14, Eqn. (2.1-110)]. For $\varrho < 0$ these power-related PDFs are identical zero. In case *all* eigenefficiencies are distinct, the PDF becomes [64, Eqn. (30)]

$$p(\varrho) = \frac{1}{\prod_{i=1}^n \lambda_i} \sum_{i=1}^n \frac{e^{-\varrho/\lambda_i}}{\prod_{\substack{j=1 \\ j \neq i}}^n \left(\frac{1}{\lambda_j} - \frac{1}{\lambda_i} \right)}, \quad \text{for } \varrho > 0. \quad (4.13)$$

For other eigenefficiency multiplicities, which arise in circular array arrangements, for instance, the corresponding form must be worked out individually by expanding (4.11) into partial fractions. The following subsections demonstrate that a number of important parameters can nonetheless be derived without requiring an explicit expression of $p(\varrho)$.

4.2.2 Array gain of a mutually coupled array

The mean improvement of the SNR at the combiner's output over a single perfectly matched radiator is called the *array gain* G_a [12, Section 1.2.1]. It is simply the expected value of ϱ and, in principle, could be derived from the PDF by integration [14, Eqn. (2.1-61)]:

$$G_a = E\{\varrho\} = \int_0^\infty r p(r) dr \quad (4.14)$$

As Pierce and Stein [66, Eqn. (25)] pointed out, this integral can be evaluated in terms of the Laplace representation of the PDF as

$$G_a = E\{\varrho\} = -\left. \frac{dP(s)}{ds} \right|_{s=0}. \quad (4.15)$$

If we rewrite (4.11) in polynomial form as

$$P(s) = \frac{1}{1 + c_1 s + c_2 s^2 + \cdots + c_n s^n}, \quad (4.16)$$

where the c_i are placeholders for the expanded coefficients of the denominator, then

$$-\frac{dP(s)}{ds} = \frac{c_1 + 2c_2 s + \cdots + n c_n s^{(n-1)}}{(1 + c_1 s + c_2 s^2 + \cdots + c_n s^n)^2}. \quad (4.17)$$

Clearly, if $s = 0$, Eqn. (4.15) becomes (cf. [8, pp. 40–42])

$$E\{\varrho\} = c_1 = \sum_{i=1}^n \lambda_i = \text{tr}\{\tilde{\Lambda}\} = \text{tr}\{\tilde{H}\}. \quad (4.18)$$

Since ϱ is a power quantity, the array gain is expressed in dB as

$$G_a(\tilde{H}) \Big|_{\text{dB}} = 10 \log E\{\varrho\} \text{ dB} = 10 \log \text{tr}\{\tilde{H}\} \text{ dB}. \quad (4.19)$$

For ideal arrays, where all $\lambda_i = 1$, the array gain equals the number of radiators n . For an ideal single radiator the array gain is 0 dB in accordance with the previous normalisation (4.10). Furthermore, this result agrees with our intuitive understanding that the amount of power collected by an antenna array is proportional to the sum of the efficiencies of its degrees of freedom.

4.2.3 Diversity gain over a single receive antenna

Diversity not only yields an improvement of the average SNR but, most importantly, changes the statistics of the received SNR in a way that reduces the probability of deep fades. This effect is best visualized by means of the cumulative distribution function (CDF) $d(\varrho)$ of ϱ . The CDF is defined as

$$d(\varrho) = \int_0^{\varrho} p(r) dr \quad (4.20)$$

and yields the probability that ϱ is *below* some specified value. Again, for the reasons stated earlier, a general closed-form expression in terms of λ_i is not available. For ideal n -branch diversity (see (4.12), [9, Eqn. (5.2-15)], [14, Eqn. (2.1-114)]), $d(\varrho)$ becomes

$$d(\varrho) = 1 - e^{-\varrho} \sum_{k=0}^{n-1} \frac{\varrho^k}{k!}, \quad \text{for } \varrho > 0. \quad (4.21)$$

By integration of (4.13) the CDF becomes

$$d(\varrho) = \frac{1}{\prod_{i=1}^n \lambda_i} \sum_{i=1}^n \frac{\lambda_i (1 - e^{-\varrho/\lambda_i})}{\prod_{\substack{j=1 \\ j \neq i}}^n \left(\frac{1}{\lambda_j} - \frac{1}{\lambda_i} \right)}, \quad \text{for } \varrho > 0 \quad (4.22)$$

if all eigenefficiencies are distinct.

Figure 4.2 plots the CDFs of ideal diversity systems with up to four branches on double-logarithmic scales. It is evident that an increasing number of radiators n not only shifts the curves towards higher SNRs (which would correspond to array gain only), but also changes their slope. The slope approaches the constant value of n for small SNRs and thus reflects the *order* of the diversity system.

The CDF plots let us determine the so-called *outage probability* of the communications link. For instance, the probability that the instantaneous SNR falls more than 10 dB below its mean value is around 10 % if only one radiator is used for reception. With two radiators, the probability is reduced to 0.5 %; with three radiators the probability is less than 0.02 %. One or two additional receiver branches obviously suffice to improve the reliability of the communications link substantially in a strongly fading environment.

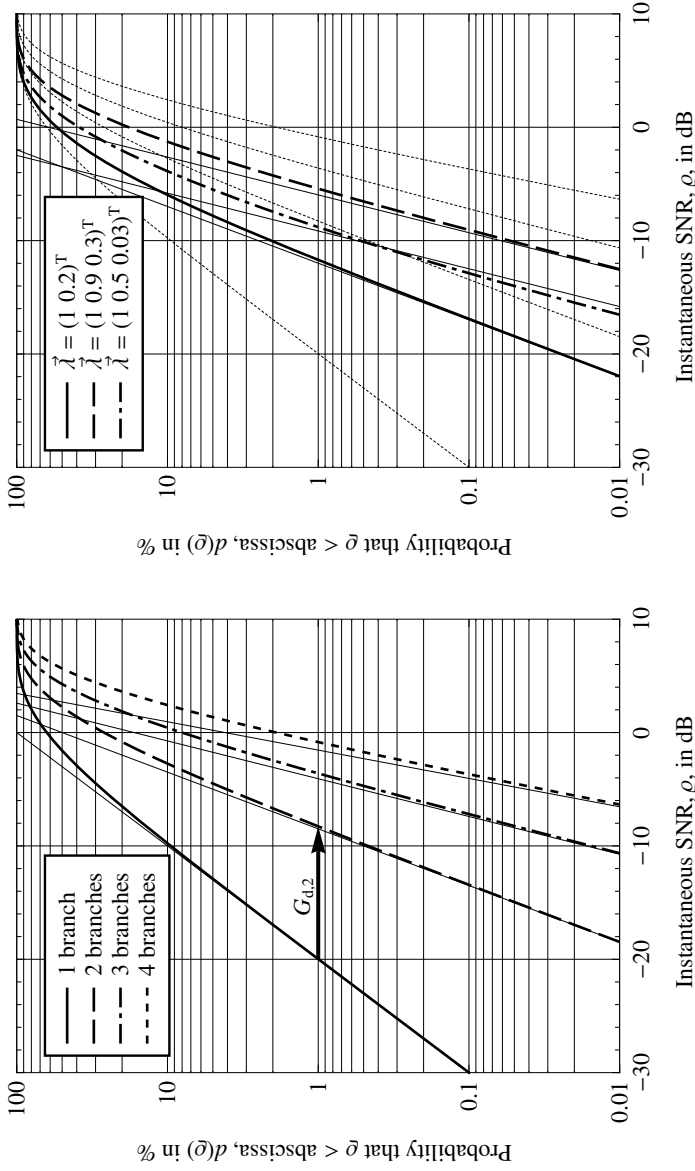


Fig. 4.2: Example plots of the cumulative SNR distribution functions for ideal, uncorrelated MRC.

Fig. 4.3: Example plots of the cumulative SNR distributions for non-ideal, correlated MRC. The legend indicates the eigenvalue distributions used in the creation of these plots.

The benefits due to diversity are usually not expressed in terms of probabilities but rather as an equivalent system insertion gain, called the *diversity gain* G_d [26], [79, Eqn. (67)]. For this, an outage probability p is chosen, for instance $p = 1\%$. Then the diversity gain is defined as the SNR ratio of the *diversity system* in question to the SNR of the single-branch system at the specified outage probability. Figure 4.2 clarifies this definition with an arrow indicating the diversity gain $G_{d,2}$ of an ideal two-branch system. The value of the diversity gain is 11.7 dB in this case, which is considerably better than the 3 dB array gain alone. The diversity gain thus expresses the amount of transmit power that can be saved with respect to a non-diversity system whereby the reliability of the mobile link is unchanged.

Some examples of the effects of mutual coupling are shown in Fig. 4.3. The figure plots the CDFs of one two-branch system and two different three-branch systems. The legend provides information about the eigenefficiencies λ_i that were used in (4.22) for the production of these graphs. In general, mutual coupling causes the graphs to shift towards lower SNRs with respect to the corresponding ideal systems. For instance, the two-branch system, whose second eigenefficiency is only 20 %, delivers a diversity gain of 8.3 dB at the 1 % probability level—around 3.4 dB worse than the ideal system.

The development and optimisation of compact antenna arrays would benefit greatly from closed-form formulae for the diversity gain in terms of the signal covariance matrix. Engineers could then rely on simple scattering parameter measurements to judge the diversity capabilities of their array.

In mathematical terms, the diversity gain G_d as a function of \tilde{H} and the probability level p can be written as

$$G_d(\tilde{H}, p) = \frac{d_{\tilde{H}}^{-1}(p)}{d_1^{-1}(p)}, \quad (4.23)$$

where $d_1^{-1}(\cdot)$ and $d_{\tilde{H}}^{-1}(\cdot)$ signify the *inverse functions* of the CDFs of a single radiator and of a diversity system characterised by \tilde{H} , respectively. The denominator turns out as $-\log(1 - p)$, but, unfortunately, no closed-form expression of the numerator is available in the literature. In principle, the numerator can be evaluated numerically by iterative root-finding algorithms. However, this whole process is rather cumbersome to implement: one first has to determine the eigenvalues of \tilde{H} , check if there are any duplicates, then construct the CDF, and finally search for the root of $d_{\tilde{H}}(\varrho) = p$.

A simpler and faster approach is via the Maclaurin series expansion of $d_{\tilde{H}}^{-1}(p)$. The derivation of the first four terms is discussed in Appendix A.6, however, the first two terms usually provide sufficient accuracy. We define

$$q = \sqrt[n]{n! \det\{\tilde{H}\}} p, \quad (4.24)$$

and obtain for the inverse CDF

$$d_{\tilde{H}}^{-1}(p) \approx q + \frac{\text{tr}\{\tilde{H}^{-1}\}}{n(n+1)} q^2 + \dots \quad (4.25)$$

The diversity gain with respect to an ideal single radiator is then given by the following second-order approximation:

$$G_d(\tilde{H}, p) \approx \frac{q}{p} \left[1 + \frac{\text{tr}\{\tilde{H}^{-1}\}}{n(n+1)} q \right], \quad (4.26)$$

The denominator in (4.23) was replaced by p , its first-order approximation, in order to counteract the error introduced by the approximation of the numerator. It is difficult to give a clear statement about the accuracy of the above approximation because it not only depends on the outage probability chosen but also on the eigenefficiencies of the array. Thus, Table 4.2 reports some numeric examples at three different probability levels and for varying eigenmode degradations, so the reader can get an idea about the accuracy. Empirical test show that, at $p = 1\%$, the error in G_d is less than 0.5 dB for up to four radiators if the ratio $\lambda_{\max}/\lambda_{\min} \leq 100$. The accuracy not only increases towards smaller values of p but also for smaller numerical spreads of the eigenefficiencies λ_i .

4.2.4 Diversity loss over an ideal antenna array

In case less accuracy is sought, an even simpler indicator for diversity performance can be derived. According to [17, Eqn. (10-5-29)] the first term in the series expansion of (4.22) is

$$d(\varrho) \approx \frac{\varrho^n}{n! \prod_{i=1}^n \lambda_i} = \frac{\varrho^n}{n! \det\{\tilde{\Lambda}\}} = \frac{\varrho^n}{n! \det\{\tilde{H}\}}, \quad \text{for } \varrho \rightarrow 0. \quad (4.27)$$

n	Eigenefficiencies $\vec{\lambda}^r$	Diversity Gain in dB					
		$p = 10 \%$		$p = 1 \%$		$p = 0.1 \%$	
		Exact	Est.	Exact	Est.	Exact	Est.
2	(1.0 1.0)	7.03	7.11	11.7	11.7	16.6	16.6*
	(1.0 0.2)	3.81	3.80	8.28	8.28	13.1	13.1*
	(1.0 0.02)	0.760	-0.121	3.80	3.69	8.25	8.24
3	(1.0 1.0 1.0)	10.2	10.1	16.4	16.3	22.8	22.8*
	(1.0 0.9 0.3)	8.50	8.32	14.6	14.5	20.9	20.9*
	(1.0 0.5 0.03)	5.90	5.30	11.2	11.0	17.1	17.1*
	(1.0 0.3 0.01)	4.70	3.98	9.60	9.25	15.2	15.1
4	(1.0 1.0 1.0 1.0)	12.2	11.9	19.1	19.0	26.3	26.3*
	(1.0 1.0 0.9 0.3)	11.0	10.6	17.8	17.7	25.0	24.9
	(1.0 0.9 0.5 0.03)	9.56	9.07	16.0	15.8	22.9	22.8
	(1.0 0.6 0.1 0.005)	6.87	6.52	12.7	12.6	19.1	19.0
5	(1.0 1.0 1.0 1.0 1.0)	13.6	13.2	21.0	20.9	28.7	28.6
	(1.0 0.9 0.6 0.1 0.01)	9.81	9.40	16.5	16.3	23.6	23.5
	(1.0 0.5 0.2 0.01 0.001)	7.23	7.00	13.4	13.5	20.0	20.2

Table 4.1: Numeric examples demonstrating the accuracy of the diversity gain approximation G_d according to (4.26). The starred (*) examples are plotted in Figs. 4.2 and 4.3.

n	Eigenefficiencies	Approx. L_d	Exact L_d in dB			
	$\tilde{\lambda}^r$	in dB	$p = 1 \%$	0.1%	10%	
2	(1.0 0.2)	3.49	3.42	3.47	3.23	*
	(1.0 0.02)	8.49	7.90	8.32	6.27	
3	(1.0 0.9 0.3)	1.90	1.82	1.86	1.70	*
	(1.0 0.5 0.03)	6.08	5.20	5.68	4.30	*
	(1.0 0.3 0.01)	8.41	6.78	7.61	5.49	
4	(1.0 1.0 0.9 0.3)	1.42	1.31	1.36	1.21	
	(1.0 0.9 0.6 0.05)	3.92	3.13	3.45	2.63	
	(1.0 0.6 0.1 0.005)	8.81	6.42	7.20	5.33	

Table 4.2: Numeric examples demonstrating the accuracy of the diversity loss approximation L_d according to (4.28). The starred (*) examples are plotted in Fig. 4.3.

This linear approximation is included as thin lines in Figs. 4.2 and 4.3. It clearly serves as a reasonable approximation to $d(\varrho)$ at small probability levels. We note two things in the graphs of non-ideal diversity in Fig. 4.3. First, the slope of the limiting line depends only on the number of branches n and is independent of the eigenefficiencies. For this reason the slope cannot be used as a measure for non-ideal diversity performance. Second, the limiting line undergoes a shift towards lower SNRs as the eigenefficiencies decrease. We can interpret this shift as a system insertion loss caused by the efficiency reduction due to radiator coupling. This *diversity loss* of a coupled n -port antenna array with respect to its ideal n -port counterpart is found by rearranging (4.27):

$$L_d \Big|_{\text{dB}} \approx -\frac{10}{n} \log \det \{ \tilde{H} \} \text{ dB}. \quad (4.28)$$

Table 4.2 reports some numerical examples of this approximation. The CDF of the first three-port example (third row from the top of the table) is plotted in Fig. 4.3 as the dashed curve. We find that it runs almost parallel to the graph of ideal three-branch diversity. The diversity loss estimate (4.28) of 1.90 dB agrees nicely with the exact value of 1.82 dB at the 1 % probability level. In the second three-port example, which is also plotted in Fig. 4.3, the curves

are not as much in parallel and the diversity loss estimate consequently overestimates the true loss by almost 0.9 dB at the same probability level. On the other hand, there is probably limited practical relevance to the second example because it actually performs worse than a two-element array at probability levels greater than 0.3 %. As with the diversity gain approximation, the diversity loss estimate becomes more accurate towards lower probability levels. Further tests revealed that at $p = 1\%$ the error in L_d is less than 0.5 dB for up to four radiators if the ratio $\lambda_{\max}/\lambda_{\min} \leq 10$. So, if a particular antenna array design exhibits only moderate coupling, then (4.28) is a useful and simple measure for the diversity loss due to mutual coupling *independent* of the probability level.

Notice how in the single-port case L_d reduces to

$$-10 \log \left(1 - |s_{11}|^2 \right) \text{ dB}, \quad (4.29)$$

which equals the loss due to impedance mismatch at the antenna input. The diversity loss may therefore be considered a generalisation of this term to multi-port arrays.

In contrast to the mean radiation efficiency (2.16) defined earlier, the diversity loss particularly penalises low eigenefficiencies. In view of the examples on page 15 this means that the example array with eigenefficiencies $\vec{\lambda} = (0.97 \ 0.97 \ 0.01)^T$ induces a diversity loss of 6.75 dB whereas the array with $\vec{\lambda} = (0.65 \ 0.65 \ 0.65)^T$ achieves a loss of only 1.87 dB—although both arrays possess the same mean efficiency of 65 %. This insight is consistent with intuitive reasoning, namely that an array with three acceptable degrees of freedom ought to be superior to an array where one eigenmode is hardly existent.

An alternative way to express the diversity loss is in terms of the arithmetic mean of the eigenmode insertion losses:

$$\begin{aligned} L_d \Big|_{\text{dB}} &\approx -\frac{10}{n} \log \det \{ \tilde{H} \} \text{ dB} = -\frac{10}{n} \log \left[\prod_{i=1}^n \lambda_i \right] \text{ dB} \\ &= \frac{1}{n} \sum_{i=1}^n \left(-10 \log \lambda_i \right) \text{ dB}. \end{aligned} \quad (4.30)$$

The influence of individual degraded eigenefficiencies therefore shrinks with increasing number of radiators n . For example, a single radiator with 25 %

radiation efficiency introduces a 6 dB insertion loss in the system. In two, three, and four-branch systems on the other hand, a single degraded eigenmode with the same efficiency reduces the diversity gain by 3 dB, 2 dB, and 1.5 dB, respectively. By implication, the possible gains that can be achieved with decoupling and matching networks also scale inversely with n , i.e., if a network provides a 6 dB improvement in one eigenmode of a three-port array, the net diversity gain increase will only be 2 dB. In this context, however, we have to keep in mind that the diversity gain brought about by additional receiving branches diminishes considerably beyond $n > 2$, even for ideal systems (cf. Fig. 4.2).

The approximation formulae developed in this section facilitate the frequency-dependent characterisation of mutually coupled arrays in terms of their diversity capabilities. An earlier example in Fig. 3.27 on page 84 demonstrates the usefulness of this possibility, especially if decoupling and matching networks are employed, whose properties generally change considerably with frequency.

Figure 4.4 portrays another example of diversity evaluation versus frequency with the intent to compare the accuracies of the approximation formulae graphically. The antenna array used was manufactured by Weber et al. [146]. The thick, solid graph represents the approximation according to (4.26) and the thin, dotted line shows the exact values. Both graphs are in excellent agreement; at the high end of the frequency range, where $\lambda_{\min} = 0.8 \%$, the approximation error is only 0.36 dB. Also shown is a plot based on the diversity loss according to (4.28). (thick, dashed line; L_d was subtracted from the value of ideal three-port diversity.) At the centre frequency $\lambda_{\min} = 33 \%$ and the diversity loss $L_d = 1.98$ dB is very close to the exact value (1.92 dB). Only towards the ends of the frequency range, where the three-port array becomes worse than an ideal two-port array, the discrepancy grows considerably. Since we now have the ability to express the diversity capabilities as a single number, we may readily establish the bandwidth of an array or a decoupling and matching network. For instance, the bandwidth in Fig. 4.4 where the array outperforms an ideal two-port system is around 23 MHz.

As a final example of broadband evaluation, Fig. 4.5 plots the diversity gain of a simple multi-band array. The array consists of three dipole-radiators with a separation of $0.15\lambda_0$ at 1 GHz, and exploits the fact that dipoles are not only resonant at their design frequency, but also at odd multiples thereof [2, Fig. 4.9]. The graph reveals the clear performance difference between the

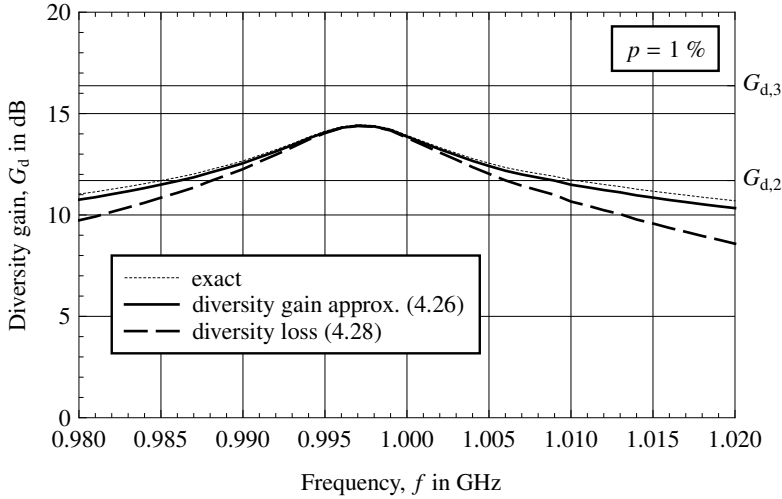


Fig. 4.4: Demonstration of the accuracy of the diversity figures of merit (4.26) and (4.28) by means of a frequency sweep of a manufactured $\lambda_0/10$ array with DMN [146]. $G_{d,2}$ and $G_{d,3}$ identify ideal two- and three-port diversity.

two frequency bands arising from the different effective radiator separations at these frequencies.

4.3 Extensions to the diversity model

Due to its simplicity, there are obvious limitations to the model and to the formulae derived from it. The assumptions of a lossless array, a uniformly distributed multi-path environment, and uncorrelated receiver noise seldom apply in practice, and the calculations based on the scattering matrix of the antenna array evidently cannot capture these effects. Still under the condition of Rayleigh fading, we may interpret these cases in the sense that our previous assumption of equal and independent eigenmode fading (4.8) is violated. This in turn implies that merely the value of the covariance matrix \tilde{H} is affected; the approximation formulae for array gain, diversity gain, and diversity loss, on the other hand, remain valid without modification. For instance,

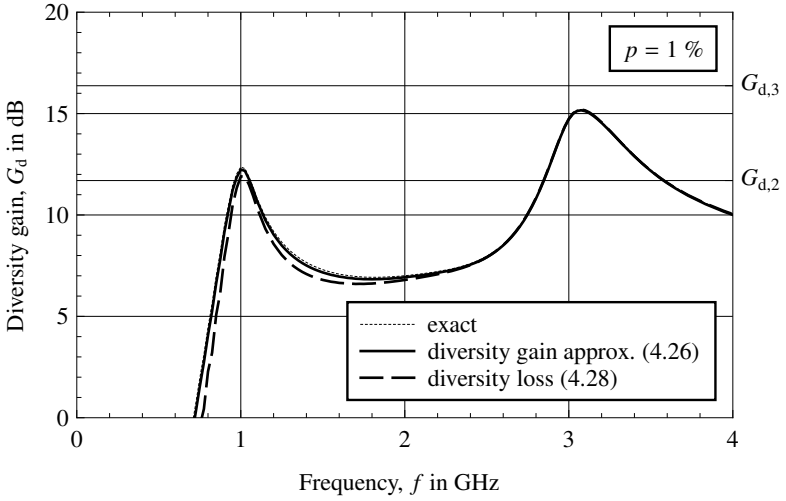


Fig. 4.5: Similar to Fig. 4.4 but showing the first two resonances of a simulated $0.15\lambda_0$ dipole array as an example of a multi-band application.

it was mentioned previously that the matrix \tilde{H}_{rad} can be substituted for the matrix \tilde{H}_{acc} to account for array losses in the system [81]. The following subsections explain in some more detail what other factors may influence array performance and how these can be accounted for in the calculation of \tilde{H} .

4.3.1 Influence of the communications environment

Although we shall see in the next subsection that the diversity loss derived from the array scattering matrix can be understood as the sole result of mutual radiator coupling, it is important to discuss aspects of the communications environment in which the antenna array is to be deployed. For an outdoor mobile satellite terminal for example, there is no point obviously in using an antenna array that is most sensitive to waves arriving in the horizontal plane. Any antenna array with main beam directions pointing towards the sky clearly will be the better choice.

Several formulae that account for the characteristics of the environment

are available in the literature. Wallace and Jensen [81], for instance, propose a highly general formula that essentially extends (2.26) with a probability density function. The covariance matrix of the received signal envelopes is then given by

$$\text{Var} \{ \vec{b}_R \} = E \{ \vec{b}_R \vec{b}_R^H \} = \tilde{H}_{\text{env}}^T \quad (4.31)$$

with

$$\tilde{H}_{\text{env},ij} = \int P_{\text{in}} \vec{F}_i^H(\phi, \theta) \vec{e}^* \vec{e}^T \vec{F}_j(\phi, \theta) p(P_{\text{in}}, \vec{e}, \phi, \theta) dP_{\text{in}} d\vec{e} d\Omega, \quad (4.32)$$

where $p(P_{\text{in}}, \vec{e}, \phi, \theta)$ is the joint probability density function of the incident power P_{in} , the complex polarisation vector \vec{e} , and the far-field angles of arrival ϕ and θ . The new subscript “env” refers to the communications *environment*. For meaningful comparisons between different environments, care must be taken that the incident power P_{in} is scaled appropriately. In practice one would usually evaluate the integral numerically by creating a large sample of \vec{b}_R with the desired statistics in a *channel simulator* and estimating the expectation operation in (4.31) via the sample mean [81].

An alternative and simpler expression for $\tilde{H}_{\text{env},ij}$ based on the most widely applied channel model for mobile systems [79] is given by

$$\tilde{H}_{\text{env},ij} = \frac{1}{2\pi(1 + \text{XPR})} \int_0^{2\pi} \vec{F}_i^H(\phi, 0) \cdot \begin{pmatrix} \text{XPR} & 0 \\ 0 & 1 \end{pmatrix} \cdot \vec{F}_j(\phi, 0) d\phi. \quad (4.33)$$

The “surface” of integration has been reduced to an infinitesimal strip around zero elevation because this is considered the principal direction of arrival in an indoor environment [99]. XPR (cross-polar ratio) signifies the mean ratio of the received co-polar to the cross-polar component [12, p. 27]. Typical values range from 0 dB to 6 dB, where 0 dB indicates that the received power is shared equally between the co-polar and the cross-polar component. The main diagonal elements $\tilde{H}_{\text{env},ii}$ evaluate to the mean effective gain (MEG), i.e., the branch efficiencies in our terminology, used for instance in [30, Eqn. (5)], [52, Eqn. (6)], [101, Eqn. (3)], [77, Eqn. (6)]. The off-diagonal elements are chosen so that calculations of the correlation coefficient ρ_{ij} (see (2.30))

$$\rho_{ij} = \tilde{H}_{\text{env},ij} / \sqrt{\tilde{H}_{\text{env},ii} \tilde{H}_{\text{env},jj}} \quad (4.34)$$

yield the popular expression [30, Eqn. (5)], [46, Eqn. (5)], or [52, Eqn. (5)]. The above integral thus unites two essential components of antenna array

diversity analysis into a single matrix, and enables the application of the diversity figures of merit developed to *established channel models*.

Since we now have several different ways at hand to determine the matrix “ \tilde{H} ” for diversity analysis, it is time to summarise and to straighten out the notation employed on the following pages. The covariance matrix of the *received* signal envelopes will be denoted by

$$\text{Var} \{ \vec{b}_R \} = E \{ \vec{b}_R \vec{b}_R^H \} = \tilde{H}_R^T \quad \text{from now on.} \quad (4.35)$$

The word “received” refers to the inputs of the combiner (see Fig. 4.1); the new subscript “R” is introduced at this point to be consistent with the temperature covariance matrix \tilde{T}_R of the received noise to be defined later. Depending on whether or not there is a feed network in the system, we have two ways to calculate \tilde{H}_R :

$$\begin{aligned} & \tilde{H}_R = \tilde{H}, & \text{without network,} \\ \text{or } & \tilde{H}_R = \tilde{H}_S = \tilde{t}_a^H \tilde{H} \tilde{t}_a, & \text{with network, (3.16), } \tilde{t}_a = (\tilde{I} - \tilde{S}_{N,22} \tilde{S})^{-1} \tilde{S}_{N,21}. \end{aligned}$$

Furthermore, there are three different possibilities to establish \tilde{H} , depending on the accuracy sought and the information available about the antenna array:

$$\begin{aligned} & \tilde{H} = \tilde{H}_{\text{acc}}, & \text{lossless arrays, uniform environment, (2.6),} \\ \text{or } & \tilde{H} = \tilde{H}_{\text{rad}}, & \text{lossy arrays, uniform environment, (2.26),} \\ \text{or } & \tilde{H} = \tilde{H}_{\text{env}}, & \text{non-uniform environment, (4.32) or (4.33).} \end{aligned}$$

We have to keep in mind that the formulae for array gain, diversity gain, and diversity loss compare the antenna array in question relative to some ideal system. When the properties of the communications environment come into play, however, an “ideal system” is difficult if not impossible to define. So, if the covariance matrix is calculated by virtue of (4.33), for instance, essentially two things can happen. Suppose the XPR is equal to 0 dB, i.e., there is no preference in the direction of polarisation of the received wave fronts. Since an antenna array can only be sensitive to *one* direction of polarisation at a time in a particular far-field direction, it misses half the power that is theoretically available from the field (cf. [51, Section “MEG, MED, and Radiation Efficiency”]). The diversity figures of merit (array gain, diversity gain, and

diversity loss) are consequently biased with a 3 dB loss.¹

On the other hand, suppose the XPR is very large, the incident wave fronts therefore arrive mainly in the co-polar orientation. Further suppose the antenna array is sensitive to this co-polar component only. This time, there is no such 3 dB penalty; moreover, the diversity loss L_d may actually turn out negative since a properly designed array for a cellular environment would specifically exploit the field concentration around the horizontal plane, and thus produce a gain with respect to a uniform environment.

Much of this confusion can be avoided if, for the comparison between array designs, the different definitions of \tilde{H} are not mixed. For evaluations based on \tilde{H}_{acc} and \tilde{H}_{rad} the formulae can be applied as is. If \tilde{H}_{env} is used, the array gain (4.19) or the diversity gain (4.26) based on the ratio of the gain values of $\tilde{H}_{\text{env}}^{(\text{array})}$, the matrix of the array in question, and $\tilde{H}_{\text{env}}^{(\text{ref})}$, the matrix of an arbitrary single-port reference antenna, should be preferred. The reference antenna can be an isotropic antenna, a dipole antenna, or anything else that seems appropriate. In a similar fashion, an arbitrary reference antenna *array* must be chosen for the diversity loss calculation according to (4.28).

This insight that *relative* comparison between array designs should be preferred over absolute measures of array performance is reinforced when we include aspects of the received noise in our analysis later on.

4.3.2 Effects of a decoupling and matching network

In Chapter 3 the influence of a passive decoupling and matching network (DMN) on the antenna array eigenmodes was investigated. The same formula (3.16) can be shown to work for covariance matrices as well [144, Eqn. (32)]. Let us, in particular, take a closer look at the effects of a DMN on the diversity loss $L_{d,S}$ of the system. With (4.28) we have

$$\begin{aligned} L_{d,S} \Big|_{\text{dB}} &\approx -\frac{10}{n} \log \det \{ \tilde{H}_R \} \text{ dB} \\ &= -\frac{10}{n} \log \det \{ \tilde{t}_a^H \tilde{H} \tilde{t}_a \} \text{ dB} \\ &= \left[-\frac{10}{n} \log \det \{ \tilde{H} \} - \frac{20}{n} \log \det \{ \tilde{t}_a \} \right] \text{ dB} \end{aligned}$$

¹This seeming inconsistency could readily be resolved by multiplying Eqn. (4.33) by a factor of two; however, such a formulation is not generally applied in the literature.

$$= L_d \Big|^{dB} - G_{d,N} \Big|^{dB}, \quad (4.36)$$

where the last term $G_{d,N}$ may be interpreted as the diversity gain brought about by the network. Further expansion yields

$$G_{d,N} \Big|^{dB} \approx \frac{20}{n} \log \det \{ \tilde{t}_a \} \text{ dB} = \frac{20}{n} \log \left[\frac{\det \{ \tilde{S}_{N,21} \}}{\det \{ \tilde{I} - \tilde{S}_{N,22} \tilde{S} \}} \right] \text{ dB}. \quad (4.37)$$

Evidently, the above expression depends only on the scattering parameters of the DMN and of the antenna array. It is independent of the matrix \tilde{H} . That is, the diversity gain provided by a DMN may be estimated regardless of the way \tilde{H} was obtained. It is therefore a measure *independent* of the communications environment and of ohmic losses in the antenna array. This result holds for any reciprocal network connected to the array, whether lossless or not. The scattering matrices of the antenna array \tilde{S} and of the network \tilde{S}_N have to be known separately, of course, either by measurements or by simulation.

This insight leads us to another fundamental conclusion. Suppose L_d is the diversity loss of a lossless antenna array calculated from its scattering parameters. Further, imagine an ideal and lossless DMN for this array. Since the scattering matrix of the resulting system would be the zero matrix, its diversity loss $L_{d,S}$ would be 0 dB. When losses are present in the DMN, the resulting diversity loss will be greater than zero:

$$0 \text{ dB} < L_{d,S} \Big|^{dB} = L_d \Big|^{dB} - G_{d,N} \Big|^{dB}, \quad (4.38)$$

and thus

$$G_{d,N} \Big|^{dB} < L_d \Big|^{dB}. \quad (4.39)$$

In other words, the diversity loss as calculated from the scattering parameters expresses the maximum gain that may be achieved with a passive DMN. Since $G_{d,N}$ was shown to be independent of the covariance matrix \tilde{H}^T , we may finally conclude that the diversity loss based on the scattering parameters of the antenna array expresses the loss caused by mutual coupling and impedance mismatch in a Rayleigh environment *irrespective* of any other factors that affect diversity.

At first glance this statement seemingly contradicts findings by other researcher, namely that mutual coupling can actually be beneficial in certain

cases [81, 96, 114]. To resolve this contradiction we have to understand two distinct effects: mutual coupling and beam-pattern distortion. Mutual coupling impairs the flow of power between the antenna array and the receiver front-end. This was just proved to hold without exception. On the other hand, mutual coupling also affects the shapes of the beam-patterns. That is, the pattern space covered by a pair of closely spaced radiators can be very different from the pattern space of the same radiators placed further apart. Thus, it may well happen that a mutually coupled array takes advantage of a non-uniform environment in a way that more than compensates for the loss due to port coupling itself. Still, the general statement that mutual coupling can be beneficial is misleading, since it is the pattern shapes and the environment, which are responsible for these improvements, and not the mutual coupling.

Although (4.37) becomes exact in the limit of zero probability, it tends to overestimate the gain provided by the network significantly at practical levels. The reason is that those antenna arrays that benefit from a DMN the most are usually of such poor quality that the diversity loss approximation of the array itself is rather inaccurate. Nonetheless, a gain estimate, even a rough one, is an indispensable tool for the design and optimisation of broadband DMNs. If higher accuracy is sought, the designer can always resort to the second-order diversity gain formula (4.26).

4.3.3 Spatially coloured receiver noise

For the initial description of the diversity combiner in (4.5), we have assumed that the branch noise is equal and uncorrelated, i.e., the receiver noise was assumed spatially “white”. This assumption, however, is not always justified in practical receiver systems, as we shall soon see. To include the effects of *coloured* receiver noise in our description, Eqn. (4.5) is rewritten as

$$\mathcal{Q}_C(\vec{w}) = \frac{1}{kB} \frac{\vec{w}^H [\vec{b}_R \vec{b}_R^H] \vec{w}}{\vec{w}^H \tilde{T}_R \vec{w}}; \quad (4.40)$$

the only modification is that the received noise is modelled by a *temperature covariance matrix* \tilde{T}_R rather than a scalar temperature. The next section presents a complete receiver noise model, so \tilde{T}_R can actually be calculated from measured or simulated component data. Before we do this, however, we wish to extend the existing formulae to account for coloured noise. To this end, we

introduce a transformation

$$\vec{w} = \tilde{W}^H \vec{w}' \quad (4.41)$$

on the combiner weights \vec{w} , where \tilde{W} is some non-singular matrix. The transformation is thus one-to-one. We then express (4.40) in terms of the new combiner weights \vec{w}' :

$$\varrho_C(\vec{w}') = \frac{1}{kB} \frac{\vec{w}'^H \tilde{W} \vec{b}_R \vec{b}_R^H \tilde{W}^H \vec{w}'}{\vec{w}'^H \tilde{W} \tilde{T}_R \tilde{W}^H \vec{w}'}. \quad (4.42)$$

Choosing \tilde{W} such that $kB \tilde{W} \tilde{T}_R \tilde{W}^H = \tilde{I}$, e.g., $\tilde{W} = \tilde{T}_R^{-1/2} / \sqrt{kB}$, we have

$$\varrho_C(\vec{w}') = \frac{\vec{w}'^H [(\tilde{W} \vec{b}_R) (\vec{b}_R^H \tilde{W}^H)] \vec{w}'}{\vec{w}'^H \vec{w}'}, \quad (4.43)$$

which has the same form as the initial white-noise combiner (4.5). For this reason the transformation \tilde{W} is commonly referred to as a *pre-whitening filter*. Following the derivation of Section 4.2.1 we finally obtain

$$\varrho = \varrho_{C,\max} = |\tilde{W} \vec{b}_R|^2 \quad \text{with} \quad \text{Var} \{ \tilde{W} \vec{b}_R \} = \tilde{W} \tilde{H}_R^T \tilde{W}^H. \quad (4.44)$$

Thus, in order to incorporate coloured noise into the existing diversity formulae, all we need to do is replace \tilde{H}_R^T by the covariance matrix $\tilde{W} \tilde{H}_R^T \tilde{W}^H$ of the filtered signal $\tilde{W} \vec{b}_R$. Since the performance of the MRC combiner depends on only the eigenvalues of the covariance matrix, we can, by Proposition 2 on page 206,

$$\text{replace} \quad \tilde{H}_R \quad \text{by the matrix}^2 \quad \frac{1}{kB} \tilde{H}_R (\tilde{T}_R^{-1})^T, \quad (4.45)$$

which possesses the same eigenvalues as $\tilde{W} \tilde{H}_R^T \tilde{W}^H$ but avoids the explicit calculation of \tilde{W} . Note that we must formally assign a power unit (e.g., Watts) to \tilde{H}_R for the new matrix to be dimensionless. Let us apply this substitution to the diversity loss L_d (4.28):

$$L_d \Big|_{\text{dB}} \approx -\frac{10}{n} \log \det \left\{ \frac{\tilde{H}_R (\tilde{T}_R^{-1})^T}{kB} \right\} \text{dB} = -10 \log \left(\frac{\sqrt[n]{\det \{ \tilde{H}_R \}}}{kB \sqrt[n]{\det \{ \tilde{T}_R \}}} \right) \text{dB}. \quad (4.46)$$

²Bear in mind that until the matrix \tilde{H}_R was introduced in Section 4.3.1, the notation \tilde{H} without the subscript was employed in the formulae.

The fraction inside the logarithm represents a signal-to-noise ratio: the numerator is a signal power quantity and the denominator a noise power quantity of the form “ kTB ”. We may therefore define a first-order approximation to the *equivalent mean temperature of the received noise* of an equivalent receiver with equal and uncorrelated branch noise:

$$T_R \approx \sqrt[n]{\det\{\tilde{T}_R\}}. \quad (4.47)$$

This term may be considered a generalisation of the familiar *system noise temperature* to MRC diversity systems. By the same reasoning as with the (signal) diversity loss due to mutual coupling, the effect of coloured noise and the calculation of the equivalent temperature are independent of any other factors that otherwise affect the diversity gain of the system. (We are still assuming a Rayleigh environment, though.)

The above diversity loss formula enables us to carry out relative comparisons between different systems with known \tilde{H}_R and \tilde{T}_R . Its value, however, does not represent the loss with respect to some ideal system as the original definition (4.28) in terms of the signal covariance matrix does. As with the definition of an ideal antenna array in a non-uniform communications environment, the definition of an ideal system in terms of noise is not a trivial one. Noiseless systems do not exist in practice and even if they did, their diversity gain would be infinite. Such a system would hence not be a meaningful reference in the definition of a diversity gain or loss. The next section examines more closely the various sources of the noise received by a system, and suggests possible reference systems for a “noisy” diversity loss definition.

4.4 A complete receiver model

Receiver noise is the ultimate parameter limiting sensitivity. Whereas the previous subsection investigated the influence of noise on the diversity performance, the following subsections are concerned with a detailed noise model of a multi-branch receiver front-end. The aim is to be able to predict the receiver noise covariance matrix $k\tilde{T}_R B$ from as few parameters as possible.

A noisy front-end model was introduced by Straumann and Mönich [113] and subsequently refined by a research team around Jensen [62, 83, 84] to include the effects of a decoupling and matching network. However, except for the work by Warnick and Russer [115], the thermal noise picked up by the

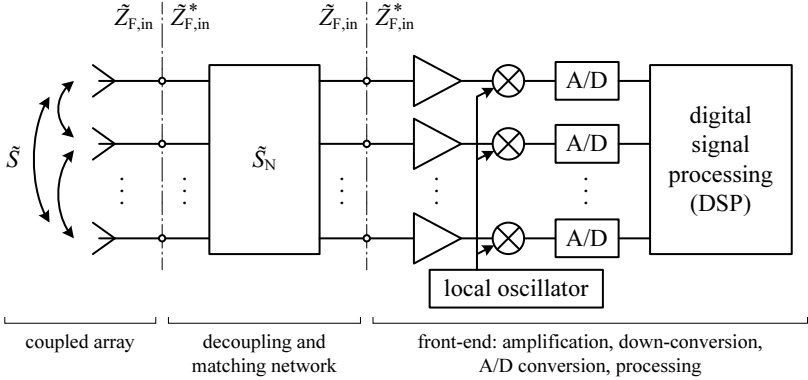


Fig. 4.6: Block diagram of a typical diversity receiver with antenna array and decoupling and matching network. The scattering matrices of the individual blocks are normalised to the input impedances $\tilde{Z}_{F,in}$ of the front-end branches, as indicated.

antenna array is neglected. Furthermore, all authors assume a lossless network and hence disregard the noise produced by it. As power consideration from Chapter 3 have revealed, however, network losses cannot be ignored. The following analysis will therefore extend the model appropriately. We also remember the previous requirement that the scattering matrix of the antenna array and of the feed network be normalised to the input impedances of the receiver branches. In the mathematical description, this eliminates any waves reflected from the receiver inputs, reduces the number of loops in the corresponding signal flow graph representation, and, in contrast to the works cited above, minimises the number of matrix inverses and auxiliary matrices necessary.

The following description is based on the notion of noise waves [4, 16, 65, 118] because, unlike the traditional approach with equivalent noise voltage and current sources, they fit in seamlessly with the usual scattering parameter description of microwave systems. A short introduction on working with noise waves and signal flow graphs is presented in Appendix B.2.

Figure 4.6 portrays the major building blocks of a typical diversity receiver including antenna array and DMN. All components to the right of the DMN are referred to as the “front-end”. The front-end usually consists of low-noise amplifiers (LNA) followed by one or more stages of frequency

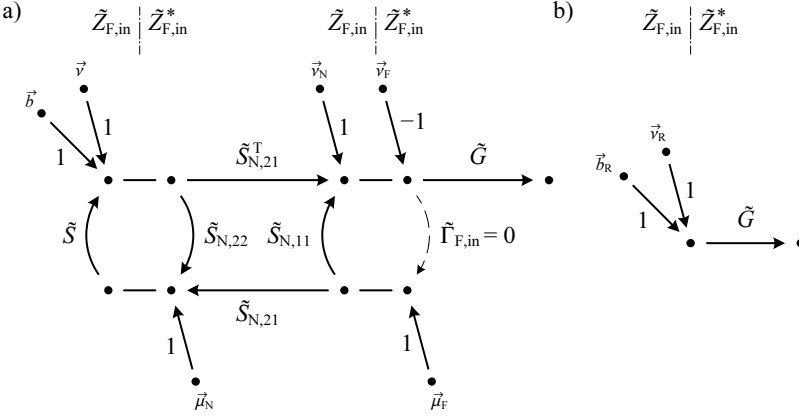


Fig. 4.7: (a) Complete matrix signal flow graph of the receiver of Fig. 4.6 including the antenna array signal waves \vec{b} , and the noise waves \vec{v} and $\vec{\mu}$ of the constituent parts. (b) Collapsed signal flow graph involving the received signal vector \vec{b}_R and a combined received noise vector \vec{v}_R at the front-end inputs.

conversion down to a low intermediate frequency (IF). Analogue down-conversion directly into the complex baseband is also possible with quadrature mixers. The IF or baseband signal is then quantised and sampled, with the final processing usually done in the digital domain. The latter includes SNR estimation, branch combining, and recovery of the original data stream.

To understand better the origins and the propagation of both the signal and the noise through the receiver system, we inspect the complete signal flow graph of the receiver shown in Fig. 4.7a. Symbols without a subscript refer to the antenna array. The subscripts “N” and “F” refer to the *network* and the *front-end*, respectively. The vector \vec{b} represents the only signal source present, namely the signals received by the antenna array. Noise is signified by the wave vectors \vec{v} and $\vec{\mu}$, which travel towards and away from the front-end, respectively. The choice of -1 for the edge weight at noise wave \vec{v}_F is arbitrary and follows the convention employed by other authors [4, 84]. The front-end noise waves not only describe the noise by the low-noise amplifiers but also include any other type of noise generated anywhere within the front-end, i.e., noise in the frequency converters, quantisation noise of the analogue-to-digital converters, and round-off noise in the digital compu-

tations. Note that the loop between the network and the amplifiers has disappeared as the result of the normalisation of the scattering matrices. There is only one loop left between the antenna array and the feed network.

The vast complexity of the complete signal flow graph can actually be reduced to the simple graph shown to its right in Fig. 4.7b. The signal vector \vec{b}_R and the noise vector \vec{v}_R are known from past discussions (see Fig. 4.1). The different ways to obtain the covariance matrix \tilde{H}_R of \vec{b}_R were summarised on page 113.

The covariance matrix of the received noise \vec{v}_R is the superposition of several noise sources: the antenna array, the network and the front-end. As before, noise and noise correlation is expressed in terms of equivalent temperature matrices:

$$\begin{aligned} \text{Var}\{\vec{v}_R\} &= k\tilde{T}_R B, \\ \text{with} \quad \tilde{T}_R &= \tilde{T}^R + \tilde{T}_N^R + \tilde{T}_F^R. \end{aligned} \quad (4.48)$$

Subscripts refer to the origin of the noise and the superscript reminds us that the matrices refer to the received noise wave \vec{v}_R in Fig. 4.7b. The matrix \tilde{T}_R was termed the temperature covariance matrix of the received noise.

The diagonal matrix \tilde{G} comprises the internal (voltage) gains of the front-end channels resulting from the various amplification and frequency conversion stages, and presents a major simplification over the original model by Warnick and Jensen [83], which requires a number of auxiliary matrices. Since it operates equally on both the signal and the noise, the received SNR and thus the receiver performance are unaffected by \tilde{G} . Its value is therefore irrelevant for the subsequent discussion, yet it becomes helpful during the practical characterisation of the receiver as explained in the next chapter.

Before we proceed with the calculation of the noise matrices, we note that the edge weights in the graphs are matrices, which in general do not commute under multiplication. For this reason, the graph cannot be analysed with the familiar Mason-formula [6, Chapter 9]. A Mason-like approach by Riegle and Lin [72] specifically developed for matrix signal flow graphs in principle could be applied to our problem, but, since the graph contains one single loop only, the systems of equations that arise during the following derivations are easily solved by standard methods of equation solving. The matrix \tilde{t}_a first introduced in Section 3.5 is, by the way, the result of the remaining loop in the flow graph and hence continues to appear in the formulae below.

4.4.1 Antenna array noise

A lossless antenna array produces no noise itself. The noise power measured at its terminals is the result of noise collected from its environment. If the reciprocal array is placed in a passive environment of uniform equivalent temperature T_{env} , such as an indoor environment, then the noise covariance matrix and the equivalent noise temperature covariance matrix of \vec{v} are given according to [16, Eqn. (2.46)], [118, Section 2.6.5]:

$$\text{Var}\{\vec{v}\} = k\tilde{T}B,$$

with

$$\tilde{T} = T_{\text{env}} (\tilde{I} - \tilde{S}\tilde{S}^H) = T_{\text{env}} (\tilde{I} - \tilde{S}^T\tilde{S}^*) = T_{\text{env}} \tilde{H}_{\text{acc}}^T. \quad (4.49)$$

If the antenna array possesses ohmic losses then, by superposition,

$$\tilde{T} = T_{\text{env}} \tilde{H}_{\text{rad}}^T + T_{\text{amb}} (\tilde{H}_{\text{acc}} - \tilde{H}_{\text{rad}})^T, \quad (4.50)$$

where T_{amb} is the ambient temperature of the antenna array. In case environment noise is non-uniformly distributed over azimuth and elevation, \tilde{T} is found by integrating the noise temperature over the array far-field patterns in the manner of (2.26) (cf. Dijk et al. [36]):

$$\tilde{T} = \left[\frac{1}{4\pi} \oint T_{\text{env}}(\phi, \theta) \vec{F}_i^T(\phi, \theta) \vec{F}_j^*(\phi, \theta) d\Omega \right] + T_{\text{amb}} (\tilde{H}_{\text{acc}} - \tilde{H}_{\text{rad}})^T. \quad (4.51)$$

Finally, the noise covariance of the received noise waves \vec{v}_R due to the antenna is given by

$$\tilde{T}^R = \tilde{T}, \quad \text{without network}, \quad (4.52)$$

$$\text{or } \tilde{T}^R = \tilde{t}_a^T \tilde{T} \tilde{t}_a^*, \quad \text{with network}. \quad (4.53)$$

4.4.2 Network noise

If the feed network of the antenna array is lossless it does not contribute any noise and \tilde{T}_N^R is the zero matrix. Otherwise the joint covariance matrix of the

waves \vec{v}_N and $\vec{\mu}_N$ of the reciprocal network \tilde{S}_N at ambient temperature $T_{\text{amb},N}$ is given by:

$$\begin{aligned} \text{Var} \left\{ \begin{pmatrix} \vec{v}_N \\ \vec{\mu}_N \end{pmatrix} \right\} &= kT_{\text{amb},N} B \left(\tilde{I} - \tilde{S}_N \tilde{S}_N^H \right) \\ &= kB \begin{pmatrix} \tilde{T}_{v,N} & \tilde{T}_{v\mu,N} \\ \tilde{T}_{v\mu,N}^H & \tilde{T}_{\mu,N} \end{pmatrix}, \end{aligned} \quad (4.54)$$

with

$$\tilde{T}_{v,N} = T_{\text{amb},N} \left(\tilde{I} - \tilde{S}_{N,11} \tilde{S}_{N,11}^* - \tilde{S}_{N,21}^T \tilde{S}_{N,21}^* \right), \quad (4.55)$$

$$\tilde{T}_{\mu,N} = T_{\text{amb},N} \left(\tilde{I} - \tilde{S}_{N,22} \tilde{S}_{N,22}^* - \tilde{S}_{N,21} \tilde{S}_{N,21}^H \right), \quad (4.56)$$

$$\tilde{T}_{v\mu,N} = T_{\text{amb},N} \left(-\tilde{S}_{N,11} \tilde{S}_{N,21}^H - \tilde{S}_{N,21}^T \tilde{S}_{N,22}^* \right). \quad (4.57)$$

As the signal flow graph reveals, the noise waves $\vec{\mu}_N$ travelling away from the network are fed back into the system by the antenna array. The network's noise contribution \tilde{T}_N^R to the total receiver noise is therefore dependent on the array scattering matrix \tilde{S} . Following the rules of noise superposition of Appendix B.2 we have

$$\begin{aligned} \tilde{T}_N^R &= \begin{pmatrix} \tilde{I} & \tilde{t}_a^T \tilde{S} \end{pmatrix} \begin{pmatrix} \tilde{T}_{v,N} & \tilde{T}_{v\mu,N} \\ \tilde{T}_{v\mu,N}^H & \tilde{T}_{\mu,N} \end{pmatrix} \begin{pmatrix} \tilde{I} \\ \tilde{S}^H \tilde{t}_a^* \end{pmatrix} \\ &= \tilde{T}_{v,N} + \tilde{T}_{v\mu,N} \tilde{S}^H \tilde{t}_a^* + \tilde{t}_a^T \tilde{S} \tilde{T}_{v\mu,N}^H + \tilde{t}_a^T \tilde{S} \tilde{T}_{\mu,N} \tilde{S}^H \tilde{t}_a^*. \end{aligned} \quad (4.58)$$

The term $\tilde{t}_a^T \tilde{S}$ is the matrix transmission coefficient from the node $\vec{\mu}_N$ to the node pointed to by \vec{v}_N .

Considerable simplifications are possible if the antenna array and the network are at the same ambient temperature, i.e., if $T_{\text{amb},N} = T_{\text{amb}}$, because then the ohmic losses of the network and of the antenna array can be combined into an equivalent lossy array without network. We can then determine the total noise contribution $\tilde{T}^R + \tilde{T}_N^R$ of the newly created system by virtue of (4.50). All we need are the new matrices of accepted power $\tilde{H}_{\text{acc},S}$ and radiated power $\tilde{H}_{\text{rad},S}$. These can be computed with (2.7) and (3.17) according to

$$\tilde{H}_{\text{acc},S} = \tilde{I} - \tilde{S}_S^H \tilde{S}_S, \quad \text{where} \quad \tilde{S}_S = \tilde{S}_{N,11} + \tilde{S}_{N,21}^T \tilde{S} \tilde{t}_a, \quad (4.59)$$

and by (3.16):

$$\tilde{H}_{\text{rad},S} = \tilde{t}_a^H \tilde{H}_{\text{rad}} \tilde{t}_a, \quad (4.60)$$

where \tilde{H}_{rad} is the radiation matrix of the array without network. Of course, the matrices $\tilde{H}_{\text{rad},S}$ and \tilde{S}_S can be measured directly if a manufactured array with feed network is at hand.

4.4.3 Front-end amplifier noise

The characterisation of the front-end channels is similar to that of the feed network. The joint covariance matrix of the noise waves \vec{v}_F and $\vec{\mu}_F$ is given by

$$\text{Var} \left\{ \begin{pmatrix} \vec{v}_N \\ \vec{\mu}_N \end{pmatrix} \right\} = kB \begin{pmatrix} \tilde{T}_{v,F} & \tilde{T}_{v\mu,F} \\ \tilde{T}_{v\mu,F}^H & \tilde{T}_{\mu,F} \end{pmatrix}, \quad (4.61)$$

and the front-end noise contribution \tilde{T}_F^R to the total receiver noise is calculated according to (cf. [4, (4.50)])

$$\begin{aligned} \tilde{T}_F^R &= \begin{pmatrix} -\tilde{I} & \tilde{S}_S \end{pmatrix} \begin{pmatrix} \tilde{T}_{v,F} & \tilde{T}_{v\mu,F} \\ \tilde{T}_{v\mu,F}^H & \tilde{T}_{\mu,F} \end{pmatrix} \begin{pmatrix} -\tilde{I} \\ \tilde{S}_S^H \end{pmatrix} \\ &= \tilde{T}_{v,F} - \tilde{T}_{v\mu,F} \tilde{S}_S^H - \tilde{S}_S \tilde{T}_{v\mu,F}^H + \tilde{S}_S \tilde{T}_{\mu,F} \tilde{S}_S^H, \end{aligned} \quad (4.62)$$

where \tilde{S}_S is the antenna system matrix given above in (4.59).

The principal difference between the active front-end and the passive feed network is that the matrices $\tilde{T}_{v,F}$, $\tilde{T}_{\mu,F}$, and $\tilde{T}_{v\mu,F}$ cannot be derived from scattering parameters or the ambient temperature; they must be known, either by simulation or by measurement. Since internal coupling between receiver branches is usually negligible, the matrices are diagonal. If, in addition, all front-end branches are equal, the matrices reduce to scalar coefficients.

In Chapter 5 we will learn to measure the noise waves of a manufactured receiver front-end directly. Simulation software, measurement equipment, and datasheets provided by amplifier manufactures, however, usually specify the noise performance of a circuit or device in terms of a different set of parameters, for instance, the minimum noise figure F_{\min} , the optimum reflection coefficient Γ_{opt} (complex), and the equivalent noise resistance R_n . There is a one-to-one correspondence between these parameters and the noise wave description above. Conversion formulae between various representations are provided by Engberg and Larsen [4, Section 4.3.1].

It is generally known that the noise figure expresses the SNR degradation due to an amplifier. The noise figure is dependent on the reflection coefficient

seen by the amplifier input terminal, and reaches a minimum for some reflection coefficient Γ_{opt} . Further implications of this fact for multi-port receivers follow below.

4.4.4 Discussion of the front-end model

The complete noise characterisation of a diversity receiver including antenna array, decoupling and matching network, and front-end amplifiers is rather laborious. In spite of that, the preceding sections enable us to predict the noise performance under many practical circumstances. Before we apply these formulae to a fabricated system in Chapter 5, in the upcoming sections we shall discuss some limiting cases of the model, in which one or more contributors of noise become negligible for some reason.

Very noisy amplifiers. Let us first consider a poorly designed receiver that produces a great amount of noise internally. This may be the case if ready-made integrated circuits are used that take care of the entire down-conversion process. These chips have the disadvantage of a high noise-floor. (e.g., the AD8347 down-converter by Analog Devices [124] with a specified noise figure of 11 dB.) The analogue-to-digital converter is also a potential candidate for a bad overall noise performance if the gain of the analogue amplification chain is insufficient to overcome the quantisation noise floor for very weak signals. We will see an example of such a receiver in the next chapter.

We now assume that the antenna array and the feed network do not contribute any noise. It is further assumed that the amplifier noise is independent of the impedance connected to its input terminal. Thus, by (4.48) and (4.62):

$$\tilde{T}_R = \tilde{T}_{v,F} = \text{constant.} \quad (4.63)$$

It is almost needless to say, that this allows the comparison of different antenna arrays and DMNs solely by means of the signal covariance matrix \tilde{H}_R . An analysis of receiver noise is not required. Decoupling and matching networks can provide significant SNR gains in this case because they improve the signal transfer between the antenna array and the front-end branches. The noise produced by lossy DMN implementations is negligible compared with the front-end noise generated internally.

Noiseless amplifiers. The opposite extreme is attained if we assume noiseless front-end channels. Let us further suppose for the time being that any network inserted between antenna array and front-end is lossless and, hence, produces no noise either. For the signal covariance matrix, we have

$$\tilde{H}_R = \tilde{H}, \quad \text{without network} \quad (4.64)$$

$$\tilde{H}_R = \tilde{H}_S = \tilde{t}_a^H \tilde{H} \tilde{t}_a, \quad \text{with network,} \quad (4.65)$$

and, by (4.52),

$$\tilde{T}_R = \tilde{T}^R = \tilde{T}, \quad \text{without network} \quad (4.66)$$

$$\tilde{T}_R = \tilde{T}^R = \tilde{t}_a^T \tilde{T} \tilde{t}_a^*, \quad \text{with network.} \quad (4.67)$$

According to the discussion around Eqn. (4.45) the system diversity gain is defined by the matrix product $\tilde{H}_R(\tilde{T}_R^{-1})^T$ or, more specifically, the eigenvalues thereof. With the above definitions we obtain for the case without network

$$\tilde{H}_R(\tilde{T}_R^{-1})^T = \tilde{H}(\tilde{T}^{-1})^T, \quad (4.68)$$

and for the system with network

$$\tilde{H}_R(\tilde{T}_R^{-1})^T = \tilde{t}_a^H \tilde{H} \tilde{t}_a \left((\tilde{t}_a^T \tilde{T} \tilde{t}_a^*)^{-1} \right)^T = \tilde{t}_a^H \tilde{H}(\tilde{T}^{-1})^T (\tilde{t}_a^H)^{-1}. \quad (4.69)$$

By Proposition 2 on page 206, the eigenvalues of these two expressions are identical. A noiseless (e.g., a lossless) network in conjunction with noiseless amplifiers thus seems to have no influence on diversity whatsoever. To apprehend this matter of fact we suppose an ordinary single-port antenna that is impedance mismatched to a noiseless front-end. Because, from an electrical point of view, there is no difference between what we call the “signal” and the “noise”—both are signals after all—the noise experiences the same mismatch, and therefore the same mismatch loss, as the (desired) signal. Any lossless matching network inserted will thus enhance the noise power transfer in the same way as the signal and have *no influence on the SNR* at all. For multi-port antennas, matters are very similar since previously in Section 2.6 we interpreted mutual coupling as a generalisation of impedance mismatch. Only the calculations are more cumbersome as they involve covariance matrices instead of scalar power quantities.

Since practical network implementations are usually lossy, they not only attenuate the signal received by the array, but contribute their own noise. The SNR available at the outputs of a DMN will consequently *always be worse* than the SNR directly at the array terminals. The SNR gains due to a network discussed in the above description of very noisy amplifiers are only possible because additional noise is introduced *after* the network has improved the power matching of the signal. Although practical amplifiers always produce some noise, they can nowadays be manufactured very quiet indeed, with a noise contribution far below thermal noise at room temperature. For instance, the NE3515S02 hetero-junction field-effect transistor (HJ-FET) manufactured by NEC Electronics Corporation [133] possesses a specified noise-figure of 0.2 dB. The additional noise contributed by the amplifier is less than 5 % of the thermal noise produced by a passive load (e.g., an antenna) at room temperature. So, if the noise contributed by the receiver front-ends is below or of the order of the noise received by the antenna array, we should be wary by now that improvements due to a DMN may turn out less than anticipated unless a careful noise analysis is carried out.

This insight is also relevant to systems whose performance is primarily limited by external random-like interference rather than receiver noise. Naturally, the power ratio between the desired signal and the unwanted interference is affected neither by mutual coupling [112] nor by the insertion of a DMN.

The original definition of the diversity loss (4.28) expressed the *signal* loss of a mutually coupled n -port system with respect to some “ideal” n -port system. In terms of *signal* power, an ideal system was readily defined as an uncoupled, matched, and lossless antenna array in a uniform Rayleigh environment. We will now propose a possible definition for the *SNR* loss of a noisy system that takes a noiseless front-end as the reference where the only noise is contributed by an ideal antenna array (lossless, uncoupled, and matched) seeing a uniform temperature T_{env} :

$$L_d^{(\text{SNR})} \Big|_{\text{dB}} \approx -\frac{10}{n} \left[\log \det \left\{ \frac{1}{kB} \tilde{H}_R (\tilde{T}_R^{-1})^T \right\} - \log \det \left\{ \frac{1}{kB} \tilde{H}_{R,\text{ref}} (\tilde{T}_{R,\text{ref}}^{-1})^T \right\} \right] \text{ dB}.$$

With $\tilde{H}_{\text{R,ref}} = \tilde{I}$ and $\tilde{T}_{\text{R,ref}} = T_{\text{env}}\tilde{I}$, we obtain

$$\begin{aligned} L_d^{(\text{SNR})} \Big|_{\text{dB}} &\approx \left[-\frac{10}{n} \log \left(\frac{\det\{\tilde{H}_{\text{R}}\}}{(kB)^n \det\{\tilde{T}_{\text{R}}\}} \right) \right. \\ &\quad \left. + \frac{10}{n} \log \left(\frac{\det\{\tilde{I}\}}{(kT_{\text{env}}B)^n \det\{\tilde{I}\}} \right) \right] \text{ dB} \\ &= - \left[\frac{10}{n} \log \left(\frac{\det\{\tilde{H}_{\text{R}}\}}{\det\{\tilde{T}_{\text{R}}\}} \right) + 10 \log T_{\text{env}} \right] \text{ dB}. \end{aligned} \quad (4.70)$$

In uniform environments, this loss definition is always positive. However, it bears the same problem as our original diversity loss definition in that the loss may become negative if the statistical properties of the surrounding environment are included in the analysis (cf. end of Section 4.3.1). As long as we understand how to interpret such a result, this is a perfectly valid and even desirable one, since it informs us that our antenna array design takes particular advantage of the narrow elevation angular spread of the communications environment.

We can also think of an alternative diversity loss definition that, however, only makes sense if the choice of antenna array and target environment is already *fixed*, and if the design focus is on the decoupling and matching network and on the front-end amplifiers. Since the network and the amplifiers always degrade the SNR available at the array terminals, the latter is another possible choice as a reference system for the diversity loss:

$$L_d^{(\text{NF})} \Big|_{\text{dB}} \approx -\frac{10}{n} \left[\log \left(\frac{\det\{\tilde{H}_{\text{R}}\}}{\det\{\tilde{T}_{\text{R}}\}} \right) - \log \left(\frac{\det\{\tilde{H}\}}{\det\{\tilde{T}\}} \right) \right] \text{ dB}. \quad (4.71)$$

This definition is always positive irrespective of the way the reference system (i.e., \tilde{H} and \tilde{T}) is calculated—for instance by (4.33) and (4.51). The only requirement is that the same \tilde{H} and \tilde{T} are used in the calculations of \tilde{H}_{R} and \tilde{T}_{R} . It expresses the SNR degradation due to the front-end components, and thus provides us with a generalisation of the traditional *noise-figure* concept to multiple receiver branches. Hence the superscript “(NF)” in the definition.

For lossless (but possibly coupled and mismatched) antenna arrays in a uniform environment, both definitions yield identical values. In all other cases it is vital that we understand the subtle differences between these two

diversity-loss concepts, and that we are aware of the system characteristics that we actually wish to compare or investigate. Definition (4.70) enables the comparison between *all kinds of systems* (with the same number of radiators) and accounts for all conceivable losses and gains. Definition (4.71), on the other hand, only accounts for aspects of the components that follow the antenna array, i.e., the DMN, the amplifiers, the down-converters, and the digital signal processing. The expression is useful, for instance, to optimise a DMN or to choose the right type of low-noise amplifier for a *given* antenna array in a *given* environment.

For uniform environments, we may work out an approximation formula of the diversity gain (4.26) for noisy systems. The substitutions are the same as in (4.70) above, so the final expression is

$$G_d(\tilde{H}, p) \approx \frac{T_{\text{env}}}{p} \left[q + \frac{\text{tr}\{\tilde{T}_R^T \tilde{H}_R^{-1}\}}{n(n+1)} q^2 \right], \quad \text{with} \quad q = \sqrt[n]{\frac{\det\{\tilde{H}_R\}}{\det\{\tilde{T}_R\}}} n! p. \quad (4.72)$$

No such formula can be established for non-uniform environments since the properties of the single-branch reference system are not well defined. Relative comparisons between arbitrary systems with known signal and noise properties can nonetheless be carried out at all times.

Noiseless antenna array and lossless network. We will now investigate the noise produced by the amplifiers. To this end, we disregard the noise due to the antenna array and assume a lossless and thus noise-free feed network. We mentioned earlier that the SNR degradation caused by an amplifier is generally dependent on the source impedance seen by its input terminal, and that optimum operation is achieved for a single source reflection coefficient Γ_{opt} only. The amplifier is then said to be noise-matched. Noise matching usually occurs at a different impedance than power matching. Warnick and Jensen [84] extended this idea to multi-port receivers and proved that optimum SNR performance is achieved if and only if the amplifiers face uncoupled and individually noise-matched array ports.

Figure 4.8 may help us gain more insight into this fact. Shown is the front-end part of Fig. 4.7 together with the relevant noise wave vectors \vec{v}_F and $\vec{\mu}_F$. The front-end sees a scattering matrix \tilde{S}_S , i.e., an arbitrary antenna array with optional network. In the single-port case, v_F and μ_F as well as the noise temperatures $T_{v,F}$, $T_{\mu,F}$, and $T_{\gamma\mu,F}$ are scalars. The complex tem-

perature $T_{\nu\mu,F}$ describes the amount of correlation between ν_F and μ_F , and is usually non-zero. The reflection coefficient of the load impedance, which in the single-port case we denote by Γ_S rather than S_S , causes part of the “reverse” noise wave μ_F emerging from the amplifier input to superimpose on the wave ν_F already travelling in the forward direction. Due to non-zero correlation between these waves, the superposition can be either constructive or destructive in nature depending on the arguments of Γ_S and $T_{\nu\mu,F}$. Thus, by appropriate choice of Γ_S , the noise produced by the amplifier can actually be reduced below ν_F . In a multi-port system, on the other hand, the noise waves produced by separate amplifiers are uncorrelated. Hence, noise reaching from one amplifier to another as the result of mutual coupling increases the noise level. Optimum noise performance evidently cannot be achieved unless \tilde{S}_S is a diagonal matrix, i.e., describes an uncoupled set of impedances [84].

Let us return to single-branch systems for the moment. Although Γ_S can be chosen to minimise amplifier noise, non-zero Γ_S also has the opposite effect of introducing power mismatch into the signal flow. For optimum SNR, a compromise between amplifier noise reduction and signal power mismatch must therefore be found. If the noise waves of an amplifier are known, e.g., by direct measurement as in Chapter 5, then the optimum reflection coefficient is given by³

$$\Gamma_{S,\text{opt}} = \frac{T_{\nu,F} + T_{\mu,F} - \sqrt{(T_{\nu,F} + T_{\mu,F})^2 - 4|T_{\nu\mu,F}|^2}}{2T_{\nu\mu,F}^*}, \quad (4.73)$$

although most datasheets and simulation software report the optimum impedance directly. For multi-port loads $\tilde{S}_{S,\text{opt}}$, the above formula applies to each port individually. Substitution into (4.62) finally yields the (diagonal) front-end noise covariance matrix of a noise-matched multi-port receiver. Note that a decoupled and noise-matched receiver system is a desirable goal from a theoretical point of view. Whether this is a sensible condition to strive for in practical mutually coupled receiver systems is another matter due to the unavoidable noise contribution of the decoupling and (noise-)matching network required.

³The original work by Warnick and Jensen [84] includes the positive square root in its solution; however, with [4, Eqn. (4.56)] it can be shown that this never yields a passive $\Gamma_{S,\text{opt}}$ as the result.

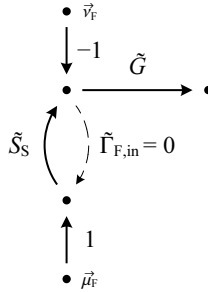


Fig. 4.8: Signal flow graph of a multi-port front-end amplifier showing the equivalent noise waves \vec{v}_F and $\vec{\mu}_F$.

At this point, we could pursue the formulation of a diversity loss expression that quantifies the decibel departure from optimum noise-matching. However, this produces yet another diversity loss definition, which may be useful in one situation but not another. Moreover, the complete formula is not compact at all, so its derivation is omitted here.

In principle, these insights allow DMNs to have a two-fold positive effect on system performance: first, the signal transfer between the antenna array and the front-end is improved. Second, the noise produced by the front-end is reduced by means of noise matching. Hence, the resulting SNR gain would be greater than the signal gain alone. In reality, this situation will rarely occur since we already learned that the noise received by the antenna array is also amplified by the network and that lossy networks contribute significant amounts of noise themselves. The front-ends would therefore have to be particularly sensitive to noise mismatch ($T_{\mu,F} \gg T_{v,F}$). For the majority of practical applications, however, we can expect network losses to outweigh invariably the benefits of (perfect) amplifier noise matching.

4.5 Summary

In this chapter, we have looked at diversity reception as a specific application of compact antenna arrays in mobile communications systems. First, we revised the theory of maximal ratio combining (MRC) in a correlated Rayleigh fading channel, and thereby identified the close relationship with array eigenmodes. What used to be the radiation matrix of the previous two chapters

has now become the *covariance matrix* of the received signal envelopes. The corresponding eigenefficiencies uniquely define the fading statistics.

We then proceeded to derive figures of merit for the simple yet accurate quantification of diversity performance in the presence of mutual coupling. A second-order approximation calculates the familiar *diversity gain* with respect to a single radiator at a given outage probability. In the case of moderate mutual coupling, a first-order approximation yields a particularly simple expression for the *diversity loss* with respect to an ideal antenna array that is roughly independent of the probability level chosen. The various methods introduced in previous chapters of calculating the radiation matrix also apply to diversity system characterisation. In particular, this allows for the use of simple scattering matrix measurements to estimate the prospective diversity performance. The impairments due to mutual coupling can thus be expressed as a *single quantity*, which facilitates performance evaluation over frequency, simplifies the definition of a *diversity bandwidth*, and is easily employed as a *cost function* for array optimisation.

Because these initial derivations were based on the simplifying assumption of a completely uniform scattering environment, more advanced formulae for the covariance matrix were given that allow for the seamless application of the derived figures of merit to *established channel models*. A formula for the diversity enhancements due to a decoupling and matching network (DMN) was also proposed. In this connection, it became clear that, under the supposition of a Rayleigh environment, the impairments due to mutual coupling as manifested in the scattering matrix are *independent of any* other factors that influence diversity, e.g., ohmic losses or a non-uniform environment.

Until this point, we had been looking at *signal* power transfer only. It is the signal to *noise* ratio (SNR), however, which ultimately determines the quality of a mobile transmission. For this reason, a *front-end model* was developed to include the principal sources of noise in the analysis, i.e., noise picked up from the environment, noise due to ohmic losses in a DMN, as well as noise produced by the receiving amplifiers. The diversity loss formula and the diversity gain formula were amended accordingly, and an *equivalent mean temperature* of the received noise was defined.

Discussion of the noise model revealed that the noise captured by the antenna array experiences precisely the same power mismatch due to mutual coupling as the signal. If the rest of the receiver were noiseless, mutual

coupling would have *no effect at all* on the SNR. Indeed, if a DMN were introduced into such a system, it would *degrade* the SNR because DMN ohmic losses attenuate the signal but keep the noise floor constant. Although practical noiseless receivers do not exist, modern amplifiers can be manufactured with an equivalent noise temperature far below room temperature. This insight is also relevant to systems that are primarily limited by strong external, random-like interference rather than internal receiver noise. In this case, too, mutual coupling will have little impact on link quality. Therefore, unless the receiver under consideration is *very noisy*, the improvements due to a DMN can only be correctly quantified if front-end noise, network noise, antenna noise, and interference are accounted for in the calculations.

Chapter 5

Compact antenna arrays in practice: a diversity receiver

The previous chapter has put forward a number of figures of merit related to the diversity performance of mutually coupled antenna arrays as an alternative and an extension to the evaluation methods currently established in the literature. In order to substantiate these results further, a diversity receiver was manufactured. The measurement results will be the topic of the following sections.

In principle, a continuous wave transmitter and a high dynamic range power detector is all that is required to evaluate the diversity performance of antenna arrays [33, 98]. The power detectors would record the signal fading at each antenna terminal and the resulting combined signal would be worked out mathematically according to the desired combining scheme.

The reasons why nonetheless the design of a full-featured digital diversity receiver was pursued are manifold. First, it was felt necessary not only to demonstrate the usefulness of decoupling and matching networks by academic means, but to examine the effects on realistic systems. Indeed, this was a requirement of the project that funded the present work. Second, an intended goal was the estimation of the complex signal covariance matrix \tilde{H}_R at the receiver terminals for comparison with theoretical considerations. It was decided that this is best accomplished using digital signal processing on the complex baseband representation. Third, this also applies to the practical

verification of the receiver noise model devised.

In the upcoming sections, the close agreement between the measured SNR fading distributions and the predictions based on array and DMN scattering parameters will be revealed. At the same time, this will also confirm the applicability of the diversity figures of merit, since these were derived by manipulation of the SNR distribution function (CDF). We conclude the chapter with a complete noise characterisation of the receiver and a discussion of the effects of mutual coupling, noise, and decoupling and matching networks (DMNs) for several example systems.

5.1 Overview of the diversity system

Before we begin with an overview over the various system components, it is important to understand that the diversity system is not meant to be a scientific treatise of communications system design. It rather embodies a straight implementation of textbook concepts; many aspects would probably be implemented differently if this were a commercial system. The intention was to keep development efforts as low as possible, and at the same time achieve an accurate verification of the theoretical framework devised in this thesis. The measurement results presented in later sections clearly demonstrate that this goal has been achieved. To keep the following presentation concise, the reader is expected to be familiar with basic communications system concepts, e.g. Proakis and Salehi [15].

The diversity system features a single-channel transmitter unit and a modular multi-channel receiver unit. Both units were designed from the ground up and geared towards one another for optimum cooperation. The general idea is to transmit a predefined pseudo-random symbol pattern that is known to the receiver. The receiver then compares the received symbol stream to the expected one, estimates the instantaneous SNR of each channel, performs diversity combining, and finally estimates the SNR of the combined stream. Quadrature phase-shift keying (QPSK) was the modulation scheme of choice due to its straightforward implementation in both the transmitter as well as the receiver hardware.

To accelerate development, only the down-conversion into the complex baseband is implemented in hardware. The baseband data are digitised as early as possible and sent to a personal computer (PC) for further processing via the well-established universal serial bus (USB). The PC performs mat-

ched filtering, clock and symbol recovery, carrier recovery, SNR estimation, and diversity combining. In order to enable experimenting with the received data without having to redo the measurement, all symbols including noise are recorded on hard disk drive.

Figure 5.1 portrays a block diagram of the diversity system, which operates at a centre frequency of 2.45 GHz within a license-free ISM (industrial, scientific and medical) band at a QPSK symbol rate of 504 kBaud. Since one symbol encodes two bits, the system transmits about 1 Mbit of data per second. The system occupies an RF bandwidth of around 1 MHz, which is the result of the pulse shape chosen. Consequently, the baseband bandwidth is about 500 kHz each for in-phase and the quadrature channel.

5.1.1 The transmitter

The transmitter is built around the AD8349 direct up-conversion quadrature modulator integrated circuit manufactured by Analog Devices [124]. It takes the carrier frequency and the in-phase and quadrature baseband waveforms as inputs, and produces the modulated carrier at its output without the need for an intermediate frequency. Circuitry that derives the quadrature carrier necessary for direct up-conversion is included on-chip. An SMT06 Rohde & Schwarz signal generator supplies the 2.45 GHz carrier externally. The transmit power is -2 dBm, equivalent to 0.6 mW.

Figure 5.2 shows a photograph of the insides of the transmitter module. During normal operation, the aluminium chassis is closed to avoid carrier leakage. A Spartan3 field programmable gate array (FPGA) by Xilinx [135] presents the heart of the transmitter.¹ Additional auxiliary components include a frequency divider, a Cypress CY7C68014A USB microcontroller [127] and two Analog Devices AD9774 digital-to-analogue converters (DAC) to interface the digital baseband outputs of the FPGA to the analogue inputs of the modulator. An advantageous feature of this particular DAC is its up-sampling capability: it contains a phased-locked loop (PLL) and a high-order digital interpolation filter to increase the user-supplied sampling rate by a factor of four. This considerably alleviates the requirements of the analogue reconstruction filter—a simple RC low-pass proved sufficient.

¹The author thanks his student assistants Ulf Wetzker and Christian Großmann for their support with the development of the transmitter and receiver hardware and firmware.

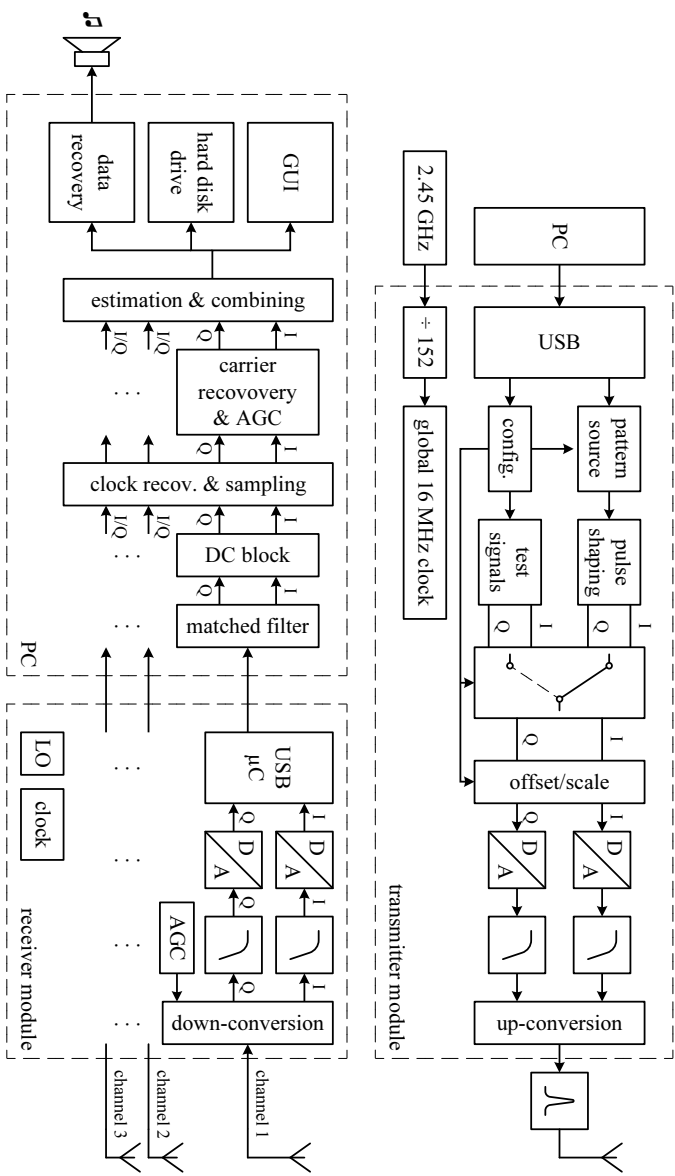


Fig. 5.1: Block diagram of the diversity system comprising the transmitter module, the receiver module, and baseband processing done on the PC. LO = local oscillator, D/A = digital/analogue conversion, AGC = automatic gain control, GUI = graphical user interface.

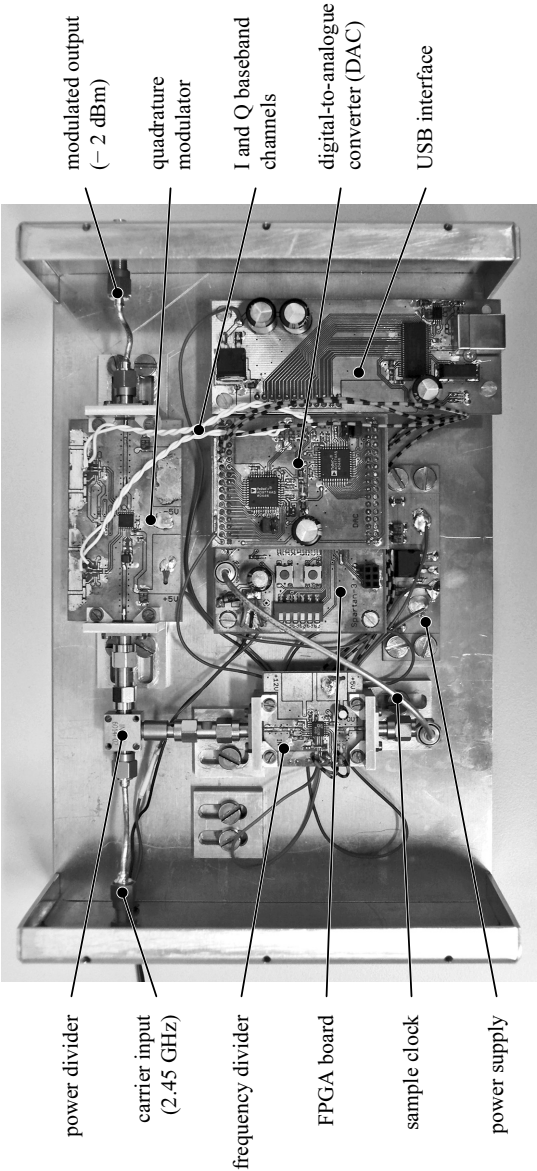


Fig. 5.2: Photograph of the insides of the transmitter module.

The USB controller serves two basic purposes: first, to alter the configuration of the various building blocks seen in Fig. 5.1 without having to reprogramme the FPGA. And second, to supply any user data if the system is used for actual data transmission.

Let us go through the individual transmitter components from right to left. We have already mentioned the up-converter, the reconstruction filters, and the DACs. Next in line is a block labelled “offset/scale”. It is meant to compensate for linear imbalances of the up-converter: DC offsets cause the carrier to feed through to the modulated waveform causing unnecessary radiation of power bearing no information. More relevant to our application, however, is the fact that the demodulated constellation points become shifted from their designated positions, which limits the dynamic range of the SNR measurement. This last point also applies to an amplitude imbalance between the in-phase and the quadrature component.

For easy configuration of the “offset/scale” block, the transmitter employs a “test signals” block. One test signal outputs a sine wave on one channel and no waveform on the other channel. In this configuration, the DC offset of either channel is most easily zeroed. Another configuration outputs a sine wave on one channel and a cosine wave on the other to produce single-sideband amplitude modulation. One of the sidebands will not be fully suppressed unless the channel amplitudes are balanced.

The block labelled “pulse shaping” is a finite impulse response (FIR) filter implementation specially optimised for the pulse shaping operation. In order to minimise the processing power for matched filtering at the receiver, the pulse length is limited to four symbol durations. The pulse function is a root-raised-cosine pulse with roll-off factor $\beta = 0.1$ multiplied by a Hann window. It is shown as thick graphs in Fig. 5.3 and was chosen for its comparatively narrow bandwidth. The figure includes two wider bandwidth pulse waveforms with different roll-off factors and window functions that were previously taken into consideration but then discarded due to their broader bandwidth. All three waveforms have the important property that they are free of inter-symbol interference (ISI) *after* matched filtering at the receiver.

The pulses are oversampled at 32 samples per symbol duration to minimise the complexity of the reconstruction filter. A symbol rate of 500 kBaud therefore necessitates an appropriate sample clock at 16 MHz. At the very beginning of the design, it was considered beneficial if RF carrier and symbol clock were phase locked. For this reason, the 16 MHz clock is derived

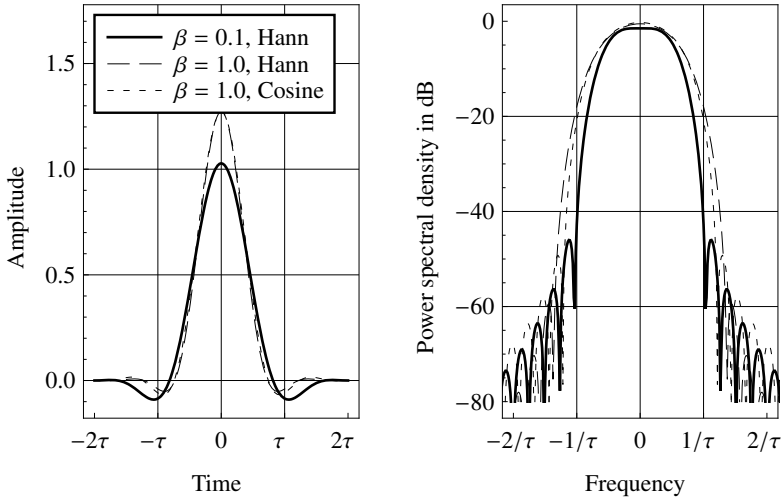


Fig. 5.3: Three different pulse functions and the associated power spectral densities. The function with the thick, solid line is used in the present system. Symbol duration $\tau \approx 2 \mu\text{s}$.

from the RF carrier by means of a digital divide-by-152 counter—the modulus counter present in the Analog Devices ADF4112 PLL chip was used for that purpose. Of course, 2.45 GHz divided by 152 is not exactly 16 MHz but rather about 16.12 MHz, which explains the odd symbol rate of 504 kBaud.

One task of the “pattern source” block is to emit a continuous pseudo-random symbol sequence for SNR measurement purposes. A random search was conducted until an acceptable sequence, called *synchronisation sequence*, based on the following criteria was found:

- A sequence of fixed length is transmitted periodically so the receiver can quickly resynchronise in case synchronisation is lost due to noise or interference.
- The sequence length must be a power of two to enable fast code execution on the receiver PC. A length of 32 QPSK symbols was chosen arbitrarily.

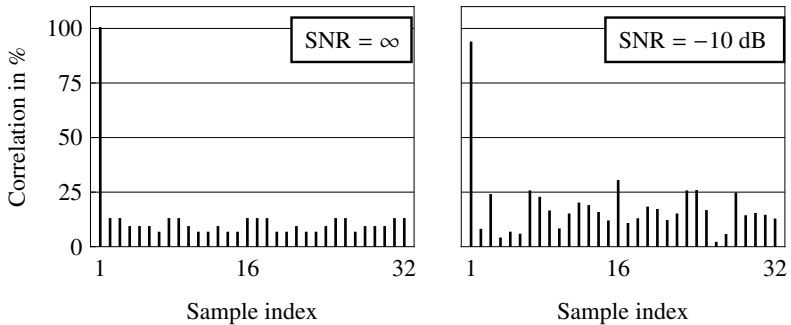


Fig. 5.5: Receiver synchronisation with the help of the synchronisation symbol sequence. The beginning (peak) of the sequence is clearly identified even in the presence of strong noise.

The second task of the pattern source is to interleave any user data supplied via USB cleanly into the transmitted symbol stream. For easy detection and synchronisation at the receiver, the length of the data packets must be an integer multiple of the synchronisation sequence length. Furthermore, data packets are only inserted between transmissions of entire synchronisation sequences. To mark the beginning of a data packet, a *packet sequence* with essentially the same properties as above was found that is orthogonal to the synchronisation sequence for reliable detection. The VHDL source code of the transmitter hardware counts more than 1000 lines.

5.1.2 The receiver front-end

The photograph in Figure 5.6 portrays the modular hardware of the receiver. The receiver consists of three receiver branches and auxiliary modules: a power supply, a clock and carrier generator, and an RF power divider.

The power supply module comprises two 3.3 V voltage regulators, one for the digital circuitry and the other one for the analogue components of the system. Regulated power is then supplied to all modules via the black ribbon cable on the rear side of the receiver (the one seen on the picture). Power-on-reset circuitry required for proper start-up of the microcontrollers employed in the receiver branch modules is also included in this module.

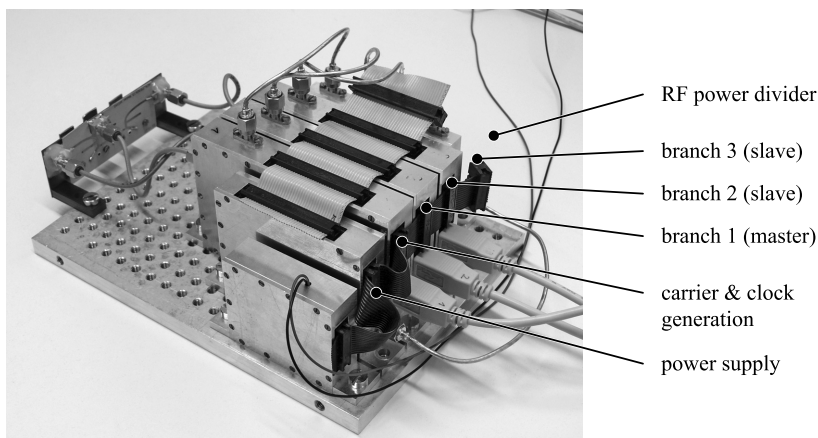


Fig. 5.6: Photograph of the receiver and its constituent modules. On the left-hand side the receiver is connected to a three-port planar inverted-F antenna (PIFA) array with decoupling and matching network designed by Weber [121].

For carrier generation, the ready-made MAX2750 voltage controlled oscillator (VCO) chip manufactured by Maxim Integrated Products [131] is locked to a 25 MHz crystal oscillator reference using the Analog Devices ADF4112 PLL. An external passive Wilkinson power divider distributes the carrier to the receiver branch modules using coaxial cables. As with the transmitter, a 16 MHz clock signal necessary for received baseband waveform digitisation is derived from the RF carrier by digital frequency division. The clock is shared between the branch receiver modules via the gray ribbon cable at the top of the modules. The ribbon cable also communicates configuration waveforms to the PLL chips.

Essentially, the three receiver branch modules are identical; only the first module is different in that it acts as a “master” module responsible for the configuration of the clock and carrier module and for proper synchronisation between the branch modules. All modules consist of a down-converter chip (AD8347, Analog Devices), analogue baseband filters, a dual-channel analogue-to-digital converter (ADC, AD9281, Analog Devices) and a USB microcontroller (CY7C68014A, Cypress), as seen in Figs. 5.1 and 5.7.

Similar to the modulator chip used at the transmitter, the demodulator

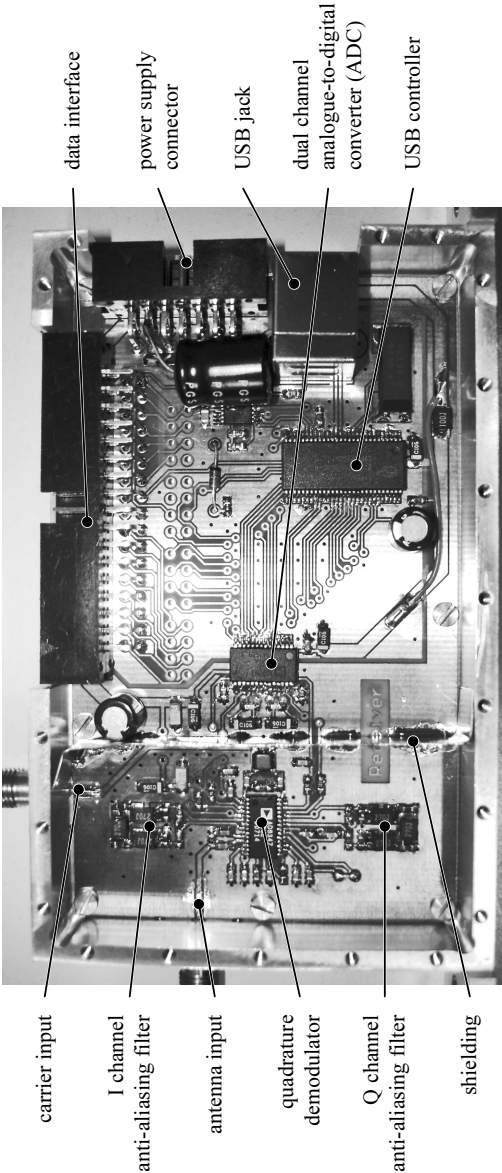


Fig. 5.7: Photograph of the insides of a receiver branch module.

converts straight down to the baseband, and produces the in-phase and the quadrature channels as separate outputs. It also features an automatic gain control (AGC) loop with a dynamic range of almost 70 dB. The baseband filters are modified seventh order Chebyshev low-pass filters [7, Section 3.2.2] optimised for flat group delay response within the bandwidth of the transmitted signal on the one hand, and, to avoid frequency aliasing at the ADCs, maximum attenuation towards the Nyquist frequency on the other hand. Note that these filters are not the matched filters yet; matched filtering is done at a later stage by the PC.

The filtered baseband waveforms are finally digitised at 4 Msamples/s. This rate corresponds to eight digital complex samples per transmitted symbol. With one 8 bit ADC each for the in-phase and for the quadrature channel, the total amount of digital data that must be transferred to the PC for further processing amounts to 8 Mbyte/s. Given the maximum data rate of high-speed USB of around 40 Mbyte/s—which is shared between all devices connected to the same host-controller—we could connect up to four receiver branches to the PC and still have sufficient headroom for any additional traffic on the bus.

The Cypress CY7C68014A USB microcontroller used inside the receiver modules is the same as the one employed at the transmitter. Aside from its 8051-based microcontroller core used for low-speed tasks such as configuring the carrier and clock generation module, it features a dedicated high-speed data interface for the seamless transport of data from an arbitrary data source, in our case the baseband ADCs, to the PC. The USB controller includes first-in-first-out (FIFO) memory buffers to prevent data from becoming lost if the bus is congested and the acquired data cannot be deployed to the PC immediately. Another handy feature is Cypress' "general programmable interface" (GPIF) of the USB controller, which can be programmed to take care of any controlling waveforms required for the dual-channel baseband ADC. In our case, the ADC cycles through four states: sample both analogue inputs at the same time, read data from the first channel, switch channels, and read data from the second channel. Since the baseband waveforms are sampled every four GPIF states, the 16 MHz clock from the carrier and clock generation module produces the abovementioned sampling rate of 4 Msamples/s. Synchronisation of the data acquisition processes between the modules is accomplished by the gray ribbon cable. There are more than 1000 lines of C source code for the essential parts of the microcontroller firmware.

5.1.3 Baseband processing

Once the baseband data has arrived at the PC, processing proceeds as shown earlier in Fig. 5.1. Matched filtering is performed on each channel using a 32-tap FIR filter [19, Chapter 7]. For performance reasons, the filtering operation is hand-optimised and written in assembly language to take advantage of the “single instruction, multiple data” (SIMD) extended instruction set available in the Intel Pentium 4 family of processors. These instructions are akin to the ones found in dedicated DSP chips and were introduced to satisfy the digital processing demands of today’s multimedia and internet applications. The filter implementation is inspired by the methods outlined by Shahbahrani et al. [108] for an older SIMD instruction set. Next, any DC offset present in the baseband waveforms is removed by an efficient implementation of a digital high-pass filter with a very low cut-off frequency.

The subsequent processing stage, labelled “clock recovery”, is required because the symbol clock at the receiver runs asynchronous to the clock at the transmitter. Thus, the correct sampling instants at which the SNR of the recovered symbol stream becomes maximised must continuously be adjusted and determined from the received waveform. The method employed is called the “square-law synchroniser” [45, 97]: it calculates the magnitude square of the received complex waveform of each branch, adds the results together, and passes the summed waveform through a narrow bandpass filter centred around the anticipated sampling frequency. The symbol clock is then derived from the zero-crossings of the quasi-sinusoidal output of the bandpass.

A major problem with this sort of digital clock recovery implementation is that the optimum sampling instant usually falls *between* two of the eight digital samples available per symbol duration. As Fig. 5.8 illustrates, simply choosing the closest neighbouring sample is not an option, since it introduces ISI and, in consequence, causes the apparent SNR of the recovered symbols to vary dramatically with time. Measurements revealed that in the high-SNR regime the (apparent) SNR swung periodically between 25 dB and 35 dB, which is clearly undesirable for accurate SNR measurements. It turns out that simple linear interpolation can alleviate this effect considerably. Although the variations are still of the order of 3 dB at high SNRs, the effect quickly diminishes as soon as reception becomes impaired by random noise. It was therefore decided that the performance is sufficient for the measurement tasks ahead.

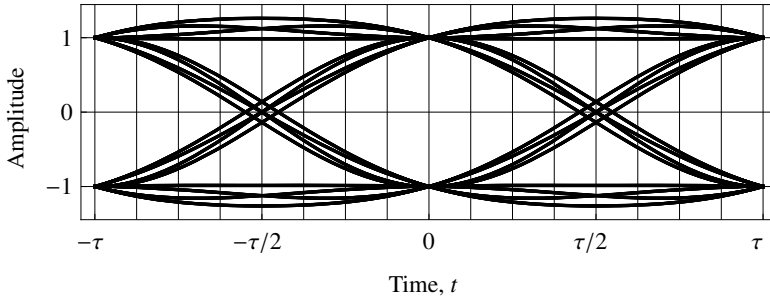


Fig. 5.8: Eye diagram of the output signal of a hypothetical analogue matched filter implementation in the absence of noise. Only the sampling instants at $t = k\tau$, $k \in \mathbb{Z}$ are free of ISI. Not hitting these instants exactly, due to coarse sampling of the waveform for instance, impairs the SNR of the recovered QPSK symbols.

Although the symbols that drop out of the clock recovery block are free of ISI, their carrier states are yet unknown. Unless transmitter and receiver are precisely synchronised, the four QPSK constellation points will spin around the centre of the state diagram with an angular speed proportional to the carrier frequency difference as illustrated in figure Fig. 5.9a. In order to counteract this effect, the receiver employs the “carrier recovery” block, which implements the digital second-order PLL described by Cupo and Gitlin [32]. The loop, also known as a Costas-loop, ensures that the recovered carrier states assume the familiar positions shown in Fig. 5.9b. The coefficients of the loop filter were adjusted manually for fast loop-acquisition and low susceptibility to noise.

Even with carrier synchronisation loop, there remains a rotational 90° uncertainty in the recovered QPSK symbols, which can only be resolved with the help of *training sequences* that are transmitted at regular intervals and that are known to the receiver. In the present system such a sequence is continuously transmitted for the purpose of SNR measurements.

The “estimation and combining” block in Fig. 5.1 operates on units of 512 QPSK symbols, which we shall call a “baseband block”. Each baseband block, which comprises 16 synchronisation sequences, is correlated with the known sequence and yields a result similar to the one shown in Fig. 5.5 earlier

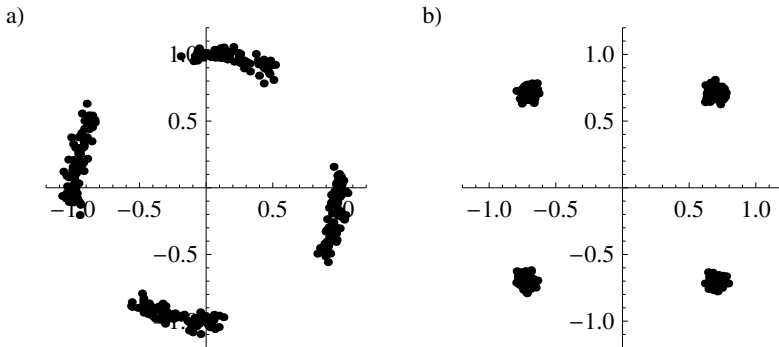


Fig. 5.9: Snapshot of 300 consecutive received QPSK carrier states before (a) and after (b) carrier recovery in the presence of additive noise.

on. By the *position* of the peak, the receiver knows the temporal relation of the received symbols. The 90° phase uncertainty of the carrier recovery loop is finally resolved by means of the *phase* of the peak.

Now that the receiver has an exact noiseless copy of the (noisy) received symbol stream, the signal power can be estimated from the noiseless copy and the noise power from the vector difference between the received symbols and the noiseless version. The SNR in each branch is thus easily established. As a final step, maximal ratio combining (MRC) between all branches is performed and the resulting SNR is estimated in a similar manner.

The receiver branches each have an SNR dynamic range of about 40 dB. At SNRs below -8 dB, the carrier recovery loop loses lock. Above 32 dB, noise of non-thermal origin, e.g., quantisation noise and clock jitter, begins to prevail, and eventually limits the measurable SNR span.

For later analysis, the following information about every baseband block is stored to the hard disk drive:

- Complete complex output of the carrier recovery loop including noise but after resolution of the abovementioned 90° uncertainty.
- Index of the first sample within the synchronisation sequence.
- Estimated SNR of each receiver branch.

- Estimated SNR of the combined stream.
- Phase state information of the carrier recovery loop of each branch. Together with the SNR information, this lets us reconstruct the complex received signal envelope vector \vec{b}_R , and subsequently estimate the complex covariance matrix \tilde{H}_R (4.10).

In spite of numerous manual optimisations, the amount of processing described in this section cannot be handled by even the fastest “single-core” consumer PCs available at the time of writing. A major challenge was therefore the manual parallelisation of the receiver architecture to multiple processors. To this end, the various parts of the receiver chain are assigned to different processors: processor 1 performs USB reads and matched filtering. Processor 2 is responsible for clock recovery. And processor 3 performs carrier recovery and SNR estimation. Baseband blocks are then passed on through these different stages. Once processor 1 has finished its work on the first baseband block, it can hand it on to processor 2 and *immediately* begin work on the next baseband block in line—and so on. Thus, three processors are kept busy at a time, and the workload that cannot be handled by a single processor alone is shared between multiple processors.

An Intel “Core2 Quad Q9450” based machine with four cores, i.e., essentially four processors, was used to run the measurements. The source code of the PC part of the receiver implementation comprises more than 2300 lines of C++ source code.

5.1.4 The graphical user interface

In addition to the possibility of storing the received baseband data to disk, a graphical user interface (GUI) was developed to provide visual feedback to the operator while the measurement is being conducted. Monitoring information about the received waveforms proved to be a valuable aid not only for the development of the receiver firmware and software, but also for the measurements. The GUI thus saved tens of hours of needless measurements because errors due to broken coaxial cables, short circuits between the ground plane and the radiators of an antenna array, as well as interference from nearby wireless local area network (WLAN) access points were identified the moment they happened and not during the later evaluation of the SNR data.

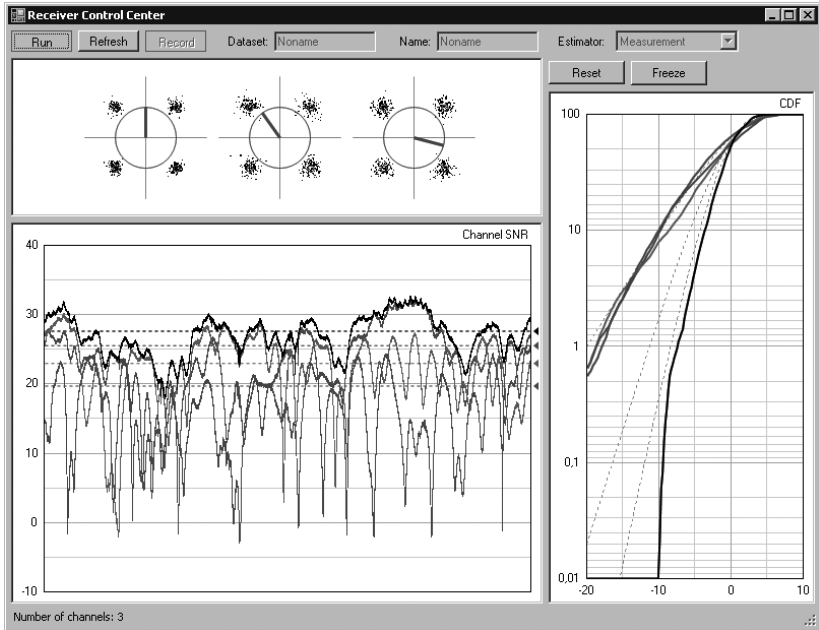


Fig. 5.10: Screen shot of the graphical user interface (GUI) of the receiver software.

The screen shot in Fig. 5.10 reveals that the GUI is divided into three different sections: the top left section displays not only the recovered carrier states of the received QPSK symbols of all branches but also the phase states of the carrier recovery loops, i.e., the relative phase delays between the individual branch signals. Directly beneath is the display of the estimated branch SNRs and the combined SNR as they vary with time. The diagram to the right constructs the CDFs of the SNRs and draws them along with the theoretical graphs of up to four branches. These CDFs represent rough approximations that allow the operator to check quickly the order of diversity during the measurement. A more precise evaluation of the SNR data after the entire measurement is nonetheless indispensable.

The GUI includes a visual indicator of the rare event that a USB transmission error, which disrupts the synchronisation between the receiver branches, has occurred. In this case, the measurement must be repeated. Also included

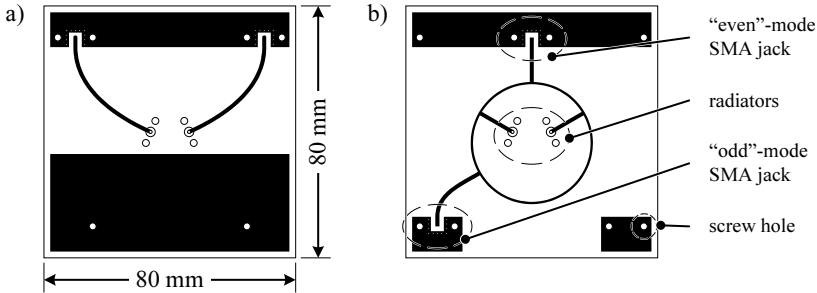


Fig. 5.11: Printed circuit boards (PCB) used as feed networks for a two-element $\lambda_0/10$ array. Network (a) feeds the radiators directly, whereas network (b) decouples the radiators. Matching of the “odd”-mode is accomplished manually with small strips of copper foil.

is a means to specify a destination file name for storing the received data. These file names are numbered automatically for consecutive measurements. Finally, the GUI offers a choice between two acquisition modes, namely the SNR measurement mode discussed so far, as well as a special mode for user data transmission (e.g., music) implemented for live demonstration purposes. The GUI automatically detects and adapts to the number of receiver branches connected to the PC. Its implementation is another 1200 lines of C# code.

5.2 Benefits of decoupling and matching networks

The first diversity measurements were conducted before any of the diversity theory of Chapter 4 had been developed. At that time, the mere goal was to provide evidence that decoupling and matching networks (DMN) can in fact improve diversity reception in practical systems [143].

To this end, arrays with radiator separations $\lambda_0/5$, $\lambda_0/10$, and $\lambda_0/20$ were manufactured. Two types of feed networks were designed, one feeding the radiators directly (Fig. 5.11a), and a decoupling-network based on a rat-race hybrid coupler (Fig. 5.11b, cf. Section 3.3.1). Rogers RO3203 was used as the substrate with a thickness of 0.5 mm, $\epsilon_r = 3.02$, and $\tan \delta = 0.0016$ [134]. The networks can be bolted to an aluminium ground plane with the monopole radiators sticking out on the other side in the manner of Fig. 2.6 on page 31. In both Figs. 5.11a and b, the radiators are situated at the centre of the network.

The networks feature surface-mounted SMA jacks, and are connected to the receiver branch modules via coaxial cables.

The hybrid coupler decoupling method was chosen for its simplicity because the decoupling part of the network can be manufactured independent of the scattering parameters of the antenna array. The “odd” port was matched manually with thin strips of copper foil as shunt open-stubs. No matching networks were implemented at the “even” port, as its return loss was already better than 10 dB at all radiator separations.

Two additional antennas were fabricated for reference: one single monopole and a $\lambda_0/2$ -spaced two-port monopole array. In order to carry out the measurements and to produce a time-varying multi-path environment, the antenna arrays and the PC were placed on a trolley and moved along a corridor. The transmitter was located in an office adjacent to that corridor with no (optical) line-of-sight to the receiver. Each antenna array under test was manually moved eight times over a distance of about 7 m along roughly the same path with the radiators oriented in the vertical polarisation. For every antenna array, four measurements were taken with the line of the array aligned with the direction of movement and another four were taken with the arrays perpendicular to the direction of movement. This way each antenna array produced about 9 minutes of recorded baseband data and SNR information.

In order to obtain a range of SNR values that is more intuitive to work with, the same normalisation as in the theoretical analysis of the previous chapter was applied (4.10), i.e., the SNR data of each antenna array was normalised to the mean SNR of the single-element antenna that was measured for reference. To assess the diversity performance of the antenna arrays further, the cumulative distribution functions (CDFs) $d(\varrho)$ (see Section 4.2.3) of the received SNRs were estimated. This was accomplished by means of the definition of the CDF: for some given SNR value ϱ the number of SNR samples less than or equal to ϱ was counted, and the results subsequently normalised so that $d(\infty) = 1$.

Figure 5.12 shows the graphs of the CDFs of the antenna arrays without DMN. Also shown is the CDF of the single-radiator measurement (thin solid line), which is in excellent agreement with the theoretical graph of Rayleigh fading (thin dotted line). This is a clear indication that the measurement environment was in fact sufficiently rich in multi-path to produce a complex Gaussian distribution of the received signal envelopes, and that no line-of-sight component was present.

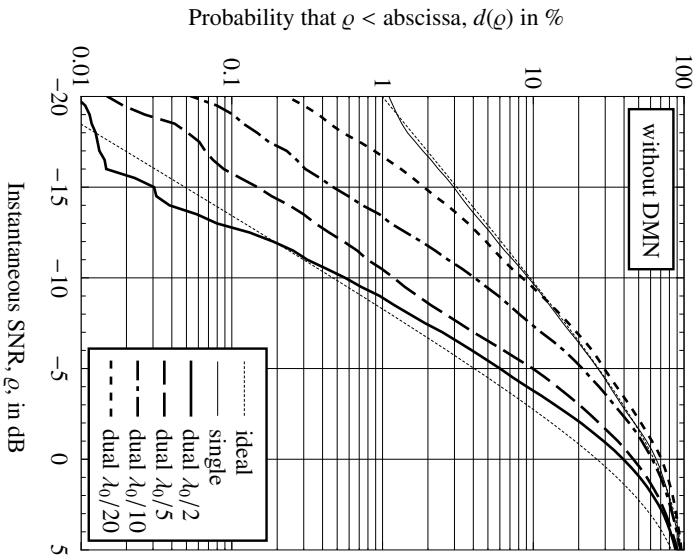


Fig. 5.12: Comparison between two-port antenna array with different radiator spacings and without decoupling and matching network (DMN).

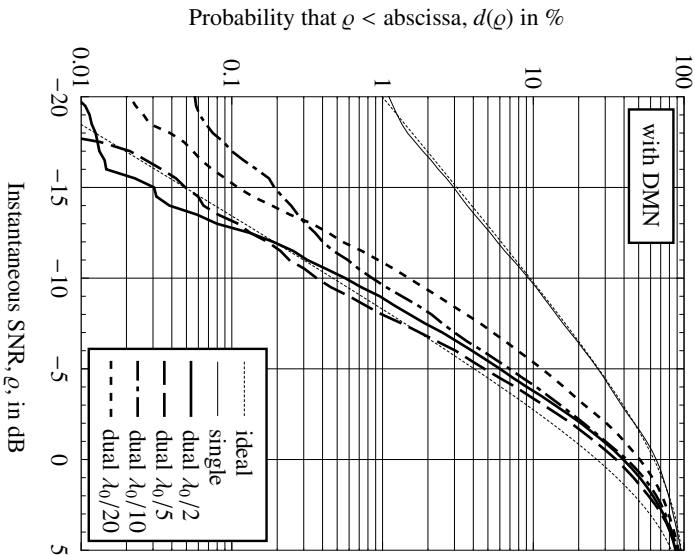


Fig. 5.13: Comparison between two-port antenna array with different radiator spacings and with DMN.

If we look at the CDF of the $\lambda_0/2$ array, on the other hand, we have to admit that it deviates considerably from the graph of ideal two-branch diversity. Since mutual coupling is small at this radiator separation, the cause of this discrepancy must lie elsewhere. Before we discuss possible reasons, let us first continue with a qualitative analysis of the remaining antenna arrays.

The figure reveals that the mutual radiator coupling present in the $\lambda_0/5$, $\lambda_0/10$, and $\lambda_0/20$ arrays substantially degrades diversity reception; with decreasing radiator separation the graphs move in the direction of lower SNR values. The degraded CDFs run in parallel to the theoretical graph of two-branch diversity at low probability levels as anticipated by the discussion of the diversity loss in Section 4.2.4. Only the measured graph of the $\lambda_0/2$ -array deviates from this behaviour. However, this can be attributed to the immanent statistical uncertainty at lower probability levels: without resorting to a rigorous uncertainty analysis here, we can reason that an outage probability of 0.1 % implies that the corresponding part of the CDF graphs is based on this very fraction of the entire measurement data. At a total measurement duration of 540 s this corresponds to a mere half of a second.

For the rather strongly coupled $\lambda_0/20$ array, the impairments are also evident in the plots in Fig. 5.14a of the SNR variations against the distance moved. The close proximity of the radiators essentially causes them to behave like a single radiator: both diversity branches show very similar, i.e., correlated, fading characteristics. This is also reflected in the CDF graph, which follows the graph of the single radiator at higher outage probabilities. The diversity gain at lower probabilities comes about because the rare event of a deep fade occurs at slightly different instants in the two branches (e.g., at around $x = 2.2$ m in the figure), or differs in depth (e.g., $x = 4.7$ m).

Figure 5.14b conveys the effect of the network, where clearly the two branches exhibit independent fading. Further inspection reveals that the second branch, which was connected to the “odd” port of the DMN, has a lower mean SNR than the first one due to ohmic losses in the network. This behaviour is not so evident at the right end of the graph because the first branch becomes limited by the dynamic range of the receiver.

The CDFs in Fig. 5.13 of the decoupled and matched antenna arrays more explicitly portray the improvements brought about by the DMN. All graphs have moved towards higher SNRs with respect to the graphs without DMN. Note that the graphs of the single antenna and the $\lambda_0/2$ antenna array are the same as in Fig. 5.12. At $\lambda_0/20$ the additional diversity gain brought about

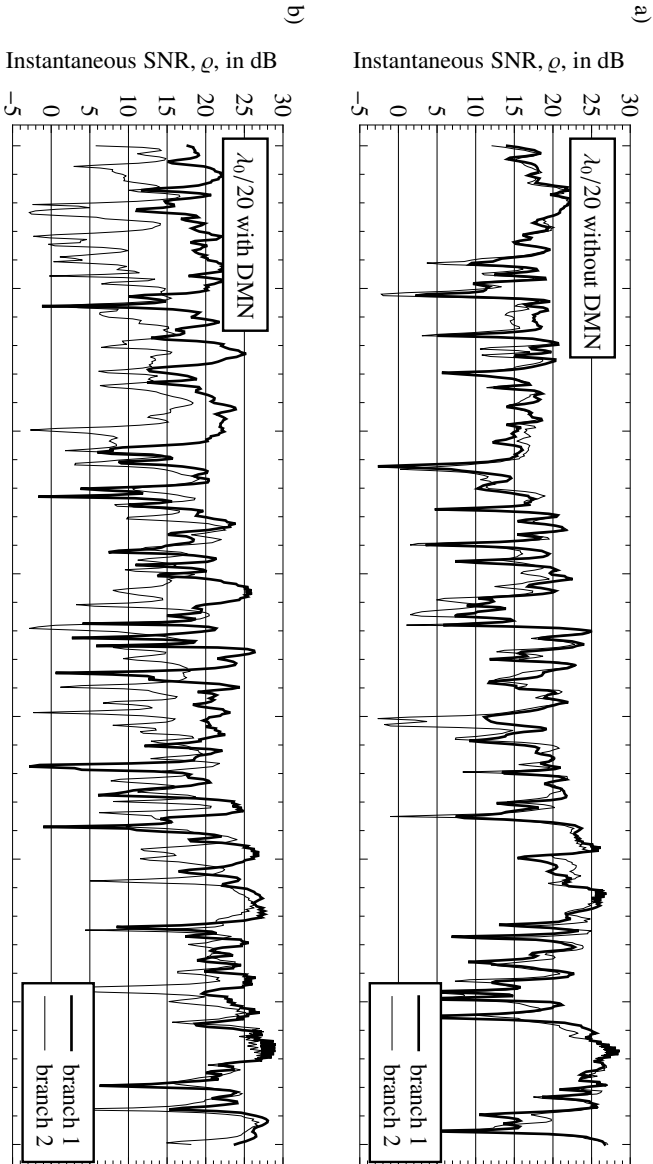


Fig. 5.14: Recorded SNR fading data of the two diversity branches of the $\lambda_0/20$ antenna array without (a) and with (b) decoupling and matching network. The graphs in (a) reveal considerable correlation between the branches whereas the graphs in (b) do not.

Separation d/λ_0	Eigenefficiencies				Diversity gain	
	without DMN $\lambda_1^{(\text{even})}$	$\lambda_2^{(\text{odd})}$	with DMN $\lambda_1^{(\text{even})}$	$\lambda_2^{(\text{odd})}$	due to network Measurement	Prediction
1/2	0.93	0.92	n/a	n/a	n/a	n/a
1/5	0.94	0.61	0.93	0.92	2.5 dB	0.89 dB
1/10	0.88	0.25	0.87	0.81	4 dB	2.5 dB
1/20	0.80	0.088	0.79	0.52	6 dB	3.9 dB

Table 5.1: Eigenmode data of the antenna arrays under test and comparison between measured and expected diversity gain improvements due to the network.

by the network at the 1 % outage level is around 6 dB, as estimated from the graphs. At $\lambda_0/10$ the gain is about 4 dB, and at $\lambda_0/5$ the DMN gain is still 2.5 dB. These numbers demonstrate that DMNs can in fact lead to noteworthy improvements in practical communications systems.

5.3 Verification of the diversity figures of merit

In Fig. 5.13, it appears that the $\lambda_0/5$ antenna array with DMN performs slightly better than the uncoupled $\lambda_0/2$ reference array. This observation does call the usefulness of the idea of using scattering parameter measurements for diversity performance estimation into question; the derivations of the previous chapter state that a mutually coupled antenna array—with or without DMN—cannot be better than an uncoupled array unless there are other factors influencing diversity, e.g., the statistics of the communications environment.

To help investigate this issue, Table 5.1 lists the eigenefficiencies of the antenna arrays without and with the DMN. Because the scattering parameters of the feed networks cannot be measured reliably due to the absence of appropriate RF connectors at both ends of the network, the numbers are partly based on simulations. The procedure was as follows: first, the direct feed network of Fig. 5.11a was simulated taking conductor and substrate losses into account. Then, the scattering parameters of the antenna arrays including this feed network were measured. Since the scattering parameters of the feed network were known from the simulations, the scattering parameters of the

antenna array *itself*, i.e., without the network, could be de-embedded. The eigenefficiencies in the second and third column of the table were thus evaluated using (3.16).

In a next step, the decoupling network of Fig. 5.11b was loaded into an electromagnetic simulator [122], amended with a single-stub matching network at the odd-port, and, together with the array's scattering matrix obtained in the previous step, optimised for impedance match. The simulation thus yielded an estimate of the four-port scattering matrix of the DMN, and finally for the eigenefficiencies in the fourth and fifth column of the table.

From these numbers, the theoretical diversity loss (4.28) can be calculated if we recall that the determinant of the matrix \tilde{H} is the product of the two eigenefficiencies. The differences between these diversity loss numbers finally yield the diversity gain improvements due to the DMNs. They are reported in the rightmost column of Table 5.1. The numbers in the "Measurement" column were estimated from the CDF plots.

The great disagreement between the theoretical gains and the measured ones is obvious. This impression is reinforced by the fact that, according to Section 4.3.2, the theoretical figures constitute optimistic estimates. Moreover, these discrepancies cannot simply be attributed to the possible influence of the communications environment, because the network gain was shown to be independent thereof.

As it turned out, a subtle shortcoming of the measurement setup is responsible for this large mismatch between theory and practice. Let us inspect Fig. 5.15, which shows a photograph of the trolley on which the receiver setup was moved along the corridor. On the top surface, there is the receiver with the two monopole-antennas, a power supply unit, a flatscreen monitor, and keyboard and mouse. The PC itself was placed on the bottom shelf of the trolley. The operator stood on the left-hand side in the picture and pulled the trolley in the direction indicated by the arrow.

During the measurements, the transmitted signal not only reflects off the corridor walls, but also off parts of the receiver equipment, most notably the metal parts of the trolley, the flatscreen monitor, and the operator moving the trolley. Put another way, these objects become part of the antenna array and effectively disturb its radiation characteristics. Every time the antenna array or its feed network was replaced, the relative positions of these objects changed, and so did the characteristics of the antenna array. Moreover, the data acquisition took two days to complete, so on the second day the measurement



Fig. 5.15: Mobile trolley carrying the receiver setup. The arrow indicates the position of the operator and the direction of movement. The photograph was taken from inside the office where the transmitter was situated.

setup could have been a different one altogether.

The following examples conducted specifically to investigate the connection between array scattering parameters and diversity performance, reveal the dramatic effects these additional scatterers have on the quality of the recorded fading data [145]. For the upcoming measurements, only the array and the receiver front-end were placed on the top surface of the trolley; everything else was put on the bottom shelf. In addition, the operator made sure to keep his body as far down as possible during data acquisition in order to minimise his interaction with the antenna array under test.

To produce a reasonably uniform communications environment seen by the antenna array, twelve measurements were carried out for each array. Between measurements, the arrays were successively turned by 30° . This procedure even reflects a realistic scenario if we imagine a mobile phone user on the corridor walking and turning around freely. Of course, this only ensures uniformity in azimuth and not in elevation.

Another reason for rotating the arrays between measurements has to do

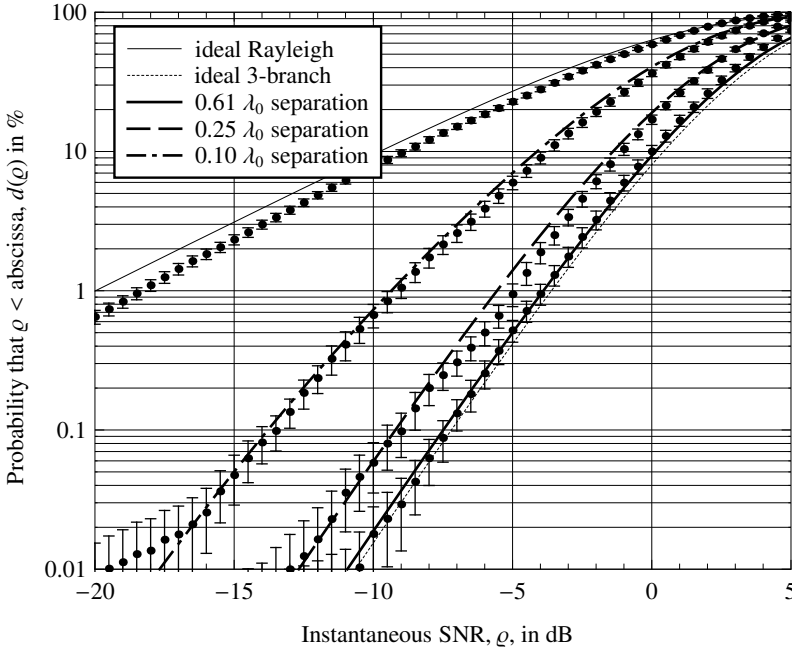


Fig. 5.16: Theoretical (lines) and measured CDFs (dots) of a single radiator and various three-port monopole arrays. Error bars indicate the estimated standard error.

with directions of preference both of the communications environment and of the antenna array. Suppose a satellite communications link with a dish antenna, where, due to its high directivity, small alignment errors cause large variations in the received SNR. If we recall the strong angular dependence especially of the “odd” and the “ π ”-mode beam patterns of a three-port array (Fig. 2.8, page 34), we can imagine similar effects in the present scenario, albeit less pronounced. Rotating the antenna arrays by a full 360° minimises any systematic errors introduced by misalignment. A test measurement was conducted that undeniably showed that rotating the antenna array alone, i.e., without removing the aforementioned scatterers in its proximity, has no bearing on the stark discrepancies listed in Table 5.1.

The corridor, where the measurements were carried out, leads to a stair-

case. For the new measurements, the transmitter was set up on the floor below at the bottom of that staircase. The first set of measurements compares the performances of three three-port antenna arrays with radiator spacings of $0.61 \lambda_0$, $0.25 \lambda_0$, and $0.10 \lambda_0$, respectively. Figure 5.16 shows the measured CDFs (dots) along with the theoretical graphs calculated from the scattering matrix of the antenna array (thick graphs with various patterns) using (4.22).

Since the measured CDFs represent the average of several measurements, the figures include estimates of their standard error (estimate of the standard deviation of the mean-estimate) as error bars. The interpretation of the standard error is as follows: if the same measurement is repeated an infinite number of times, 68 % of them will likely include the true mean within the interval defined by their standard error. We must keep in mind, however, that the standard error is an estimate itself, and is based on a number of assumptions. Most notably, it requires the measurements to be repeatable and independent. Neither is true in our scenario, because the antenna arrays were rotated between measurements (i.e., the setup was changed), and because all measurements followed similar paths along the corridor (i.e., they are dependent). The error bars must therefore not be considered a rigorous statistical measure but rather an indicator for the factual deviations in a particular set of measurement data.

In contrast to the previous results of Fig. 5.12, we observe considerable differences of up to 2 dB between the new single-radiator reference measurement (thin, solid line) and the theoretical graph of Rayleigh fading. Since the theoretical graph lies far beyond the error bounds of the measurement, it is unlikely that this deviation is caused by purely random effects. A possible explanation is that the new communications environment was not entirely free of a line-of-sight component so that the received SNR did not exactly follow the Rayleigh distribution. (cf. Dietrich et al. [35, Fig. 6b])

On the other hand, the plots of the three-port antenna arrays (thick lines) show remarkable agreement with the predicted distributions on a quantitative level. Although the $0.25 \lambda_0$ measurement deviates from the theoretical graph around $p = 1 \%$, the fit is close both at the low and at the high end of the probability range.

Next, the $\lambda_0/20$ two-port array measurements of the previous section, without and with DMN, were repeated with the new measurement setup. The obtained graphs in Fig. 5.17 not only draw a completely different picture compared with Figs. 5.12 and 5.13 but, this time, they also conform well to the predicted CDFs, mostly at higher probability levels. The measured additio-

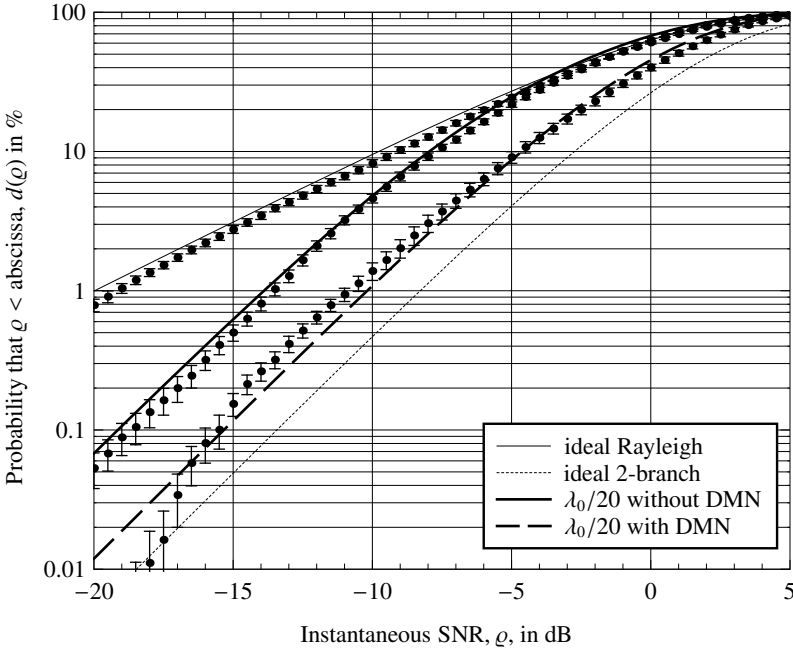


Fig. 5.17: Calculated and measured CDFs for a $\lambda_0/20$ two-port monopole array without and with DMN in relation to a single monopole.

nal diversity gain brought about by the network is now consistent with the predicted value of 3.9 dB in Table 5.1.

Although the new reference measurement lies closer to the theoretical Rayleigh graph than the previous one in Fig. 5.16, the discrepancy again cannot be explained by the estimated standard error. So, this observation supports our previous suspicion that the environment may not be completely free of a line-of-sight component. The graphs of the antenna arrays, on the other hand, raise doubts as to the expressiveness of the standard error. Both measurements employed the same radiating structure; the only difference was the absence or presence of a DMN, which should manifest itself as a mere horizontal shift in the graphs. However, both graphs exhibit significant deviations from the theoretical CDF in *opposing* directions, yet this is not accounted for

by the magnitude of the standard error. The interquartile range (not shown) of the acquired data shows similar behaviour: strong bias away from the theory, but no indication that the measurements are especially uncertain in the region of interest. Aside from purely random variations, it seems additional factors affect the quality of the measurements. These may include the position of the person operating the trolley (although it was attempted to minimise the effect) and the path along the corridor chosen.

One last example is presented in Fig. 5.18 where the performances of planar inverted-F antenna arrays (PIFA array, photograph see Fig. 5.19) without and with DMN are compared. Since no reliable scattering parameters of the DMN were available, the theoretical plots are based on the matrix \tilde{H}_{rad} , i.e., on the measured far-field patterns of the array (see (2.26)). Apart from deviations at lower probability levels, the agreement with the predicted graphs is excellent. The diversity gain due to the DMN is about 1.7 dB according to both the measurements and the theory.

In summary, the above results demonstrate a number of important aspects of diversity reception with compact arrays. They show the severe negative impact of mutual radiator coupling on the received signal strength and verify the beneficial effects of decoupling and matching networks in the context of a practical receiver system. Most importantly, they reveal the close consistency between the theoretically predicted and the measured SNR distributions in a realistic communications scenario, and thus emphasise the practical value of the diversity figures of merit developed in the previous chapter.

5.4 Measurements of the signal envelope covariance matrix

The CDF graphs are not the only information we can extract from the acquired baseband data. Knowing the received signal SNR in both amplitude and phase essentially means knowing the complex received signal envelope vector \vec{b}_R introduced in Fig. 4.1 up to a constant factor. The received signal covariance matrix \tilde{H}_{env}^T is then estimated by approximation of the expectation operator in (4.31) via the sample mean, i.e.,

$$\tilde{H}_{\text{env}} = \text{E} \{ \vec{b}_R \vec{b}_R^H \}^T \approx \frac{1}{N} \sum_{k=1}^N \vec{b}_R^*[k] \vec{b}_R^T[k]. \quad (5.1)$$

The sample index is denoted by k , and N is the total number of samples acquired. For comparison with the theoretical matrix $\tilde{H}_{\text{acc}} = \tilde{I} - \tilde{S}^H \tilde{S}$, \tilde{H}_{env} is

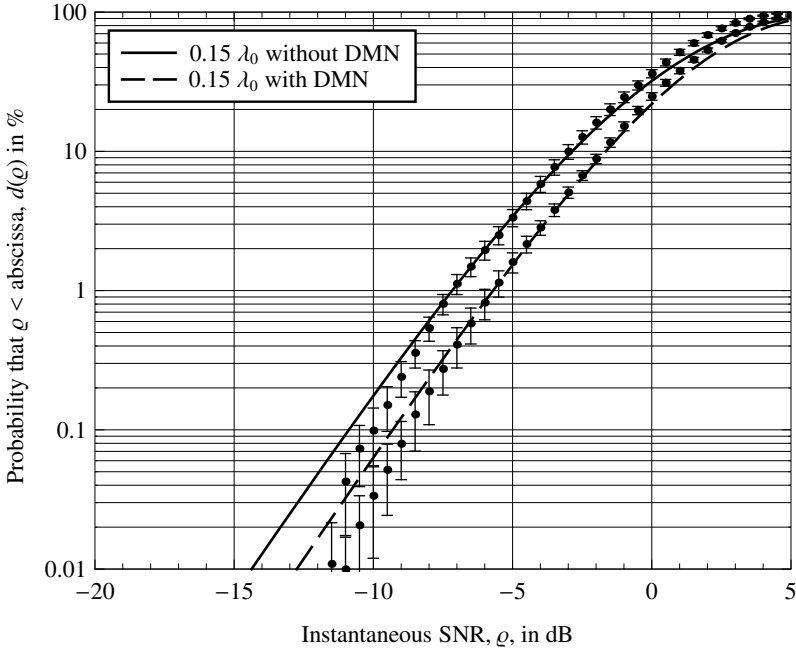


Fig. 5.18: Calculated and measured CDFs of the $0.15\lambda_0$ three-port planar inverted-F antenna (PIFA) array in Fig. 5.19 without and with DMN.

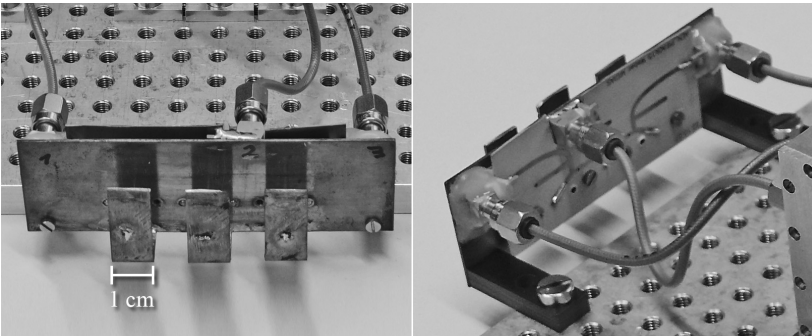


Fig. 5.19: Photographs of the planar inverted-F antenna (PIFA) array under test [121].

Antenna array under test	— Diversity Loss, L_d , in dB —		
	Prediction	Measurement	Difference
3-port, $0.61\lambda_0$	0.29	0.38 ± 0.12	-0.086
3-port, $0.25\lambda_0$	2.1	1.7 ± 0.12	0.39
3-port, $0.10\lambda_0$	7.5	7.0 ± 0.15	0.49
$\lambda_0/20$ w/o DMN	5.8	5.3 ± 0.22	0.50
$\lambda_0/20$ w/ DMN	1.9	1.3 ± 0.20	0.65
DMN gain:	3.9	4.1 ± 0.30	-0.14
PIFA w/o DMN	3.8	3.5 ± 0.16	0.31
PIFA w/ DMN	2.1	2.3 ± 0.083	-0.15
DMN gain:	1.7	1.2 ± 0.18	0.46

Table 5.2: Overview of the diversity loss L_d as calculated from the matrix $\tilde{H}_{acc} = \tilde{I} - \tilde{\xi}^H \tilde{\xi}$ or \tilde{H}_{rad} (for the PIFA array) and the covariance matrix \tilde{H}_{env} estimated from measured envelope data. The measured values include the estimated standard error.

Antenna array under test	— Eigen efficiencies —			
	Prediction		Measurement	Standard error
3-port, $0.61\lambda_0$	0.97	0.94	0.89	1.1 0.90 0.82
3-port, $0.25\lambda_0$	0.95	0.94	0.27	0.96 0.83 0.40
3-port, $0.10\lambda_0$	0.87	0.57	0.012	0.90 0.66 0.014
$\lambda_0/20$ w/o DMN	0.93	0.074		1.1 0.078
$\lambda_0/20$ w/ DMN	0.79	0.52		0.86 0.65
PIFA w/o DMN	0.77	0.74	0.13	0.63 0.57 0.25
PIFA w/ DMN	0.74	0.70	0.45	0.84 0.56 0.45

Table 5.3: Overview of the eigen efficiencies of the predicted covariance matrix $\hat{H}_{\text{acc}} = \hat{I} - \hat{S}^H \hat{S}$ or \hat{H}_{rad} (for the PIFA array) and the measured covariance matrix \hat{H}_{env} . The measured values include the estimated standard error.

normalised to the mean received power of the corresponding single-radiator measurement.

Table 5.2 summarises the diversity losses (4.28) predicted from the matrices $\hat{H}_{\text{acc}} = \tilde{I} - \tilde{S}^H \tilde{S}$ or \hat{H}_{rad} (for the PIFA arrays) in comparison with the values obtained from the measurement-based matrices \hat{H}_{env} . The numbers in the table are derived from the same sets of data as the CDF plots of the previous section. The estimated standard error is also shown and is generally below 0.3 dB.

The maximum difference between measured and predicted diversity loss is with the decoupled and matched $\lambda_0/20$ array and amounts to about 0.65 dB. This corresponds to an uncertainty in the linear diversity loss of around 16 %. The disagreement between most pairs of values again cannot be explained by the standard error alone. On the one hand, most measured diversity losses are smaller compared with the theoretical ones, i.e., according to the measurement most arrays perform better than predicted. On the other hand, this is in contrast to the CDF graphs, where, strictly speaking, the measured arrays perform worse than predicted when compared with the *single-radiator* measurement. Furthermore, given that the influence of a DMN ought to be independent of the communications environment, the measurements of the $\lambda_0/20$ and the PIFA array strongly suggest that the error is non-systematic: whereas the measured and the predicted DMN gains show excellent agreement for the $\lambda_0/20$ array, the discrepancy is rather large for the PIFA array. Judging by the corresponding CDF graphs, though, we would probably consider the PIFA measurement more accurate than the $\lambda_0/20$ measurement.

Table 5.3 lists the eigenvalues (eigen efficiencies) of the corresponding covariance matrices. Since we interpreted the effect of a non-uniform communications environment as an uneven distribution of received signal power over the array eigenmodes (cf. Section 4.3), we would certainly tolerate any disagreement between theory and practice, but, at the same time, would expect some consistency in these deviations. This is not the case, particularly with the PIFA arrays. Without DMN the measured “ π ”-mode eigen efficiency is almost twice the predicted value, whereas with DMN the “ π ”-mode values conform exactly, although both arrays only differ in their feed network and therefore possess the same beam-pattern space. Similar contradictions exist between the $0.25\lambda_0$ and the $0.10\lambda_0$ array and in fact between all arrays, albeit to a far lesser extent.

We can now conclude that the observed deviations both in the envelope

covariance matrix as well as in the CDF graphs cannot be explained by statistical uncertainty alone. Yet the errors seem arbitrary and in this way do not suggest a general and reproducible bias in the diversity theory or the formulae derived from it. Instead, the measurements manifestly support the practical applicability of scattering parameter measurements for the evaluation of the diversity performance of mutually coupled antenna arrays. This applies to the effects of the antenna arrays themselves as well as to the evaluation of DMNs based on simulated network data.

On a final note, we must keep in mind that, between measurements, the antenna arrays were rotated in order to achieve a uniform power distribution in the azimuth plane. The elevation angle, on the other hand, certainly experienced a non-uniform power profile, which violates the basic prerequisite of the diversity gain and loss formulae of the previous chapter. The measurements nonetheless conform well to the theory. The reason is that we compare antennas and antenna arrays that exhibit similar far-field characteristics and thus similar focusing properties over elevation. That is, monopole arrays are compared with a monopole antenna and the PIFA array is compared with itself without and with DMN. If we investigated the performances of antenna arrays with greatly differing focusing properties, we could expect considerable disagreements. The reason why no comparison between the PIFA and the monopole arrays is given at this point is because the measurements were carried out on different days and no reference data for the PIFA is available. Even if the measurements agreed, we would not learn anything from it, because such an agreement would contradict the theoretical expectation and would therefore likely be caused by happenstance. Still, this discussion is irrelevant to the fact that the diversity loss calculated from the scattering matrix is a measure for the system loss due to port coupling independent of any other factors that influence the absolute diversity performance of the system. For comparisons between different types of arrays, Section 4.3.1 explains how the statistics of the environment can be included in the calculations on the basis of widely accepted channel models.

5.5 Front-end noise characterisation

During the derivation of the diversity model in the previous chapter, we found that diversity performance is governed not only by the correlation properties of the received signal power but also by the correlation and the amount of

noise present in the received waveforms. The reason why we could nonetheless interpret the diversity measurements without spending a thought on receiver noise is that the receiver with its noise figure of 12.2 dB belongs to the class of very noisy front-ends discussed in Section 4.4.4. That is, the noise created internally within the receiver is so strong that it covers up any noise produced at the front-end inputs. The temperature covariance matrix of the received noise \tilde{T}_R (4.48) is thus a constant and as such independent of the antenna array or the network connected to the system inputs.

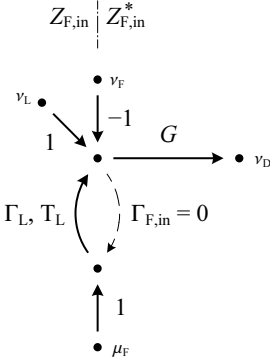
Section 4.4.4 also revealed that, in the case of a low-noise front-end, the SNR diversity gain due to a DMN is often less than its signal gain (4.37) alone, as the result of the noise floor created by ohmic losses in the network. In the present section, we will therefore pursue a reduction of the receiver noise-figure with the help of fabricated low-noise pre-amplifiers. We will then develop and verify a detailed noise characterisation procedure that will subsequently allow us to calculate the SNR performance of practical low-noise receivers for a variety of antenna arrays and DMNs.

Three different low-noise amplifiers (LNA) were designed in order to have different sets of noise parameters at hand for comparison later on. The first amplifier is based on the BFP640 bipolar NPN transistor manufactured by Infineon [130]. This transistor is a good starting point for a decent low-noise amplifier because it is straightforward to bias and to stabilise, and happens to be noise-matched to $50\ \Omega$ at the 2.45 GHz centre frequency without the need for a matching network. The final design exhibits a noise figure of 1 dB and an insertion gain of 16.5 dB.

The second LNA employs the NE3515S02 hetero-junction field effect transistor (HJ-FET) manufactured by NEC Electronics Corporation [133]. A charge pump integrated circuit negates the supply voltage and, after additional stabilisation and filtering, provides the negative gate-voltage for biasing. Because the transistor is very unstable up to high frequencies, a combination of broadband and selective stabilisation techniques was employed. The final amplifier also displays a gain of 16.5 dB with a noise-figure between 0.3 dB and 0.5 dB, depending on the measurement equipment used. A matching network was implemented to noise-match the transistor to $50\ \Omega$.

A third amplifier was manufactured using the ready-made HMC478 amplifier integrated circuit provided by Hittite Microwave Corporation [129]. Its gain is 16 dB with a noise figure of 3 dB. All three amplifiers are placed in an aluminium chassis to shield them from external interference and noise.

a)



b)

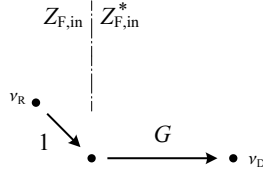


Fig. 5.20: Signal flow graphs for the discussion of the front-end noise characterisation procedure. (a) Full signal flow graph and (b) simplified signal flow graph. The subscript “L” identifies quantities related to the load connected to the front-end.

Further implementation details on these LNAs can be found in [117]. The fact that all amplifiers are noise-matched to $50\ \Omega$ is an important one because this causes all previous antenna array and DMN designs, which we optimised with respect to $50\ \Omega$ from a *power* matching perspective, to be noise-matched to the receiver front-end.

5.5.1 Noise characterisation of a single receiver-branch

We proceed with the practical characterisation of the amplifiers’ noise properties when connected to the receiver channels. Commercial noise characterisation equipment is of no use since the receiver has no output terminal that we could connect to the measurement instrument. In the following, the receiver is therefore device under test and measurement equipment at the same time. The goal is to have all information at hand necessary to predict the noise covariance matrix of a given receiver front-end upon connection to a mutually coupled antenna array with known scattering matrix.

Figure 5.20a shows the signal flow graph of a single noisy front-end branch (subscript “F”) connected to a noisy single-port load (subscript “L”).

The front-end is characterised by its equivalent noise waves ν_F and μ_F , and some internal linear gain, denoted by G . All quantities in the graph are normalised to the front-end input impedance $Z_{F,\text{in}}$, which can be determined with a vector network analyser. As we know from previous discussions, this normalisation procedure simplifies the signal flow graph by elimination of a loop. The load, which we assume passive, is fully described by its reflection coefficient Γ_L and the noise wave ν_L .

Following Section 4.4 and Appendix B.2 we can express the noise wave power in terms of the equivalent temperature T_L of the load, which in our case corresponds to its physical temperature [118, Eqn. (2.94)]:

$$\text{Var}\{\nu_L\} = \text{E}\{\nu_L \nu_L^*\} = \text{E}\{|\nu_L|^2\} = kT_L B(1 - |\Gamma_L|^2), \quad (5.2)$$

where k is Boltzmann's constant, and B is the equivalent receiver noise bandwidth introduced in Section 4.2.1. A description of the front-end noise waves was given in (4.61) in terms of the equivalent front-end noise temperatures T_{ν_F} , T_{μ_F} , and $T_{\nu\mu_F}$. In contrast to passive devices, these quantities must be determined by measurements or simulations.

The above noise waves combine as wave ν_R in Fig. 5.20b, which then becomes amplified, down-converted to baseband, digitised, and finally *displayed* on screen as the expected value of the quantity denoted as ν_D . The constant $|G|^2$ is the factor of proportionality between the actual noise power $\text{E}\{|\nu_R|^2\}$ at the front-end input terminal and the power value $P_D = \text{E}\{|\nu_D|^2\}$ reported by the receiver software. In general, G is complex. We have

$$\nu_D = G\nu_R = G\left[\nu_L - \nu_F + \Gamma_L\mu_F\right], \quad (5.3)$$

and thus for the displayed noise power (cf. (4.62) and [4, (4.47)])

$$\begin{aligned} P_D &= \text{E}\{|\nu_D|^2\} \\ &= kB|G|^2\left[T_L(1 - |\Gamma_L|^2) + T_{\nu_F} + |\Gamma_L|^2 T_{\mu_F} - \Gamma_L^* T_{\nu\mu_F} - \Gamma_L T_{\nu\mu_F}^*\right], \end{aligned} \quad (5.4)$$

which is a function of the load reflection coefficient Γ_L . The receiver software approximates the expectation operator by an exponential moving average filter, and yields three stable significant digits after around 60 seconds of averaging. Since P_D is merely a number in computer memory, we can assign arbitrary power units to it. To keep the value of the internal gain G within

reasonable bounds it was decided that the readout is in fW, i.e., 1×10^{-15} W. The unknown constants G , $T_{\nu,F}$, $T_{\mu,F}$, and $T_{\nu\mu,F}$ are established via the measurement procedure outlined in the following.

The absolute value $|G|$ of the gain is found by the familiar Y-factor method, also referred to as the hot-cold method [16, Section 3.5]. This requires a switchable noise source with constant known terminal impedance (usually 50Ω) and two different known noise temperatures. The “cold” temperature $T_{L,cold}$ usually corresponds to ambient temperature but is often assumed 290 K.² The “hot” temperature $T_{L,hot}$ is specified by the (known) excess noise ratio (ENR) of the source according to

$$T_{L,hot} = (1 + \text{ENR})T_{L,cold}. \quad (5.5)$$

If we perform two noise power measurements $P_{D,cold}$ and $P_{D,hot}$, it is straightforward to show that the gain is given by

$$|G|^2 = \frac{P_{D,hot} - P_{D,cold}}{kB(T_{L,hot} - T_{L,cold})(1 - |\Gamma_L|^2)}. \quad (5.6)$$

Note that Γ_L is generally non-zero since the 50Ω impedance of the source is normalised as indicated in the flow graph. A method to determine the argument of G will be explained later.

Let us rewrite (5.4) with the remaining unknowns on the left-hand side and all known quantities on the right-hand side of the equal sign:

$$T_{\nu,F} + |\Gamma_L|^2 T_{\mu,F} - \Gamma_L^* T_{\nu\mu,F} - \Gamma_L T_{\nu\mu,F}^* = \frac{P_D}{kB|G|^2} - T_L(1 - |\Gamma_L|^2). \quad (5.7)$$

If we treat $T_{\nu\mu,F}$ and $T_{\nu\mu,F}^*$ as independent variables, the above is a linear equation in four unknown variables. In order to solve for the unknowns, we can establish a system of four such equations by conducting a series of measurements with different load impedances Γ_L . In fact, we can record more than four measurements and use the resulting over-determined system of equations

²Of course, this is not correct for most laboratory setups and correction methods exist for arbitrary ambient temperature. Since the resulting error is below 3 % at room temperature (say 296 K) we will refrain from such methods.

to smooth out any measurement errors. In matrix notation we have

$$\begin{pmatrix} 1 & |\Gamma_{L,1}|^2 & \Gamma_{L,1}^* & \Gamma_{L,1} \\ 1 & |\Gamma_{L,2}|^2 & \Gamma_{L,2}^* & \Gamma_{L,2} \\ \vdots & \vdots & \vdots & \vdots \\ 1 & |\Gamma_{L,N}|^2 & \Gamma_{L,N}^* & \Gamma_{L,N} \end{pmatrix} \cdot \begin{pmatrix} T_{\nu,F} \\ T_{\mu,F} \\ T_{\nu\mu,F} \\ T_{\nu\mu,F}^* \end{pmatrix} = \begin{pmatrix} \frac{P_{D,1}}{kB|G|^2} - T_L(1 - |\Gamma_{L,1}|^2) \\ \frac{P_{D,2}}{kB|G|^2} - T_L(1 - |\Gamma_{L,2}|^2) \\ \vdots \\ \frac{P_{D,N}}{kB|G|^2} - T_L(1 - |\Gamma_{L,N}|^2) \end{pmatrix} \quad (5.8)$$

$$\tilde{L} \cdot \vec{t} = \vec{m},$$

where \tilde{L} is the matrix of load reflection coefficients, \vec{t} the unknown vector of front-end noise temperatures, \vec{m} the vector based on the measured powers, and N the number of measurements. A solution that minimises the error

$$\|\tilde{L} \cdot \vec{t} - \vec{m}\|_2 \quad (5.9)$$

between the left-hand and the right-hand side is found with the help of the Moore-Penrose pseudo-inverse of \tilde{L} :

$$\vec{t} = \tilde{L}^\dagger \vec{m}. \quad (5.10)$$

If only $N = 4$ measurements are available, the Moore-Penrose pseudo-inverse is identical with the regular matrix inverse \tilde{L}^{-1} .

The precision of the solution is dependent on the particular set of load impedances chosen. Obviously, there is no point in determining the front-end noise temperatures based on $\Gamma_{L,i}$ that are all very similar, and subsequently expect the result to accurately extrapolate over the entire complex reflection coefficient plane (Smith-chart). We would therefore choose the $\Gamma_{L,i}$ as diverse as possible so they test a wide range of different load conditions. In mathematical terms, we would aim to minimise the condition number c of the matrix \tilde{L} . The condition number is the ratio of the largest to the smallest singular value of the matrix, and defines an upper bound on the factor by which the relative error in our solution \vec{t} possibly exceeds the relative error in our input data \tilde{L} and \vec{m} [3, p. 523], [8, Section 5.8]. Put differently, the base-10 logarithm of c is an upper bound on the number of decimal digits of precision that may become lost in the result.

Since the $\Gamma_{L,i}$ are normalised to and thus are dependent on the input impedance of the front-end, one set of loads that is suitable for one type of

front-end may be inappropriate for another if their input impedances differ greatly. For the characterisation of the amplifiers presented above, a set of eleven complex test impedances with $c < 8$ for all amplifiers was determined empirically and manufactured.

For the noise parameter extraction, each amplifier was connected to one of the front-end channels: the BFP640 was connected to channel one, the NE3515S02 to channel two, and the HMC478 to channel three. Then the magnitudes of the channel gains G and the noise temperatures were determined as outlined above. Table 5.4 lists the extracted noise parameters (the extraction of the phase of G is explained in a moment) of the *complete* front-end branches, i.e., the numbers include the noise generated by the pre-amplifiers as well as the noise of the remaining branch components. For this reason, the branch noise-figures listed in the last column are considerably greater than the noise-figures of the sole LNAs stated earlier. Based on the extracted model parameters, Table 5.5 compares the actual powers recorded to the predictions according to (5.4) for the test impedances. The maximum relative error between any pair of numbers is 1.2 %, which proves the validity of the noise model and the feasibility of the measurement procedure chosen.

5.5.2 Noise characterisation of the multi-port receiver

The amplifier data from the previous subsection can be implemented directly into the multi-port receiver formulae developed in Section 4.4 by filling the diagonal entries of the matrices $\tilde{T}_{v,F}$, $\tilde{T}_{\mu,F}$, and $\tilde{T}_{v\mu,F}$ with the noise temperatures of the corresponding amplifiers. The covariance matrix of the noise emitted by the load can be determined using (4.49). For various passive multi-port loads we would now like to investigate to what extent the received noise covariance predicted by (4.48) agrees with measurements. The only pieces of information still missing from the noise parameters are the phases of the internal receiver branch gains G_k .

For this, consider the diagonal *matrix* \tilde{G} (see Fig. 4.7), which contains the branch gains G_k on its main diagonal. The covariance matrix of the wave vector \vec{v}_D displayed by the receiver software is related to the covariance matrix of the received noise vector \vec{v}_R via

$$\text{Var}\{\vec{v}_D\} = \tilde{G} \text{Var}\{\vec{v}_R\} \tilde{G}^H. \quad (5.11)$$

Writing out the individual matrix elements and substituting the polar form

Amplifier	$Z_{F,in}$ in Ω	G in dB	Noise temperatures in K			NF in dB
			$T_{\nu,F}$	$T_{\mu,F}$	$T_{\nu\mu,F}$	
BFP640	$74.5 + j 18.0$	$70.9 \angle 0^\circ$	181	53.9	$24.3 \angle 135^\circ$	2.13
NE3515S02	$11.7 - j 7.0$	$73.2 \angle -60^\circ$	199	128	$123 \angle -5^\circ$	1.88
HMC478	$48.0 + j 26.0$	$67.9 \angle -46^\circ$	517	158	$62.8 \angle 80^\circ$	4.52

Table 5.4: Extracted noise parameters of the three front-end branches each equipped with one of the amplifiers.

Load impedance, $Z_{L,i}$, in Ω	— Displayed power, P_D , in fW —					
	BFP640		NE3515S02		HMC478	
	Meas.	Pred.	Meas.	Pred.	Meas.	Pred.
$0.6 + j 23.9$	33.0	33.1	78.1	78.5	46.7	46.6
$180 - j 119$	72.8	72.7	36.7	36.7	63.6	63.0
$38.8 - j 2.5$	72.8	73.1	86.4	87.4	64.2	64.0
$1.4 - j 65.2$	44.8	44.5	26.3	26.2	67.8	67.3
$0.4 + j 6.7$	32.7	32.9	165.0	165.0	48.1	48.3
$1.5 - j 54.0$	43.4	43.3	27.8	27.7	67.3	67.2
$13.1 + j 26.8$	50.1	49.7	95.0	94.0	52.8	53.1
$62.6 - j 7.5$	78.7	78.7	68.3	68.0	65.7	65.9
$2.32 + j 69.3$	37.3	37.3	32.6	32.9	48.0	47.8
$3.45 - j 106$	49.5	49.8	24.9	24.8	65.7	66.5
50.0	75.8	75.7	77.8	77.9	64.5	64.7

Table 5.5: Result of the noise characterisation procedure with eleven complex test impedances.

$G_k = |G_k|e^{j\varphi_k}$ of the branch gains yields

$$\text{Var}\{\vec{v}_D\}_{ij} = \left[|G_i||G_j| e^{j(\varphi_i - \varphi_j)} \right] \text{Var}\{\vec{v}_R\}_{ij}. \quad (5.12)$$

We notice that the absolute values of all elements of $\text{Var}\{\vec{v}_D\}$ are unaffected by the phases of the G_k . The elements on the main diagonal ($i = j$) remain real-valued (as is the case for any covariance matrix), and the phases of the off-diagonal elements are affected by the phase *difference* $\varphi_i - \varphi_j$ between corresponding branch gains. As their absolute phases need not be known, we can arbitrarily set the phase of the first branch to 0° .

For the remaining phases, we measure the scattering parameters of a high-quality coaxial cable that we subsequently connect between the first branch and the branch k in question. Next, the 2×2 covariance matrix between these two branches is measured and compared with the prediction according to (4.48). The absolute values of all matrix elements should be consistent; the

Coaxial cable between ports...	1st branch		2nd branch		Covariance	
	Meas.	Pred.	Meas.	Pred.	in fW	Pred.
1 — 2	42.0	42.6	35.5	34.8	$9.7 \angle 84^\circ$	$9.1 \angle 85^\circ$
1 — 3	52.7	52.7	46.1	46.8	$5.2 \angle -119^\circ$	$5.8 \angle -119^\circ$
2 — 3	57.1	56.6	52.1	52.5	$17 \angle -27^\circ$	$16 \angle -27^\circ$

Table 5.6: Measured and predicted covariance matrix upon connection of a coaxial cable between pairs of ports for determining the phases of the branch gains G in Table 5.4.

phase error in the off-diagonal elements is finally equal to the phase of the k th branch gain. This procedure is repeated until all phases are known. Table 5.6 shows the results of this calibration procedure.

For final verification, three measurements with passive three-port junctions were carried out. The following are the results of a T-junction made by soldering three semi-rigid coaxial lines together:

$$\begin{aligned} \text{Measurement: } & \begin{pmatrix} 43.1 & 15.7 \angle -58^\circ & 5.8 \angle 92^\circ \\ 15.7 \angle 58^\circ & 68.6 & 19.5 \angle 149^\circ \\ 5.8 \angle -92^\circ & 19.5 \angle -149^\circ & 52.5 \end{pmatrix} \text{ fW,} \\ \text{Prediction: } & \begin{pmatrix} 43.8 & 15.9 \angle -58^\circ & 6.1 \angle 87^\circ \\ 15.9 \angle 58^\circ & 68.1 & 19.0 \angle 148^\circ \\ 6.1 \angle -87^\circ & 19.0 \angle -148^\circ & 52.8 \end{pmatrix} \text{ fW.} \end{aligned}$$

A T-junction is essentially a lossless component, which causes noise to couple between amplifier terminals but which adds little noise itself. For this reason, a measurement with a three-port 6 dB power divider was performed:

$$\begin{aligned} \text{Measurement: } & \begin{pmatrix} 65.0 & 12.9 \angle -156^\circ & 2.5 \angle 75^\circ \\ 12.9 \angle 156^\circ & 56.7 & 10.4 \angle -162^\circ \\ 2.5 \angle -75^\circ & 10.4 \angle 162^\circ & 56.7 \end{pmatrix} \text{ fW,} \\ \text{Prediction: } & \begin{pmatrix} 64.7 & 12.8 \angle -156^\circ & 2.8 \angle 79^\circ \\ 12.8 \angle 156^\circ & 55.8 & 9.9 \angle -163^\circ \\ 2.8 \angle -79^\circ & 9.9 \angle 163^\circ & 56.9 \end{pmatrix} \text{ fW.} \end{aligned}$$

And finally, the $\lambda_0/10$ antenna array of Fig. 2.6 was measured. Since the electromagnetic interference captured by the antenna array in an ordinary laboratory room would obstruct the sensitive noise measurements, the recordings were carried out in an anechoic chamber. This has the additional advantage that the array sees a uniform temperature environment so that the noise it produces is predicted easily and accurately by virtue of (4.49). The results are

$$\text{Measurement: } \begin{pmatrix} 73.6 & 12.1 \angle 27^\circ & 4.2 \angle -79^\circ \\ 12.1 \angle -27^\circ & 37.9 & 9.7 \angle -22^\circ \\ 4.2 \angle 79^\circ & 9.7 \angle 22^\circ & 64.8 \end{pmatrix} \text{ fW,}$$

$$\text{Prediction: } \begin{pmatrix} 72.0 & 11.1 \angle 25^\circ & 3.2 \angle -97^\circ \\ 11.1 \angle -25^\circ & 37.5 & 8.4 \angle -21^\circ \\ 3.2 \angle 97^\circ & 8.4 \angle 21^\circ & 63.7 \end{pmatrix} \text{ fW.}$$

Although the relative errors in some of the off-diagonal elements may seem large at first, they are in fact small compared with the mean of the main diagonal elements, i.e., the mean noise power received. The excellent agreement between measurements and predictions validates the proposed multi-channel noise model. In conjunction with the previously verified model of the received *signal* covariance matrix, we are finally able to investigate reliably the true diversity performance of compact antenna arrays in terms of their SNR without and with DMN under a variety of operating conditions.

5.5.3 Influence of noise on the SNR diversity gain

In the following, we will be looking at a number of compact antenna array receivers in terms of signal power transfer, noise temperature, and available SNR, as well as the consequent effects on diversity.

The antenna arrays under test include the three-port monopole arrays already known from the CDF measurements in Fig. 5.16 with separations $0.1\lambda_0$, $0.25\lambda_0$, and $0.61\lambda_0$, and also include a hypothetical ideal array (lossless, decoupled, and matched to $50\ \Omega$). All these arrays have a $50\text{ cm} \times 50\text{ cm}$ ground plane. The final array in the list is a second $0.1\lambda_0$ array (Fig. 2.6) whose only difference is its $14\text{ cm} \times 14\text{ cm}$ ground plane. Table 5.7 lists the performance results, which we will discuss below.

We then examine the effects of DMNs. To this end, we have three of the two-port $\lambda_0/10$ array systems from Section 3.6.3 on our list: the directly fed array with coupled radiators, the decoupled and matched array with hybrid coupler and single-stub matching network, and the decoupled and matched array using the alternative DMN technique. These arrays are listed in Table 5.8. The parenthesized letters correspond with Fig. 3.23 on page 79. For comparison, a hypothetical ideal array is also included.

The final pair of arrays in Table 5.8 without and with DMN was developed by Weber [121], [146]. It was chosen because at the time of writing this DMN with its diversity gain of 3.66 dB at low outage probabilities was the best design available for a linear $\lambda_0/10$ three-port array in terms of signal power efficiency.³

³Weber states a diversity gain of 2.86 dB at the 0.5 % level. In the present work, however,

All these arrays will be analysed in conjunction with four different receiver front-ends with varying noise performance. The first front-end is a hypothetical front-end with $50\ \Omega$ input impedance. Its noise temperatures of $T_{\nu,F} = 4500\ \text{K}$ and $T_{\mu,F} = T_{\nu\mu,F} = 0\ \text{K}$ approximate the noise properties of the diversity receiver lacking low-noise pre-amplification.

The remaining three front-ends use the noise data collected in the previous subsection (see Table 5.4). Although for the practical verification of the noise model each front-end branch used a different LNA, we assume for the following investigation that all front-end branches are identical. We remember that the front-end amplifiers are noise matched—not power matched—to $50\ \Omega$.

For each antenna array and front-end, Table 5.7 lists a number of parameters. L_d denotes the signal diversity loss approximation according to (4.28), which, until now, represented the principal figure of merit of mutually coupled antenna arrays. It only accounts for power mismatch between the array and the receiver front-end, and disregards the effects of noise. The received noise is characterised by its equivalent mean temperature T_R (4.47). Both effects together are accounted for by the SNR diversity loss $L_d^{(\text{SNR})}$ defined in (4.70). The SNR diversity loss is the quantity that *ultimately* describes the diversity performance of a given constellation of antenna array, DMN, and receiver front-end. As explained previously, $L_d^{(\text{SNR})}$ quantifies the SNR loss with respect to an ideal system with noiseless front-end branches. The necessary matrices \tilde{H}_R and \tilde{T}_R were calculated according to Eqns. (2.7), (2.26), (4.48), (4.50), and (4.62), depending on the information available. Because far-field data is available for the arrays without and with DMN, the influence of the network could be accounted for by treating the decoupled and matched array as an equivalent lossy array without network as suggested at the end of Section 4.4.2. Attention was paid that all matrices, i.e., both the scattering and the covariance matrices, were appropriately normalised to the front-end input impedances \tilde{Z}_{in} (see Appendix B.1.3). We assume an ambient temperature and a uniform environment temperature of $T_{\text{amb}} = T_{\text{env}} = 290\ \text{K}$.

We begin with the first four antenna arrays in Table 5.7. The second column in the table reports the signal diversity loss L_d at a $50\ \Omega$ receiver as used throughout the present work; the loss increases considerably with decreasing radiator separation. The equivalent temperature T_R of the noise received by

the diversity gain due to (4.37) is used, which yields a larger value and which represents the limiting gain towards low outage probabilities. Also, the array actually operates at 1 GHz, but we nonetheless use the data for the 2.45 GHz front-end.

$T_{\text{env}} = 290 \text{ K}$ $T_{\text{amb}} = 290 \text{ K}$	<div>High noise → Low noise</div>									
	No LNA, 50 Ω					BFP640				
Array name	L_d	T_R	$L_d^{(\text{SNR})}$	$L_d^{(\text{SNR})}$	$L_d^{(\text{SNR})}$	$L_d^{(\text{SNR})}$	$L_d^{(\text{SNR})}$	$L_d^{(\text{SNR})}$	T_R	$L_d^{(\text{SNR})}$
	in dB	in K	in dB	in dB	in dB	in dB	in dB	in dB	in K	in dB
3-port $0.1\lambda_0$	7.42	4639	19.5	11.1	7.65	11.0	165	8.54		
3-port $0.25\lambda_0$	2.05	4708	14.2	6.53	3.36	5.16	198	3.50		
3-port $0.61\lambda_0$	0.29	4771	12.5	4.91	2.29	2.52	260	2.04		
3-port ideal	0	4790	12.2	4.52	2.13	2.17	271	1.88		
3-port $0.1\lambda_0$ (b)	7.59	4645	19.6	12.3	8.63	9.39	202	7.81		

Table 5.7: Computed effects of radiator coupling on the SNR performance of various receiver front-ends.

the system is listed in the third column. It represents the superposition of the front-end noise temperature $T_{v,F} = 4500$ K and the thermal noise picked up by the array. In the ideal case, this is 4500 K + 290 K = 4790 K. With decreasing radiator separation, the antenna noise experiences the same amount of impedance and coupling mismatch as the signal. The received noise consequently decreases too. However, since most noise is contributed by the very noisy front-end itself, the relative change in noise power remains small. The SNR loss $L_d^{(SNR)}$ in the fourth column thus very closely tracks the signal loss L_d . Because the SNR loss specifies the loss relative to a noiseless front-end, it does not drop to zero for the ideal antenna array; it rather becomes equal to the noise-figure of a single receiver branch at a $50\ \Omega$ load.

Let us skip the columns of the HMC478 and the BFP640 amplifiers for the moment and turn to the NE3515S02-based front-end (rightmost three columns), the lowest noise front-end we have available. We observe that the signal diversity loss of the ideal array is greater than zero, which stems from the fact that the amplifier input impedance is very different from $50\ \Omega$ (see Table 5.4). In this example, we have the additional effect that the signal diversity loss increases more rapidly than with the high-noise front-end in the presence of mutual coupling, though this behaviour cannot be generalised to all non- $50\ \Omega$ front-ends. As with the high-noise example, there is a reduction of the equivalent received noise temperature T_R as radiator move closer together. This time, since the noise contribution by the front-end is small, the relative change is much more significant compared with the high-noise front-end. Putting these two pieces of information together, we arrive at the SNR loss column $L_d^{(SNR)}$, which tells us that the SNR degradations due to mutual coupling are in fact considerably less pronounced than we would expect from the signal loss analysis alone. The SNR loss of the $0.1\lambda_0$ array with respect to the ideal case, for instance, amounts to 6.66 dB, which is more than 2 dB better than the corresponding signal loss difference, and still 0.76 dB better than the signal loss at the $50\ \Omega$ front-end. Recall that the amplifiers are noise-matched to $50\ \Omega$, so the SNR performance of $L_d^{(SNR)} = 1.88$ dB of the ideal three-port $50\ \Omega$ array is actually the best we can achieve with this amplifier (cf. the noise figure in Table 5.4).

The noise figure of the noise-matched BFP640-based front-end is 0.25 dB worse than the NE3515S02-based front-end. It seems remarkable that this fact is only reflected by the ideal and by the $0.61\lambda_0$ array; the $0.25\lambda_0$ and $0.1\lambda_0$ arrays perform *better* than with the NE3515S02, the $0.1\lambda_0$ array by as

much as 0.89 dB. Two mechanisms can be identified that possibly give rise to this effect. One is that the input impedance of the BFP640 is closer to $50\ \Omega$ compared with the NE3515S02, which reduces the impact of signal power mismatch for the particular example arrays reported in the table. The other one is that the noise produced by different amplifiers differs in its sensitivity to impedance variations at the amplifiers' inputs. For instance, the noise contributed by an amplifier lacking a backward travelling wave μ_F would be constant regardless of the impedance connected to it. The other extreme would be an amplifier with T_μ very large and strong correlation between its noise waves v_F and μ_F . In our example, the sensitivities of the BFP640 and the NE3515S02 are difficult to compare because of their unequal input impedances. The example does demonstrate, however, that the amplifier with the lower noise figure specification is not necessarily the wiser choice if mutual coupling is involved.

Lastly, the HMC478-based front-end with its noise figure of 4.52 dB is yet another example that the signal diversity loss is an insufficient measure for diversity performance evaluation. Whereas the SNR loss seems to track the $50\ \Omega$ signal loss down to $0.25\lambda_0$ separation, the deviation is almost 1 dB with the $0.1\lambda_0$ array.

The second $0.1\lambda_0$ array with the smaller ground plane demonstrates that seemingly similar arrays can perform very differently in terms of the SNR: even though its $50\ \Omega$ signal loss is comparable with that of the previous $0.1\lambda_0$ array, the associated SNR losses differ with all front-ends. With the HMC478 LNA, the difference is as large as 1.2 dB. The plain reason is that the scattering matrices of the two arrays have little in common, other than their signal loss.

We move on to the examples involving DMNs in Table 5.8. According to the signal column of the $50\ \Omega$ front-end, the single-stub matching network "C" achieves an improvement of 2.18 dB with respect to the direct feed network "A". The improvement of the alternative DMN "F" amounts to 3.87 dB. As we move towards lower noise front-ends, however, the achieved SNR gain considerably diminishes. The performance is especially poor with the lowest noise NE3515S02 amplifier: the gain due to network "C" is only 0.58 dB and the gain of network "F" is 2.14 dB. One explanation for this outcome is that, in terms of the signal loss L_d , the directly fed array is obviously matched better to the NE3515S02 than to the $50\ \Omega$ front-end. The second cause is the unequal influence of the DMN on the signal and on the

<div><div>$T_{\text{env}} = 290\text{ K}$ $T_{\text{ant}} = 290\text{ K}$</div></div>	High noise				Low noise			
Array name	No LNA, 50 Ω		HMC478		BFP640		NE3515S02	
	L_d in dB	T_R in K	$L_d^{(\text{SNR})}$ in dB	$L_d^{(\text{SNR})}$ in dB	$L_d^{(\text{SNR})}$ in dB	$L_d^{(\text{SNR})}$ in dB	L_d in dB	T_R in K
Direct (A)	5.62	4676	17.7	9.81	7.07	4.78	359	5.71
Single (C)	3.44	4762	15.6	7.81	5.34	5.80	248	5.13
Alternative (F)	1.75	4781	13.9	6.11	3.79	3.97	264	3.57
2-port ideal	0	4790	12.2	4.52	2.13	2.17	271	1.88
Weber w/o DMN	6.58	4648	18.6	11.1	7.81	5.17	369	6.22
Weber w/ DMN	2.92	4785	15.1	7.46	5.02	5.12	268	4.78

Table 5.8: Computed effects of decoupling and matching networks on the SNR performance of various receiver front-ends.

noise: without DMN, the signal and the noise captured by the antenna array are subjected to the same impedance mismatch. Since the DMN provides uncoupled $50\ \Omega$ terminals, it induces the same amount of noise into the system as an ideal array. Ohmic losses, however, cause the transfer of signal power to be less than ideal. We have addressed this matter previously in Section 4.4.4. There we concluded that practical DMN implementations cause a degradation of the SNR available directly at the array terminals. In fact, the only reason why DMNs are nonetheless able to enhance system SNR performance is the noise contributed by the receiver front-end *after* the DMN.

The final example of the three-port DMN due to Weber [121], [146] bears the same problems. Although the $50\ \Omega$ signal gain is 3.66 dB the actual SNR gain is merely 1.44 dB with the low-noise NE3515S02 front-end.

To conclude the discussion on noisy receiver front-ends, we examine the role of the noise picked up from the environment. Suppose that this environmental noise is not of thermal origin but is rather the result of interference from other systems operating in the same frequency band. If we further suppose a large number of interfering devices (e.g., cellular phones) we can assume a random behaviour in amplitude and space and can thus roughly model its effects by raising the equivalent noise temperature T_{env} of the environment. Table 5.9 shows what happens when interference is about 22 dB above the thermal noise floor, i.e., if $T_{\text{env}} = 50000\ \text{K}$. We are not going to discuss the full table in detail, it is mainly provided for informational purposes. It is however obvious that, in accordance with previous discussions, the degradations due to mutual coupling become noticeable only at very low radiator separations. Since there is little degradation, there is little need for a DMN, at least for the front-ends that employ a pre-amplifier of some sort.

So, if a high-noise environment alleviates the effects of mutual coupling, it would be interesting to investigate the other extreme of a very “cold” environment. Table 5.10 thus lists the receiver parameters at an equivalent environment temperature of $T_{\text{env}} = 10\ \text{K}$ as encountered in space communications. The SNR quantities are generally higher than at room temperature, because the amount of noise added by the system is much greater in relation to the noise collected by the arrays. For the same reason, the adverse effects of mutual coupling are also considerably more pronounced. On the converse, this fact does not seem to help the effectiveness of the DMNs. The respective DMN gains of the “Single (C)” network and the “Weber” network are still 0.5 dB and 1.4 dB, as with the 290 K-environment in Table 5.8. This

$T_{\text{env}} = 50000 \text{ K}$ $T_{\text{amb}} = 290 \text{ K}$		No LNA, 50 Ω			HMC478		BFP640		NE3515S02	
Array name	L_d in dB	T_R in K	$L_d^{(\text{SNR})}$ in dB	$L_d^{(\text{SNR})}$ in dB	$L_d^{(\text{SNR})}$ in dB	L_d in dB	T_R in K	$L_d^{(\text{SNR})}$ in dB		
3-port 0.1 λ_0	7.42	20038	3.45	1.00	0.39	11.0	4641	0.68		
3-port 0.25 λ_0	2.05	36442	0.68	0.11	0.03	5.16	15364	0.04		
3-port 0.61 λ_0	0.29	51267	0.40	0.05	0.02	2.52	28076	0.02		
3-port ideal	0	54500	0.37	0.05	0.02	2.17	30439	0.01		
3-port 0.1 λ_0 (b)	7.59	20054	3.71	1.57	0.69	9.39	6270	0.46		
Direct (A)	5.62	20369	1.72	0.34	0.16	4.78	16986	0.09		
Single (C)	3.44	27761	0.88	0.15	0.07	5.80	13354	0.07		
Alternative (F)	1.75	38170	0.57	0.08	0.04	3.97	20219	0.03		
2-port ideal	0	54500	0.37	0.05	0.02	2.17	30439	0.01		
Weber w/o DMN	6.58	21712	2.96	0.97	0.45	5.17	16006	0.22		
Weber w/ DMN	2.92	31855	0.97	0.18	0.09	5.12	15677	0.08		

Table 5.9: Computed performances of various compact antenna arrays and receiver front-ends in the presence of strong external noise or interference.

$T_{\text{env}} = 10 \text{ K}$ $T_{\text{amb}} = 290 \text{ K}$	No LNA, 50 Ω				HMC478				BFP640				NE3515S02			
	Array name	L_d in dB	T_R in K	$L_d^{(\text{SNR})}$ in dB	$L_d^{(\text{SNR})}$ in dB	$L_d^{(\text{SNR})}$ in dB	$L_d^{(\text{SNR})}$ in dB	$L_d^{(\text{SNR})}$ in dB	$L_d^{(\text{SNR})}$ in dB	$L_d^{(\text{SNR})}$ in dB	$L_d^{(\text{SNR})}$ in dB	$L_d^{(\text{SNR})}$ in dB	L_d in dB	T_R in K	L_d in dB	$L_d^{(\text{SNR})}$ in dB
	3-port $0.1\lambda_0$	7.42	4505	34.0	24.8	20.3	11.0	99.2	21.0							
	3-port $0.25\lambda_0$	2.05	4507	28.6	19.8	15.0	5.16	98.3	15.1							
	3-port $0.61\lambda_0$	0.29	4509	26.8	17.9	13.2	2.52	103	12.7							
	3-port ideal	0	4510	26.5	17.3	12.9	2.17	101	12.2							
	3-port $0.1\lambda_0$ (b)	7.68	4510	34.2	26.1	21.4	9.39	126	20.5							
	Direct (A)	5.62	4550	32.2	23.6	20.1	4.78	227	18.3							
	Single (C)	3.44	4619	30.1	21.5	18.2	5.80	160	17.8							
	Alternative (F)	1.75	4588	28.4	19.5	16.0	3.97	146	15.6							
	2-port ideal	0	4510	26.5	17.3	12.9	2.17	101	12.2							
	Weber w/o DMN	6.58	4497	33.1	24.7	20.2	5.17	198	18.1							
	Weber w/ DMN	2.92	4596	29.5	20.9	17.2	5.12	144	16.7							

Table 5.10: Computed performances of various compact antenna arrays and receiver front-ends in the lack of external noise.

is because the DMNs operate at ambient temperature $T_{\text{amb}} = 290$ K and thus contribute noise that is an order of magnitude stronger than the environmental noise at $T_{\text{env}} = 10$ K. Only the “Alternative (F)” network shows slightly better performance with an SNR network gain of 2.7 dB in the cold environment instead of 2.14 dB in the 290 K environment.

5.6 Summary

The past chapter was dedicated to the verification of some of the diversity formulae and models developed previously. After a description of the measurement system that had specifically been developed for this purpose, we discussed measured cumulative distribution functions (CDF) of the received SNR for a number of antenna arrays. These results clearly confirmed the anticipated impairments due to mutual radiator coupling. It was also demonstrated that, in these examples, decoupling and matching networks were able to enhance the quality of the mobile link considerably.

However, these results were not very consistent with the diversity figures of merit derived in Chapter 4. After errors in the execution of these initial measurements had been identified, another set of antenna arrays without and with DMN was tested. The new results are in *good agreement* with the predicted behaviour in terms of both the statistics of the fading as represented by the CDF, as well as the signal covariance matrix as estimated from the collected complex envelope data. The practical applicability of the suggested figures of merit for diversity reception has thus been *confirmed*. Because of the high noise figure of the receiver system, we could dispense with a detailed noise analysis and thus base the above predictions solely on the signal power analysis.

The preceding chapter also proposed a complete receiver model that includes noise of various origins. Discussions indicated that for low-noise systems a detailed noise description is inevitable for an accurate assessment of the implications of radiator coupling. In order to verify this noise model, the receiver was equipped with three different low-noise pre-amplifiers. These were subsequently characterised in a way that enabled an *accurate prediction* of the complex received noise covariance matrix upon connection of a passive multi-port load (e.g., a mutually coupled antenna array) based on the load’s scattering matrix.

With the help of these two *practically verified models*—one for the signal

and one for the noise—we spent the last part of the chapter on an *SNR* diversity analysis of several mutually coupled antenna arrays and DMNs. The results confirm earlier suspicions that with low-noise front-ends the SNR impairments due to mutual coupling are not as severe as they first seem from a signal-only analysis. Unfortunately, this observation applies to DMNs as well in that their actual SNR gains typically turn out considerably lower than anticipated on the basis of signal efficiency considerations alone. Finally, we investigated the influence of the equivalent noise temperature of the communications environment. We observed that the influence of both mutual coupling and DMNs becomes negligible when system performance is primarily limited by external noise or random interference. Although towards lower external temperatures the implications of mutual coupling become increasingly severe, the DMN gains on the other hand show little improvement due to the additional noise produced by ohmic network losses.

Chapter 6

Summary and outlook

The established way to characterise mutual radiator coupling is based on the scattering parameters of the antenna array or, alternatively, on the correlation coefficient between the far-field patterns associated with the array ports. In order to assess the *implications* of radiator coupling, a number of *figures of merit* related to the *performance* of mobile communications systems have been devised. Some are straightforward to work with—for instance, the scattering-matrix based worst-case efficiency or the signal diversity loss—others require considerably more effort, such as the SNR diversity loss. They all have one important aspect in common: they express system performance as a *single number*.

As such, they open up new possibilities for the successful implementation of compact yet effective antenna arrays for several reasons. First, it has become possible for the first time to compare easily and *quantitatively* array designs where mutual coupling cannot be eliminated due to areal requirements. Second, array performance can be evaluated *over frequency*, which considerably eases the characterisation of *broadband* or *multi-band* designs. Lastly, these figures of merit lend themselves as cost-functions for the non-linear optimisers found in modern electromagnetic simulators, and thus foster the automated determination of optimum design parameters.

We learned to interpret the radiation process of an arbitrary n -port antenna array in terms of its n underlying *degrees of freedom*, which we called the *eigenmodes*, and the associated *eigen efficiencies*. Based on this eigenmode

concept, an *array equivalent circuit* was developed that portrays mutual coupling as a manifestation of *impedance mismatch*. We can thus expect that lowly efficient eigenmodes represent those degrees of freedom that are largely underrepresented during normal array operation—in the transmitting as well as the receiving direction.

We then considered diversity reception as a specific application of compact antenna arrays and developed *closed-form expressions* related to the *diversity gain* of the system. Both the efficiency-based and the diversity-based concepts have a central parameter in common: the radiation matrix “ \hat{H} ”. There are three different ways to compute \hat{H} . The first method is *very simple to apply* in practice because all that is required is the *scattering matrix* of the antenna array. If ohmic losses inside the array are of concern, the radiation matrix can be calculated by numerical integration over the measured or simulated *far-field patterns*. Both approaches were shown to yield *identical results* for lossless arrays. The third method is relevant to diversity reception and *accounts for the statistics* of the multi-path communications environment. A formula was proposed that is the logical consequence of a channel model often assumed in the literature. The diversity formulae therefore enhance the *established procedure of diversity analysis* and do not mean to replace it.

Until this point, we had been looking at the properties of the *signal* transmitted or received by an antenna array. The quality of a mobile link, however, is ultimately determined by the *signal-to-noise ratio* (SNR) at the receiver. In order to analyse the effects of receiver noise, a *complete front-end model* was proposed that includes noise sources of several origins: noise or random interference collected by the array, noise due to ohmic losses of the array and its feed network, as well as the noise produced by the receiving front-end components such as amplifiers, mixers, or quantisation noise. For low-noise front-ends in particular, we realised that from an SNR point of view, the impairments due to mutual coupling are *far less pronounced* than in terms of signal power alone. This result also applies to systems, whose performance is primarily limited by external random interference. Signal power considerations are therefore *by no means sufficient* to predict the reception quality of a mutually coupled receiver system.

Considerable efforts were spent on the verification of the proposed models and formulae. Fading measurements with up to three diversity branches were carried out, and the statistics of the combined signals as well as estimates of the complex covariance matrices of the received signals were com-

pared with theoretical predictions. The close agreement between theory and measurements not only *confirms* the validity of the models developed, but substantiates the *practical applicability* of simple scattering-parameter-based expressions for predicting system diversity performance. Measurements also support the accuracy of the *front-end noise model*. In view of these results, we can therefore expect that the conclusions drawn from the final examples in Chapter 5 closely reflect the true capabilities of the systems in question.

Chapter 3 investigated decoupling and matching networks (DMN) as a possible means to combat the degradations due to mutual coupling. A systematic eigenmode-based design approach using directional couplers was proposed and shown to be applicable to a *wide class* of antenna arrays. Its prominent advantage is that decoupling can often be achieved *without knowledge of the array's scattering parameters* by explicit exploitation of electrical *symmetries* of the array. The *broad decoupling* bandwidth makes the approach *less susceptible* to manufacturing tolerances. An example demonstrated that these properties are especially attractive for the *mass-production* of decoupling chips, because the latter can be deployed in a *wide range of products* as long as certain symmetry conditions are fulfilled. The resulting decoupled set of ports can then be matched by virtue of *familiar* single-port techniques. Varactor-tunable matching networks are thinkable to *adapt* the system electronically to changing frequency bands of operating.

Based on the DMN scattering matrix, a method was introduced to account for the influence of the network on the eigenmodes and the diversity gain of the system. This enables the broadband characterisation and thus a bandwidth definition of the decoupled and matched system including *ohmic network losses* as well as any *residual coupling and mismatch* at the network input terminals. On this connection, the two major drawbacks of DMNs became evident: although they can be manufactured to achieve the theoretical optimum condition of decoupled and matched ports, their ohmic losses to a great part outweigh the benefits of decoupling and matching. And even if lossless networks existed, their practical applicability would still be rather limited due to their extremely narrow bandwidth. We also outlined the reasons why DMNs are even less effective when implemented at low-noise receivers. These drawbacks are inherent to DMNs in general and are not specific to the approach presented here. However, we argued that the eigenmode method may be especially susceptible to these issues due to the insertion loss of the directional couplers involved.

Considering the aforementioned drawbacks of DMNs, it seems sensible first to exhaust all possibilities to maximise the performance of the antenna array itself. Only then should we examine the potential benefits of a DMN. In view of this optimisation procedure, we are aware of by now that pattern orthogonality (decorrelation) is not the principal goal to strive for, because impedance mismatch has equally adverse effects. Rather, a compromise between correlation and mismatch should be sought that maximises system performance over the bandwidth of interest. On this connection, we revealed that, in general, different criteria apply to the transmitting and the receiving ends of the system. Whereas transmitters benefit from seamless power transfer to the antenna array, receivers must be optimised with respect to the SNR.

It is worth noting that there is nothing special about the familiar $50\ \Omega$ reference impedance. It is therefore not sensible to first build an amplifier inclusive of a $50\ \Omega$ matching network, and then design the antenna array with respect to that impedance. Instead, the antenna array should be optimised with respect to whatever impedances the amplifiers happen to have without any intermediate networks. The frameworks in this thesis were explicitly developed to allow for arbitrary reference impedances. Moreover, it may be worthwhile to try out several types of amplifiers because it is likely that certain output impedances (transmitter) or noise parameters (receiver) are more favourable to a particular compact array design than others.

The example arrays presented in this work were merely provided for demonstration purposes and are evidently inappropriate for implementation in compact mobile devices. More sophisticated designs targeting small physical dimensions in addition to low mutual coupling have been carried out by Braun et al. [25], Chiau et al. [30], Diallo et al. [93], and Karaboikis et al. [49], for instance. Examples of compact multi-band diversity arrays are given by Lindmark and Garcia-Garcia [57] or Minard et al. [100], amongst others. The considerable influence of the ground plane size on the mutual impedance was investigated by Solbach and Fandie [111]. Chaudhury et al. [91] showed that even the ground plane itself can be utilised as a multi-port antenna. It is anticipated that, in the future, these and similar developments can benefit from the compact expressions for mutually coupled array performance devised herein.

Decoupling and matching networks can be employed as a next step when antenna array and amplifier optimisation does not yield satisfactory results. Network losses were shown to play a major role and should therefore be ac-

counted for early in the design process with the help of the framework presented. Systematic and mathematically ideal design strategies such as the ones discussed in Chapter 3 or by Weber [121] or Wang [120] are desirable from a theoretical point of view. The practical applicability of these networks is however limited as the result of their narrow bandwidth, high losses, and often large footprints. Losses can be minimised to some extent by moving the DMN as close to the radiating parts as possible, or by even incorporating the DMN into the array as was accomplished by Eßer and Chaloupka [95] and Shaker et al. [109]. These techniques however, cannot resolve the inherent bandwidth limitations of mutual coupling. It is therefore supposed that “non-ideal” networks exist that do not yield a perfectly decoupled and matched set of ports, but that nonetheless achieve better results than mathematically correct networks in terms of bandwidth and overall system performance. Such networks could comprise fewer components, be smaller, and in the end suffer less dissipation due to ohmic losses. Objective means to judge and compare the actual effectiveness of such networks have been developed in this thesis.

At a transmitter, we could think about *deliberately* introducing losses into a DMN to achieve adequate matching and linear operation of the power amplifiers over a broad bandwidth. At the same time, the network can be optimised to keep the associated degradations of system efficiency as small as possible with the help of the loss characterisation formulae given. Receiver DMNs could take advantage of the fact that different transistor types (e.g., the BFP640 and the NE3515S02) are noise matched to greatly differing impedances. A possible design would consist of an eigenmode decoupling network and then, at each port, employ the transistor closest to the emerging decoupled port impedance. To some extent, this procedure would reduce ohmic dissipation losses by avoiding the large impedance transformation ratios involved if all ports had to be (noise-)matched to the same impedance.

These are only some of the potential alternative antenna array and DMN approaches that merit further investigation. We must not forget, though, that mutual coupling imposes physical restriction on the amount of miniaturisation obtainable. No design, no matter how clever, can overcome these limits; however, we can attempt to approach these limits as close as possible.

The techniques introduced in this work aim to provide an alternative vantage point on the problem of mutual radiator coupling, which seemingly impedes the successful miniaturisation of antenna arrays. It should have become clear by now that future designs of compact arrays and feed networks must

concentrate on optimising system performance rather than attempt to minimise mutual coupling. Of course, the present work only investigated the power efficiency of a transmitting system and the diversity capabilities of maximal ratio combining at a receiver. Thus, it remains to be seen if and how these results can be generalised to other mobile communications techniques, such as MIMO or multi-user systems. It is hoped that the concepts and the framework put forward in this thesis present a decent starting point for subsequent research and prove useful in meeting our future communications needs.

Kapitel 7

Zusammenfassung und Ausblick

Der übliche Weg zur Charakterisierung der Strahlerverkopplung geht von den Streuparametern einer Antennengruppe, beziehungsweise dem Korrelationskoeffizienten zwischen den mit den Antennentoren verknüpften Fernfeldern aus. Um nun die *Auswirkungen* dieser Verkopplung einschätzen zu können, wurden einige neuartige *Kenngößen* entwickelt, die im Zusammenhang mit der *Leistungsfähigkeit* eines mobilen Kommunikationssystems stehen. Einige davon lassen sich besonders einfach einsetzen, so zum Beispiel die Worst-case-Effizienz oder der Signalverlust bei Diversitätsempfang, die sich beide aus den Streuparametern der Gruppe berechnen lassen. Andere, beispielsweise der SNR-Verlust bei Diversitätsempfang, erfordern zusätzlichen Aufwand. Alle Kenngößen haben jedoch eines gemeinsam: sie fassen die Leistungsfähigkeit eines Systems in einer *einzig*en Zahl zusammen.

Aufgrund dieser Tatsache ergeben sich neue Möglichkeiten bei der Entwicklung sowohl kompakter als auch effizienter Mobilfunkantennen. Es ist nun erstmalig möglich, auf einfache Weise und auf *quantitativer Ebene* verschiedene Entwürfe von Gruppenantennen zu vergleichen, bei denen aufgrund von Platzbeschränkungen die Strahlerverkopplung nicht ganz vermieden werden kann. Die Leistungsfähigkeit der Gruppe kann in *Abhängigkeit von der Frequenz* aufgetragen werden. Dadurch wird die Einschätzung von *Breitband-* oder *Mehrbandantennengruppen* deutlich vereinfacht. Schließlich eig-

nen sich diese Kenngrößen als Kostenfunktionen für die nicht-linearen Optimierungsverfahren, die zum üblichen Lieferumfang moderner elektromagnetischer Simulationssoftware gehören.

Es ist dargestellt worden, wie man den Abstrahlvorgang einer beliebigen n -Tor Antennengruppe als Superposition ihrer n zugrundeliegenden *Freiheitsgrade* interpretieren kann, welche als die *Eigenmoden* der Gruppe bezeichnet wurden. Jedem Freiheitsgrad kann eine *Eigeneffizienz* zugeordnet werden. Ausgehend von dieser Idee wurde ein *Ersatzschaltbild* entwickelt, welches die Strahlerverkopplung auf eine besondere Erscheinungsform von (Impedanz-) *Fehlanpassung* zurückführt. Man kann nunmehr davon ausgehen, dass Eigenmoden mit einer niedrigen Strahlungseffizienz diejenigen Freiheitsgrade beschreiben, die bei Normalbetrieb der Antennengruppe maßgeblich unterrepräsentiert sind. Dies gilt gleichermaßen für die Sende- als auch die Empfangsrichtung.

Anschließend wurde eine konkrete Anwendung kompakter Gruppenantennen, der Diversitätsempfang, näher beleuchtet. In diesem Zusammenhang wurden *geschlossene Ausdrücke* für den Diversitätsgewinn hergeleitet. Beide genannten Ansätze – der effizienzbasierte wie auch der diversitätsbasierte – haben dabei einen zentralen Parameter gemeinsam: die Strahlungsmatrix „ \tilde{H} “, wobei es drei verschiedene Möglichkeiten gibt, diese Matrix zu bestimmen. Die erste Methode ist praktisch sehr einfach anzuwenden, da sie lediglich die Kenntnis der *Streuparameter* der Antennengruppe voraussetzt. Falls Ohm'sche Verluste in der Antennengruppe selbst eine Rolle spielen, so kann die Matrix durch Integration über die gemessenen oder auch simulierten *Fernfelder* ermittelt werden. Im verlustlosen Fall liefern beide Methoden die *gleichen Ergebnisse*. Speziell für Diversitätsuntersuchungen gibt es darüber hinaus eine dritte Möglichkeit, welche die *Eigenschaften des Mobilfunkkanals* einbezieht. Insbesondere wurde ein Formel vorgestellt, die sich als logische Konsequenz aus einem Kanalmodell ergibt, welches in der Literatur häufig Anwendung findet. Die Diversitätskenngrößen sind also dazu gedacht, die *bisherigen Möglichkeiten der Diversitätsbetrachtung* zu ergänzen und nicht, diese zu ersetzen.

Bisher galt die Darstellung den Eigenschaften der Signalübertragung zwischen Antennengruppe und Sender beziehungsweise Empfänger. Die Qualität einer Mobilfunkübertragung wird jedoch letztendlich über den *Signal-Rauschabstand* (SNR) am Empfänger bestimmt. Um dieser Tatsache weiter auf den Grund zu gehen, wurde ein *vollständiges Empfängermodell* unter

Einbeziehung sämtlicher Rauschquellen entwickelt: Rauschen oder zufällige Störeinstrahlungen an den Antennen, Rauschen aufgrund von Ohm'schen Verlusten im Speisernetzwerk, sowie Rauschen, welches von den Empfängerkomponenten stammt, also den Verstärkern, Mischern oder das Quantisierungsrauschen. Dabei ist festgestellt worden, dass insbesondere bei rauscharmen Empfangszweigen die negativen Einflüsse der Strahlerverkopplung *nicht annähernd so stark ausgeprägt* sind, wie es eine reine Signalanalyse vermuten lassen würde. Dies gilt ebenso für Systeme, die in erster Linie unter externen zufälligen Störeinstrahlungen an der Antenne leiden. Die Schlussfolgerung ist, dass Untersuchungen, die lediglich die Signalleistung betrachten *in keiner Weise ausreichen*, um die Empfangsqualität eines verkoppelten Mehrkanalempfängers vorherzusagen.

Es wurde nennenswerter Aufwand getrieben, die erarbeiteten Modelle und Formeln zu verifizieren. Dazu wurden Kanalschwundmessungen mit bis zu drei Diversitätszweigen durchgeführt. Die Statistiken der kombinierten Signale, sowie Schätzungen der Signalkovarianzmatrizen wurden mit theoretischen Vorhersagen verglichen. Die gute Übereinstimmung zwischen Theorie und Praxis bestätigt nicht nur die Gültigkeit der beschriebenen Modelle, sondern untermauert vor allen Dingen die *praktische Anwendbarkeit* von Streuparametermessungen zur Vorhersage der Diversitätseigenschaften eines Systems. Die Gültigkeit des Rauschmodells wurde ebenfalls mithilfe von Messungen belegt. In Anbetracht dieser Ergebnisse ist letztendlich davon auszugehen, dass die Schlussfolgerungen, die aus den abschließenden Beispielen in Kapitel 5 gezogen wurden, ein ziemlich genaues Bild der Leistungsfähigkeit der jeweiligen Systeme zeichnen.

Eine Möglichkeit den Auswirkungen von Strahlerverkopplung entgegenzuwirken, ist der Einsatz von Anpass- und Entkoppelnetzwerken (AEN). Diese wurden in Kapitel 3 untersucht. Es wurde ein systematischer Ansatz zum Netzwerkentwurf basierend auf der Eigenmodentheorie vorgestellt und gezeigt, dass dieser für eine *breite Klasse* von Antennengruppen anwendbar ist. Ein besonderer Vorteil dieser Art von Netzwerken besteht darin, dass der entkoppelnde Teil des Netzwerkes oft *ohne Kenntnis der Streuparameter* der Antennengruppe hergestellt werden kann, indem man sich elektrische *Symmetrieeigenschaften* der Gruppe zu Nutze macht. Die Netzwerke zeichnen sich weiterhin durch eine breite Entkoppelbandbreite aus, was ihre Anfälligkeit gegenüber *Herstellungstoleranzen* herabsetzt. Ein Beispiel hat gezeigt, dass diese Eigenschaften besonders für die Massenfertigung von „Entkop-

pelchips“ interessant sein könnten, da ein solcher Chip in einer Vielzahl von Produkten Einsatz finden kann, solange gewisse Symmetrievoraussetzungen erfüllt werden. Die entstehenden, nun entkoppelten, Tore können abschließend mit *herkömmlichen* Eintornnetzwerken angepasst werden. Es sind auch Varaktor-abstimmbare Netzwerke denkbar, die das System während des Betriebes verschiedenen Frequenzbändern *anpassen* können.

Auf Grundlage der Streuparameter eines AEN wurde eine Methode eingeführt, mit der die Einflüsse des Netzwerkes auf die Eigenmoden sowie den Diversitätsgewinn des Systems berechnet werden können. Dies ermöglicht eine breitbandige Beschreibung und eine Bandbreitendefinition des entkoppelten und angepassten Systems unter Einbeziehung *Ohm'scher Netzwerkverluste* sowie *restlicher Verkopplung und Fehlanpassung* an den Eingangstoren. In diesem Zusammenhang wurden auch die Hauptschwächen von AENs offensichtlich: Obgleich diese Netzwerke so hergestellt werden können, dass sie das theoretische Optimum angepasster und entkoppelter Tore erreichen, so werden die daraus resultierenden Vorteile zu einem großen Teil durch Ohm'sche Verluste aufgezehrt. Selbst wenn man völlig verlustfreie Netzwerke herstellen könnte, so wäre die nächste Beschränkung ihre sehr schmale Bandbreite. Diese Nachteile gelten naturgemäß für alle AEN-Formen, nicht nur für den hier vorgestellten Ansatz. Allerdings war festzustellen, dass aufgrund der Einfügedämpfung der eingesetzten Richtkoppler, die Eigenmodenmethode möglicherweise besonders anfällig für die genannten Schwächen ist.

In Anbetracht dieser Nachteile von AENs scheint es sinnvoll, zunächst alle Möglichkeiten zur Optimierung der Gruppenantenne selbst auszuschöpfen. Erst dann sollte über den Einsatz eines AEN nachgedacht werden. Im Hinblick auf die Optimierung der Gruppenantenne sollte nun klar sein, dass die Orthogonalität beziehungsweise Dekorrelation der Tore nicht das unbedingte Ziel darstellen, da eine Impedanzfehlanpassung an den Einzeltoren gleichermaßen zu Verschlechterungen führt. Es sollte vielmehr ein Kompromiss zwischen Korrelation und Fehlanpassung angestrebt werden, welcher die Leistungsfähigkeit des Gesamtsystems über die erforderliche Bandbreite maximiert. Dabei ist nun ebenfalls klar, dass für Sender und Empfänger jeweils unterschiedliche Bewertungskriterien gelten. Während es am Sender auf reibungslosen Leistungstransport zur Antennengruppe ankommt, so muss der Empfänger im Hinblick auf sein SNR optimiert werden.

Es sei an dieser Stelle angemerkt, dass die geläufige $50\ \Omega$ Bezugsimpedanz einen willkürlichen Wert darstellt. Es ist daher nicht ratsam, erst einen

Verstärker inklusive $50\ \Omega$ Anpassnetzwerk herzustellen, um anschließend die Antennengruppe auf die gleiche Impedanz hin zu entwerfen. Die Antenne sollte vielmehr auf die Impedanz hin optimiert werden, die der Verstärker (beziehungsweise der Transistor) zufällig besitzt. Die Kenngrößen dieser Arbeit sind zu diesem Zwecke darauf ausgerichtet, mit beliebigen Bezugsimpedanzen arbeiten zu können. Darüber hinaus kann es sich lohnen, verschiedene Verstärkertypen auszuprobieren, da möglicherweise bestimmte Ausgangsimpedanzen (am Sender) beziehungsweise Rauschparameter (am Empfänger) für einen konkreten Gruppenantennenentwurf besser geeignet sind als andere.

Die Antennenbeispiele, die im Laufe dieser Arbeit präsentiert wurden, galten lediglich Demonstrationszwecken und sind für den Einsatz in mobilen Endgeräten ganz offensichtlich ungeeignet. Elegantere Entwürfe, die neben einer geringen Strahlerverkopplung auch kleine Abmessungen anstreben, wurden unter anderem von Braun et al. [25], Chiau et al. [30], Diallo et al. [93], und Karaboikis et al. [49] veröffentlicht. Entwürfe kompakter Mehrbandantennen wurden beispielsweise von Lindmark und Garcia-Garcia [57] oder Minard et al. [100] durchgeführt. Der deutliche Einfluss der Größe der Massefläche auf die Strahlerverkopplung wurde von Solbach und Famdie [111] untersucht und es wurde von Chaudhury et al. [91] sogar gezeigt, dass die Massefläche selbst als Mehrtorstrahler eingesetzt werden kann. Diese oder ähnliche Untersuchungen könnten möglicherweise von den in dieser Arbeit entwickelten kompakten Kenngrößen für die Leistungsfähigkeit einer verkoppelten Antennengruppe profitieren.

Entkoppel- und Anpassnetzwerke stellen nun den nächsten Schritt dar, wenn die Optimierung von Antennengruppe und Antennenverstärker nicht zu zufriedenstellenden Ergebnissen führt. Es wurde gezeigt, dass Netzwerkverluste eine große Rolle spielen und dass diese deshalb mithilfe der entwickelten Beschreibungsformeln möglichst früh in den Entwurfsprozess eingebunden werden sollten. Systematische und mathematisch ideale Entwurfsstrategien, wie die aus Kapitel 3, aber auch andere, wie zum Beispiel von Weber [121] oder Wang [120], sind von einem theoretischen Standpunkt aus natürlich wünschenswert. Die praktische Anwendbarkeit dieser Netzwerke ist auf der anderen Seite begrenzt, aufgrund von Verlusten, schmaler Bandbreite und oft auch großen Abmessungen. Verluste können in gewissen Grenzen reduziert werden, indem man sich bemüht, das Netzwerk so nah wie möglich an die Antennen heranzusetzen. Noch besser ist es, das Netzwerk gleich als

Teil der Antenne zu entwerfen, wie Eßer und Chaloupka [95] sowie Shaker et al. [109] gezeigt haben. Aber selbst diese Techniken können die inhärenten Bandbreitebeschränkungen aufgrund der Strahlerverkopplung nicht umgehen. Es wird daher angenommen, dass „nicht-ideale“ Netzwerke existieren, die zwar keine perfekt entkoppelten und angepassten Tore erzeugen, trotzdem aber aus System Sicht größere Verbesserungen bewerkstelligen, als mathematisch korrekte Ansätze. Derartige Netzwerke bestünden aus weniger Komponenten, könnten kleiner ausfallen und letztendlich geringere Ohm'sche Verluste verursachen. Objektive Mittel, um die tatsächliche Effektivität dieser Ansätze beurteilen zu können, wurden in dieser Arbeit entwickelt.

An einem Sender könnte man darüber nachdenken, vorsätzlich Verluste in ein AEN einzubauen, um die Anpassung und somit die Linearität der Sendeverstärker bei vorgegebener Bandbreite zu verbessern. Gleichzeitig können mithilfe der erarbeiteten Formeln zur Verlustbeschreibung die damit verbundenen Einbußen der Systemeffizienz so gering wie möglich gehalten werden. An einem Empfänger könnte man die Tatsache ausnutzen, dass verschiedene Transistortypen (zum Beispiel der BFP640 und der NE3515S02) an völlig unterschiedliche Impedanzen rauschangepasst sind. Ein möglicher Entwurf könnte aus einem Eigenmodenentkoppelnetzwerk bestehen und dann an jedem Tor den Transistor einsetzen, der am nächsten an der entstandenen entkoppelten Torimpedanz liegt. Auf diese Weise könnten Verluste, die ansonsten mit den hohen Impedanztransformationsverhältnissen verbunden wären, reduziert werden.

Dies ist nur eine kleine Aufzählung von möglichen Entwurfsalternativen für Antennengruppen und AENs bei denen sich weitere Nachforschungen lohnen könnten. Dabei darf man allerdings nicht vergessen, dass Strahlerverkopplung der Miniaturisierung physikalische Grenzen setzt, die von keinem Entwurf, sei er noch so ausgefeilt, überschritten werden können. Wir können dennoch versuchen diese Grenzen so nah wie möglich zu erreichen.

Die Ansätze, die in dieser Arbeit vorgestellt wurden, möchten eine alternative Auffassung des bekannten Problems der Strahlerkopplung vermitteln, welches offensichtlich die erfolgreiche Verkleinerung von Antennengruppen erschwert. Es sollte nun deutlich geworden sein, dass zukünftige Entwürfe von kompakten Gruppenantennen und Speisernetzwerken die optimale Leistungsfähigkeit des Gesamtsystems und nicht nur die Verringerung der Strahlerverkopplung zur Zielsetzung haben sollten. Die vorliegende Arbeit hat natürlich nur die Leistungseffizienz eines Senders sowie die Diversitätseigen-

schaften von Maximal-Ratio-Combining näher untersucht. Es bleibt daher abzusehen ob und auf welche Weise diese Ergebnisse auf andere Mobilfunkkonzepte, wie zum Beispiel MIMO oder Mehrbenutzersysteme, verallgemeinert werden können. Die Hoffnung ist, dass die vorgeschlagenen Konzepte einen vernünftigen Ausgangspunkt für anschließende Forschungsarbeiten darstellen und einen Beitrag zur Bewältigung unseres zukünftigen Kommunikationsbedarfs leisten.

Appendix A

Proofs and derivations

A.1 Diagonalisation of eigen-reflections

Proposition 1. *If \tilde{Q} is unitary, \tilde{S} symmetric, $\tilde{H} = \tilde{I} - \tilde{S}^H \tilde{S}$, and $\tilde{Q}^H \tilde{H} \tilde{Q} = \tilde{\Lambda}$ is diagonal with distinct elements, then $\tilde{Q}^T \tilde{S} \tilde{Q} = \tilde{\Gamma}$ is also diagonal.*

Proof. The singular value theorem [8, Theorem 7.3.5] states that any matrix \tilde{S} can be decomposed as

$$\tilde{S} = \tilde{U} \tilde{\Sigma} \tilde{V}^H, \quad (\text{A.1})$$

with \tilde{U} and \tilde{V} unitary, and $\tilde{\Sigma}$ real and diagonal. It also states that the columns of \tilde{U} are eigenvectors of $\tilde{S} \tilde{S}^H$ and the columns of \tilde{V} are eigenvectors of $\tilde{S}^H \tilde{S}$.

Observe that eigenvectors of $\tilde{H} = \tilde{I} - \tilde{S}^H \tilde{S}$ are also eigenvectors of $\tilde{S}^H \tilde{S}$. From $\tilde{S} = \tilde{S}^T$ it follows that eigenvectors of $\tilde{S} \tilde{S}^H$ are the complex conjugates of the eigenvectors of $\tilde{S}^H \tilde{S}$. If all eigenvalues are distinct, the eigenvectors will each be arbitrary to within multiplication by a unit phasor. Thus:

$$\tilde{V} = \tilde{Q} \tilde{\xi} \quad \text{and} \quad \tilde{U} = \tilde{Q}^* \tilde{\eta}, \quad (\text{A.2})$$

where $\tilde{\xi}$ and $\tilde{\eta}$ are diagonal and unitary to account for this arbitrariness. Now (A.1) becomes

$$\tilde{S} = \tilde{Q}^* \tilde{\eta} \tilde{\Sigma} \tilde{\xi}^H \tilde{Q}^H, \quad (\text{A.3})$$

and

$$\tilde{Q}^T \tilde{S} \tilde{Q} = \tilde{\eta} \tilde{\Sigma} \tilde{\xi}^H \quad (\text{A.4})$$

the right-hand side being the product of three diagonal matrices. \square

A.2 Ohmic eigenefficiencies and decoupling and matching networks

Proposition 2. *The eigenvalues of a product of N non-singular matrices $\tilde{Y} = \tilde{X}_1 \tilde{X}_2 \cdots \tilde{X}_N$ are invariant under cyclic shifts (e.g., $\tilde{X}_2 \cdots \tilde{X}_N \tilde{X}_1$) of the constituent factors.*

Proof. The eigenvalues λ_i of a matrix \tilde{Y} are the roots of its characteristic polynomial $\det\{\tilde{Y} - \lambda \tilde{I}\}$. For above product we have

$$\det\{\tilde{Y} - \lambda \tilde{I}\} = \det\{\tilde{X}_1 \tilde{X}_2 \cdots \tilde{X}_N - \lambda \tilde{I}\}. \quad (\text{A.5})$$

The characteristic polynomial of a cyclic shift can be written and rearranged as

$$\det\{\tilde{X}_2 \cdots \tilde{X}_N \tilde{X}_1 - \lambda \tilde{I}\} \quad (\text{A.6})$$

$$= \det\{\tilde{X}_1^{-1} \cdot \tilde{X}_1 \tilde{X}_2 \cdots \tilde{X}_N \cdot \tilde{X}_1 - \lambda \tilde{I}\} \quad (\text{A.7})$$

$$= \det\{\tilde{X}_1^{-1} \tilde{Y} \tilde{X}_1 - \lambda \tilde{X}_1^{-1} \tilde{X}_1\} \quad (\text{A.8})$$

$$= \det\{\tilde{X}_1^{-1}\} \det\{\tilde{Y} - \lambda \tilde{I}\} \det\{\tilde{X}_1\} \quad (\text{A.9})$$

$$= \det\{\tilde{Y} - \lambda \tilde{I}\}, \quad (\text{A.10})$$

which is the characteristic polynomial of the original product. \square

Proposition 3. *The eigenvalues of the product $\tilde{H}_{acc}^{-1} \tilde{H}_{rad}$ define an upper limit to the eigenefficiencies that can be achieved with a passive decoupling and matching network (DMN).*

Proof. The proof determines the eigenvalues of the system radiation matrix $\tilde{H}_{rad,S}$ which results from the interconnection of the antenna array with scattering matrix \tilde{S} and radiation matrix \tilde{H}_{rad} to a lossless and reciprocal DMN with scattering matrix \tilde{S}_M .

Equations for calculating $\tilde{H}_{rad,S}$ based on its constituent components were given in Section 3.5. The general solution for a DMN is derived below and given in (A.62). The fact that the set of DMNs for a given antenna array is infinite is accounted for by a unitary but otherwise arbitrary matrix \tilde{U} .

We start with (3.16)

$$\tilde{H}_{rad,S} = \tilde{r}_a^H \tilde{H}_{rad} \tilde{r}_a, \quad (\text{A.11})$$

and substitute (3.14)

$$\tilde{t}_a = (\tilde{I} - \tilde{S}_{M,22}\tilde{S})^{-1} \tilde{S}_{M,21} \quad (\text{A.12})$$

and the submatrices of the DMN (A.62)

$$\tilde{S}_{M,22} = \tilde{S}^H, \quad (\text{A.13})$$

$$\tilde{S}_{M,21} = \left([\tilde{I} - \tilde{S} \tilde{S}^H]^{1/2} \right)^T \tilde{U} = \tilde{Q}_{\text{acc}} \tilde{\Lambda}_{\text{acc}}^{1/2} \tilde{Q}_{\text{acc}}^H \tilde{U} \quad (\text{A.14})$$

to obtain

$$\tilde{H}_{\text{rad},S} = \left((\tilde{I} - \tilde{S}_{M,22}\tilde{S})^{-1} \tilde{S}_{M,21} \right)^H \tilde{H}_{\text{rad}} (\tilde{I} - \tilde{S}_{M,22}\tilde{S})^{-1} \tilde{S}_{M,21} \quad (\text{A.15})$$

$$= \tilde{U}^H \tilde{Q}_{\text{acc}} \tilde{\Lambda}_{\text{acc}}^{1/2} \tilde{Q}_{\text{acc}}^H \tilde{Q}_{\text{acc}} \tilde{\Lambda}_{\text{acc}}^{-1} \tilde{Q}_{\text{acc}}^H \tilde{H}_{\text{rad}} \tilde{Q}_{\text{acc}} \tilde{\Lambda}_{\text{acc}}^{-1} \tilde{Q}_{\text{acc}}^H \tilde{Q}_{\text{acc}} \tilde{\Lambda}_{\text{acc}}^{1/2} \tilde{Q}_{\text{acc}}^H \tilde{U} \quad (\text{A.16})$$

$$= \tilde{U}^H \tilde{Q}_{\text{acc}} \tilde{\Lambda}_{\text{acc}}^{-1/2} \tilde{Q}_{\text{acc}}^H \tilde{H}_{\text{rad}} \tilde{Q}_{\text{acc}} \tilde{\Lambda}_{\text{acc}}^{-1/2} \tilde{Q}_{\text{acc}}^H \tilde{U} \quad (\text{A.17})$$

$$= \tilde{U}^H \tilde{H}_{\text{acc}}^{-1/2} \tilde{H}_{\text{rad}} \tilde{H}_{\text{acc}}^{-1/2} \tilde{U}. \quad (\text{A.18})$$

Above expression defines the set of radiation matrices $\tilde{H}_{\text{rad},S}$ obtainable with a *lossy* antenna array and a *lossless* decoupling and matching network. Since we are interested the eigenvalues of $\tilde{H}_{\text{rad},S}$, we set $\tilde{H}_{\text{rad},S} = \tilde{A}\tilde{B}\tilde{C}$ with $\tilde{A} = \tilde{U}^H \tilde{H}_{\text{acc}}^{-1/2}$, $\tilde{B} = \tilde{H}_{\text{rad}}$, and $\tilde{C} = \tilde{H}_{\text{acc}}^{-1/2} \tilde{U}$. According to Proposition 2 the eigenvalues of the two products $\tilde{A}\tilde{B}\tilde{C}$ and $\tilde{C}\tilde{A}\tilde{B}$ are identical. The second product finally simplifies to

$$\tilde{C}\tilde{A}\tilde{B} = \tilde{H}_{\text{acc}}^{-1/2} \tilde{U} \tilde{U}^H \tilde{H}_{\text{acc}}^{-1/2} \tilde{H}_{\text{rad}} = \tilde{H}_{\text{acc}}^{-1} \tilde{H}_{\text{rad}}. \quad (\text{A.19})$$

The eigenefficiencies obtained by using a *lossless* network to decouple and match the ports of a *lossy* antenna array are given by the eigenvalues of above matrix product and are thus independent of the type of DMN chosen. \square

A.3 Matrix-form of a single-port matching network

The following derives the 2×2 scattering matrix of a lossless and reciprocal network for matching an arbitrary impedance with reflection coefficient Γ to the system normalising impedance. First, the scattering matrix is partitioned into its elements, the scalar scattering coefficients:

$$\tilde{S}_M = \begin{pmatrix} s_{M,11} & s_{M,12} \\ s_{M,21} & s_{M,22} \end{pmatrix}. \quad (\text{A.20})$$

These are the unknowns in the system of equations we are going to establish. As mentioned above, the network is supposed to be reciprocal, therefore $\tilde{S}_M = \tilde{S}_M^T$ and hence

$$s_{M,12} = s_{M,21}. \quad (\text{A.21})$$

Furthermore, the network ought to be lossless, which requires \tilde{S}_M to be unitary. We have $\tilde{S}_M^H \tilde{S}_M = \tilde{I}$, which imposes the following conditions on the network

$$|s_{M,11}|^2 + |s_{M,12}|^2 = 1, \quad (\text{A.22})$$

$$|s_{M,22}|^2 + |s_{M,12}|^2 = 1, \quad (\text{A.23})$$

and

$$s_{M,12}^* s_{M,11} + s_{M,22}^* s_{M,12} = 0. \quad (\text{A.24})$$

Equation (B.14) provides an expression for the input reflection coefficient Γ_S , which we would like to vanish. So the final requirement is

$$\Gamma_S = s_{M,11} + \frac{s_{M,12}^2 \Gamma}{1 - s_{M,22} \Gamma} = 0, \quad (\text{A.25})$$

or, alternatively

$$-s_{M,11}(1 - s_{M,22} \Gamma) = s_{M,12}^2 \Gamma. \quad (\text{A.26})$$

Rearranging (A.24) for $s_{M,11}$ and substituting into (A.26) yields

$$\begin{aligned} \frac{s_{M,22}^* s_{M,12}}{s_{M,12}^*} (1 - s_{M,22} \Gamma) &= s_{M,12}^2 \Gamma \\ s_{M,22}^* (1 - s_{M,22} \Gamma) &= |s_{M,12}|^2 \Gamma \\ s_{M,22}^* (1 - s_{M,22} \Gamma) &= (1 - |s_{M,22}|^2) \Gamma \\ s_{M,22}^* - |s_{M,22}|^2 \Gamma &= \Gamma - |s_{M,22}|^2 \Gamma \\ s_{M,22} &= \Gamma^*, \end{aligned} \quad (\text{A.27})$$

where condition (A.23) was used in the third step. This determines $s_{M,22}$. In order to solve for $s_{M,12}$ we recognise that requirement (A.23) is fulfilled for

$$s_{M,12} = u \sqrt{1 - |\Gamma|^2} \quad (\text{A.28})$$

with arbitrary u having unit modulus, i.e., $u = e^{j\varphi}$ for arbitrary real φ . For the final parameter $s_{M,11}$, we rearrange (A.24) and obtain:

$$\begin{aligned} s_{M,11} &= \frac{-u \Gamma \sqrt{1 - |\Gamma|^2}}{u^* \sqrt{1 - |\Gamma|^2}} \\ &= -u^2 \Gamma. \end{aligned} \quad (\text{A.29})$$

Note that requirement (A.22) was not explicitly used in the derivation, but it can easily be shown that it is satisfied by above set of solutions.

A.4 Matrix-form of a decoupling and matching network

The derivation of a general form for the scattering matrix \tilde{S}_M of a decoupling and matching network for a reciprocal antenna array \tilde{S} follows along the same lines as the ordinary matching network. Before we begin, we need a number of propositions and definitions:

Proposition 4. *Let \tilde{H} be a complex Hermitian matrix and let $\tilde{Q}\tilde{\Lambda}\tilde{Q}^H$ be its spectral decomposition with \tilde{Q} unitary and $\tilde{\Lambda}$ real non-negative and diagonal. Then there is a matrix \tilde{A} such that $\tilde{B}\tilde{B}^H = \tilde{H}$. This matrix is not unique.*

Proof. The solution is

$$\tilde{B} = \tilde{Q} \sqrt{\tilde{\Lambda}} \tilde{U}, \quad (\text{A.30})$$

with \tilde{U} unitary and arbitrary and where the square root operates element-wise on $\tilde{\Lambda}$. Substitution into the original requirement concludes the proof

$$\tilde{B}\tilde{B}^H = \tilde{Q} \sqrt{\tilde{\Lambda}} \tilde{U} \tilde{U}^H \sqrt{\tilde{\Lambda}} \tilde{Q}^H = \tilde{Q} \tilde{\Lambda} \tilde{Q}^H = \tilde{H}. \quad (\text{A.31})$$

□

Definition 5. *We define the square-root of a Hermitian matrix \tilde{H} with spectral decomposition $\tilde{Q}\tilde{\Lambda}\tilde{Q}^H$ as*

$$\tilde{R} = \tilde{H}^{1/2} = \tilde{Q} \sqrt{\tilde{\Lambda}} \tilde{Q}^H. \quad (\text{A.32})$$

This square-root is Hermitian and thus $\tilde{R}\tilde{R} = \tilde{R}\tilde{R}^H = \tilde{R}^H\tilde{R} = \tilde{H}$.

Proposition 6. *Let \tilde{X} be a complex and normal matrix, i.e., let $\tilde{X}\tilde{X}^H = \tilde{X}^H\tilde{X}$. Then $(\tilde{I} - \tilde{X}^H\tilde{X})^{1/2} \tilde{X} (\tilde{I} - \tilde{X}^H\tilde{X})^{-1/2} = \tilde{X}$.*

Proof. Since \tilde{X} is normal [8, Section 2.5], there is a decomposition $\tilde{X} = \tilde{A}\tilde{\Phi}\tilde{A}^H$ such that \tilde{A} is unitary and $\tilde{\Phi}$ diagonal complex. We can thus write

$$(\tilde{I} - \tilde{X}^H \tilde{X})^{1/2} \tilde{X} (\tilde{I} - \tilde{X}^H \tilde{X})^{-1/2} \quad (\text{A.33})$$

$$= (\tilde{I} - \tilde{A}\tilde{\Phi}\tilde{A}^H\tilde{A}\tilde{\Phi}\tilde{A}^H)^{1/2} \tilde{A}\tilde{\Phi}\tilde{A}^H (\tilde{I} - \tilde{A}\tilde{\Phi}\tilde{A}^H\tilde{A}\tilde{\Phi}\tilde{A}^H)^{-1/2} \quad (\text{A.34})$$

$$= (\tilde{A} (\tilde{I} - \tilde{\Phi}\tilde{\Phi}) \tilde{A}^H)^{1/2} \tilde{A}\tilde{\Phi}\tilde{A}^H (\tilde{A} (\tilde{I} - \tilde{\Phi}\tilde{\Phi}) \tilde{A}^H)^{-1/2} \quad (\text{A.35})$$

$$= \tilde{A} (\sqrt{\tilde{I} - \tilde{\Phi}\tilde{\Phi}})^{1/2} \tilde{A}^H \tilde{A}\tilde{\Phi}\tilde{A}^H \tilde{A} (\sqrt{\tilde{I} - \tilde{\Phi}\tilde{\Phi}})^{-1/2} \tilde{A}^H \quad (\text{A.36})$$

$$= \tilde{A} (\sqrt{\tilde{I} - \tilde{\Phi}\tilde{\Phi}})^{1/2} \tilde{\Phi} (\sqrt{\tilde{I} - \tilde{\Phi}\tilde{\Phi}})^{-1/2} \tilde{A}^H. \quad (\text{A.37})$$

Since the three matrices between \tilde{A} and \tilde{A}^H are diagonal, they commute and the square root terms cancel:

$$\dots = \tilde{A}\tilde{\Phi}\tilde{A}^H = \tilde{X}. \quad (\text{A.38})$$

□

Proposition 7. *Given a complex symmetric matrix $\tilde{S} = \tilde{S}^T$, a complex Hermitian matrix $\tilde{H} = \tilde{I} - \tilde{S}^H \tilde{S}$, and its spectral decomposition $\tilde{H} = \tilde{Q}\tilde{\Lambda}\tilde{Q}^H$ it follows that $\tilde{X} = \tilde{Q}^T \tilde{S} \tilde{Q}$ is normal.*

Proof. We recognise that, with $\tilde{S} = \tilde{S}^T$,

$$\tilde{H}^T = \tilde{I} - \tilde{S}^T \tilde{S}^* = \tilde{I} - \tilde{S} \tilde{S}^H. \quad (\text{A.39})$$

Proceeding with the condition for matrix normality,

$$\tilde{X}\tilde{X}^H = \tilde{X}^H\tilde{X}, \quad (\text{A.40})$$

we obtain

$$\tilde{Q}^T \tilde{S} \tilde{Q} \tilde{Q}^H \tilde{S}^H \tilde{Q}^* = \tilde{Q}^H \tilde{S}^H \tilde{Q}^* \tilde{Q}^T \tilde{S} \tilde{Q} \quad (\text{A.41})$$

$$\tilde{Q}^T \tilde{S} \tilde{S}^H \tilde{Q}^* = \tilde{Q}^H \tilde{S}^H \tilde{S} \tilde{Q} \quad (\text{A.42})$$

$$\tilde{Q}^T (\tilde{I} - \tilde{H}^T) \tilde{Q}^* = \tilde{Q}^H (\tilde{I} - \tilde{H}) \tilde{Q} \quad (\text{A.43})$$

$$\tilde{I} - \tilde{\Lambda} = \tilde{I} - \tilde{\Lambda}. \quad (\text{A.44})$$

□

Proposition 8. *Given is a complex symmetric matrix $\tilde{S} = \tilde{S}^T$, a complex Hermitian matrix $\tilde{H} = \tilde{I} - \tilde{S}^H \tilde{S}$, and its spectral decomposition $\tilde{H} = \tilde{Q} \tilde{\Lambda} \tilde{Q}^H$. Then $\tilde{Q}^* \tilde{\Lambda}^{1/2} \tilde{Q}^T \tilde{S} \tilde{Q} \tilde{\Lambda}^{-1/2} \tilde{Q}^H = \tilde{S}$*

Proof. As in Proposition 7 we define a matrix $\tilde{X} = \tilde{Q}^T \tilde{S} \tilde{Q}$ and recognise that $\tilde{\Lambda} = \tilde{I} - \tilde{X}^H \tilde{X}$. We rewrite the original expression in terms of \tilde{X} :

$$\tilde{Q}^* \tilde{\Lambda}^{1/2} \tilde{Q}^T \tilde{S} \tilde{Q} \tilde{\Lambda}^{-1/2} \tilde{Q}^H = \tilde{Q}^* (\tilde{I} - \tilde{X}^H \tilde{X})^{1/2} \tilde{X} (\tilde{I} - \tilde{X}^H \tilde{X})^{-1/2} \tilde{Q}^H. \quad (\text{A.45})$$

By Proposition 6 this simplifies to $\tilde{Q}^* \tilde{X} \tilde{Q}^H$ and thus yields $\tilde{Q}^* \tilde{Q}^T \tilde{S} \tilde{Q} \tilde{Q}^H = \tilde{S}$. \square

Let us begin with the derivation of the DMN scattering matrix \tilde{S}_M . First, we write \tilde{S}_M as a block-matrix.

$$\tilde{S}_M = \begin{pmatrix} \tilde{S}_{M,11} & \tilde{S}_{M,12} \\ \tilde{S}_{M,12}^T & \tilde{S}_{M,22} \end{pmatrix}. \quad (\text{A.46})$$

The $\tilde{S}_{M,21}$ element has been replaced by $\tilde{S}_{M,12}^T$ because the DMN is supposed to be reciprocal. For the same reason we have

$$\tilde{S}_{M,11} = \tilde{S}_{M,11}^T \quad \text{and} \quad \tilde{S}_{M,22} = \tilde{S}_{M,22}^T. \quad (\text{A.47})$$

We further want the DMN to be lossless, i.e., $\tilde{S}_M \tilde{S}_M^H = \tilde{I}$. Expansion of the block-matrix yields

$$\tilde{S}_{M,11} \tilde{S}_{M,11}^H + \tilde{S}_{M,12} \tilde{S}_{M,12}^H = \tilde{I}, \quad (\text{A.48})$$

$$\tilde{S}_{M,22} \tilde{S}_{M,22}^H + \tilde{S}_{M,12}^T \tilde{S}_{M,12}^* = \tilde{I}, \quad (\text{A.49})$$

$$\text{and} \quad \tilde{S}_{M,11} \tilde{S}_{M,12}^* + \tilde{S}_{M,12} \tilde{S}_{M,22}^H = \tilde{0}. \quad (\text{A.50})$$

Lastly, we have to formulate the objective that the network actually decouples and matches the reciprocal load antenna array \tilde{S} . With (B.14) we have

$$\tilde{S}_{M,11} + \tilde{S}_{M,12} \tilde{S} (\tilde{I} - \tilde{S}_{M,22} \tilde{S})^{-1} \tilde{S}_{M,12}^T = \tilde{0}. \quad (\text{A.51})$$

We continue with above equation and multiply from the right by $\tilde{S}_{M,12}^*$. Thus

$$-\tilde{S}_{M,11} \tilde{S}_{M,12}^* = \tilde{S}_{M,12} \tilde{S} (\tilde{I} - \tilde{S}_{M,22} \tilde{S})^{-1} \tilde{S}_{M,12}^T \tilde{S}_{M,12}^*. \quad (\text{A.52})$$

The left-hand side is replaced with the help of (A.50) and the last factor on the right-hand side is replaced with (A.49):

$$\tilde{S}_{M,12} \tilde{S}_{M,22}^H = \tilde{S}_{M,12} \tilde{S} (\tilde{I} - \tilde{S}_{M,22} \tilde{S})^{-1} (\tilde{S} - \tilde{S}_{M,22} \tilde{S}_{M,22}^H). \quad (\text{A.53})$$

Disregarding the meaningless solution $\tilde{S}_{M,12} = \tilde{0}$, this equation is fulfilled for

$$\tilde{S}_{M,22} = \tilde{S}^H, \quad \text{or, since } \tilde{S} = \tilde{S}^T, \quad \tilde{S}_{M,22} = \tilde{S}^*. \quad (\text{A.54})$$

We substitute this result back into (A.49) and obtain

$$\tilde{S}_{M,12}^T \tilde{S}_{M,12}^* = \tilde{I} - \tilde{S}^* \tilde{S}^T \quad \text{and thus} \quad \tilde{S}_{M,12}^H \tilde{S}_{M,12} = \tilde{I} - \tilde{S} \tilde{S}^H. \quad (\text{A.55})$$

With Proposition 4 and Definition 5 the right-hand side factors as

$$\tilde{S}_{M,12}^H = [\tilde{I} - \tilde{S} \tilde{S}^H]^{1/2} \tilde{U}^* \quad \text{and thus} \quad \tilde{S}_{M,12} = \tilde{U}^T [\tilde{I} - \tilde{S} \tilde{S}^H]^{1/2}. \quad (\text{A.56})$$

This result is substituted into (A.50) and rearranged for $\tilde{S}_{M,11}$:

$$\tilde{S}_{M,11} = -\tilde{S}_{M,12} \tilde{S} (\tilde{S}_{M,12}^*)^{-1} \quad (\text{A.57})$$

$$= -\tilde{U}^T [\tilde{I} - \tilde{S} \tilde{S}^H]^{1/2} \tilde{S} \left(([\tilde{I} - \tilde{S} \tilde{S}^H]^{1/2})^* \right)^{-1} \tilde{U}. \quad (\text{A.58})$$

With Definition 5, (A.39), and Proposition 8 this simplifies to

$$\tilde{S}_{M,11} = -\tilde{U}^T \tilde{Q}^* \tilde{\Lambda}^{1/2} \tilde{Q}^T \tilde{S} ((\tilde{Q}^* \tilde{\Lambda}^{1/2} \tilde{Q}^T)^*)^{-1} \tilde{U} \quad (\text{A.59})$$

$$= -\tilde{U}^T \tilde{Q}^* \tilde{\Lambda}^{1/2} \tilde{Q}^T \tilde{S} \tilde{Q} \tilde{\Lambda}^{-1/2} \tilde{Q}^H \tilde{U} \quad (\text{A.60})$$

$$= -\tilde{U}^T \tilde{S} \tilde{U}. \quad (\text{A.61})$$

The general expression for the scattering matrix \tilde{S}_M of a lossless and reciprocal decoupling and matching network for a reciprocal antenna \tilde{S} is thus given by

$$\tilde{S}_M = \begin{pmatrix} -\tilde{U}^T \tilde{S} \tilde{U} & \tilde{U}^T [\tilde{I} - \tilde{S} \tilde{S}^H]^{1/2} \\ ([\tilde{I} - \tilde{S} \tilde{S}^H]^{1/2})^T \tilde{U} & \tilde{S}^* \end{pmatrix}, \quad (\text{A.62})$$

with \tilde{U} unitary but otherwise arbitrary. The computation of the matrix square-roots in this solution does not demand for the Takagi-factorisation of \tilde{S} (cf. Section A.1); the familiar unitary decomposition of the radicand is thus sufficient. Note that the derivation did not explicitly make use of (A.48). It is, however, straightforward to show that this condition is also satisfied by above result.

A.5 Eigenmodes fade independently

Proposition 9. *The eigenmodes of a lossless and reciprocal but otherwise arbitrary multi-port antenna array fade independently in a uniform Rayleigh environment.*

Proof. Although is implicated by Wallace and Jensen [81, Eqn. (31)], a more detailed proof is presented here due to its fundamental significance to the idea of eigenmodes.

Let there be a reciprocal and lossless n -port antenna. As described in Section 2.3.1 the excitation of an individual port i with all other ports terminated with matched loads produces a far-field beam pattern described by a function $\vec{F}_i(\phi, \theta)$ dependent on azimuth $\phi \in [-\pi; \pi]$ and elevation $\theta \in [-\pi/2; \pi/2]$. In order to conserve space, we will concentrate on one-dimensional beam patterns in one polarisation for the first part of the proof. Thus, the $F_i(\phi)$ are complex-valued scalars dependent on azimuth only.

Let m plane waves impinge on the array from random directions ϕ_k distributed evenly across the azimuthal range. The k th wave has a random non-negative amplitude c_k with unknown distribution and a uniformly distributed random phase ψ_k . The complex waves b_i received at the antenna ports are the superposition of these waves weighted by the far-field response F_i in the direction ϕ_k :

$$b_i = \sum_{k=1}^m c_k F_i(\phi_k) e^{j\psi_k}. \quad (\text{A.63})$$

With a large number of plane waves m the distribution of the received signal b_i will approach a normal distribution by the central limit theorem [15, p. 159]. Because the phase angles ψ_k have uniform distribution, the b_i are circularly symmetric complex and zero mean. The covariance between ports i and j is given by

$$\begin{aligned} \text{Var} \{b_i, b_j\} &= \text{E} \{b_i b_j^*\} = \\ &= \int \cdots \int \left(\sum_{k=1}^m c_k F_i(\phi_k) e^{j\psi_k} \right) \left(\sum_{k=1}^m c_k F_j^*(\phi_k) e^{-j\psi_k} \right) \cdot \\ &\quad p_c(c_1) \cdots p_c(c_m) \cdot p_\phi(\phi_1) \cdots p_\phi(\phi_m) \cdot p_\psi(\psi_1) \cdots p_\psi(\psi_m) \\ &\quad \text{dc}_1 \cdots \text{dc}_m \text{d}\phi_1 \cdots \text{d}\phi_m \text{d}\psi_1 \cdots \text{d}\psi_m, \quad (\text{A.64}) \end{aligned}$$

where the limits of integration are taken over the range of the corresponding random variables. The probability density functions $p(\cdot)$ are

$$p_\phi(\phi) = p_\psi(\psi) = \frac{1}{2\pi}, \quad \text{and} \\ p_c(c) = \text{unknown.}$$

The product of sums can be factored out as

$$\sum_{k=1}^m c_k^2 F_i(\phi_k) F_j^*(\phi_k) + \sum_{k=1}^m \left(c_k F_i(\phi_k) \left(\sum_{\substack{l=1 \\ l \neq k}}^m c_l F_j^*(\phi_l) e^{-j\psi_l} \right) e^{j\psi_k} \right). \quad (\text{A.65})$$

The second sum vanishes when integrated in turn over the ψ_k , whereas the first sum is independent of any of the ψ_k . Thus, (A.64) can be written as

$$\text{Var} \{b_i, b_j\} = \int \cdots \int \left(\sum_{k=1}^m c_k^2 F_i(\phi_k) F_j^*(\phi_k) \right) p_c(c_1) \cdots \\ p_c(c_m) \cdot p_\phi(\phi_1) \cdots p_\phi(\phi_m) dc_1 \cdots dc_m d\phi_1 \cdots d\phi_m. \quad (\text{A.66})$$

Exchanging the order of integration and summation yields

$$\text{Var} \{b_i, b_j\} = \sum_{k=1}^m \left(\int_0^\infty \int_{-\pi}^\pi c_k^2 F_i(\phi_k) F_j^*(\phi_k) \cdot p_c(c_k) p_\phi(\phi_k) dc_k d\phi_k \right), \quad (\text{A.67})$$

which can be simplified further to

$$\text{Var} \{b_i, b_j\} = \frac{1}{2\pi} \text{E} \left\{ \sum_{k=1}^m c_k^2 \right\} \int_{-\pi}^\pi F_i(\phi) F_j^*(\phi) d\phi \\ \sim \int_{-\pi}^\pi F_i(\phi) F_j^*(\phi) d\phi. \quad (\text{A.68})$$

We conclude that the signals received by different beam patterns are uncorrelated if and only if above integral vanishes, i.e., if the two beam patterns are orthogonal. Because the b_i are Gaussian random variables we can further conclude that orthogonal beams fade *independently* [15, p. 158].

In order to extend the proof for two-dimensional radiation patterns in two polarizations the following amendments are necessary. The joint PDF of the azimuth ϕ and the elevation θ must be proportional to the unit surface element of the spherical coordinate system, i.e., $p_{\phi\theta}(\phi, \theta) = (\cos \theta)/(4\pi)$. We assume that, on average, the power incident on the array is shared equally between both orthogonal polarizations. So, the sum in (A.63) has to be duplicated, one sum for each polarization. Proceeding with the integration as above yields an expression similar to (A.68):

$$\text{Var} \{b_i, b_j\} \sim \iint \vec{F}_i^T(\phi, \theta) \cdot \vec{F}_j^*(\phi, \theta) \cos \theta \, d\phi \, d\theta, \quad (\text{A.69})$$

Again, beam pattern orthogonality implies independence of fading. This concludes the proof for two-dimensional radiation patterns in two polarizations. \square

A.6 Series expansion of the diversity gain

We sketch the derivation of the Maclaurin series expansion of the inverse function $\varrho = d^{-1}(p)$ of the CDF (4.20), which is required for the calculation of the diversity gain approximation (4.26). The problem that no closed-form expression exists for $\varrho = d^{-1}(p)$ is overcome by calculating all series coefficients from the Laplace transform of $d(\varrho)$. Familiarity with the integration rule, the differentiation rule, and the initial value theorem of the Laplace transform is assumed [18, Section 7.2.2]

We define a function $x(\varrho) = n! \det\{\tilde{H}\} d(\varrho)$ and examine its Laplace transform based on (4.11):

$$\begin{aligned} X(s) &= \frac{n! \det\{\tilde{H}\}}{s} P(s) = \frac{n! \det\{\tilde{H}\}}{s \det\{\tilde{I} + s\tilde{H}\}} \\ &= \frac{n!}{s \det\{\tilde{H}^{-1}\} \det\{\tilde{I} + s\tilde{H}\}} = \frac{n!}{s \det\{s\tilde{I} - (-\tilde{H}^{-1})\}} \end{aligned} \quad (\text{A.70})$$

The determinant in the denominator of the last term is now of the form used in [73], where it is shown that the coefficients of the characteristic polynomial of a matrix can be expressed in terms of traces of integer powers of that matrix. Thus, $X(s)$ can be written as

$$X(s) = \frac{n!}{s^{n+1} + a_1 s^n + a_2 s^{n-1} + \dots}, \quad (\text{A.71})$$

and the first three coefficients are

$$\begin{aligned} a_1 &= \tau_1 \\ a_2 &= \frac{1}{2} (\tau_1^2 - \tau_2) \\ a_3 &= \frac{1}{6} (\tau_1^3 - 3\tau_1\tau_2 + 2\tau_3), \end{aligned} \quad (\text{A.72})$$

with $\tau_i = \text{tr}\{\tilde{H}^{-i}\}$. Higher order coefficients are found with a recursion formula in [73], but usually this will be neither practical nor necessary. Coefficients a_i vanish for $i > n$, so the subsequent discussion is valid for any number of radiators n .

With the aid of the differentiation rule and the initial value theorem, we find the Maclaurin series of $x(\varrho)$,

$$\begin{aligned} x(\varrho) &\approx \varrho^n - \frac{a_1}{(n+1)} \varrho^{n+1} + \frac{a_1^2 - a_2}{(n+1)(n+2)} \varrho^{n+2} \\ &\quad - \frac{a_1^3 - 2a_2a_1 + a_3}{(n+1)(n+2)(n+3)} \varrho^{n+3} + \dots, \end{aligned} \quad (\text{A.73})$$

and its derivatives:

$$\begin{aligned} x'(\varrho) &= n\varrho^{n-1} - a_1\varrho^n + \dots \\ x''(\varrho) &= (n-1)n\varrho^{n-2} - a_1n\varrho^{n-1} + \dots \\ &\dots \end{aligned} \quad (\text{A.74})$$

Then we define a function $y(\varrho) = \sqrt[n]{x(\varrho)}$ and use

$$\begin{aligned} y'(\varrho) &= \frac{1}{n} \left(x(\varrho)^{\frac{1}{n}-1} x'(\varrho) \right) \\ y''(\varrho) &= \frac{1}{n^2} \left(x(\varrho)^{\frac{1}{n}-2} \left((n-1)x'(\varrho)^2 + nx(\varrho)x''(\varrho) \right) \right) \\ &\dots \end{aligned} \quad (\text{A.75})$$

in conjunction with (A.73) and (A.74) to construct the series of $y(\varrho)$:

$$\begin{aligned} y(\varrho) &\approx \varrho - \frac{a_1}{n(n+1)} \varrho^2 \\ &\quad + \frac{(n^2 + n + 2) a_1^2 - 2n(n+1)a_2}{2n^2(n+1)^2(n+2)} \varrho^3 + \dots \end{aligned} \quad (\text{A.76})$$

Here it is important that for the evaluation of $y(0), y'(0), \dots$ a sufficient number of terms is included in the series of $x(\varrho)$, since otherwise indeterminate expression may arise. By virtue of power series inversion [1, p. 366], we obtain the series expansion of the inverse function $\varrho = y^{-1}(q)$:

$$\begin{aligned} \varrho = & q + \frac{\tau_1}{n^2 + n} q^2 + \frac{(4n + 6)\tau_1^2 - n(n + 1)\tau_2}{2n^2(n + 1)^2(n + 2)} q^3 \\ & + \frac{(16n^2 + 58n + 48)\tau_1^3 - 9n(n + 1)(n + 2)\tau_2\tau_1 + n^2(n + 1)^2\tau_3}{3n^3(n + 1)^3(n + 2)(n + 3)} q^4 \\ & + \dots, \end{aligned} \quad (\text{A.77})$$

where the coefficients a_i have been replaced by their trace-expressions (A.72). As a final step we set

$$q = \sqrt[n]{n! \det\{\tilde{H}\} p} \quad (\text{A.78})$$

and arrive at a closed-form approximation for the SNR-level ϱ , for which the CDF $d(\varrho)$ yields a given probability level p .

Appendix B

Waves, scattering parameters, and noise

In microwave engineering, scattering parameters are an established means for describing the linear behaviour of passive and active devices. Measurement equipment and device manufacturers usually specify scattering parameters with respect to a $50\ \Omega$ environment. There is nothing special about $50\ \Omega$ other than the fact that, for seamless interoperability, most commercial microwave components, such as coaxial cables, attenuators, or amplifiers, are in some way optimised with regard to this impedance. When designing components to fit into this system, $50\ \Omega$ scattering parameters present a perfectly appropriate tool for analysis. The reflection coefficient, for instance, is an intuitive indicator for the quality of the impedance match (with respect to $50\ \Omega$) at a particular device terminal.

For the development outside this standard framework, however, $50\ \Omega$ scattering parameters may be more of a hindrance than a help (cf. [125]). Consider for example an amplifier, which happens to have an output impedance of $10\ \Omega$, and an antenna with a terminal impedance of $5\ \Omega$. In many cases, the impedance match between both devices will be considered acceptable. Yet, there is no insightful way to assess the quality of the im-

pedance match from the $50\ \Omega$ -based reflection coefficient (cf. Hoffmann [6, Eqn. (5.51)]).

If we wished to optimise above antenna array for optimum power match to the amplifier, it would be desirable to express its reflection coefficient with respect to the amplifier's impedance. Especially when it comes to the evaluation of multi-port antennas, the possibility to normalise scattering matrices to arbitrary impedances presents a powerful tool because it keeps explicit occurrences of the amplifier impedances out of the analysis. Formulae become more compact and are thus easier both to interpret and to remember. Scattering parameter renormalisation essentially separates the problem of evaluating the interplay between an antenna array and a set of amplifiers into two smaller *independent* problems: *first* the normalisation with respect to the amplifier's impedances and *then* the analysis or optimisation of the antenna array as an independent problem.

Scattering parameter renormalisation is a long known concept. Unfortunately, there are two competing and incompatible extensions of classical transmission line theory to complex normalising impedances [125]. Each method has its specific advantages and drawbacks. One concept is called *pseudo-waves* and claims to closely model the wave propagation phenomena that physically take place on transmission lines even for complex line impedances [59, 60]. The other concept due to Youla [86] and Kurokawa [11, 54] is called *power waves* and yields especially simple expressions (cf. (B.4)) for the power transferred from one device to another. Since the present thesis mainly concerns the power flow between an antenna array and some load, the choice of power waves was a natural one. Additional information on traditional wave and scattering parameter theory is given by Hoffmann [6]. However, attention must be paid since not all concepts can be generalised to power waves; especially the well-known Smith chart requires special attention [54, Eqn. (13)], [63].

This appendix gives a concise review of the key concepts relevant to this thesis. Additional techniques for which no reference could be found are explained in little more detail. A final section is dedicated to the concept of noise waves, which, unlike the traditional approach based on noisy voltage and current sources, fits in with the idea of power waves and signal flow graph analysis. Familiarity with basic scattering parameter theory is assumed in the following.

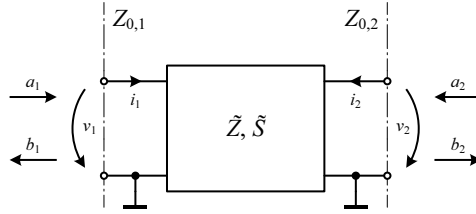


Fig. B.1: Voltages, currents, waves, and normalising impedances at a linear two-port junction described by its impedance matrix \tilde{Z} or its scattering matrix \tilde{S} .

B.1 Scattering parameters

B.1.1 Definition

Figure B.1 portrays a linear two-port junction. Both ports possess a common ground potential. One way to describe the junction is by the voltage v_k and by the current i_k at each port k . All voltages are referred to ground potential and all currents flow *into* the junction. The idea can be generalised to an arbitrary number of ports, n , by writing all voltages as a voltage column vector $\vec{v} = (v_1, v_2, \dots, v_n)^T$ and all currents as a current column vector $\vec{i} = (i_1, i_2, \dots, i_n)^T$. Then their linear relationship is written as

$$\vec{v} = \tilde{Z}\vec{i}, \quad (\text{B.1})$$

where \tilde{Z} is called the impedance matrix of the junction.

The junction can equivalently be described in terms scattering parameters. At each port we define two *power waves* a_k and b_k in terms of the port voltage v_k and i_k [54, Eqn. (1)]¹:

$$a_k = \frac{v_k + Z_{0,k}i_k}{2\sqrt{\text{Re}\{Z_{0,k}\}}} \quad \text{and} \quad b_k = \frac{v_k - Z_{0,k}^*i_k}{2\sqrt{\text{Re}\{Z_{0,k}\}}}, \quad (\text{B.2})$$

with

$$\vec{b} = \tilde{S}\vec{a}. \quad (\text{B.3})$$

The power wave a_k travels towards the junction and is commonly called the *incident wave*. Conversely the wave b_k is called the *reflected wave*. We call

¹There is a typographical error in the corresponding formulae in [11, Eqn. (5.74)]

$Z_{0,k}$ the *normalising impedance* of the k th port. The choice of $Z_{0,k}$ is entirely arbitrary as long as its real part is (strictly) greater than zero. In particular, the normalising impedance may be complex and every port may have a different impedance assigned to it. A junction port is said to be *matched* if it is terminated with its normalising impedance. This is a purely mathematical conception and holds regardless of any *physical* reflections that do or do not take place at that port.

An essential property of power waves, which is extensively exploited in the present work, is that the real power P_k transported into the junction via port k is given by [86, Eqn. (7)]

$$P_k = |a_k|^2 - |b_k|^2, \quad (\text{B.4})$$

that is, the (mathematical) power travelling towards the junction minus the power travelling away from the junction. The total amount of power dissipated in the junction is consequently given by the sum over all P_k .

Reciprocal junctions have $\tilde{S} = \tilde{S}^T$, i.e., their scattering matrix is symmetric. Lossless devices fulfil $\tilde{S}\tilde{S}^H = \tilde{I}$, i.e., their matrix is unitary [54].

Since conversion formulae between \tilde{Z} and \tilde{S} matrices are not relevant to the present thesis, they are omitted here and the interested reader is referred to Kurokawa [11, p. 222] or Kurokawa [54, Eqns. (18) and (19)]. Formulae for changing the normalising impedances of scattering matrices and related quantities are given later on. In this context we will only state the definition of the reflection coefficient Γ of an impedance Z normalised to impedance Z_0 :

$$\Gamma = \frac{b}{a} = \frac{Z - Z_0^*}{Z + Z_0}. \quad (\text{B.5})$$

Beware that certain rules apply to the choice of the $Z_{0,k}$ when it comes to connecting two junctions together. These are explained next.

B.1.2 Interconnection of multi-port junctions

In order to mathematically describe the behaviour of a combination of two or more multi-port junctions, boundary conditions must be defined at their interfaces. Consider Fig. B.2, which illustrates the voltages and currents as well as the waves at such an interface. The boundary conditions for the voltages and currents are easily established using Kirchhoff's laws:

$$v_2 = v_1 \quad \text{and} \quad i_2 = -i_1. \quad (\text{B.6})$$

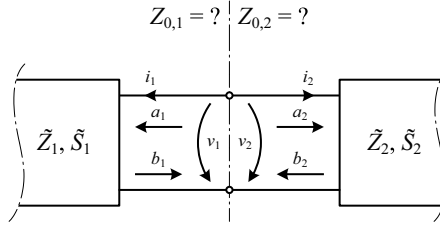


Fig. B.2: Close-up view on an interface between two connected multi-port junctions. The question is how to choose the normalising impedances of the two interfacing ports.

In the wave domain, the corresponding boundary conditions are what we would expect from intuition, i.e., the reflected wave b_1 of junction one becomes the incident wave a_2 of junction two, and vice-versa:

$$b_2 = a_1 \quad \text{and} \quad a_2 = b_1. \quad (\text{B.7})$$

Attention must be paid, however, to the normalising impedances $Z_{0,1}$ and $Z_{0,2}$ of the two interfacing ports. Let us therefore substitute the definitions of the wave quantities (B.2) as well as the voltage and current boundary conditions into $b_2 = a_1$:

$$a_1 = \frac{v_1 + Z_{0,1}i_1}{2\sqrt{\text{Re}\{Z_{0,1}\}}} = \frac{v_1 + Z_{0,2}^*i_1}{2\sqrt{\text{Re}\{Z_{0,2}\}}} = b_2 \quad (\text{B.8})$$

$$(v_1 + Z_{0,1}i_1) \sqrt{\text{Re}\{Z_{0,2}\}} = (v_1 + Z_{0,2}^*i_1) \sqrt{\text{Re}\{Z_{0,1}\}} \quad (\text{B.9})$$

$$v_1 (\sqrt{\text{Re}\{Z_{0,2}\}} - \sqrt{\text{Re}\{Z_{0,1}\}}) = i_1 (Z_{0,2}^* \sqrt{\text{Re}\{Z_{0,1}\}} - Z_{0,1} \sqrt{\text{Re}\{Z_{0,2}\}}). \quad (\text{B.10})$$

Clearly the last equation can only be fulfilled for all v_1 and i_1 if the parenthesized terms on both sides are zero, i.e., if $Z_{0,1} = Z_{0,2}^*$. The same holds for the waves $a_2 = b_1$ travelling in the opposite direction. Multi-port junctions described by scattering parameters can therefore only be combined if the normalising impedances at the respective interfaces are complex conjugates of each other. This applies to mathematical manipulations both in the form of matrix equations as well as signal flow graphs. In this thesis the correct nor-

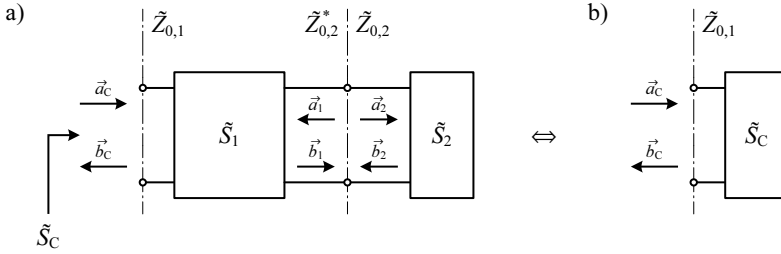


Fig. B.3: Clarification of the quantities involved in the interconnection of two multi-port junctions (a) and the resulting equivalent network (b).

malisation is therefore always indicated in block diagrams and signal flow graphs.

With this knowledge we will now derive the scattering matrix of the compound junction \tilde{S}_C that arises when a junction \tilde{S}_1 having n input and n output ports is terminated with an n -port junction \tilde{S}_2 as in Fig. B.3a. We begin by partitioning the $2n \times 2n$ matrix \tilde{S}_1 into block-matrices:

$$\tilde{S}_1 = \begin{pmatrix} \tilde{S}_{1,11} & \tilde{S}_{1,12} \\ \tilde{S}_{1,21} & \tilde{S}_{1,22} \end{pmatrix}. \quad (\text{B.11})$$

The ports indexed “1” refer to the left-hand side ports and the ports indexed “2” refer to the right-hand side ports. The linear relationship between the wave vectors in the figure can be expressed as

$$\begin{aligned} \vec{b}_C &= \tilde{S}_{1,11}\vec{a}_C + \tilde{S}_{1,12}\vec{a}_1 & \text{and} & & \vec{b}_2 &= \tilde{S}_2\vec{a}_2, \\ \vec{b}_1 &= \tilde{S}_{1,21}\vec{a}_C + \tilde{S}_{1,22}\vec{a}_1 \end{aligned} \quad (\text{B.12})$$

with the boundary conditions

$$\vec{a}_1 = \vec{b}_2 \quad \text{and} \quad \vec{a}_2 = \vec{b}_1. \quad (\text{B.13})$$

Note that *all* ports of \tilde{S}_1 may be normalised to *distinct* impedances as long as the conjugate impedance condition is met at the interface to \tilde{S}_2 . Solving above set of equations for \vec{b}_C in terms of \vec{a}_C yields

$$\vec{b}_C = \tilde{S}_C\vec{a}_C, \quad \text{with} \quad \tilde{S}_C = \tilde{S}_{1,11} + \tilde{S}_{1,12}\tilde{S}_2(\tilde{I} - \tilde{S}_{1,22}\tilde{S}_2)^{-1}\tilde{S}_{1,21}, \quad (\text{B.14})$$

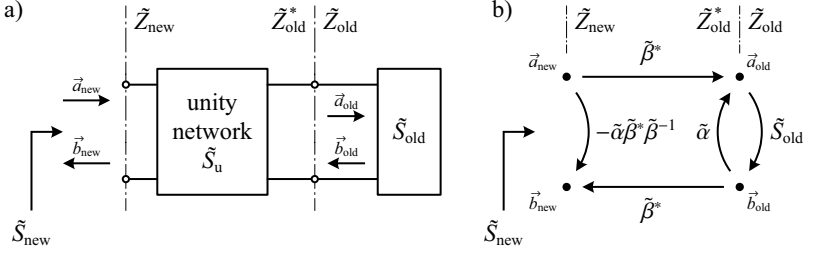


Fig. B.4: Interpretation of the renormalisation procedure by means of a unity network. (a) Wave quantities at the conceptual building blocks and (b) the corresponding signal flow graph.

where \tilde{S}_C is the scattering matrix of the combined network in Fig. B.3b. The resulting ports take on the normalisation of the input ports of \tilde{S}_1 .

B.1.3 Renormalisation

In most cases we can measure or simulate scattering matrices and far-field patterns only with respect to the standard $50\ \Omega$ normalisation impedance. In order to fully exploit the theory developed in this thesis, we need the ability to normalise our data to arbitrary complex impedances.

Renormalisation of power wave based scattering matrices was derived by Kurokawa [54, Eqn. (32)], however, the formulae given in [125, Eqn. (10)] will be preferred and stated here. We define the diagonal matrices $\tilde{Z}_{0,old}$ and $\tilde{Z}_{0,new}$ to denote the normalising impedances before and after renormalisation, respectively. The i th diagonal element contains the impedance assigned to port i . We define two diagonal auxiliary matrices

$$\tilde{\alpha} = \frac{\tilde{Z}_{0,new} - \tilde{Z}_{0,old}}{\tilde{Z}_{0,new} + \tilde{Z}_{0,old}^*} \quad \text{and} \quad \tilde{\beta} = \sqrt{\frac{\text{Re}\{\tilde{Z}_{0,new}\}}{\text{Re}\{\tilde{Z}_{0,old}\}}} \frac{\tilde{Z}_{0,old} + \tilde{Z}_{0,old}^*}{\tilde{Z}_{0,old} + \tilde{Z}_{0,new}}. \quad (\text{B.15})$$

Then the transformation between scattering matrices based on the old and the new normalisation is given by

$$\tilde{S}_{new} = \tilde{\beta}^{-1} (\tilde{S}_{old} - \tilde{\alpha}^*) (\tilde{I} - \tilde{\alpha} \tilde{S}_{old})^{-1} \tilde{\beta}^*. \quad (\text{B.16})$$

The problem of far-field pattern renormalisation can be solved by interpreting (B.16) as the interconnection of the original junction \tilde{S}_{old} and a “unity

network”, whose sole purpose is the translation of the normalising impedances. *Physically* this network is a direct (i.e., zero length) connection between its inputs and its outputs. *Mathematically* the network scattering matrix carries the new and the old normalisation at its inputs and outputs, respectively. This is illustrated in Fig. B.4a. The scattering matrix \tilde{S}_u of the unity network can be shown to be

$$\tilde{S}'_u = \begin{pmatrix} \tilde{0} & \tilde{I} \\ \tilde{I} & \tilde{0} \end{pmatrix} \xrightarrow{\text{renormalisation}} \tilde{S}_u = \begin{pmatrix} -\tilde{\alpha}\tilde{\beta}^*\tilde{\beta}^{-1} & \tilde{\beta}^* \\ \tilde{\beta}^* & \tilde{\alpha} \end{pmatrix} \quad (\text{B.17})$$

It is straightforward to prove that the cascade connection of \tilde{S}_u and \tilde{S}_{old} by virtue of (B.14) is indeed equivalent to the renormalisation according to (B.16) once one has realised that $\tilde{\alpha}\tilde{\alpha}^* + \tilde{\beta}\tilde{\beta}^* = \tilde{I}$.

The original set of n far-field patterns $\vec{F}_{\text{old},i}(\phi, \theta)$ describes the far-field response of the array when its i th port is excited with unit power and all other ports are terminated with matched loads. With reference to Fig. B.4 this is the case when the i th element of the old excitation vector \vec{a}_{old} is equal to one, and all other elements are zero. The renormalised set of far-field patterns $\vec{F}_{\text{new},i}(\phi, \theta)$ can thus be found by determining the excitations \vec{a}_{old} which belong to individual port excitations of the vector \vec{a}_{new} . From the set of matrix equations associated with the signal flow graph in the figure we obtain the following relationship between \vec{a}_{new} and \vec{a}_{old} :

$$\vec{a}_{\text{old}} = \tilde{\tau} \vec{a}_{\text{new}}, \quad \text{with} \quad \tilde{\tau} = (\tilde{I} - \tilde{\alpha}\tilde{S}_{\text{old}})^{-1} \tilde{\beta}^*. \quad (\text{B.18})$$

The excitations \vec{a}_{old} associated with individual port excitations of the renormalised antenna array are thus given by the columns of the matrix $\tilde{\tau}$. This finally leads us to the renormalisation formula for far-field patterns:

$$\vec{F}_{\text{new},i}(\phi, \theta) = \sum_{k=1}^n \tilde{\tau}_{ki} \vec{F}_{\text{old},k}(\phi, \theta), \quad (\text{B.19})$$

where $\tilde{\tau}_{ki}$ denotes the matrix element in row k and column i .

Most ideas in this thesis are, however, not based on the far-field patterns themselves but rather on a derived quantity: the radiation matrix \tilde{H} , which in later chapters becomes the covariance matrix of the received signal envelopes. Since \tilde{H} is either based on the scattering matrix or, in some way, on the far-field patterns of the array, renormalised versions can in principle be determined by renormalising the underlying quantities and then recomputing \tilde{H} .

A much simpler method makes use of the helper matrix $\tilde{\tau}$ introduced above. Pursuant to Section 3.5 on page 64 we have

$$\tilde{H}_{\text{new}} = \tilde{\tau}^H \tilde{H}_{\text{old}} \tilde{\tau}. \quad (\text{B.20})$$

B.2 Noise wave description

Working with *signal* waves and their “flow” through signal flow graphs is common practice in the field of microwave engineering. It is probably one of the reasons for the popularity of scattering parameters and signal flow graphs [6, Chapter 9]. On the contrary, the *noise* properties of a system are usually examined in terms of equivalent voltage and current sources. In order to investigate the signal *and* the noise behaviour, one has to switch between the wave domain on the one hand, and the impedance domain on the other; the system equations must consequently be derived twice and the descriptive signal flow graph analysis is available for only part of the problem.

Yet there is in fact little difference between signals and noise—both are time-varying electric and magnetic fields that propagate through a microwave circuit. Differences arise only in their respective descriptions. Whereas we can assign a definite amplitude and phase to some signal wave a , we cannot do so for a noise wave v because noise is a random phenomenon. We can however model the properties of noise waves, namely its power and, for more than one noise wave, the correlations between them. This topic was rigorously treated by Bosma [118]; the essence of his work is summarised in [16] and the application of noise waves to the analysis of noisy amplifiers is demonstrated in [4, 65].

In the following, a concise overview of the mathematics behind noise waves in the context of linear microwave systems will be given. For the understanding of the present thesis, it suffices to treat noise waves as complex zero-mean Gaussian random variables with equal variance in the real and the imaginary part. Such a random variable is uniquely characterised by its variance, which happens to be the *power* of the travelling noise wave. Compare

$$P_{\text{signal}} = |a|^2 = aa^* \quad \text{to} \quad P_{\text{noise}} = \text{E} \{ |v|^2 \} = \text{E} \{ vv^* \} = kT_v B, \quad (\text{B.21})$$

where T_v is the equivalent noise temperature, B the bandwidth under consideration, and $k = 1.3806504 \text{ J/K}$ the Boltzmann constant. The noise temperature T_v is a function of frequency in the same way as a . The expectation

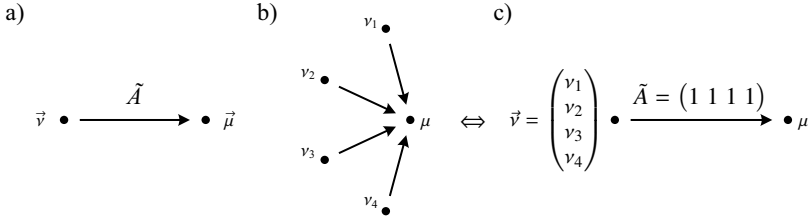


Fig. B.5: Linear transformations on noise waves. (a) Via a path in a signal flow graph or (b) by superposition. Superposition of correlated noise waves must be calculated according to its equivalent representation (c).

operator performs the necessary conversion from the random to the deterministic domain. The presence of several noise waves v_1, v_2, \dots, v_m in a system is uniquely modelled by the $m \times m$ covariance matrix or, alternatively, their equivalent matrix of temperatures:

$$\text{Var} \{ \vec{v} \} = \text{E} \{ \vec{v} \vec{v}^H \} = k \tilde{T}_v B, \quad \text{with} \quad \vec{v} = \begin{pmatrix} v_1 \\ v_2 \\ \vdots \\ v_m \end{pmatrix}. \quad (\text{B.22})$$

If all noise waves are uncorrelated, then the matrix \tilde{T}_v is diagonal. In any case, the diagonal elements equal the variances of the respective waves and thus their noise powers.

The effect on the covariance matrix when noise waves undergo a linear transformation, i.e., traverse a path in a signal flow graph, is straightforward to derive. Consider Fig. B.5a where a set of noise waves \vec{v} is transformed into waves $\vec{\mu}$ by the linear operation \tilde{A} . Then

$$\vec{\mu} = \tilde{A} \vec{v} \quad (\text{B.23})$$

and thus

$$\begin{aligned} \text{Var} \{ \vec{\mu} \} &= \text{E} \{ \vec{\mu} \vec{\mu}^H \} = \text{E} \left\{ \tilde{A} \vec{v} (\tilde{A} \vec{v})^H \right\} = \tilde{A} \text{E} \{ \vec{v} \vec{v}^H \} \tilde{A}^H \\ &= \tilde{A} \text{Var} \{ \vec{v} \} \tilde{A}^H, \end{aligned} \quad (\text{B.24})$$

where the matrix \tilde{A} need not be square necessarily. An important example of a non-square \tilde{A} is the superposition of several waves at a node, as in Fig. B.5b.

If the waves exhibit mutual correlation, their powers cannot simply be added. Instead the addition must be written in form of a matrix product

$$\mu = \nu_1 + \nu_2 + \nu_3 + \nu_4 = \begin{pmatrix} 1 & 1 & 1 & 1 \end{pmatrix} \cdot \begin{pmatrix} \nu_1 \\ \nu_2 \\ \nu_3 \\ \nu_4 \end{pmatrix} = \tilde{A} \cdot \vec{\nu} \quad (\text{B.25})$$

as in Fig. B.5c, so the variance (power) of the result μ can be calculated by virtue of (B.24):

$$\text{E} \{ |\mu|^2 \} = \tilde{A} \text{Var} \{ \vec{\nu} \} \tilde{A}^H = \begin{pmatrix} 1 & 1 & 1 & 1 \end{pmatrix} \cdot \text{Var} \{ \vec{\nu} \} \cdot \begin{pmatrix} 1 \\ 1 \\ 1 \\ 1 \end{pmatrix}. \quad (\text{B.26})$$

Bibliography

Books

- [1] G. ARFKEN and H. J. WEBER, *Mathematical Methods for Physicists*, 6th ed. Burlington, MA, USA: Elsevier Academic Press., 2005.
- [2] C. A. BALANIS, *Antenna Theorie: Analysis and Design*, 2nd ed. New York, USA: Wiley, 1997.
- [3] C. D. CANTRELL, *Modern Mathematical Methods for Physicists and Engineers*, 1st ed. Cambridge, UK: Cambridge Univ. Press, 2000.
- [4] J. ENGBERG and T. LARSEN, *Noise Theory of Linear and Nonlinear Circuits*. New York, USA: Wiley, 1995.
- [5] R. C. HANSEN, *Phased Array Antennas*, 1st ed. New York, USA: Wiley, 1998.
- [6] M. HOFFMANN, *Hochfrequenztechnik - Ein systemtheoretischer Zugang*. Berlin, Germany: Springer-Verlag, 1997.
- [7] J.-S. HONG and M. J. LANCASTER, *Microstrip Filters for RF/Microwave Applications*. New York, USA: Wiley Interscience, 2001.
- [8] R. A. HORN and C. R. JOHNSON, *Matrix Analysis*, 1st ed. Cambridge, UK: Cambridge Univ. Press, 1985.
- [9] W. C. JAKES, Ed., *Microwave Mobile Communications*, 1st ed. Piscataway, NJ, USA: IEEE Press, 1994.

- [10] J. D. KRAUS and R. J. MARHEFKA, *Antennas for all Applications*, 3rd ed. Boston, MA, USA: McGraw-Hill, 2002.
- [11] K. KUROKAWA, *An Introduction to the Theory of Microwave Circuits*. New York, USA: Academic Press, 1969.
- [12] A. J. PAULRAJ, R. NABAR, and D. GORE, *Introduction to Space-Time Wireless Communications*. Cambridge, UK: Cambridge Univ. Press, 2003.
- [13] D. M. POZAR, *Microwave Engineering*, 2nd ed. New York, USA: Wiley, 1998.
- [14] J. G. PROAKIS, *Digital Communications*, 4th ed. New York, USA: McGraw-Hill, 2001.
- [15] J. G. PROAKIS and M. SALEHI, *Communication Systems Engineering*, 2nd ed. Upper Saddle River, NJ, USA: Prentice Hall, 2002.
- [16] B. SCHIEK and H.-J. SIWERIS, *Rauschen in Hochfrequenzschaltungen*. Heidelberg, Germany: Hüthig, 1990.
- [17] M. SCHWARTZ, W. R. BENNETT, and S. STEIN, *Communication Systems and Techniques*, 1st ed. New York, USA: McGraw-Hill, 1966.
- [18] H.-U. SEIDEL and E. WAGNER, *Allgemeine Elektrotechnik*, 2nd ed. Munich, Germany: Carl Hanser Verlag, 2000, vol. 2.
- [19] S. W. SMITH, *Digital Signal Processing: A Practical Guide for Engineers and Scientists*. Oxford, UK: Elsevier Ltd., 2002.
- [20] H. L. VAN TREES, *Detection, Estimation, and Modulation Theory, Part IV*. New York, USA: Wiley Interscience, 2002.

Refereed journal papers

- [21] A. K. AGRAWAL and G. F. MIKUCKI, "A printed-circuit hybrid-ring directional coupler for arbitrary power divisions," *IEEE Trans. Microw. Theory Tech.*, vol. 34, no. 12, pp. 1401–1407, Dec. 1986.

- [22] J. BACH ANDERSEN and F. HANSEN, "Antennas for VHF/UHF personal radio: A theoretical and experimental study of characteristics and performance," *IEEE Trans. Veh. Technol.*, vol. 26, no. 4, pp. 349–357, Nov. 1977.
- [23] J. BACH ANDERSEN and H. H. RASMUSSEN, "Decoupling and descattering networks for antennas," *IEEE Trans. Antennas Propag.*, vol. 24, no. 6, pp. 841–846, Nov. 1976.
- [24] S. BLANCH, J. ROMEU, and I. CORBELLA, "Exact representation of antenna system diversity performance from input parameter description," *Electron. Lett.*, vol. 39, no. 9, pp. 705–707, May 2003.
- [25] C. BRAUN, G. ENGBLOM, and C. BECKMAN, "Evaluation of antenna diversity performance for mobile handsets using 3-D measurement data," *IEEE Trans. Antennas Propag.*, vol. 47, no. 11, pp. 1736–1738, Nov. 1999.
- [26] D. G. BRENNAN, "Linear diversity combining techniques," *Proc. IRE*, vol. 47, no. 6, pp. 1075–1102, Jun. 1959.
- [27] D. W. BROWNE, M. MANTEGHI, M. P. FITZ, and Y. RAHMAT-SAMII, "Experiments with compact antenna arrays for MIMO radio communications," *IEEE Trans. Antennas Propag.*, vol. 54, no. 11, pp. 3239–3250, Nov. 2006.
- [28] S. H. CHAE, S.-K. OH, and S.-O. PARK, "Analysis of mutual coupling, correlations, and TARC in WiBro MIMO array antenna," *IEEE Antennas Wireless Propag. Lett.*, vol. 6, pp. 122–125, 2007.
- [29] S.-C. CHEN, Y.-S. WANG, and S.-J. CHUNG, "A decoupling technique for increasing the port isolation between two strongly coupled antennas," *IEEE Trans. Antennas Propag.*, vol. 56, no. 12, pp. 3650–3658, Dec. 2008.
- [30] C. C. CHIAU, X. CHEN, and C. G. PARINI, "A compact four-element diversity-antenna array for PDA terminals in a MIMO system," *Microw. Opt. Technol. Lett.*, vol. 44, no. 5, pp. 408–412, Mar. 2005.

- [31] J. C. COETZEE and Y. YU, "Port decoupling for small arrays by means of an eigenmode feed network," *IEEE Trans. Antennas Propag.*, vol. 56, no. 6, pp. 1587–1593, Jun. 2008.
- [32] R. L. CUPO and R. D. GITLIN, "Adaptive carrier recovery systems for digital data communications receivers," *IEEE J. Sel. Areas Commun.*, vol. 7, no. 9, pp. 1328–1339, Dec. 1989.
- [33] T. A. DENIDNI, D. McNEIL, and G. Y. DELISLE, "Experimental investigations of a new adaptive dual-antenna array for handset applications," *IEEE Trans. Veh. Technol.*, vol. 52, no. 6, pp. 1417–1423, Nov. 2003.
- [34] A. DIALLO, C. LUXEY, P. LE THUC, R. STARAJ, and G. KOSSIAVAS, "Study and reduction of the mutual coupling between two mobile phone PIFAs operating in the DCS1800 and UMTS bands," *IEEE Trans. Antennas Propag.*, vol. 54, no. 11, pp. 3063–3074, Nov. 2006.
- [35] C. B. DIETRICH, JR., K. DIETZE, J. R. NEALY, and W. L. STUTZMAN, "Spatial, polarization, and pattern diversity for wireless handheld terminals," *IEEE Trans. Antennas Propag.*, vol. 49, no. 9, pp. 1271–1281, Sep. 2001.
- [36] J. DIJK, M. JEUKEN, and E. J. MAANDERS, "Antenna noise temperature," *Proc. IEE*, vol. 115, no. 10, pp. 1403–1410, Oct. 1968.
- [37] S. DOSSCHE, S. BLANCH, and J. ROMEU, "Optimum antenna matching to minimise signal correlation on a two-port antenna diversity system," *Electron. Lett.*, vol. 40, no. 19, pp. 1164–1165, Sep. 2004.
- [38] K. W. ECCLESTON and S. H. M. ONG, "Compact planar microstripline branch-line and rat-race couplers," *IEEE Trans. Microw. Theory Tech.*, vol. 51, no. 10, pp. 2119–2125, Oct. 2003.
- [39] R. M. FANO, "Theoretical limitations on the broadband matching of arbitrary impedances," *MIT Technical Report*, vol. 41, Jan. 1948.
- [40] G. J. FOSCHINI and M. J. GANS, "On limits of wireless communications in a fading environment when using multiple antennas," *Wireless Personal Commun.*, vol. 6, no. 3, pp. 311–335, Mar. 1998.

- [41] W. P. GEREN, C. R. CURRY, and J. ANDERSEN, "A practical technique for designing multiport coupling networks," *IEEE Trans. Microw. Theory Tech.*, vol. 44, no. 3, pp. 364–371, Mar. 1996.
- [42] E. N. GILBERT and S. P. MORGAN, "Optimum design of directive antenna arrays subject to random variations," *Bell Syst. Technical J.*, vol. 34, pp. 637–663, May 1955.
- [43] M. HAJIAN, H. NIKOOKAR, F. VAN DER ZWAN, and L. P. LIGTHART, "Branch correlation measurements and analysis in an indoor rayleigh fading channel for polarization diversity using a dual polarized patch antenna," *IEEE Microw. Wireless Compon. Lett.*, vol. 15, no. 9, pp. 555–557, Sep. 2005.
- [44] P. HALLBJÖRNER and K. MADSEN, "Terminal antenna diversity characterisation using mode stirred chamber," *Electron. Lett.*, vol. 37, no. 5, pp. 273–274, Mar. 2001.
- [45] J. K. HOLMES, "Tracking performance of the filter and square bit synchronizer," *IEEE Trans. Commun.*, vol. 28, no. 8, pp. 1154–1158, Aug. 1980.
- [46] M. A. JENSEN and Y. RAHMAT-SAMII, "Performance analysis of antennas for hand-held transceivers using FDTD," *IEEE Trans. Microw. Theory Tech.*, vol. 42, no. 8, pp. 1106–1113, Aug. 1994.
- [47] W. K. KAHN, "Element efficiency: a unifying concept for array antennas," *IEEE Antennas Propag. Mag.*, vol. 49, no. 4, pp. 48–56, Aug. 2007.
- [48] W. K. KAHN, "Active reflection coefficient and element efficiency in arbitrary antenna arrays," *IEEE Trans. Antennas Propag.*, vol. 17, no. 5, pp. 653–654, Sep. 1969.
- [49] M. KARABOIKIS, C. SORAS, G. TSACHTSIRIS, and V. MAKIOS, "Compact dual-printed inverted-f antenna diversity systems for portable wireless devices," *IEEE Antennas Wireless Propag. Lett.*, vol. 3, pp. 9–14, 2004.
- [50] P.-S. KILDAL and K. ROSENGREN, "Electromagnetic analysis of effective and apparent diversity gain of two parallel dipoles," *IEEE Antennas Wireless Propag. Lett.*, vol. 2, pp. 9–13, 2003.

- [51] P.-S. KILDAL and K. ROSENGREN, "Correlation and capacity of MIMO systems and mutual coupling, radiation efficiency, and diversity gain of their antennas: Simulations and measurements in a reverberation chamber," *IEEE Commun. Mag.*, vol. 42, no. 12, pp. 104–112, Dec. 2004.
- [52] S. C. K. KO and R. D. MURCH, "Compact integrated diversity antenna for wireless communications," *IEEE Trans. Antennas Propag.*, vol. 49, no. 6, pp. 954–960, Jun. 2001.
- [53] R. KOETTER, A. C. SINGER, and M. TÜCHLER, "Turbo equalization," *IEEE Signal Process. Mag.*, vol. 21, no. 1, pp. 67–80, Jan. 2004.
- [54] K. KUROKAWA, "Power waves and the scattering matrix," *IEEE Trans. Microw. Theory Tech.*, vol. 13, no. 2, pp. 194–202, Mar. 1965.
- [55] B. K. LAU, J. BACH ANDERSEN, G. KRISTENSSON, and A. F. MOLISCH, "Impact of matching network on bandwidth of compact antenna arrays," *IEEE Trans. Antennas Propag.*, vol. 54, no. 11, pp. 3225–3238, Nov. 2006.
- [56] W. C. Y. LEE, "Mutual coupling effect on maximum-ratio diversity combiners and applications to mobile radio," *IEEE Trans. Circuit Theory*, vol. 18, no. 6, pp. 779–791, Dec. 1970.
- [57] B. LINDMARK and L. GARCIA-GARCIA, "Compact antenna array for MIMO applications at 1800 and 2450 MHz," *Microw. Opt. Technol. Lett.*, vol. 48, no. 10, pp. 2034–2037, Oct. 2006.
- [58] M. MANTEGHI and Y. RAHMAT-SAMII, "Multiport characteristics of a wide-band cavity backed annular patch antenna for multipolarization operations," *IEEE Trans. Antennas Propag.*, vol. 53, no. 1, pp. 466–474, Jan. 2005.
- [59] R. B. MARKS and D. F. WILLIAMS, "A general waveguide circuit theory," *J. Res. Natl. Inst. Stand. Technol.*, vol. 97, pp. 533–561, Sep. 1992.
- [60] R. B. MARKS, D. F. WILLIAMS, and D. A. FRICKEY, "Comments on "conversions between S, Z, Y, H, ABCD, and T parameters which are valid for complex source and load impedances"," *IEEE Trans. Microw. Theory Tech.*, vol. 43, no. 4, pp. 914–915, Apr. 1995.

- [61] P. MATTHEIJSEN, M. H. A. J. HERBEN, G. DOLMANS, and L. LEYTEN, "Antenna-pattern diversity versus space diversity for use at handhelds," *IEEE Trans. Veh. Technol.*, vol. 53, no. 4, pp. 1035–1042, Jul. 2004.
- [62] M. L. MORRIS and M. A. JENSEN, "Improved network analysis of coupled antenna diversity performance," *IEEE Trans. Wireless Commun.*, vol. 4, no. 4, pp. 1928–1934, Jul. 2005.
- [63] P. V. NIKITIN, K. V. S. RAO, S. F. LAM, V. PILLAI, R. MARTINEZ, and H. HEINRICH, "Power reflection coefficient analysis for complex impedances in RFID tag design," *IEEE Trans. Microw. Theory Tech.*, vol. 53, no. 9, pp. 2721–2725, Sep. 2005.
- [64] O. NØRKLIT, P. D. TEAL, and R. G. VAUGHAN, "Measurement and evaluation of multi-antenna handsets in indoor mobile communication," *IEEE Trans. Antennas Propag.*, vol. 49, no. 3, pp. 429–437, Mar. 2001.
- [65] P. PENFIELD, JR., "Wave representation of amplifier noise," *IRE Trans. Circuit Theory*, vol. 9, no. 1, pp. 84–86, Mar. 1962.
- [66] J. N. PIERCE and S. STEIN, "Multiple diversity with nonindependent fading," *Proc. IRE*, vol. 48, no. 1, pp. 89–104, Jan. 1960.
- [67] J. R. PIERCE, "Physical sources of noise," *Proc. IRE*, vol. 44, no. 5, pp. 601–608, May 1956.
- [68] C. Y. PON, "Hybrid-ring directional coupler for arbitrary power divisions," *IRE Trans. Microw. Theory Tech.*, vol. 9, no. 6, pp. 529–535, Nov. 1961.
- [69] R. PRICE and P. E. GREEN, "A communication technique for multipath channels," *Proc. IRE*, vol. 46, no. 3, pp. 555–570, Mar. 1958.
- [70] B. REMBOLD, "Relation between diagram correlation factors and S-parameters of multiport antenna with arbitrary feeding network," *Electron. Lett.*, vol. 44, no. 1, pp. 5–7, Jan. 2008.
- [71] V. RIECH, "Überlegungen zu Entkopplungs- und Anpassungsnetzwerken für kleine Antennengruppen," *Archiv für Elektronik und Übertragungstechnik (AEÜ)*, vol. 30, no. 5, pp. 204–208, May 1976.

- [72] D. E. RIEGLE and P. M. LIN, "Matrix signal flow graphs and an optimum topological method for evaluating their gains," *IEEE Trans. Circuit Theory*, vol. 19, no. 5, pp. 427–435, Sep. 1972.
- [73] R. RODRIGUES SILVA, "The trace formulas yield the inverse metric formula," *J. Mathematical Physics*, vol. 39, pp. 6206–6213, 1998. [Online]. Available: <http://www.citebase.org/abstract?id=oai:arXiv.org:math-ph/9805006>
- [74] P. J. SMITH, S. ROY, and M. SHAFI, "Capacity of MIMO systems with semicorrelated flat fading," *IEEE Trans. Inf. Theory*, vol. 49, no. 10, pp. 2781–2788, Oct. 2003.
- [75] S. STEIN, "On cross coupling in multiple-beam antennas," *IRE Trans. Antennas Propag.*, vol. 10, no. 5, pp. 548–557, Sep. 1962.
- [76] A. STJERNMAN, "Relationship between radiation pattern correlation and scattering matrix of lossless and lossy antennas," *Electron. Lett.*, vol. 41, no. 12, pp. 678–680, Jun. 2005.
- [77] T. TAGA, "Analysis for mean effective gain of mobile antennas in land mobile radio," *IEEE Trans. Veh. Technol.*, vol. 39, no. 2, pp. 117–131, May 1990.
- [78] A. M. D. TURKMANI, A. A. AROWOJOLU, P. A. JEFFORD, and C. J. KELLET, "An experimental evaluation of the performance of two-branch space and polarization diversity schemes at 1800 MHz," *IEEE Trans. Veh. Technol.*, vol. 44, no. 2, pp. 318–326, May 1995.
- [79] R. G. VAUGHAN and J. BACH ANDERSEN, "Antenna diversity in mobile communications," *IEEE Trans. Veh. Technol.*, vol. 36, no. 4, pp. 149–172, Nov. 1987.
- [80] C. WALDSCHMIDT, S. SCHULTEIS, and W. WIESBECK, "Complete RF system model for analysis of compact MIMO arrays," *IEEE Trans. Veh. Technol.*, vol. 53, no. 3, pp. 579–586, May 2004.
- [81] J. W. WALLACE and M. A. JENSEN, "Termination-dependent diversity performance of coupled antennas: Network theory analysis," *IEEE Trans. Antennas Propag.*, vol. 52, no. 1, pp. 98–105, Jan. 2004.

- [82] J. W. WALLACE and M. A. JENSEN, "Mutual coupling in MIMO wireless systems: A rigorous network theory analysis," *IEEE Trans. Wireless Commun.*, vol. 3, no. 4, pp. 1317–1325, Jul. 2004.
- [83] K. F. WARNICK and M. A. JENSEN, "Effects of mutual coupling on interference mitigation with a focal plane array," *IEEE Trans. Antennas Propag.*, vol. 53, no. 8, pp. 2490–2498, Aug. 2005.
- [84] K. F. WARNICK and M. A. JENSEN, "Optimal noise matching for mutually coupled arrays," *IEEE Trans. Antennas Propag.*, vol. 55, no. 6, pp. 1726–1731, Jun. 2007.
- [85] B. S. YARMAN and H. J. CARLIN, "A simplified "real frequency" technique applied to broad-band multistage microwave amplifiers," *IEEE Trans. Microw. Theory Tech.*, vol. 30, no. 12, pp. 2216–2222, Dec. 1982.
- [86] D. C. YOULA, "On scattering matrices normalized to complex port numbers," *Proc. IRE*, vol. 49, no. 3, p. 1221, Mar. 1961.

Conference proceedings

- [87] J. A. G. AKKERMANS and M. H. A. J. HERBEN, "Planar beam-forming array for broadband communication in the 60 GHz band," in *Proc. 2nd Eur. Conf. Antennas Propag. (EuCAP)*, Edinburgh, UK, Nov. 2007.
- [88] H. J. CHALOUKKA and X. WANG, "Novel approach for diversity and MIMO antennas at small mobile platforms," in *Proc. 15th IEEE Int. Symp. Personal, Indoor Mobile Radio Commun. (PIMRC)*, vol. 1, Barcelona, Spain, Sep. 2004, pp. 637–642.
- [89] H. J. CHALOUKKA, X. WANG, and J. C. COETZEE, "Performance enhancement of smart antennas with reduced element spacing," in *Proc. IEEE Wireless Commun. Netw. Conf. (WCNC)*, vol. 1, New Orleans, Louisiana, USA, Mar. 2003, pp. 425–430.
- [90] H. J. CHALOUKKA, Y.-H. LU, and J. C. COETZEE, "A dual polarized microstrip antenna array with port decoupling for MIMO system," in *Proc. Int. Symp. Antennas Propag. (ISAP)*, Sendai, Japan, 2004, pp. 1229–1232.

- [91] S. K. CHAUDHURY, H. J. CHALOUPKA, and A. ZIROFF, “Novel mimo antennas for mobile terminal,” in *Proc. 38th Eur. Microw. Conf. (EuMC)*, Amsterdam, The Netherlands, Oct. 2008, pp. 1751–1754.
- [92] A. DIALLO, C. LUXEY, P. LE THUC, R. STARAJ, and G. KOSSIAVAS, “Enhanced diversity antennas for UMTS handsets,” in *Proc. 1st Eur. Conf. Antennas Propag. (EuCAP)*, Nice, France, Nov. 2006.
- [93] A. DIALLO, C. LUXEY, P. LE THUC, R. STARAJ, G. KOSSIAVAS, M. FRANZEN, and P.-S. KILDAL, “MIMO performance of enhanced UMTS four-antenna structures for mobile phones in the presence of the user’s head,” in *Proc. IEEE Antennas Propag. Soc. Int. Symp. (APS)*, Edinburgh, UK, Jun. 2007, pp. 2853–2856.
- [94] S. DOSSCHE, S. BLANCH, and J. ROMEU, “Decorrelation of a closely spaced four element antenna array,” in *Proc. IEEE Antennas Propag. Soc. Int. Symp. (APS)*, vol. 1B, 2005, pp. 803–806.
- [95] D. ESSER and H. J. CHALOUPKA, “Design approach for a class of compact multiport antennas,” in *Proc. IEEE Int. Symp. Microw., Antenna, Propag. EMC Technol. Wireless Commun. (MAPE)*, vol. 1, Beijing, China, Aug. 2005, pp. 144–147.
- [96] M. T. IVRLAČ and J. A. NOSSEK, “MIMO eigenbeamforming in correlated fading,” in *Proc. 1st Int. Conf. Circuits Syst. Commun. (ICCSC)*, St. Petersburg, Russia, Jun. 2002, pp. 212–215.
- [97] J. E. LEE, S. H. CHOI, and K. BEOMSUP, “Baseband clock recovery algorithm for $\pi/4$ -QPSK modulated signals,” in *Proc. 47th IEEE Veh. Technol. Conf. (VTC)*, vol. 3, Phoenix, AZ, USA, May 1997, pp. 1729–1733.
- [98] M. LEFEVRE, M. A. JENSEN, and M. D. RICE, “Indoor measurement of handset dual-antenna diversity performance,” in *Proc. 47th IEEE Veh. Technol. Conf. (VTC)*, vol. 3, Phoenix, AZ, USA, May 1997, pp. 1763–1767.
- [99] J. MEDBO and J.-E. BERG, “Spatio-temporal channel characteristics at 5 GHz in a typical office environment,” in *Proc. 54th IEEE Veh. Technol. Conf. (VTC)*, vol. 3, Atlantic City, NJ, USA, Oct. 2001, pp. 1256–1260.

- [100] P. MINARD, P. CHAMBELIN, and A. LOUZIR, “Cost/performance optimized IEEE802.11a/b/g front end with integrated antenna diversity,” in *Proc. 1st Eur. Conf. Antennas Propag. (EuCAP)*, Nice, France, Nov. 2006.
- [101] J. Ø. NIELSEN, G. F. PEDERSEN, K. OLESEN, and I. Z. KOVÁCS, “Computation of mean effective gain from 3D measurements,” in *Proc. 49th IEEE Veh. Technol. Conf. (VTC)*, vol. 1, Houston, TX, USA, Jul. 1999, pp. 787–791.
- [102] A. NILSSON, P. BODLUND, A. STJERNMAN, M. JOHANSSON, and A. DERNERYD, “Compensation network for optimizing antenna system for MIMO application,” in *Proc. 2nd Eur. Conf. Antennas Propag. (EuCAP)*, Edinburgh, UK, Nov. 2007.
- [103] O. NØRKLIT and R. G. VAUGHAN, “Method to determine effective number of diversity branches,” in *Proc. IEEE Global Telecommunications Conf. (GLOBECOM)*, vol. 1, Sydney, NSW, Australia, Nov. 1998, pp. 138–141.
- [104] V. PIATNITSA, D. KHOLODNYAK, P. KAPITANOVA, I. FISCHUK, T. TICK, J. JANTTI, H. JANTUNEN, and I. VENDIK, “Right/left-handed transmission line LTCC directional couplers,” in *Proc. 37th Eur. Microw. Conf. (EuMC)*, Munich, Germany, Oct. 2007, pp. 636–639.
- [105] R. R. RAMIREZ, L. JOFRE, and F. DE FLAVIIS, “Small size single and multiband antenna arrays with diversity capabilities for portable devices,” in *Proc. IEEE Radio Wireless Conf. (RAWCON)*, Waltham, MA, USA, Aug. 2001, pp. 215–218.
- [106] I. SALONEN and P. VAINIKAINEN, “Estimation of signal correlation in antenna arrays,” in *Proc. 12th Int. Symp. Antennas (JINA)*, vol. 2, Nice, France, Nov. 2002, pp. 383–386.
- [107] M. ŞENGÜL, J. TRABERT, K. BLAU, B. S. YARMAN, and M. A. HEIN, “Power transfer networks at RF frequencies—new design procedures with implementation roadmap,” in *Proc. IEEE Int. Symp. Circuits and Syst. (ISCAS)*, Island of Kos, Greece, May 2006, pp. 1768–1771.
- [108] A. SHAHBAHRAMI, B. H. H. JUURLINK, and S. VASSILIADIS, “Efficient vectorization of the FIR filter,” in *Proc. 16th Annual Workshop Circuits*,

- Syst., Signal Process. (ProRisc)*, Veldhoven, The Netherlands, Nov. 2005, pp. 432–437.
- [109] G. SHAKER, G. RAFI, S. SAFAVI-NAEINI, and N. SANGARY, “A synthesis technique for reducing mutual coupling between closely separated patch antennas,” in *Proc. IEEE Antennas Propag. Soc. Int. Symp. (APS)*, San Diego, CA, USA, Jul. 2008.
 - [110] K. SOLBACH and S. ANGENENDT, “Four-square phased array for multi-beam applications using novel matrix feed,” in *Proc. 37th Eur. Microw. Conf. (EuMC)*, Munich, Germany, Oct. 2007, pp. 1637–1640.
 - [111] K. SOLBACH and C. T. FAMDIE, “Mutual coupling and chassis-mode coupling in small phased array on a small ground plane,” in *Proc. 2nd Eur. Conf. Antennas Propag. (EuCAP)*, Edinburgh, UK, Nov. 2007.
 - [112] A. STJERNMAN, “Antenna mutual coupling effects on correlation, efficiency and Shannon capacity,” in *Proc. 1st Eur. Conf. Antennas Propag. (EuCAP)*, Nice, France, Nov. 2006.
 - [113] T. STRAUMANN and G. MÖNICH, “Effects of mutual antenna coupling on SAIR performance,” in *Proc. 8th Int. Conf. Antennas Propag. (ICAP)*, vol. 1, Edinburgh, UK, Apr. 1993, pp. 532–535.
 - [114] T. SVANTESSON and A. RANHEIM, “Mutual coupling effects on the capacity of multielement antenna systems,” in *Proc. IEEE Int. Conf. Acoust., Speech, Signal Process. (ICASSP)*, vol. 4, Salt Lake City, UT, USA, May 2001, pp. 2485–2488.
 - [115] K. F. WARNICK and P. RUSSEY, “Quantifying the noise penalty for a mutually coupled array,” in *Proc. IEEE Antennas Propag. Soc. Int. Symp. (APS)*, San Diego, CA, USA, Jul. 2008.
 - [116] L. K. YEUNG and Y. E. WANG, “An electronically scanning array with closely-spaced antenna elements,” in *Proc. IEEE Antennas Propag. Soc. Int. Symp. (APS)*, San Diego, CA, USA, Jul. 2008.

Theses

- [117] H. BAYER, “Rauschcharakterisierung eines mehrkanaligen Empfänger-systems,” diploma thesis, Ilmenau University of Technology, Ilmenau, Germany, 2009, in German.
- [118] H. BOSMA, “On the theory of linear noisy systems,” Ph.D. dissertation, Technische Hogeschool Eindhoven, Eindhoven, The Netherlands, Jan. 1967.
- [119] D. ESSER, “Kompakte Multimodenantennen für Kommunikationsanwendungen,” Ph.D. dissertation, Bergische Universität Wuppertal, Wuppertal, Germany, Nov. 2006, in German.
- [120] X. WANG, “Kompakte Mehrtorantennen für die adaptive Keulenformung,” Ph.D. dissertation, Bergische Universität Wuppertal, Wuppertal, Germany, Feb. 2004, in German.
- [121] J. WEBER, “Entwurf miniaturisierter Antennengruppen,” Ph.D. dissertation, Ilmenau University of Technology, Ilmenau, Germany, 2009, in German.

Miscellaneous

- [122] “Advanced Design System (ADS),” Agilent Technologies, 395 Page Mill Road, Palo Alto, CA 94304, USA.
- [123] “Agilent 85072A 10-GHz split cylinder resonator,” Technical Overview, Agilent Technologies, 5301 Stevens Creek Blvd, Santa Clara, CA 95051, USA, 2008. [Online]. Available: <http://cp.literature.agilent.com/litweb/pdf/5989-6182EN.pdf>
- [124] “Electronic components,” Analog Devices, Inc., 3 Technology Way, Norwood, MA 02062, USA. [Online]. Available: <http://www.analog.com>
- [125] “Arbitrary impedance,” Application Note, Anritsu Company, 490 Jarvis Drive, Morgan Hill, CA 95037-2809, USA, 2002. [Online]. Available: <http://www.us.anritsu.com/downloads/files/11410-00284B.pdf>

- [126] "CST Microwave Studio," CST GmbH, Bad Nauheimer Str. 19, 64289 Darmstadt, Germany.
- [127] "Electronic components," Cypress Semiconductor Corporation, 198 Champion Court San Jose, CA 95134, USA. [Online]. Available: <http://www.cypress.com>
- [128] T. HAHN, "Routines for the diagonalization of complex matrices," 2006. [Online]. Available: <http://www.citebase.org/abstract?id=oai:arXiv.org:physics/0607103>
- [129] "Electronic components," Hittite Microwave Corporation, 20 Alpha Road, Chelmsford, MA 01824, USA. [Online]. Available: <http://www.hittite.com>
- [130] "Electronic components," Infineon Technologies AG, Am Campeon 1-12, 85579 Neubiberg, Germany. [Online]. Available: <http://www.infineon.com>
- [131] "Electronic components," Maxim Integrated Products, Inc., 120 San Gabriel Drive, Sunnyvale, CA 94086, USA. [Online]. Available: <http://www.maxim-ic.com>
- [132] "Murata Chip Inductors," Murata Manufacturing Co., Ltd., 10-1, Higashikotari 1-chome, Nagaokakyo-shi, Kyoto 617-8555, Japan, <http://www.murata.com>.
- [133] "Electronic components," NEC Electronics Corporation, 1753 Shimonumabe, Nakahara-Ku, Kawasaki, Kanagawa 211-8668, Japan. [Online]. Available: <http://www.necel.com>
- [134] "High frequency laminates," Rogers Corporation, One Technology Drive, Rogers, CT 06263, USA, <http://www.rogerscorp.com>.
- [135] "Electronic components," Xilinx, Inc., 2100 Logic Drive, San Jose, CA 95124-3400, USA. [Online]. Available: <http://www.xilinx.com>
- [136] W. XU and S. QIAO, "A divide-and-conquer method for the Takagi factorization," Dept. of Computing and Software, McMaster University, Hamilton, Ontario, Canada, Tech. Rep. CAS 05-01-SQ, Feb. 2005.

Own publications

- [137] P. KAPITANOVA, C. VOLMER, S. HUMBLA, R. PERRONE, J. MÜLLER, and M. A. HEIN, “Miniaturized antenna decoupling network using left-handed transmission line sections,” in *Proc. 15th Int. Student Seminar Microw. Optical Appl. Novel Physical Phenomena*, St. Petersburg, Russia, May 2008, pp. 28–30.
- [138] M. SCHÜHLER, C. VOLMER, R. WANSCH, and M. A. HEIN, “Impedance measurement of a dipole above a periodically structured reflective surface,” *IEEE Antennas Wireless Propag. Lett.*, vol. 7, pp. 617–620, 2008.
- [139] M. ŞENGÜL, S. B. YARMAN, C. VOLMER, and M. A. HEIN, “Design of distributed-element RF filters via reflectance data modeling,” *Int. J. Electronics Commun. (AEÜ)*, vol. 62, no. 7, pp. 483–489, Aug. 2008.
- [140] C. VOLMER, J. WEBER, R. STEPHAN, K. BLAU, and M. A. HEIN, “Decoupling and matching network for miniaturised 3-port antenna arrays based on 180° couplers,” in *Proc. 2nd Int. ITG Conf. Antennas (INICA)*, Munich, Germany, Mar. 2007.
- [141] C. VOLMER, M. ŞENGÜL, J. WEBER, R. STEPHAN, and M. A. HEIN, “Broad-band decoupling and matching of a superdirective two-port antenna array,” *IEEE Antennas Wireless Propag. Lett.*, vol. 7, pp. 613–616, 2008.
- [142] C. VOLMER, J. WEBER, R. STEPHAN, K. BLAU, and M. A. HEIN, “An eigen-analysis of compact antenna arrays and its application to port decoupling,” *IEEE Trans. Antennas Propag.*, vol. 56, no. 2, pp. 360–370, Feb. 2008.
- [143] C. VOLMER, J. WEBER, R. STEPHAN, and M. A. HEIN, “Performance measurements of a two-branch diversity receiver with superdirective antenna array and decoupling and matching network,” in *Proc. IEEE Antennas Propag. Soc. Int. Symp. (APS)*, San Diego, CA, USA, Jul. 2008.
- [144] C. VOLMER, J. WEBER, R. STEPHAN, and M. A. HEIN, “A descriptive model for analyzing the diversity performance of compact antenna arrays,” *IEEE Trans. Antennas Propag.*, vol. 57, no. 2, Feb. 2009, in press.

- [145] C. VOLMER, J. WEBER, R. STEPHAN, and M. A. HEIN, “Mutual coupling in multi-antenna systems: Figures-of-merit and practical verification,” in *Proc. 3rd Eur. Conf. Antennas Propag. (EuCAP)*, Berlin, Germany, Mar. 2009.
- [146] J. WEBER, C. VOLMER, R. STEPHAN, and M. A. HEIN, “Eigenmode decoupling of miniaturised diversity antennas using compact quasi-lumped networks,” in *Proc. Loughborough Antennas Propag. Conf. (LAPC)*, Loughborough, UK, Mar. 2008.
- [147] J. WEBER, C. VOLMER, K. BLAU, R. STEPHAN, and M. A. HEIN, “Miniaturization of antenna arrays for mobile communications,” in *Proc. 35th Eur. Microwave Conf. (EuMC)*, Paris, France, Oct. 2005, pp. 1173–1176.
- [148] J. WEBER, C. VOLMER, K. BLAU, R. STEPHAN, and M. A. HEIN, “Miniaturized antenna arrays using decoupling networks with realistic elements,” *IEEE Trans. Microw. Theory Tech.*, vol. 54, no. 6, pp. 2733–2740, Jun. 2006.
- [149] J. WEBER, C. VOLMER, K. BLAU, R. STEPHAN, and M. A. HEIN, “Implementation of a miniaturised antenna array with predefined orthogonal radiation patterns,” in *Proc. 1st Eur. Conf. Antennas Propag. (EUCAP)*, Nice, France, Nov. 2006.
- [150] J. WEBER, G. DEL GALDO, C. VOLMER, M. HAARDT, and M. A. HEIN, “MIMO capabilities of a miniaturised antenna array with a decoupling and matching network,” in *Proc. Int. ITG/IEEE Workshop Smart Antennas (WSA)*, Vienna, Austria, Feb. 2007.
- [151] J. WEBER, C. VOLMER, K. BLAU, R. STEPHAN, and M. A. HEIN, “Miniaturized antenna arrays with an element separation down to $\lambda/10$,” in *Proc. IEEE Antennas Propag. Soc. Int. Symp. (APS)*, Honolulu, Hawaii, USA, Jun. 2007.

Notation and abbreviations

Mathematical notation

x	scalar, complex unless otherwise noted
\vec{x}, \vec{x}^T	column vector, row vector
x_i	i th element of the vector \vec{x}
\tilde{X}	matrix
\tilde{X}_{ij}	matrix element in row i , column j
$\text{Re}\{x\}, \text{Im}\{x\}$	Real and imaginary parts of a complex number
$ x $	absolute value
$ \vec{x} $	Euclidean vector norm
\log	base-10 logarithm
$x^*, \vec{x}^*, \tilde{X}^*$	complex conjugate, operates element-wise on matrices and vectors
\tilde{X}^T	matrix transpose (without conjugation)
\tilde{X}^H	Hermitian transpose (conjugate transpose)
$\text{tr}\{\tilde{X}\}$	matrix trace
$\det\{\tilde{X}\}$	matrix determinant
\tilde{X}^{-1}	matrix inverse
\tilde{X}^\dagger	Moore-Penrose pseudo-inverse
$\tilde{X}^{1/2}, \tilde{X}^{-1/2}$	square-root of a Hermitian matrix; its inverse
$\ \tilde{X}\ _2$	spectral matrix norm

$E\{x\}$	expected value of random variable x
$\text{Var}\{x\}$	variance of random variable x
$\text{Var}\{\vec{x}\}$	covariance matrix of random vector \vec{x}

Common quantities

All quantities related to electromagnetic fields are complex frequency-dependent harmonic root-mean-square amplitudes unless stated otherwise.

a, b	signal power waves, usually travelling in the transmit (a) and in the receive (b) direction
$d(\varrho)$	SNR cumulative distribution function (CDF)
G_d	diversity gain with respect to single-branch receiver
$F_i(\phi, \theta)$	embedded normalised far-field pattern of port i
\tilde{H}	radiation matrix; transposed covariance matrix
\tilde{I}	the identity matrix
k	Boltzmann constant, $k = 1.3806504 \text{ J/K}$
L_d	diversity loss with respect to ideal diversity receiver
n	number of antenna array ports
P	power
p	outage probability
$p(\cdots)$	probability density function (PDF)
\tilde{Q}	unitary matrix of eigenvectors/eigenmodes of \tilde{H}
\vec{q}_i	i th column of \tilde{Q} , i th eigenmode
\tilde{S}	scattering matrix
T, \tilde{T}	equivalent noise temperature and temperature covariance matrix
\vec{w}	vector of weights of a linear diversity combiner
Z_0	characteristic impedance of a transmission line
Z_{in}	internal or input impedance
Γ	single-port reflection coefficient

$\tilde{\Gamma}$	diagonal scattering matrix of several single-port loads
$\gamma_{m,i}$	i th modal reflection coefficient
θ	elevation
$\tilde{\Lambda}$	diagonal matrix of eigenvalues/eigen efficiencies of \tilde{H}
λ_0	free-space wavelength
λ_g	guided wavelength on a transmission line
λ_i	i th eigen efficiency
ν, μ	noise power waves, travelling in the transmit (ν) and in the receive (μ) direction
ρ_{ij}	complex envelope correlation coefficient between ports i and j
ϱ	signal-to-noise ratio (SNR)
ϕ	azimuth
φ	a phase angle
χ_i	i th ohmic eigen efficiency

Common subscripts

<i>no subscript</i>	commonly relates to the antenna array, e.g., \tilde{S} , \vec{d}
$\tilde{H}_{\text{acc}}, \lambda_{\text{acc}}$	relate to the power accepted by an array or system
$P_{\text{av}}, a_{\text{av}}$	power/power wave available from a source
$\tilde{H}_{\text{env}}, T_{\text{env}}$	relate to the communications environment
$Z_{\text{in,F}}, \nu_{\text{F}}$	relate to the receiver front-end
$Z_{\text{in}}, \Gamma_{\text{in}}$	internal or input impedance/reflection coefficient
$a_{\text{m}}, \Gamma_{\text{m}}$	indicate modal/eigenmode domain
$\tilde{S}_{\text{N}}, G_{\text{d,N}}$	relate to the array feed network
$\vec{b}_{\text{R}}, \tilde{T}_{\text{R}}$	relate to quantities at the end of the receiver chain
$\tilde{H}_{\text{rad}}, \lambda_{\text{rad}}$	relate to the power radiated by an array or system
$\tilde{S}_{\text{S}}, \tilde{H}_{\text{S}}, \vec{d}_{\text{S}}$	relate to the antenna system, i.e., the combination of array and network

Abbreviations

ADC	Analogue-to-Digital Converter
ADS	Advanced Design System (Software)
AEN	Anpass- und Enkoppelnetzwerk
AGC	Automatic Gain Control
C#	programming language, pronounce: “see sharp”
CDF	Cumulative Distribution Function
co-pol	co-polar
D/A	Digital/Analogue
DAC	Digital-to-Analogue Converter
DC	Direct Current
DMN	Decoupling and Matching Network
DSP	Digital Signal Processor
ENR	Excess Noise Ratio
FIFO	First In, First Out
FIR	Finite Impulse Reponse
FPGA	Field Programmable Gate Array
GPIF	General Programmable Interface
GUI	Graphical User Interface
HJ-FET	Hetero-Junction Field-Effect Transistor
ISI	Inter-Symbol Interference
ISM	Industrial, Scientific, Medical
LNA	Low Noise Amplifier
LO	Local Oscillator
LTCC	Low Temperature Co-fired Ceramic
MEG	Mean Effective Gain
MIMO	Multiple Input Multiple Output
MN	Matching Network
MRC	Maximal Ratio Combining
NF	Noise Figure
OFDM	Orthogonal Frequency Division Multiplex
PC	Personal Computer
PCB	Printed Circuit Board
PDF	Probability Density Function
PIFA	Planar Inverted-F Antenna
PLL	Phase-Locked Loop

PTFE	Polytetrafluorethylen, Teflon®
QPSK	Quadrature Phase-Shift Keying
RC	Resistor, Capacitor
RF	Radio Frequency
SIMD	Single Instruction Multiple Data
SMA	Sub-Miniature-A (RF connector)
SNR	Signal-to-Noise Ratio
SRFT	Simplified Real-Frequency Technique
USB	Universal Serial Bus
VCO	Voltage-Controlled Oscillator
WLAN	Wireless Local Area Network
XPR	Cross-Polar Ratio
x-pol	cross-polar